Tropical cyclone dynamics revealed by satellite ocean surface wind speeds observations : the key contribution of the near-core surface wind structure

Arthur Avenas

▶ **To cite this version:**

Arthur Avenas. Tropical cyclone dynamics revealed by satellite ocean surface wind speeds observations : the key contribution of the near-core surface wind structure. Signal and Image Processing. Ecole nationale supérieure Mines-Télécom Atlantique, 2024. English. NNT : 2024IMTA0397 . tel-04566057

HAL Id: tel-04566057

https://theses.hal.science/tel-04566057v1

Submitted on 2 May 2024

HAL is a multi-disciplinary open access archive for the deposit and dissemination of scientific research documents, whether they are published or not. The documents may come from teaching and research institutions in France or abroad, or from public or private research centers.

L'archive ouverte pluridisciplinaire **HAL**, est destinée au dépôt et à la diffusion de documents scientifiques de niveau recherche, publiés ou non, émanant des établissements d'enseignement et de recherche français ou étrangers, des laboratoires publics ou privés.

COLLEGES SCIENCES
BRETAGNE POUR L'INGENIEUR
LOIRE ET LE NUMERIQUE

IMT Atlantique
Bretagne-Pays de la Loire
École Mines-Télécom

THÈSE DE DOCTORAT DE

L'ÉCOLE NATIONALE SUPÉRIEURE
MINES-TÉLÉCOM ATLANTIQUE BRETAGNE
PAYS DE LA LOIRE – IMT ATLANTIQUE

ÉCOLE DOCTORALE N° 648
Sciences pour l'Ingénieur et le Numérique
Spécialité : *Physique et Sciences de l'Ingénieur*

Par
Arthur AVENAS

Tropical cyclone dynamics revealed by satellite ocean surface wind speeds observations

The key contribution of the near-core surface wind structure

Thèse présentée et soutenue à l'IUEM, Plouzané, le 28 mars 2024
Unité de recherche : Laboratoire d'Océanographie Physique et Spatiale/Laboratoire des Sciences et Techniques de l'Information de la Communication et de la Connaissance
Thèse N° : 2024IMTA0397

Rapporteurs avant soutenance :

Claudia PASQUERO	Associate Professor, Earth and Environmental Science Department at University of Milano-Bicocca
Paco LÓPEZ-DEKKER	Associate Professor, Geoscience and Remote Sensing Department at Delft University of Technology

Composition du Jury :

Président :	Xavier CARTON	Professor, UBO (France)
Examinateurs :	Claudia PASQUERO	Associate Professor, UNIMIB (Italy)
	Paco LÓPEZ-DEKKER	Associate Professor, TU Delft (Netherlands)
Dir. de thèse :	Ronan FABLET	Professor, IMT Atlantique (France)
Encadrants de thèse :	Bertrand CHAPRON	Researcher, IFREMER (France)
	John KNAFF	Researcher, NOAA (USA)

Invités :

Encadrants de thèse :	Alexis MOUCHE	Researcher, IFREMER (France)
	Pierre TANDEO	Associate Professor, IMT Atlantique (France)

Acknowledgement

In the same way the tropical cyclone owes its existence to a combination of processes occurring at diverse spatio-temporal scales, the completion of this thesis has benefited from numerous interactions within the professional, personal and familial spheres. Here I would like to express my deepest gratitude to all the individuals who have played a direct or indirect role in this collective work.

I am thankful to both Claudia Pasquero and Paco López-Dekker for accepting to review this manuscript, as well as Xavier Carton for agreeing to be part of the jury. I also acknowledge the members of the thesis monitoring committee, Veronica Nieves and Antohny Wimmers.

I am indebted to my supervisors, each of whom contributed in their own way to this work. Beyond your scientific expertise and availability, I would like to thank you Alexis and Bertrand, for your motivation and the autonomy you have given me during these three years; John, for your encouragement and welcoming me into your team and city for several months; Pierre and Ronan, for fruitful exchanges and constructive feedback.

I extend my heartfelt thanks to my friends and colleagues from the work environment. For your camaraderie and the moments we shared in the office or outside, thank you Édouard, Raphaël, Rémy, Alexandre, Clément, Robin, Léo, Paul, Marine, Fred, and all the others who I cannot mention if I want to remain concise. Thank you Jérôme, Fanny, and Valérie, for your help in many organisational and administrative tasks. Also, special thanks go to Chris and Naufal for the time we had in and around Fort Collins.

Finally, I would like to thank those who are close to me and have undoubtedly contributed to this academic journey. Dad, mom, for your tireless moral backing, understanding, and the determination that you have imparted to me over the years. Quentin, Gauthier, for always showing me the way, through your lucidity on both intellectual and emotional levels. Fanny, for being by my side all this time and helping me reassess my relationship with this work.

Qu'importe où nous allons, honnêtement. Je ne le cache pas. De moins en moins. Qu'importe ce qu'il y a au bout. Ce qui vaut, ce qui restera n'est pas le nombre de cols de haute altitude que nous passerons vivants. N'est pas l'emplacement où nous finirons par planter notre oriflamme, au milieu d'un champ de neige ou au sommet d'un dernier pic dont on ne pourra plus jamais redescendre. N'est plus de savoir combien de kilomètres en amont du drapeau de nos parents nous nous écroulerons ! Je m'en fiche ! Ce qui restera est une certaine qualité d'amitié, architecturée par l'estime. Et brodée des quelques rires, des quelques éclats de courage ou de génie qu'on aura su s'offrir les uns aux autres. Pour tout ça, les filles et les gars, je vous dis merci. Merci.

Alain Damasio, La Horde du Contrevent, 2004.

RÉSUMÉ EN FRANÇAIS

Les cyclones tropicaux (TCs) sont d'imposants vortex atmosphériques caractérisés par des vents violents et des pluies abondantes. Ces phénomènes se produisent ∼80-90 fois par an à l'échelle du globe, évoluent sur des périodes de ∼5-20 jours et couvrent des distances considérables, ∼100-1000 km horizontalement et ∼10-20 km verticalement. Bien que les vents les plus forts, pouvant atteindre ∼30-80 m/s, soient concentrés près du cœur (ou *œil*), à ∼10-50 km du centre de la perturbation, des rafales significatives se manifestent jusqu'à ∼100-300 km. On peut assimiler les TCs à des machines thermiques qui extraient de l'énergie sous forme de chaleur latente des couches supérieures de l'océan vers l'atmosphère, la transforment en chaleur sensible lors de la condensation, et génèrent de l'énergie cinétique en réponse aux perturbations de pression résultantes. Le potentiel destructeur de ces phénomènes est généralement caractérisé par la structure de leur champ de vent surfacique. Comprendre et prévoir ces événements est crucial pour atténuer leur impact socio-économique sur les populations côtières, en particulier dans un contexte d'augmentation de leur intensité et taux de précipitation, lié au réchauffement climatique global.

Malgré les progrès réalisés dans la prédiction de leur trajectoire et des vitesses de vent loin du centre de la perturbation, les systèmes les plus intenses souffrent d'une représentation limitée et imprécise des vents les plus forts, en particulier près du cœur, dans les modèles numériques actuels. Des défis techniques et théoriques expliquent cette difficulté à simuler les caractéristiques structurelles du champ de vent de surface près du cœur des TCs, pourtant cruciales pour estimer les ondes de tempête, les réponses de la couche supérieure de l'océan et les champs de vagues associés à ces phénomènes. Le cœur d'un système mature, de par sa faible extension radiale, nécessite une très haute résolution spatiale pour être adéquatement représenté. En outre, des lacunes dans la compréhension des interactions turbulentes dans des conditions de vents forts compliquent la paramétrisation des échanges turbulents air-mer dans les modèles numériques.

Les observations jouent un rôle crucial dans l'étude de ces phénomènes compte tenu des limites des simulations numériques. Historiquement, les estimations les plus systématiques du champ de vent surfacique des TCs reposaient sur des méthodes indirectes

utilisant des capteurs embarqués à bord d'avion et de satellites géostationnaires. Des mesures plus directes ont été mises au point grâce au développment de la diffusiomètrie et de la radiométrie satellitaire. Cependant, ces méthodes sont limitées pour résoudre les caractéristiques structurelles proche du cœur. Les récents progrès en radar à ouverture synthétique (SAR) fournissent enfin des observations haute résolution et bidimensionnelles de ces phénomènes permettant d'estimer le champ de vent de surface, y compris près du cœur. Néanmoins, des défis persistent, tels que l'échantillonnage spatio-temporel limité et le manque d'informations données par les instruments SAR sur les directions locales du vent.

Pour simplifier le champ de vent complexe bidimensionnel des TCs, les communautés opérationnelles et académiques ont recours à des simplifications stratégiques. Pour faciliter leurs opérations, les prévisionnistes se concentrent sur des paramètres clés qui quantifient entre autres l'intensité de la perturbation, la taille du cœur et celle du système entier. En recherche, de nombreux développements théoriques sont réalisés en supposant que le TC est axisymétrique. Dans ce cadre simplifié, *i.e* paramétrique et axisymétrique, qui est également celui de cette thèse, des relations entre les paramètres structurels qui caractérisent le système peuvent être mises en évidence.

Suivant une approche combinant traitement de données et analyses théoriques, la thèse vise à répondre aux questions suivantes: peut-on retrouver les caractéristiques structurelles près du cœur, telles que mesurées par des capteurs haute résolution, à partir d'instruments ou de sorties numériques de résolution plus faible ? La réduction du champ de vent de surface à des paramètres structurels spécifiques encode-t-elle la dynamique complète de ces phénomènes ? Comment les caractéristiques structurelles près du cœur contribuent au cycle de vie des TCs ?

Ces questions peuvent maintenant bénéficier d'observations de référence, à très haute résolution et bidimensionnelles (SAR) de TCs, permettant de s'appuyer sur un cadre théorique simple. Le **Chapitre 1** dresse un bref historique des instruments utilisés pour observer les TCs, ainsi qu'une synthèse des éléments théoriques permettant de décrire ces phénomènes. En particulier, les instruments satellitaires ayant été historiquement les plus souvent utilisés pour estimer le vent de surface (*i.e* les diffusiomètres et les radiomètres), ne permettent pas de représenter avec précision les forts gradients de vents près du cœur des TCs les plus intenses. Bien que ces capteurs soient adaptés pour estimer les propriétés du champ de vent en périphérie du système, les théories suggèrent que l'intensité des vents les plus forts et leur étendue radiale sont cruciales pour la dynamique des TCs.

Tant qu'un meilleur échantillonnage spatio-temporel des instruments haute résolution n'est pas atteint, il est nécessaire de s'attaquer au manque d'estimations systématiques et fiables de la structure du vent de surface près du cœur de ces phénomènes.

Une manière naturelle de traiter ce problème consiste à évaluer si les caractéristiques structurelles près du cœur peuvent être retrouvées à partir des propriétés observées du champ de vent en périphérie. Dans le **Chapitre 2**, une base de données d'estimées à haute résolution de la vitesse du vent de surface obtenues à partir de mesures SAR a été utilisée. Grâce à ces observations, une prédiction statistique de la taille du cœur peut être réalisée en fonction d'estimées de vitesses du vent en périphérie données par des instruments de résolution inférieure. En supposant l'intensité du système connue, l'approche statistique présentée s'avère efficace. Cela était attendu en raison de lois fondamentales de conservation qui gouvernent la dynamique des TCs (*i.e* conservation de la vorticité potentielle dans la partie inférieure de l'écoulement et conservation du moment cinétique dans la partie supérieure). Cependant, la variabilité du gradient de vent de surface près du cœur du système, telle qu'observée dans la base de données haute résolution, et qui module ces lois fondamentales de conservation, est trop importante pour être capturée par des relations statistiques simples. Ainsi, pour certains événements, la prédiction échoue. Les propriétés dynamiques de tels cas, qui ne peuvent être identifiées qu'avec des mesures à haute résolution, doivent être étudiées.

Cette analyse est menée dans le **Chapitre 3**, en remarquant que le gradient de vent de surface près du cœur contrôle l'amplitude des vitesses verticales dans le système. Si ces mouvements ascendants peuvent être négligés en périphérie du TC, ils deviennent significatifs et augmentent au fur et à mesure que l'on s'approche du centre de la perturbation. Cette caractéristique est notamment prononcée dans un domaine dont l'extension radiale est d'environ deux fois la taille du cœur. Dans cette région, des échanges turbulents cruciaux entre l'air et la mer ont lieu, si bien que l'amplitude des vitesses verticales peut être reliée à l'énergie gagnée par le système par chauffage, tandis que le gradient du vent de surface renseigne sur l'énergie perdue par friction. Cette région, qui peut efficacement être étudiée avec une observation haute résolution, est donc cruciale pour l'équilibre énergétique du système. L'analyse de ces observations et de changements temporels de l'énergie cinétique estimés à partir de jeux de données de référence corrobore le fait qu'une connaissance instantanée du gradient du vent de surface près du cœur informe sur l'évolution énergétique du système.

Une extension naturelle de ces résultats consiste à développer un modèle pour l'évolution

de la structure complète du vent de surface à partir d'une estimation instantanée à haute résolution de ce dernier. C'est ce qui est tenté et évalué dans le **Chapitre 4**, où un tel modèle est obtenu analytiquement. Dans le cadre théorique proposé, l'évolution du vent de surface peut être prédite sur une courte période ($\sim$12 heures) lorsque le changement d'intensité est connu. La solution analytique est en accord avec des estimées d'évolution de vitesses de vent données par des mesures SAR, pour les quelques cas observés où l'échantillonnage temporel est suffisant. L'analyse montre également les limites de l'utilisation d'un modèle simplifié: sous l'hypothèse d'axisymétrie et en l'absence d'information sur la direction du vent, le profil radial de vent est persistant en temps dans la périphérie du système sur une courte durée, tandis que les vitesses du vent près du cœur peuvent varier drastiquement sur le même laps de temps. Un tel résultat empêche la correction potentielle de mesures réalisées avec des instruments à basse résolution près du cœur du système uniquement à partir des variations de la vitesse du vent observées en périphérie.

La thèse évalue pour la première fois des hypothèses fondamentales sur les lois de conservation des TCs à l'aide d'estimations haute résolution et bidimensionnelles du champ de vent surfacique. Comme démontré, cela ouvre la voie à une extension de la théorie des échanges turbulents air-mer aux vents forts. Malgré les limites du cadre théorique présenté, ce travail souligne la nécessité d'un guide méthodologique pour interpréter la richesse d'informations fournies par des mesures haute résolution, tandis qu'une augmentation de l'échantillonnage spatio-temporel des instruments SAR grâce au lancement de nouveaux satellites, ainsi qu'une meilleure capacité d'observation de la direction du vent proche du cœur du TC grâce au développement de technologies de mesures aéroportées et satellitaires, sont à venir. Ces avancées technologiques combinées au cadre d'analyse proposé par cette thèse permettront d'approfondir notre connaissance des TCs pour mieux anticiper leur évolution court- et long-terme.

Table of Contents

INTRODUCTION

Evolving in almost every ocean basins, tropical cyclones (TCs) are large atmospheric vortices characterized by violent winds and extreme rainfall rates. Persisting during typically ∼5-20 days, these events occur on average ∼80-90 times per year and extend over ∼100-1000 km horizontally and ∼10-20 km vertically. In the range ∼30-80 m/s, the strongest winds occur near the core - or "eye" - of the TC, ∼10-50 km far from its center where wind speeds are typically much weaker. Away from the core, the wind speeds quickly decay with the distance from the TC center, but significant gales still occur on the first ∼100-300 km.

In order to mitigate their socio-economic impacts on coastal populations, better understanding and forecasting TCs is essential, especially in a global warming context where the intensity of the most intense events and the average rainfall rates are expected to increase. The destructive potential of these phenomena is typically characterized by their surface wind structure. Despite significant advances in the prediction of TCs trajectory and outer-core (*i.e* far away from the vortex core) wind speeds over the last decades, state-of-the-art numerical and neural network models fail to accurately represent the amplitude and the radial extent of the strongest surface winds occurring near the core of mature events. Yet, these near-core structural features and their time variations are crucial to estimate the wave field, storm surge, and upper ocean responses associated with TCs passages, which in turn strongly affect the coastal communities and the carbon cycle.

Several reasons may be invoked to explain why the prediction of these near-core structural features is still an issue. From a technical perspective, the core of a mature and intense TC has a small radial extent and can only be represented by high-resolution numerical models. Because of the large size of the complete system, such a high resolution is difficult to achieve on the whole numerical domain. Some key processes governing the TC, such as turbulent air-sea exchanges, can not explicitly be resolved and are parameterized, strongly affecting the near-core structural features. Yet, from a theoretical perspective, the properties of turbulent air-sea exchanges at high winds (above ∼30 m/s) are still badly understood and constitute an active field of research. This lack of knowledge certainly impacts numerical simulations and their parametrization schemes. From an observational

perspective, the field experiments that were designed to quantify TCs air-sea exchanges are hampered by our limited capacity to perform accurate measurements in extreme winds conditions. In addition, geostationary satellites, which were classically used for the operational monitoring of TCs based on their cloud patterns, do not directly inform on the air-sea interface.

Because of the limited predictive ability of numerical simulations and the gaps in theoretical frameworks, observations remain crucial to monitor and study TCs. Figure 1 summarizes the major observation categories for TCs applications ordered by chronological order (x-axis), by their ability to resolve near-core structural features (y-axis), and by sampling frequency (z-axis).

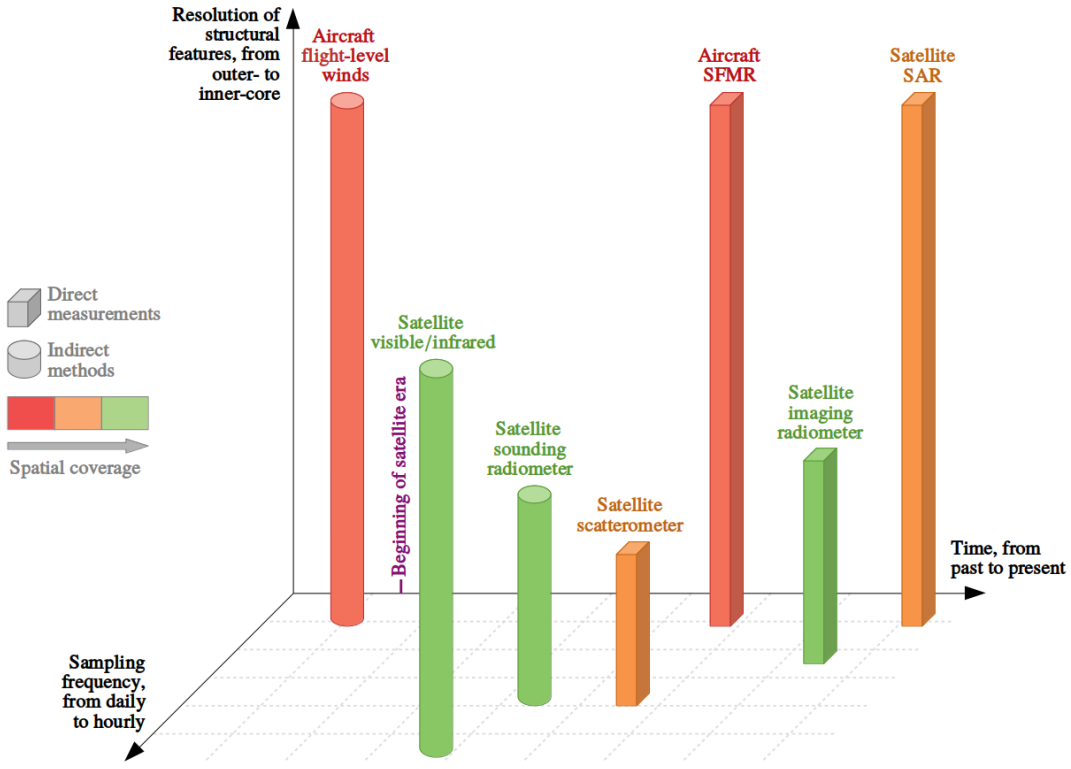

Figure 1 – Synthesis of observational capabilities for the estimation of TCs ocean surface wind structure.

Historically, estimates of TCs ocean surface wind structure were first determined indirectly, based on aircraft wind measurements at flight-level, or using empirical relationships from the cloud characteristics well observed using visible and infrared channels of geostationary satellites sensors. Complementing these observations, passive microwave radiometers onboard Earth-orbiting platforms were sounding the TC atmospheric tem-

perature properties and vertical distribution, from which wind structure estimates could be statistically achieved. Nevertheless, these methods were subject to large uncertainties, especially when approaching the core of the TC.

Later, more direct estimates of the two-dimensional ocean surface wind field from space were obtained by Earth-orbiting scatterometers and passive microwave imagers. However, near-core structural features, associated with the TCs strongest winds, wind gradients, and rain rates are poorly resolved by these low-resolution ($\sim$25-50 km) spaceborne instruments. In parallel, also using microwave channels, new airborne sensors were developed, allowing for direct ocean surface measurements and at very high radial resolution ($\sim$1 km). Yet, these aircraft observations require temporal compositing for two-dimensional analyzes and lack azimuthal coverage.

Recently, it has became possible to process spaceborne synthetic aperture radar (SAR) high-resolution ($\sim$1 km) and wide-swath observations, with new acquisition modes (combining co- and cross-polarized channels), to provide two-dimensional ocean surface wind speed estimates in nearly all-weather conditions, covering the whole vortex and including a fine description of the TC core. Yet, lacking spatio-temporal sampling and not informing on the wind directions, current SAR instruments and algorithms cannot alone meet the demand for systematic and reliable surface winds estimates near the TC core necessary for monitoring and research applications. These observations should certainly be combined with lower resolution tools, which often have a better spatio-temporal sampling, to analyze or predict short- (*e.g* a few hours to a few days) and long-term (*e.g* climatological) trends in the TC wind structure. Lastly, although they do not directly quantify turbulence, the high-resolution SAR observations provide an excellent opportunity to improve our understanding of TCs air-sea exchanges.

Due to the complexity of the TC system and the amount of information contained in a two-dimensional wind field, both operational and research communities have attempted to reduce the problem dimension using judicious simplifications. In particular, forecasters in operation centers, aiming at facilitating decision-making processes and warning issues, are focusing on the amplitude of the strongest winds (V_{max}) and their distance from the TC center (R_{max}). They also report measures of the TC outer-size to complement the core information, in particular the radial extent of the gale-force winds (R_{34}), in each of the four geographical quadrants of the system. In research studies, theoreticians aim at developing methodological guides to anticipate and interpret changes in the characteristics of these events. In such works, the geographical quadrants view is abandoned in favour

of an axisymmetric assumption. To illustrate how these structural parameters vary over time in an axisymmetric framework, Fig. 2 presents V_{max}, R_{max} and R_{34} times series from two days before the lifetime maximum intensity (LMI) of each TC and up to six days after, averaged over several hundreds of events. On average, the system outer-size (R_{34}) continuously grows over time. In parallel, while the TC maximum winds (V_{max}) first increase towards their peak value (*i.e* the LMI) and then decrease, they are negatively correlated to their radial extent (R_{max}), closely following angular momentum conservation.

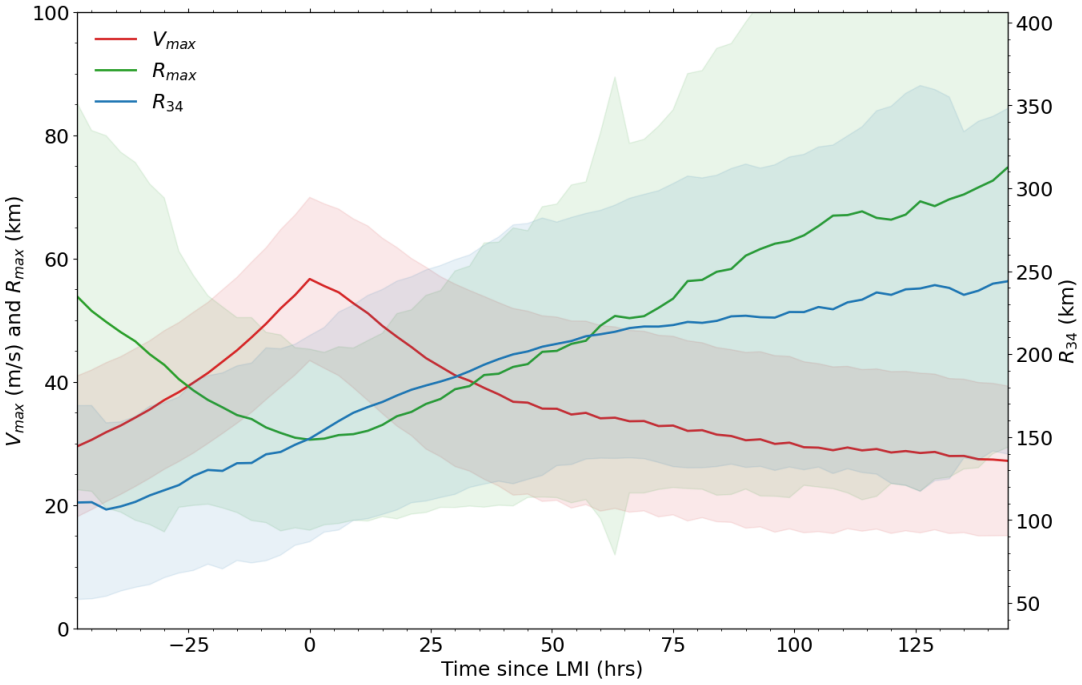

Figure 2 – Average best-track time series of surface wind structure parameters. TCs from the IBTrACS database since January 1^{st}, 2000 have been aggregated provided that their LMI exceeded 33 m/s and that their R_{max} was recorded for at least three consecutive days.

Even though the quality of a near-core parameter estimate such as R_{max} can be questioned in Fig. 2, essentially because of observational limitations, these average trends raise three research questions. First, they suggest that physical and dynamical restrictions are constraining the set of structural parameters in space and time. The question arises whether, based on these restrictions, the near-core structural features resolved by high-resolution sensors can be retrieved from lower resolution instruments or numerical outputs. Second, it is essential to determine whether the reduction of the surface wind field to such a set of structural parameters encodes the complete TC dynamics. Third, be-

cause they are poorly resolved by low-resolution instruments or numerical simulations, the relative importance of near-core structural features to the TC life cycle must be evaluated.

In this thesis, these three questions are addressed using SAR observations of TCs and a simple theoretical framework. Fundamental assumptions on the TC conservation laws are for the first time evaluated with two-dimensional high-resolution surface wind structure estimates, paving the way for an extension of air-sea turbulent exchanges theory at high winds. In **Chapter 1**, we present an overview of TCs and their wind structure, including a historical synopsis of observational capabilities used by research and operational communities and a synthesis of theoretical elements describing the TC system. Then, we question in **Chapter 2** whether the complete parametric TC surface wind structure, including near the core, may be retrieved from structural estimates that are either sufficiently accurate in reference reanalysis datasets or well resolved by low-resolution instruments. In **Chapter 3**, we assess how an instantaneous high-resolution observation of the surface wind speeds in TCs, and especially of their near-core wind structure, informs on potential changes in their life cycle. Finally, in **Chapter 4**, we investigate the short-term TC dynamics and examine whether temporal modifications of the wind structure far from the core may support the estimation of the near-core surface wind speeds.

Chapter 1

General background on tropical cyclones

At tropical latitudes, coastal city dwellers aiming at minimizing socio-economic damage, farmers in arid regions who want to anticipate the next rains, or surfers looking for the next big swell, all may have a common interest in TCs. In this chapter, we present a few generalities about these phenomena, and then draw a brief history of the measurement instruments that were developed to monitor and study their characteristics, before introducing the main theoretical elements that describe the TC system. In these last two sections, emphasis is given to the TC wind structure, to lay the foundations for the next chapters.

1.1 General overview

The literature on TCs is extensive. These natural phenomena are remarkable in several respects, and a plethora of researchers in atmospheric and ocean sciences all around the world have assessed and recorded their characteristics. In this section, we only present a tiny fraction of what is known about these events. After briefly defining TCs, we introduce some of their main properties.

1.1.1 Definition

> «A tropical cyclone is a rapid rotating storm originating over tropical oceans from where it draws the energy to develop.»

This concise definition of TCs is proposed on the World Meteorological Organization (WMO) website and highlights the energy source of TCs. More precisely, TCs act as thermal machines that extract energy in the form of latent heat from the upper layers

of the ocean to the atmosphere, transform it into sensible heat during condensation, and generate kinetic energy in response to the resulting pressure perturbations (Beucher et al., 2010). By developing internal available potential energy from which kinetic energy can be generated, TCs differ from extratropical cyclones, which extract available and kinetic energy from the mean flow.

TCs are linked to the tropics in that the ocean water must be warm enough in order to fuel the heat engine. A sea surface temperature (SST) of more than 26 °C was early identified as a necessary condition for the TC development (Gray, 1968). In addition, TCs form in low baroclinic (*i.e* when density and pressure surfaces are nearly coincident) and low vertical wind shear (*i.e* when there are small differences in the wind speeds and directions throughout the depth of the troposphere) environments. However, for formation to occur, some planetary vorticity must also exist, so that TCs rarely form equatorward of 5° latitude.

The structure of TCs follows from the above stated principles. A mature TC's structure exemplifies that of a warm core low pressure system without fronts. The maximum atmospheric temperature anomalies are located at the center and in the upper troposphere with pressure gradients and rotating winds that increase toward the Earth's surface, with the strongest winds occurring at the top of the planetary boundary layer (BL). The center of the TC is often nearly cloud free and is much warmer than its surroundings, forming an "eye" with the maximum surface winds lying on the inner edge of the eye, or eyewall where thunderstorms extend to the tropopause. Due to the TC vertical structure, the eyewall slopes outward roughly following angular momentum surfaces.

While their thermo-mechanical nature is universal, the word used to describe TCs depends on the considered region. In Asia, they are known as typhoons as soon as their intensity exceeds 33 m/s (or 64 kts [1]), or equivalently, reaches the category 1 on the Saffir-Simpson scale [2]. In the United States (US), weaker TCs may be known as tropical depressions or tropical storms, while people refer to hurricanes when their intensity exceeds 33 m/s. Wind speeds that reach 33 m/s are thus often referred to as hurricane-force winds. Similarly, wind speeds of 26 m/s (50 kts) or 17 m/s (34 kts) are referred to as damaging-force winds or gale-force winds, respectively.

1. 1 kt = 0.514 m/s.
2. All along the manuscript, the word "category" is always relative to the Saffir-Simpson scale.

1.1.2 Occurrences and societal implications

Figure 1.1 displays a worldwide map of ∼150 years of accumulated TCs tracks, revealing many characteristics of these events.

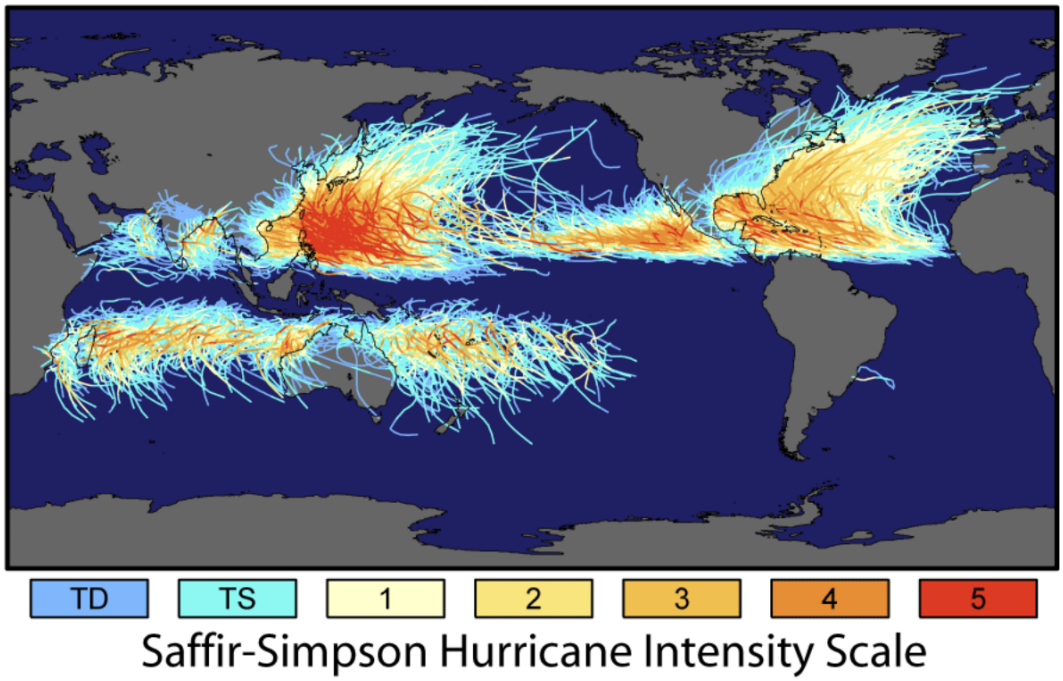

Figure 1.1 – Accumulated TCs tracks from ∼1850 to 2006 and based on NHC and JTWC best-track data. Colors denote TCs intensity on the Saffir-Simpson scale. TD (tropical depression): less than 17 m/s. TS (tropical storm): 18-32 m/s. 1: 33-42 m/s. 2: 43-49 m/s. 3: 50-58 m/s. 4: 58-70 m/s. 5: more than 70 m/s. Figure taken from National Aeronautics and Space Administration (NASA) Earth Observatory website.

First, they occur in almost every ocean basins. This has led the community to establish a worldwide coordinated system to ensure that TCs meteorological previsions would cover each region. For instance, the Atlantic and Eastern Pacific are covered by the US National Hurricane Center (NHC), while the Northwest Pacific is covered by the Japan Meteorological Agency (JMA). Note that no TC occurs in the easternmost South Pacific nor West of South Africa because of the Peru Current and the Benguela Current, respectively. These currents carry cool water masses from the polar region, hindering the necessary condition of warm SST for the TC development. With unfavorable conditions for TCs, the South Atlantic hosted only one TC in recent history (McTaggart-Cowan et al., 2006), Catarina, in 2004, which had dramatic implications for the unprepared coastal regions.

Second, TCs are moving from where they form at low latitudes to higher latitudes and to a first order they follow large-scale atmospheric patterns (*i.e* prevailing easterlies and westerlies). While in reality a beta effect [3] also affects TCs trajectory (Holland, 1982), comparably to what occurs with ocean eddies (Robinson, 2012), this influences the motion only to a second order. The observed total translation speed of TCs ranges between ∼1 and ∼10 m/s.

Third, there are regional differences in TCs intensity and the length of the tracks. For instance, there are several category 5 TCs in the Northwest Pacific, while very few occur in the Indian Ocean where the tracks also seem shorter. These differences are the result of various environmental constrains, such as basin size and configuration as well as ocean- and atmosphere basin-average characteristics. No TC is observed near the equator, because the vertical component of the Coriolis effect, responsible for the rotation of the air masses converging toward the perturbation center, vanishes there. In addition, inside each basin, the lowest intensities are observed at low latitudes, where TCs develop; over land, where they lose fluxes of energy from the ocean and are only subject to friction; and at higher latitudes, where SSTs are colder. Overall, the highest intensities are observed at subtropical latitudes, where there is the best compromise between the Coriolis effect increasing the spinning nature of converging air masses and ocean characteristics providing the fuel for the whole system.

While Fig. 1.1 reveals where TCs events occur, it says nothing about their seasonality. Figure 1.2 represents the average monthly counts of TCs occurrences in each regions. The most active period for the Northern Hemisphere, which accounts for ∼90% of the TC activity, goes from June to November, while in the Southern Hemisphere, ∼94% of the TC activity occurs between November and April (Ramsay, 2017). There is a variability in the TC active season even for a single hemisphere. For example, the distribution of TC events is sharp and peaks in September for the North Atlantic, while the distribution appears more flattened and peaks in August for the Western North Pacific. Like for the regional variability in intensity, the discrepancies in frequency may be attributed to basin size and configuration as well as ocean- and atmosphere basin-average characteristics.

All over the world, the destructiveness of TCs is manifested by riverine floods associated with extreme rainfall rates, storm surge floods and violent winds. Threatening

3. Because of a vorticity gradient between the equator and the poles, air with anticyclonic anomaly is carried on the eastern side of the TC, while air with cyclonic anomaly is carried on the western side of the TC. Taken together, these anomalies imply that TCs drift poleward and westward with respect to the surrounding winds.

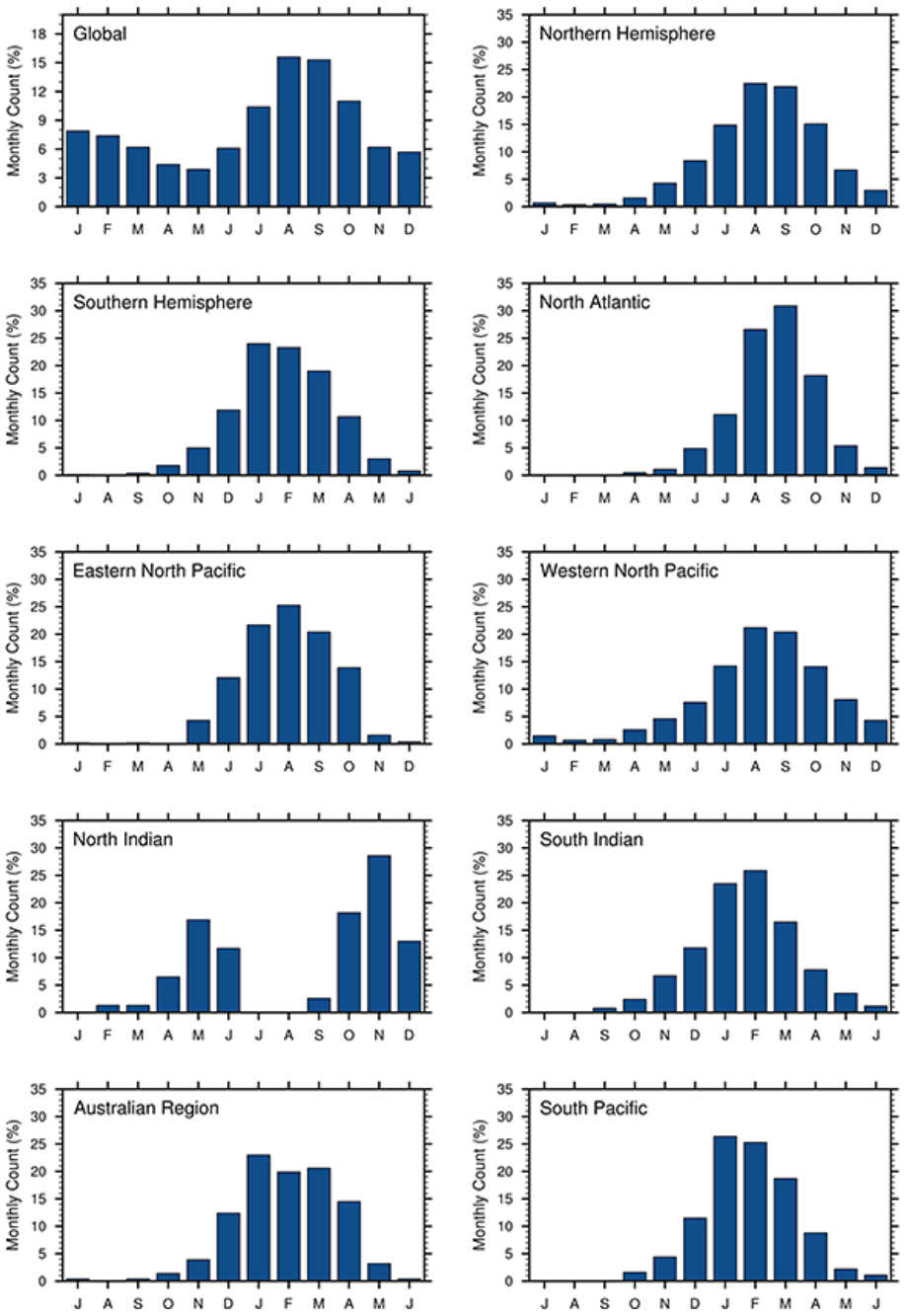

Figure 1.2 – Histograms of TCs monthly occurrences in each region, from 1985 to 2014 and based on NHC and JTWC best-track data. Extracted from Ramsay, 2017.

human lives, these events may thus be fatal for coastal populations and cause tremendous damages. For example, approximately 500,000 deaths were reported during the deadliest TC in history, the Great Bhola Cyclone which struck Bangladesh in 1970 (Scowcroft et al.,

2011). Furthermore, each year, average normalized [4] damages are estimated to represent ∼$17 billions for the US only (Weinkle et al., 2018). It is thus crucial to better understand and forecast such events in order to mitigate their disastrous consequences.

1.2 Observations

Observational capabilities were developed in order to better forecast and understand these extreme phenomena. In this section, a glimpse into the long history of TCs observations is given, with a focus on the wind structure, from both direct measurements or indirect methods. Today more than ever before, measurement instruments are continuously improving. The sensors that are currently in development phase are not covered by the present section.

Many of these techniques rely on remote sensing capabilities. Historically, the electromagnetic frequency ranges used by remote sensors are designated by letters. This designation system was standardized by the institute of electrical and electronics engineers (IEEE) in 1984. Table 1.1 summarizes the letters associated with the frequency ranges which are the most relevant to our purpose.

IEEE band	Frequency range (GHz)	Wavelength (cm)
L	1 - 2	15 - 30
S	2 - 4	5 - 15
C	4 - 8	3.75 - 5
X	8 - 12	2.5 - 3.75
Ku	12 - 18	1.6 - 2.5
K	18 - 26	1.2 - 1.6
Ka	26 - 40	0.75 - 1.2

Table 1.1 – Frequency bands in the electromagnetic spectrum (IEEE Standard 521-1984).

1.2.1 Before the 1960s: the pre-satellite era and the need for routine observations

The development of accurate observational technologies was largely hampered by the fact that TCs evolve over the ocean. Before the 20^{th} century, most observations of TCs

4. In order to account for inflation, population changes, and economic development, financial damage loss estimates are often normalized by those of a reference year, 2018 in Weinkle et al., 2018.

consisted in reports from ships at sea. They were complemented by terrestrial observations when TCs moved over islands or coastal regions at landfall. In the middle of the 19^{th} century, these information were sufficient to provide a crude description of TCs, at least for navigation purposes. TCs characteristics, such as their preferred tracks, translation speeds, sizes, intensities, as well as the associated wave field and currents, were eventually gathered into books (Piddington, 1848).

A milestone toward a more modern approach was set in 1943 with the first airborne reconnaissance of a TC. With the aim of facilitating the navigation of navy warships across the storms, and galvanized by several US naval disasters, the breeding ground for routine observations of TCs was set up. Rapidly, aircraft reconnaissance was extensively used for providing TCs fixes, *i.e* the location of their center (Sumner, 1944). Along with flight-level wind estimates from the aircraft inertial navigation system, temperature estimates were conducted using vortex thermometers, humidity measurements with infrared hygrometers and pressure estimates using a Kollsman pressure altimeter (Hilleary & Christensen, 1957). These along-track measurements were sometimes completed by vertical soundings of temperature, moisture, pressure and winds performed by meteorological dropsondes that were released during the flight. In a typical reconnaissance mission, up to three aircrafts eventually penetrated the TC to assess the physical parameters at different altitudes. Fig. 1.3 displays typical aircraft tracks conducted in the late 1950s. Despite the apparent lack of azimuthal coverage, numerous studies emerged, thanks to aircraft data, that documented the TCs structure, including the eye (C. L. Jordan, 1952; La Seur & Hawkins, 1963).

In the meantime, the US deployed a system of weather surveillance coastal radars. These coastal radars were active sensors, meaning that they emit a pulse that is reflected in all directions by the encountered atmospheric particles (*i.e* raindrops, ice, but also birds, etc...). The part of the backscattered signal which is reflected towards the radar is measured by the radar receiver, and its intensity is called the reflectivity. Already in 1955, SP-1M radars installed in three different locations over North Atlantic coastal areas and operating at S-band were demonstrated to improve the live tracking of TCs (Whiton et al., 1998a). Yet, a few TCs events in 1954 and 1955 on the US East coast fostered the development of improved coastal radars. The WSR-57 [5] was designed and inaugurated in 1957 to meet the demand. Several tens of WSR-57 were rapidly deployed with a spacing of ∼350-400 km. Operating at S-band and with a beamwidth of 2°, precipitation rates could

5. See Bigler, 1981 for more details and illustrations.

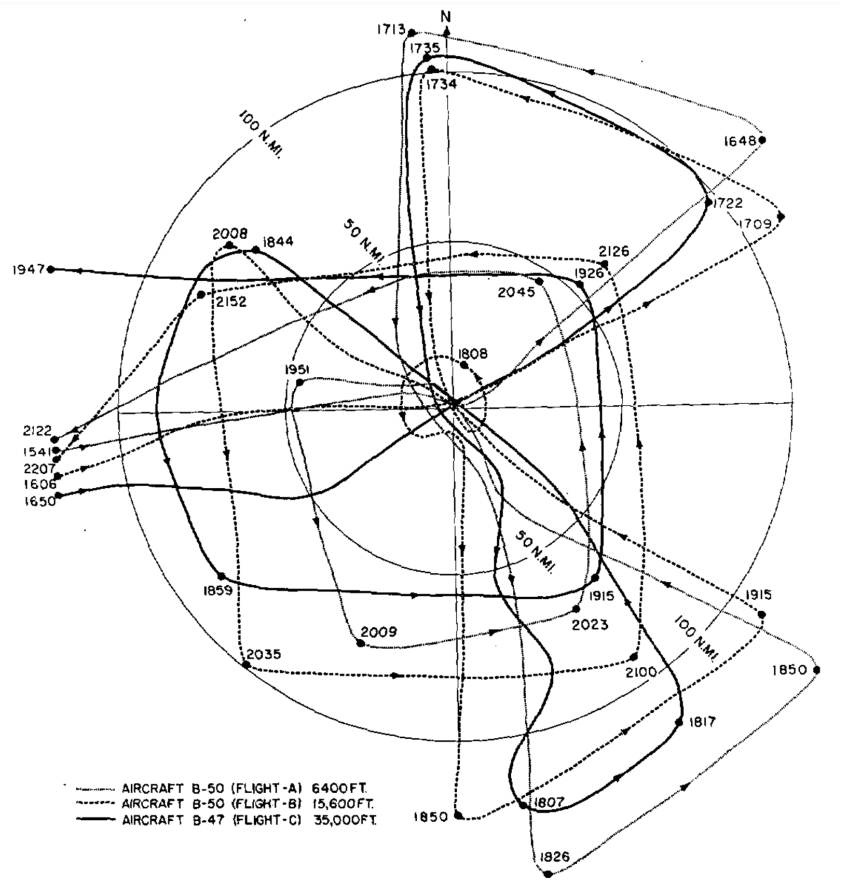

Figure 1.3 – Aircraft tracks relative to TC Cleo on 18^{th} August 1958. Three aircrafts flew into TC Cleo, at an altitude of ∼2, ∼5 and ∼11 km, respectively, within a radius of ∼220 km of the center. Extracted from La Seur and Hawkins, 1963.

be retrieved from the radar echoes within a ∼450-km radius of a station. These radars thus helped better estimating TCs location and extent near landfall. The WSR-57 was continuously improved over the following decades and remained used until the 1990s [6].

1.2.2 From 1961 to 1978: the early days of the satellite era with the first visible acquisitions

The 1960s mark the start of the satellite era, which completely revolutionized the tropical meteorology community. TIROS-3, the third of a series of television infrared observation satellites, was launched on 12^{th} July 1961. Orbiting at an altitude of ∼750-800 km,

6. The last operational WSR-57 was removed in 1996.

TIROS-3 carried different instruments, including two independent television cameras and a scanning radiometer operating at infrared and visible wavelengths. It became the first satellite to ever provide a picture of a TC from space when it overflew Anna, the first TC of the 1961 Atlantic season. A TIROS-3 television acquisition of Anna on 22^{th} July 1961 is depicted in Fig. 1.4. The wide angle acquisition highlights extensive areas of cirrus-like clouds partially surrounded by convective outer bands (Fett, 1964). During these days, Anna was also observed by TIROS-3 infrared/visible radiometer, but limited inferences on the water vapor content were made because of both poor technological capabilities and insufficient knowledge at that time (Bandeen et al., 1964).

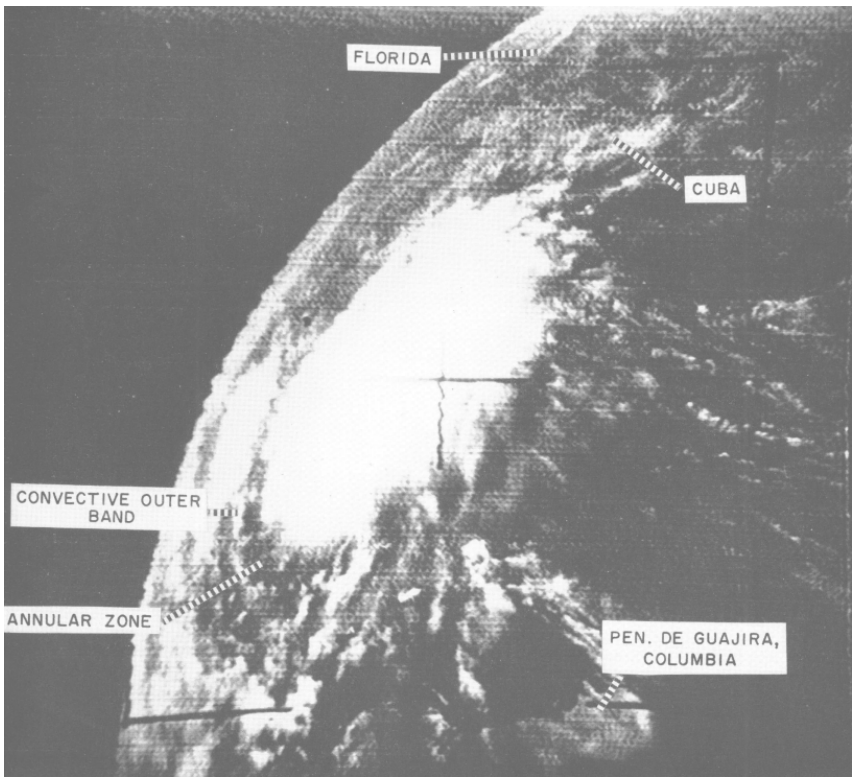

Figure 1.4 – Satellite acquisition of TC Anna on 22^{th} July 1961, from TIROS III. Extracted from Fett, 1964.

Rapidly, researchers discovered a relationship between the organization and size of the cloud shield observed with spaceborne visible imagery and the maximum wind speed measured by reconnaissance aircraft (Fritz et al., 1966). They also wondered whether the cloud patterns could be used to predict whether tropical storms or depressions will evolve into stronger TCs or not. For instance, Gentry et al., 1970 analyzed measurements

of TC Gladys (1968) from two aircraft, three WSR-57 coastal radars and two satellites, completed by five color pictures from the Apollo 7 spacecraft crew. By estimating the three-dimensional mass circulation, they confirmed that the expansion and motion of the high-level circulation (*i.e* clouds) were induced by the low-level circulation in their data. The clouds may then encode the possible evolution from weaker storms into more intense TCs.

In practice, the relationship highlighted by (Fritz et al., 1966) to estimate intensity was not used because of the coarse resolution of satellite sensors at that time. With the increasing number of satellites and their improvement, a more robust method for systematically detecting TCs current intensity and future changes from the cloud patterns observed by satellites was proposed in 1972: the Dvorak method [7] (Dvorak, 1972, 1973, 1975). Figure 1.5 displays the patterns that must be recognized in the method. The key points were to determine whether the central area of the clouds was overcast and whether it was partially or totally encircled by wide convective outer bands. A subjective analysis of these patterns combined with an objective step-by-step procedure was used to determine a "tropical number" that was directly linked to the current intensity. In addition, by comparing the cloud patterns from the current satellite acquisition with those from an acquisition of the previous day, it was possible to estimate the future intensity change.

Despite its subjective nature, the Dvorak method was surprisingly robust, and because most TCs were regularly covered by satellite acquisitions by the late 1970s (Denney, 1969), it became systematically used by tropical operation centers all over the world. With continuous satellite advances (see below), the Dvorak method was improved in 1984 to include information from eye patterns revealed by cloud-top infrared temperature estimates (Dvorak, 1984). Research efforts on the Dvorak method continued until recently, in particular to make it more automatic and less subjective, by taking advantage of further improvements on satellite capabilities (C. S. Velden, Olander, & Zehr, 1998; Olander & Velden, 2007). The success of the Dvorak method illustrates how the rapid progress of satellite capabilities transformed the operational and research communities.

In parallel, space-based capabilities were rapidly improving. While the potential of geostationary satellites for space applications was demonstrated since 1964 with the launch of Syncom (the world's first geostationary satellite) a milestone was set in 1975 with the launch of the geostationary operational environmental satellite 1 (GOES-1). At an altitude of ∼36,000 km, GOES-1 carried a visible infrared radiometer allowing for day and

7. For a detailed review of the Dvorak method, see C. Velden et al., 2006

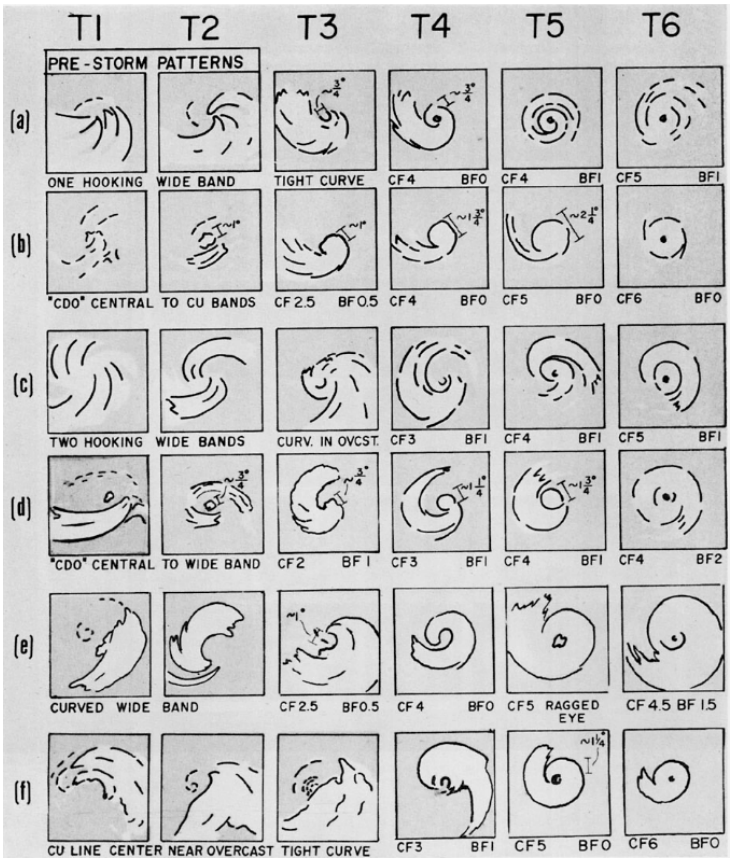

Figure 1.5 – Example of TCs and corresponding tropical numbers ("T-numbers") in the Dvorak method. Depending on the central and outer bands features, a given TC is assigned a T-number in order to determine its current intensity. Extracted from Dvorak, 1975.

night enhanced infrared acquisitions. With geostationary satellites, systematic acquisitions of the clouds could be performed, making the Dvorak method particularly efficient for monitoring the TC intensity over a fixed geographical area. In addition, these new infrared/visible capabilities allowed to better appreciate the TC rain and eventually to estimate wind fields by analyzing cloud motions in successive observations (E. Rodgers et al., 1979).

Spaceborne radiometers were also improved [8]. Nimbus-5, an orbiting satellite launched at the end of 1972, carried an electrically scanning microwave radiometer (ESMR). Passive microwave instruments measure the brightness temperature radiated by the ocean surface. In theory, the natural radiation of the ocean surface is controlled by the foam coverage and bubble surface layer thickness, which both increase with surface wind speed. The

8. The first spaceborne microwave radiometer was that onboard Cosmos 243, launched in 1968.

latter may thus be retrieved from passive microwave measurements even under extreme wind conditions. Yet, the received signal is also influenced by the state of the atmosphere (humidity and water vapor, temperature) and the ocean (temperature, salinity). For instance, the signal received by Nimbus-5 ESMR, which operates at a short wavelength (∼19 GHz, K-band), was heavily influenced by atmospheric rain. Thus, Nimbus-5 mainly allowed to assess the TC rainfall structure, which may in turn be related to intensity (Allison et al., 1974; E. Rodgers & Adler, 1981).

Nimbus-6, launched in 1975, carried a scanning microwave spectrometer (SCAMS). Spectrometers, or "sounders", sound the atmosphere at intermediate levels. Nimbus-6 SCAMS operated at three different frequencies close to ∼54 GHz (along with two other K- and Ka-band channels to measure the atmospheric water vapor and liquid water content). These three frequencies are situated at the lower shoulder of the oxygen absorption band, so that vertical profiles of temperatures may be estimated from the measured signals. Atmospheric temperature anomalies in TCs are related to the surface pressure deficit through hydrostatic and gradient wind balance. Thus, surface wind speed estimates could be performed with microwave passive sounders such as Nimbus-6 SCAMS (Kidder et al., 1978). Later, microwave sounding units (MSU) were deployed in space, for example on TIROS-N in 1978. Operating at four channels between ∼50 and ∼58 GHz, they allowed for atmospheric temperature estimates at a slightly higher resolution. Surface wind speeds could also be estimated from MSU (C. S. Velden & Smith, 1983).

The 1970s also marked an important watershed for TCs measurements from ocean buoys. Even though the deployment of ocean research buoys dates back to the 1940s (Soreide et al., 2001), it's not until 1975 that the first reliable surface wind speed measurement from ocean buoys was performed, when TC Eloise passed over two buoys that were deployed by the NOAA in the Gulf of Mexico (Withee, 1975). Ocean buoys measurements of TCs wind field not only improved our understanding of the planetary boundary layer (BL) (Sprigg et al., 1998), but also helped calibrating surface wind estimates from spaceborne and airborne sensors.

1.2.3 From 1978 to 1991: operational oceanography with combined active and passive remote sensing techniques

Gradually, attempts were made to complement these spaceborne passive capabilities with active methods. Successful demonstrations were conducted with aircraft and the

Skylab space station (Ross, 1975; A. K. Jordan et al., 1976) to prepare the Seasat mission, launched in 1978 by the NASA. Although this orbiting satellite operated for only ∼100 days, its sensors had great implications not only for TCs, but for the whole oceanography community (Born et al., 1979). Four of the five Seasat sensors [9] were operating at microwave wavelengths.

First, Seasat carried an active microwave scatterometer (SASS), which senses the roughness of the ocean surface. The emitted signal interacts with structures whose size is of the order of the pulse's wavelength, such as capillary-gravity waves, which are controlled by both the wind speed and direction. Once backscattered by the directional geometry of the ocean surface, the signal is received with different viewing angles, so that with an inversion called a "geophysical model function" (GMF), one may accurately retrieve the ocean surface wind speed and direction (Jones et al., 1982). Based on this principle, Seasat SASS demonstrated the ability to measure ocean surface wind vectors from space for the first time, including in TCs at low wind speeds (Gonzalez et al., 1982; Hawkins & Black, 1983). Nevertheless, the estimated wind speeds were shown to be underestimated in TCs (Jones et al., 1982). Operating at Ku-band, Seasat SASS signal was also contaminated by rain, especially for TCs wind speed estimates (Moore et al., 1983).

Second, a SAR instrument was embedded on Seasat. Operating at L-band and with HH polarization (*i.e* the sensor both emits and receives only horizontally polarized signals), Seasat SAR instrument allowed for high-resolution acquisitions of the ocean surface. For example, Fig. 1.6 depicts a Seasat SAR acquisition of TC Iva in the Eastern Pacific in 1978. Like with scatterometers, the backscattered signal also depends on the ocean surface roughness and the wind-generated capillary waves. The advantage of using SAR lies in its high spatial resolution. With a Doppler processing in the along-track direction, a resolution comparable to that of optical systems may be achieved. Yet, the SAR does not allow to retrieve the wind direction. To estimate the wind speeds with a GMF, the wind directions must thus be taken from ancillary data. For TCs, the relationship between the backscattered signal measured by the SAR instrument and the effective wind speeds at the ocean surface was not well understood at this time. In addition, because the sensor operated with a co-polarized (HH) channel, the measured signal saturated for winds higher than ∼20 m/s. To complement and better exploit these satellite SAR measurements, airborne SAR L-band surface wind speed measurements in TCs only started in the late

9. The fifth instrument was a visible and infrared radiometer (VIRR) providing information on both cloud patterns and cloud-top temperatures.

1970s (Weissman et al., 1979).

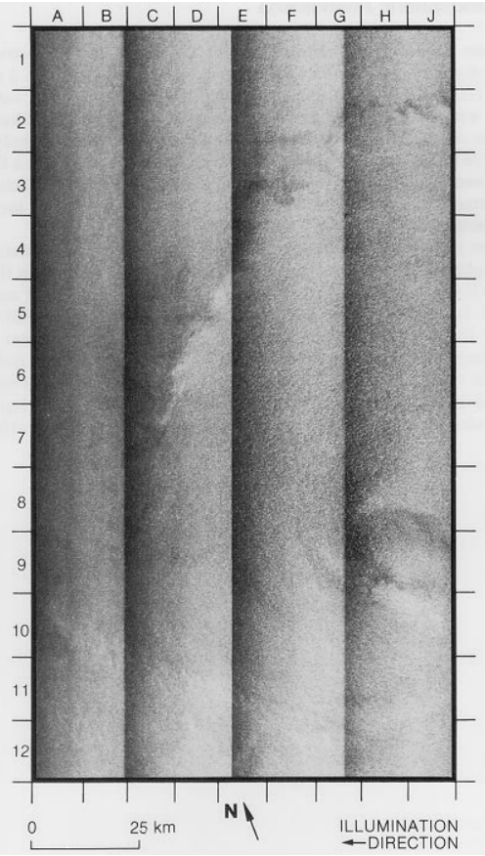

Figure 1.6 – Seasat SAR acquisition of TC Iva in the Eastern Pacific in 1978. Estimated maximum intensity was 34 m/s. Extracted from Fu, 1982.

Third, Seasat also carried a scanning multi-channel microwave radiometer (SMMR). Since the first spaceborne radiometers and Nimbus-5 ESMR, wind speed inversions from these sensors were developed and improved. Operating at five different frequencies from C- to Ka-band, Seasat SMMR allowed for wind speed estimates in TCs (Gonzalez et al., 1982) with a coarse (∼50 km) spatial resolution. Wind speed estimates near the TC center were however not possible using these channels due to rain contamination of the signals. Furthermore, it is worth mentioning that SMMR was the first instrument to provide wind speed maps at the global scale (Njoku & Swanson, 1983).

Lastly, Seasat payload included a radar altimeter (ALT). Three years before Seasat, the first spaceborne altimeter in history was launched on the geodynamics experimental ocean satellite 3 (GEOS-3), with the aim of investigating the structure of the Earth's

gravitational field. Later, active radar altimeters were shown to be very efficient at measuring the Earth's topography. Usually operating at Ku- or Ka-bands, they can measure the sea surface height (SSH) with a centimetric precision, from which the ocean circulation and currents may then be derived using the geostrophic approximation. In addition, the backscattered signal's shape and amplitude may also be used to infer the ocean surface wind speed. However, because of the sensor's narrow swath and the late development of wind speed algorithms for winds above gale-force wind speed (Young, 1993; Quilfen et al., 2011), altimeters were barely used for operational or research applications on TCs surface wind speeds.

Seasat marked the start of a prolific period for microwave spaceborne sensors, which kept continuously improving over the next decades. After Seasat, numerous meteorological satellites emerged, and it's perhaps at this time that a more operational approach could really start. Progressively, the scientific community would be overwhelmed by ever more data sources, as stressed in C. Velden et al., 2006: "*As the number of satellites increased and their capabilities improved, it became clear that the science of deploying remote sensing in space was outpacing the ability of meteorologists to apply it.*"

In the meantime, other observational technologies were developed. Built in 1978, the stepped-frequency microwave radiometer (SFMR) has been carried by reconnaissance aircrafts since that time (Harrington, 1980). SFMR is a passive microwave radiometer that measures the natural radiation from the ocean surface at four different frequencies between ∼4.5 and ∼7.2 GHz (C-band). At such frequencies, attenuation of the surface radiation by the interfering atmosphere (absorption by oxygen, water vapor, or rain) is small. The frequency stepping capacity, *i.e* the ability to measure differences in brightness temperatures at the four frequencies, provides a coincident estimate of the rain rate. Then from differences between observed brightness temperatures and those expected given a known or assumed SST and coincident rain rates, wind speeds can be estimated. Hence, SFMR provides estimates of both atmospheric rain rate and surface wind speeds. Figure 1.7 presents the ocean surface wind speeds estimated from SFMR data obtained in TC Allen in 1980, when a linear dependence of these brightness temperatures on wind speed is assumed (Jones et al., 1981). These surface estimates (solid curve) compare well with independent surface estimates (circles) deduced from flight-level wind estimates (obtained from a concurrent aircraft's inertial navigation system). Despite this success, no SFMR was flown into TCs before 1985, and the development of more robust SFMR wind speed retrievals took long time (see below).

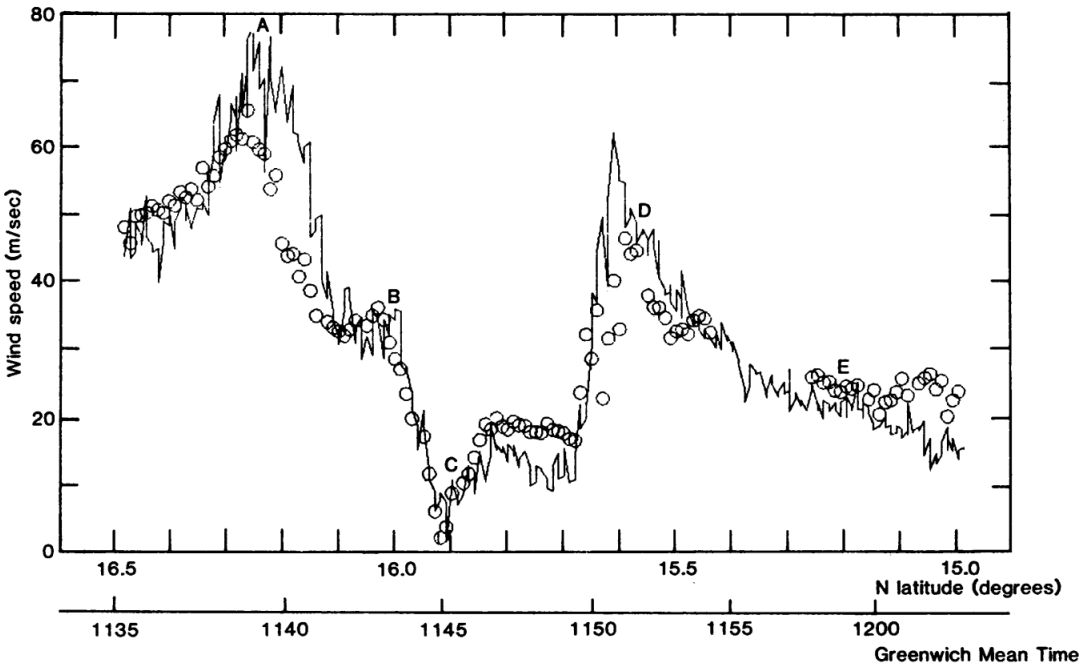

Figure 1.7 – Airborne SFMR surface wind speed estimates (solid curve) in TC Allen in the North Atlantic on 5^{th} August 1980. Concurrent flight-level wind speeds estimates (circles) from the inertial navigation system of another aircraft are also displayed. A and D: Northern and Southern locations of the eyewall; B: inner eye; C: TC center; E: outer rainband. Extracted from Jones et al., 1981.

Reconnaissance aircrafts were also equipped with Doppler radars. With a rotating radar antenna, echo volumes were received from several viewing angles, allowing for retrieving the horizontal wind vectors at different altitudes using dual-Doppler radar analysis. From 1982, aircraft Doppler radars allowed to inform on TCs global structure, including near the eye, like for TC Debby in 1982 (Marks Jr & Houze Jr, 1984).

Doppler radar capabilities were also implemented with coastal radars. In the late 1980s, former coastal radars were progressively replaced by the WSR-88D (Whiton et al., 1998b), a Doppler radar also called the next-generation weather radar (NEXRAD, with the "D" standing for "Doppler"). Operating at S-band with a 1° beamwidth, this radar measures echo reflectivity allowing for precipitation rates retrievals within a ∼450-km radius from the station. Compared to its WSR-57 predecessor, the most significant innovation is the use of the Doppler effect to also provide estimates of the radial component of the wind speed relative to the radar site. In Doppler mode, NEXRAD radars have a three-dimensional ∼250-km range. Their wind speed estimates were shown to improve the estimation of TCs wind structure near landfall (Y. Wang & Pu, 2021), while their pre-

cipitation rates estimates are still being used as ground truth for other sensors measuring rainfall (Zagrodnik & Jiang, 2013).

The defense meteorological satellite program (DMSP), an orbiting satellite embedding a special sensor microwave imager (SSM/I), was launched in 1987. This multi-channel radiometer operates at K- and Ka-bands, allowing for large acquisitions (swath of ∼1400 km width) of TCs precipitation structure (E. B. Rodgers et al., 1994). Surface wind speeds may be retrieved with this instrument. However, like with its predecessors, wind speed gradients in the core regions are still smoothed out by the coarse spatial resolution (∼50 km) of the sensor, and the received signal is severely affected by the occurrence of rain (Goodberlet et al., 1989; Hollinger et al., 1989). Thus, wind speed estimates were rarely available near the TC core.

1.2.4 From 1991 to 2006: an exploding number of remote sensors with ever-increasing spatio-temporal resolution

The 1990s set a milestone for the estimation of ocean surface wind speeds within TCs using scatterometers. Two European remote-sensing satellites, ERS-1 and ERS-2, were launched in 1991 and 1995, respectively. These two orbiting satellites both carried an active C-band scatterometer among others [10]. Less contaminated by rain than their Ku-band predecessors but still with narrow swaths (∼500 km) and low/medium nominal resolution (∼50 km and ∼25 km for operational and experimental products, respectively), these two sensors allowed to more precisely estimate ocean surface wind speeds below damaging-force winds (Quilfen et al., 1998). Figure 1.8 displays surface wind vectors estimates from the 25-km spatial resolution experimental product in TC Elsie in 1992. Notably, Elsie's peak intensity, reached on 5^{th} November, was largely underestimated by ERS-1 scatterometer (∼30 m/s versus ∼75 m/s in other data sources). In the meantime, the coverage, spatial resolution and accuracy of Ku-band scatterometers were improved. Despite their limitations, the Ku-band scatterometers NSCAT onboard the advanced Earth observing satellite 1 (ADEOS-1, launched in 1996) and QuikScat (deployed in 1999), along with their ERS C-band counterparts provided surface wind speeds measurements in TCs that have since then been used extensively by operation centers (Sampson & Schrader, 2000; Brennan et al., 2009).

10. They also carried a SAR (see below), an altimeter, a microwave radiometer, an IR/visible radiometer, and a visible/ultraviolet spectrometer.

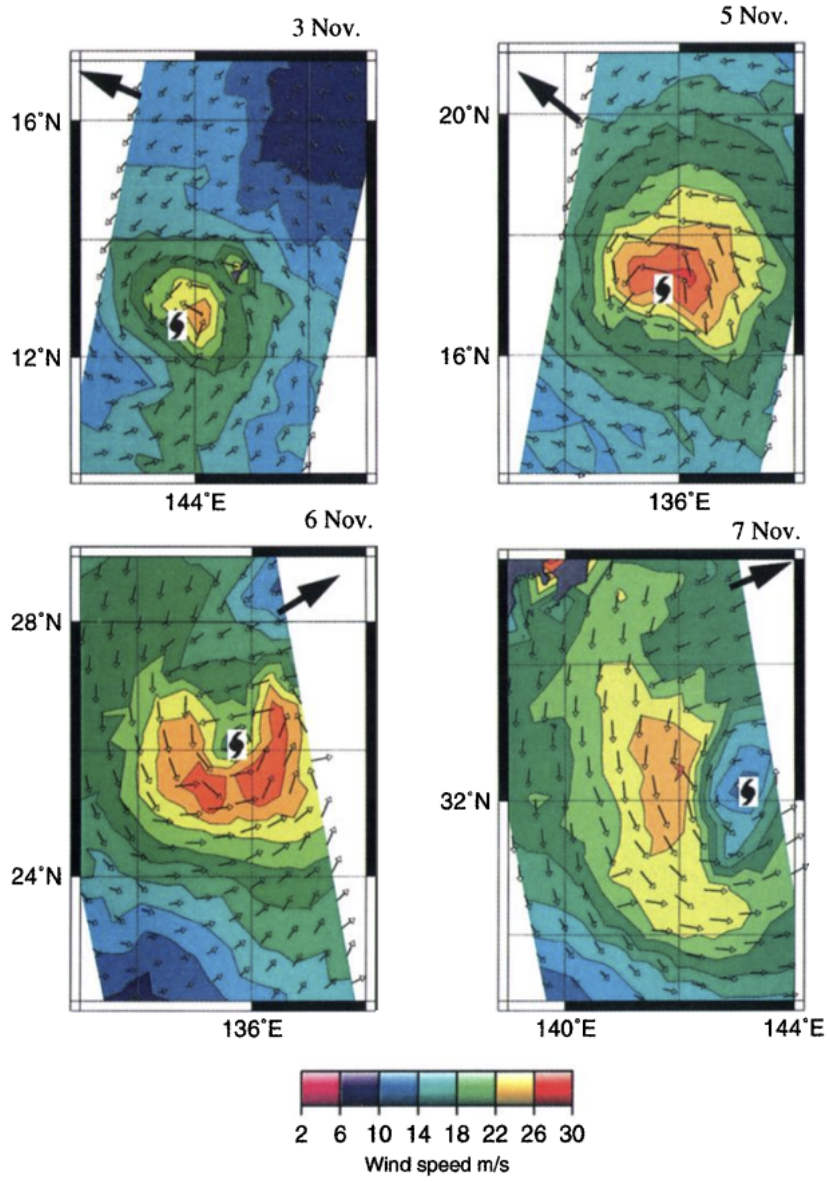

Figure 1.8 – ERS-1 scatterometer surface wind vectors estimates from the 25-km spatial resolution experimental product in TC Elsie in 1992 on (a) 3^{rd} November, (b) 5^{th} November, (c) 6^{th} November, and (d) 7^{th} November. Extracted from Quilfen et al., 1998.

Dropsondes deployed from reconnaissance aircrafts also knew a major improvement in the late 1990s. Even though the possibility of improving them with Global Positioning System (GPS) was discussed since the mid-1980s, it is only in 1997 that such a development took place (Hock & Franklin, 1999). With this system, no positions or velocities are computed directly in the dropsonde, as it was the case with previous technologies. As a

result, sonde tracking and the resulting wind measurements were more accurate.

An other advancement that is worth mentioning that is the launch of advanced microwave sounding unit (AMSU) in the late 1990s. In 1998, AMSU, consisting of AMSU-A and AMSU-B, were deployed to replace MSU. Compared to its predecessors, AMSU-A has fifteen channels, meaning that the atmospheric temperature may be estimated at many more layers than with former MSU. This allowed to refine statistical relationships between vertical temperature profiles and TCs intensity and size (Goldberg et al., 2001; Demuth et al., 2004; Demuth et al., 2006). Later, AMSU were also deployed on other satellites, including the European Metop-A and -B missions, as well as the NASA Aqua orbiting platform (see below).

Since Seasat, which operated for only ∼100 days, no significant advancements had occurred with regard to estimating oceanic surface winds in TCs using SAR measurements until the 1990s. ERS-1 and -2 were launched in 1991 and 1995, respectively, and both carried a SAR instrument. Operating at C-band and with VV polarization (*i.e* the sensor both emits and receives only vertically polarized signals), this instrument had a spatial resolution close to that of Seasat SAR. ERS-1 and -2 operated for 9 and 16 years, respectively, providing an extensive catalogue of ocean surface acquisitions. These two satellites were complemented by the Japanese Earth resources satellite 1 (JERS-1, launched in 1992, terminated late 1998) and Radarsat-1 (launched in 1995, terminated in 2013). Compared to ERS-1 and -2, JERS SAR achieved similar spatial resolution but operated at L-band and with HH polarization. Radarsat-1 SAR operated at C-band, with HH polarization, and achieved a slightly better spatial resolution than that of ERS-1 and -2. At this time, TCs wind speed retrievals were hampered by the fact that traditional GMFs underestimated the wind values for winds higher than ∼20 m/s (Donnelly et al., 1999). Existing GMFs were applied using wind direction estimates directly extracted from the SAR acquisitions by an analysis of the low wavenumber energy (Vachon et al., 1999) or the local gradients associated with wind streaks or BL rolls (Horstmann et al., 2005). These studies concluded that SAR measurements were promising for TCs wind speed retrievals and that they may improve our knowledge of TCs dynamics in the future (Katsaros et al., 2000).

In 2002 and 2003 two low-Earth orbiting satellites were launched, Aqua and Coriolis, respectively. While they both carried a multi-channel microwave scanning radiometer, they were not designed for the same purposes. The first one (AMSR-E) was developed by the Japan aerospace exploration agency (JAXA) to investigate the Earth's hydrological cycle and energy exchanges in and between the ocean and the atmosphere, while the

second one (WindSat) was developed by the US for military applications. Compared to their predecessor (SSM/I onboard DMSP), channels in the C- and X-bands complemented the K- and Ka-bands frequencies and allowed to measure ocean surface wind speeds for AMSR-E (Shibata, 2002) or ocean surface wind vectors [11] for WindSat (Meissner & Wentz, 2005). Yet, wind speed retrievals from both AMSR-E and WindSat still suffer from influence of rain and from the sensors coarse spatial resolution (∼50 km). Later, by combining different channels to minimize the influence of rain, all-weather algorithms were developed to account for TCs heavy rain conditions (Shibata, 2006; Meissner & Wentz, 2009).

In parallel, conforming to the philosophy of the Dvorak method, algorithms to indirectly complement these ocean surface wind observations with geostationary satellites were developed. With the advances in both temporal and spatial resolutions of geostationary satellites, it became possible to estimate wind vectors in the TCs outer circulation (up to the gale-force winds) from the cloud-drift winds, which track low-level (∼700 hPa) clouds, using visible imagery (C. S. Velden, Olander, & Wanzong, 1998; Dunion et al., 2002). In addition, statistical methods were developed in order to estimate TCs surface wind structure from geostationary infrared data (Mueller et al., 2006; Kossin et al., 2007).

Almost one decade later, an other aircraft capability, the SFMR, has benefited from the technological breakthrough of GPS dropsondes. As a consequence, since its first success in TC Allen in 1980, SFMR calibration had been greatly improved. In addition, the GPS dropsondes highlighted that previous BL models to extrapolate flight-level wind speeds to the surface were not accurate for winds greater than ∼50 m/s and should be reexamined (Franklin et al., 2003). Then, by analyzing concurrent SFMR and GPS dropsondes measurements, an algorithm to retrieve accurate surface wind speed estimates at a ∼1 km spatial resolution from SFMR instruments was developed (Uhlhorn & Black, 2003; Uhlhorn et al., 2007).

With the growing number of spaceborne sensors to observe TCs and the development of methods to also indirectly estimate physical quantities, the use of multimodal approaches to estimate TCs structure was natural. Rapidly, methodologies to estimate the surface wind field or the intensity of TCs from different spaceborne sensors were set (Powell et al., 1998; Knaff & DeMaria, 2006; Herndon et al., 2010) and still continue to be developed today (C. S. Velden & Herndon, 2020). Figure 1.9 shows such a multimodal analysis for

11. WindSat is unique in that it uses several fully polarimetric channels. By separating the brightness temperatures that have a vertical, horizontal, left-hand circular, and right-hand circular polarizations, they allow to retrieve the full wind vector (Gaiser et al., 2004).

TC Wilma in 2005. In this example, data from Quikscat, SSM/I, AMSU, and infrared imagery are combined to produce this wind field estimate.

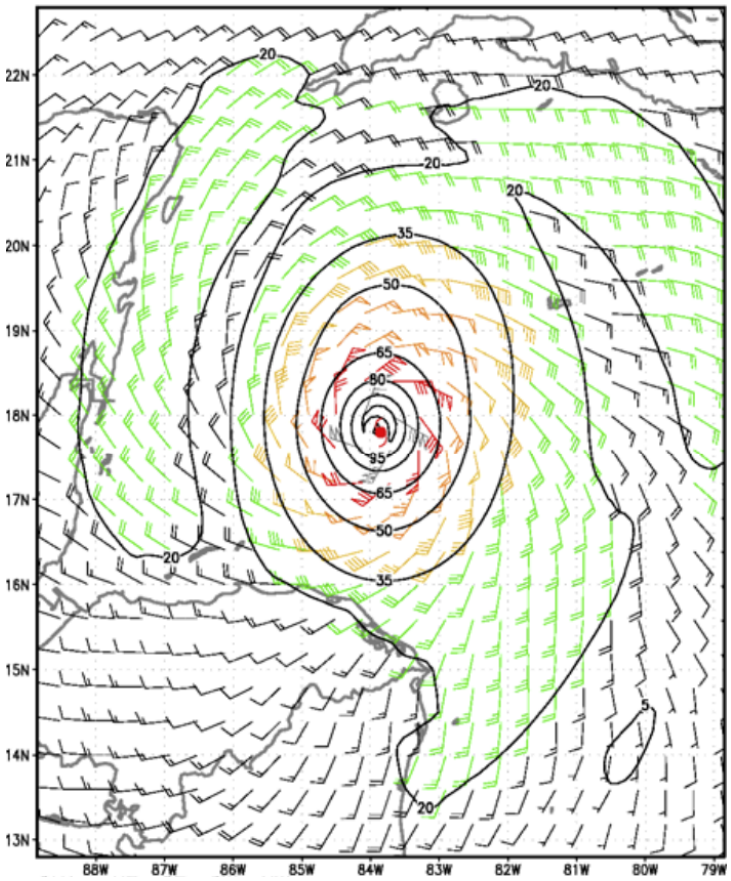

Figure 1.9 – Multimodal surface winds analysis for TC Wilma on 20^{th} October 2005. Contour values are in knots. Extracted from Knaff and DeMaria, 2006.

1.2.5 From 2006 to today: towards high spatio-temporal resolution wind speed retrievals

Since ERS-1, -2, and QuikScat, the place occupied by scatteormeters in operational meteorology did not cease to grow. Based on the success of the ERS missions, ESA made a commitment to C-band scatterometry that culminated with the launch of Metop-A, -B and -C (in 2006, 2012 and 2018, respectively). With two swaths of ∼550 km width, these scatterometers can perform wide acquisitions of the ocean surface at a nominal spatial resolution of ∼12.5 km (∼6.5 km in experimental mode). An other illustration of

how scatterometers had become popular at that time is given by the case of QuikScat. When QuikScat's antenna rotation mechanism failed in 2009, a substitute was actively requested by both the operational and scientific communities. In less than five years, a scatterometer, RapidScat, was mounted on the international space station and operated from 2014 to 2016 to meet this demand. In the meantime, the scatterometry landscape was completed by several Ku-band scatterometers embedded on OceanSat-2 (launched in 2009), ScatSat-1 (2016), Hai Yang-2A (2011), -2B (2018) and -2C (2020), among others. Despite the advances in spatio-temporal resolution for both C- and Ku-band scatterometers, the signal sensitivity above hurricane-force winds is still an open issue (Donnelly et al., 1999; A. Mouche et al., 2019). Yet, spaceborne scatterometers were shown to provide useful information on the TC outer-wind structure (Yueh et al., 2001; Jaiswal et al., 2019; Polverari et al., 2021).

In 2009, ESA launched the soil moisture and ocean salinity (SMOS) satellite, an orbiting satellite designed to measure the sea surface salinity (SSS) and the soil moisture. On the other side of the Atlantic, the NASA launched the soil moisture active and passive (SMAP) satellite in 2015, whose passive payload was also designed to measure the soil moisture, while its active payload should be used to examine TCs. Until these two missions, most spaceborne radiometers and scatterometers were operating at frequencies between the C- and Ka-band. They were thus affected by rain, prominent in TCs, and had a reduced sensitivity to wind at high winds. Unlike their predecessors, SMOS and SMAP both carry a radiometer that operates at L-band (∼1.4 GHz) and allows for wind speed retrievals in TCs even under high precipitation rates (up to ∼50 mm/hr) and strong winds (up to ∼70 m/s) (Reul et al., 2012; Yueh et al., 2016; Meissner et al., 2017). In the meantime, the multi-channel radiometer AMSR-E was replaced by AMSR2, onboard global change observation mission water 1 (GCOM-W1), and wind speed algorithms were developed for TCs (Zabolotskikh et al., 2015). With large spatial coverage (swath width of more than ∼1000 km), SMOS, SMAP and AMSR2 can provide essential information on TCs surface wind structure (Reul et al., 2017). Nevertheless, wind speed estimates from these sensors are limited by their coarse spatial resolution (∼40 km).

In the 2010s, advances in SAR capabilities allowed to go one step further in TCs wind speed retrievals at high-resolution. Since 2007 and the launch of Radarsat-2, soon followed by Sentinel-1A and -1B in 2014 and 2016, multi-polarized SAR measurements are available. This means that for a signal emitted with vertical polarization, the sensor may either measure the component with vertical (VV) or horizontal (VH) polarization of

the backscattered signal (similarly, for a signal emitted with horizontal polarization, the sensor may operate in either HH or HV mode). This had important implications. From a theoretical point of view, it had long been known that the backscattered signal has a linear dependence on wind speed when the ocean surface roughness is dominated by Bragg resonance mechanisms, and a cubic dependence when breaking waves events dominate (Phillips, 1988). Before multi-polarized SAR instruments were launched, only the linear dependence of the signal on wind speed was confirmed by observations. The cubic dependence was observed for the first time with the newest Radarsat-2 cross-polarized measurements (Hwang et al., 2010; Vachon & Wolfe, 2010). Once wind speeds reach approximately 25 m/s, ocean roughness becomes dominated by the contribution of breaking waves. Wave breaking also induces volume scattering, but that signal is depolarized, and cross-polarized measurements (VH or HV) can be utilized to evaluate the degree of wave breaking and depolarization. Rapidly, GMFs to retrieve TCs ocean surface wind speeds from SAR cross-polarized measurements were developed (B. Zhang & Perrie, 2012; Hwang et al., 2015) and soon improved by combining the co- and cross-polarized contributions to accurately retrieve wind speed at both low, moderate and high winds (B. Zhang et al., 2014; A. A. Mouche et al., 2017; A. Mouche et al., 2019). Figure 1.10 displays Sentinel-1B SAR surface wind speed estimates for TC Sam in 2021. High wind speed radial gradients are apparent in the eyewall of the TC, as well as spiraling features.

These last advances conclude our synopsis of TCs observations. However, to better appreciate the remainder of the manuscript, it must be remembered that with continuously improving technological capabilities, wind speed measurements at higher spatio-temporal resolution have yet to come.

1.2.6 Reanalyses

A myriad of different sensors are available to assess TCs ocean surface wind structure. Reanalyses are thus crucial to harmonize and correct these estimates. For TCs, reanalyses are compiled in the so-called *best-track* datasets. For each ocean basin, the reanalysis is usually performed after each TC season by the responsible agency and based on all available data (*e.g*, aircraft, satellite and in-situ observations).

Historically, best-tracks included both TCs intensity and location reanalyzed on a six-hourly basis. Later, other important parameters such as the wind radii were also included in the datasets. Typical wind radii are the radius of gale-force winds R_{34} (which either

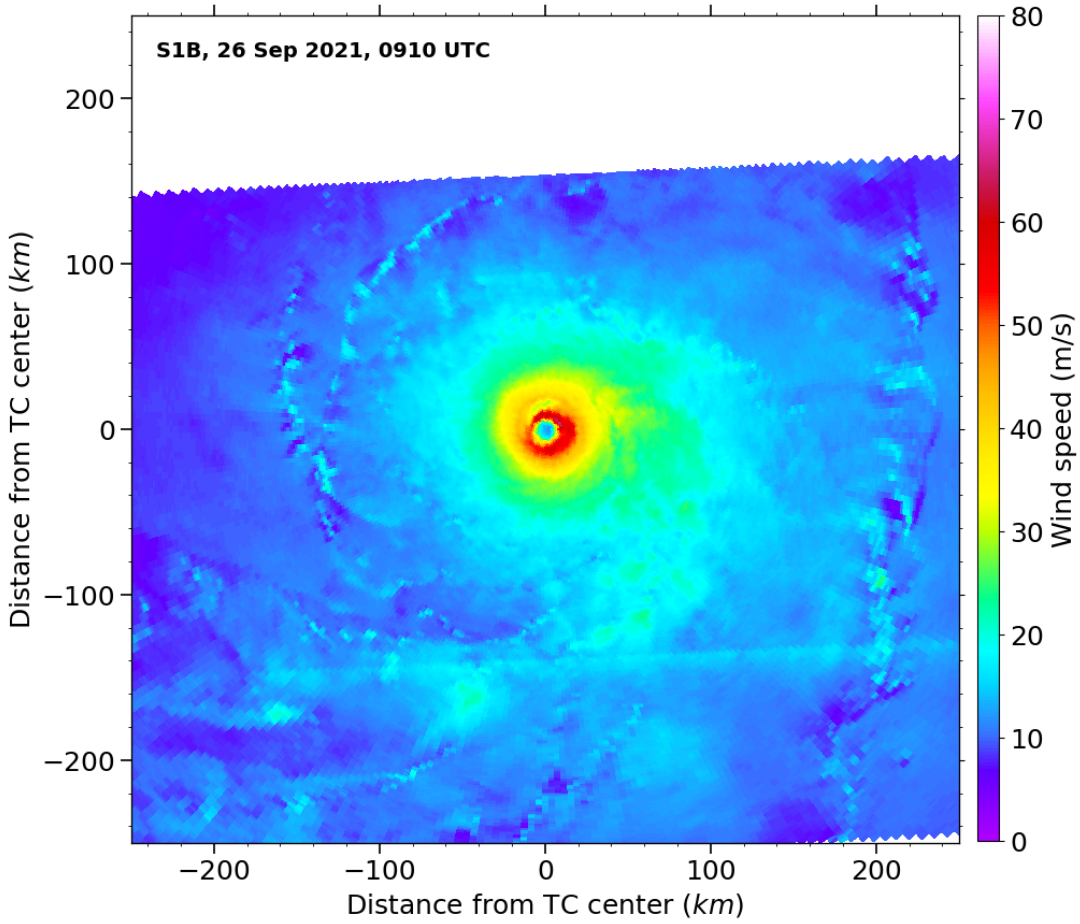

Figure 1.10 – SAR surface wind speeds estimates for TC Sam in 2021 on 26^{th} September. The data was rotated so that the system moves toward the top of the page.

corresponds to the average location or the maximum extent of the 34-knot [12] winds), damaging-force winds R_{50} (50-knots), hurricane-force winds R_{64} (64-knots), and maximum winds R_{max} (associated to V_{max}). However, these wind radii were not necessarily reanalyzed, their values usually coming from operational estimates. For instance for the North Atlantic and East Pacific ocean, wind radii are recorded in best-tracks since the 1980s, but they are reanalyzed only since 2004 (Landsea & Franklin, 2013; Knaff et al., 2021). As a consequence, while the uncertainty on TCs intensity and location reanalyses is rather low, and best-track wind radii estimates may suffer from larger uncertainties (Torn & Snyder, 2012; Landsea & Franklin, 2013; Sampson et al., 2017; Knaff et al., 2021).

The best-track datasets from the different agencies were then compiled in the IBTrACS

12. 1 knot ≈ 0.51 m/s

database (Knapp et al., 2010). Nevertheless, it is important to understand that this global database may suffer from spatial and temporal heterogeneities (Schreck III et al., 2014). First, the reanalysis is subjective, each agency or specialist conducting their own weighting of the available observations. This leads to spatial heterogeneities across the database. Second, the reanalysis methodology depends on the available data at each reanalysis time: best-track estimates of TC events covered by aircraft data are for instance more trustworthy (Landsea & Franklin, 2013). This creates temporal heterogeneities that may even arise between two consecutive six-hourly time steps. A third complication arises from agencies creating the best tracks using different definitions for wind radii (*e.g* maximum extent *vs* average) and the use of different wind averaging standards (*e.g* one-minute maximum sustained *vs* ten-minute average). Lastly, best-tracks are finalized annually and are not updated with evolving reanalysis methodology, creating a temporal discontinuity in the final IBTrACS database.

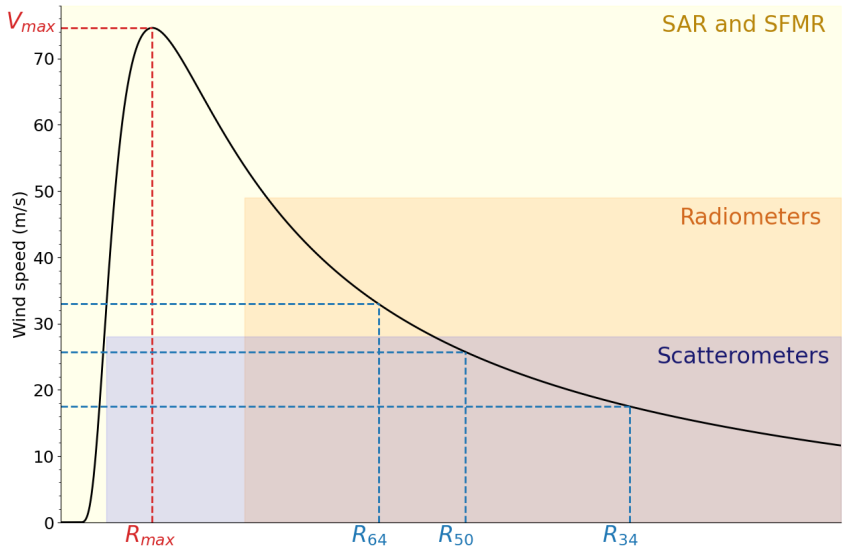

Figure 1.11 – TCs structural parameters typically resolved by microwave instruments. Adapted from Combot, 2023.

In addition, best-tracks also suffer from observational limitations, especially regarding wind radii. Figure 1.11 summarizes the ability of different microwave instruments to directly measure the typical best-track wind radii. In particular, direct estimates of surface R_{max} are only accurately performed by SAR and SFMR for the most intense TCs, while the outermost wind radius R_{34} is resolved by all the different sensors. As a result, the most reliable wind radius from best-tracks is R_{34}, while R_{max} best-track estimates are

known to be rather uncertain in the absence of SFMR and SAR (Combot, Mouche, et al., 2020; Knaff et al., 2021).

In an effort to mitigate best-track spatio-temporal heterogeneities, multi-platform approaches are essential. Based on weighted variational analyzes, products such as the MTCSWA (multi-platform tropical cyclone surface wind analysis, Knaff and DeMaria, 2006; Knaff et al., 2011) or SATCON (satellite consensus, C. S. Velden and Herndon, 2020) provide objective estimates of TCs ocean surface wind field or intensity from multi-modal satellite data. The use of different instruments increases the robustness of the estimates and the spatio-temporal sampling, while the statistical methodologies used are objective, as opposed to the subjective nature of the traditional best-track process.

An other opportunity to produce TCs surface wind structure reanalyses is the use of numerical schemes along with data assimilation. However, state-of-the-art numerical reanalyses fail to accurately reproduce both TCs intensity and size (Schenkel & Hart, 2012; Hodges et al., 2017; Bian et al., 2021), perhaps because of their low spatial resolutions or misrepresentations of fine-scale turbulent air-sea interactions (Momen et al., 2021; Li et al., 2023).

The need for reliable TCs reanalyses is well recognized by the community and was further expressed as one of the recommendations from the last international workshop on TCs (IWTC-10, held in 2022), organized every four years by the WMO to synthesize the latest advances in TC research and operations (see for instance Duong et al., 2023; Ricciardulli et al., 2023):

IWTC-10, Recommendation 4

«Develop high-quality wind structure datasets to advance understanding of processes that affect TC structure in an operationally-relevant framework:

1. Datasets based on long-term data (e.g scatterometer, reanalysis data) made available to the research and operational community;
2. Global high-quality best track parameters for wind radii (e.g R_{max}, R_{34}) to facilitate operationally-relevant research and technique development.»

1.3 Theories

Along with the drastic increase in the number of observations, several theoretical results about TCs were established during the 20^{th} century. In this section, the governing equations of the system are introduced before presenting the main theoretical elements that describe TCs, focusing on their wind structure. This state-of-the-art knowledge was used as a starting point in the present work. The chronological point of view employed in the previous section is abandoned in favour of a thematic approach.

1.3.1 Governing equations

To a first order, the TC wind structure may be considered axisymmetric. The flow above the ocean is described by the equations of conservation of momentum, mass, and energy. In the atmosphere, it may be assumed that the deviations of pressure and density from their vertical mean are small. More precisely, air density is decomposed as $\rho := \bar{\rho}(z) + \rho'$ with $\rho' \ll \bar{\rho}(z)$. Pressure then reduces to $P := \bar{P}(z) + P'$ with $P' \ll \bar{P}(z)$ and potential temperature to $\theta := \bar{\theta}(z) + \theta'$ with $\theta' \ll \bar{\theta}(z)$.

The equation of conservation of momentum is usually projected on the tangential, radial and vertical directions. Along the radial direction, it is often assumed that the pressure gradient is balanced by the centrifugal acceleration and the Coriolis effect. This equilibrium is called the *gradient wind balance*. Along the vertical, *hydrodstatic balance* is assumed, *i.e* gravity is balanced by pressure variations. With these assumptions, and in the absence of friction and heating, the governing equations are

$$\frac{\partial v}{\partial t} + u\frac{\partial v}{\partial r} + w\frac{\partial v}{\partial z} + \frac{uv}{r} + fu = 0 \tag{1.1}$$

$$\frac{v^2}{r} + fv = \frac{\partial \Phi}{\partial r} \tag{1.2}$$

$$\frac{\partial \Phi}{\partial z} = g\tilde{\theta} \tag{1.3}$$

$$\frac{1}{r}\frac{\partial}{\partial r}(ru) + \frac{1}{\bar{\rho}}\frac{\partial}{\partial z}(\bar{\rho}w) = 0 \tag{1.4}$$

$$\frac{\partial \tilde{\theta}}{\partial t} + u\frac{\partial \tilde{\theta}}{\partial r} + w\frac{\partial \tilde{\theta}}{\partial z} + \Gamma w = 0 \tag{1.5}$$

where u, v, and w are the radial, azimuthal and vertical components of velocity, r, z the radial and vertical coordinates, t the time, f the Coriolis parameter [13], and where we used the notations $\Phi := \frac{P'}{\bar{\rho}}$, $\tilde{\theta} := \frac{\theta'}{\bar{\theta}}$, $\Gamma := \frac{1}{\bar{\theta}}\frac{d\bar{\theta}}{dz}$. In this manuscript, the air density ρ is further assumed constant, unless otherwise specified.

A large part of the TC dynamics can be described by examining the absolute angular momentum of an air parcel

$$M := rv + \frac{1}{2}fr^2 \tag{1.6}$$

By definition, M is the sum of the relative angular momentum $m := rv$ and the planetary angular momentum $\frac{1}{2}fr^2$. The equation of evolution for M may be obtained by multiplying Eq. 1.1 by r, leading to

$$\frac{\partial M}{\partial t} + u\frac{\partial M}{\partial r} + w\frac{\partial M}{\partial z} = 0 \tag{1.7}$$

where there is still no friction term. With these governing equations, we will dive into theories that describe TCs, starting with the most general and accepted properties, and gradually moving to more complex topics and issues that are still undergoing today.

1.3.2 The axial circulation

In TCs, the prevailing winds are rotating around an axis located at the center of the system. The amplitude of this axial (primary) circulation is characterized by the tangential wind speed v. Numerous studies attempted to determine a universal formulation expressing v as a function of r. Perhaps the simplest formulation is that of a Rankine vortex formulation, in which solid body rotation $\frac{v}{r} = \text{cst}$ is assumed inside the TC core region and conservation of relative angular momentum $rv = \text{cst}$ is assumed outside (Deppermann, 1947). The wind structure is then described by

$$v(r) = \begin{cases} V_{max}\frac{r}{R_{max}} & 0 < r \leq R_{max} \\ \\ V_{max}\frac{R_{max}}{r} & r > R_{max} \end{cases} \tag{1.8}$$

where V_{max} and R_{max} are the maximum azimuthal velocity and its corresponding radius. With only two parameters, such a formulation provides a parametric profile close

13. The Coriolis parameter is defined as $f = 2\Omega sin(\phi)$, where $\Omega = 7.292\ 10^{-5}\ \text{s}^{-1}$ is the Earth angular velocity and ϕ is the latitude of the TC center.

to observed wind profiles when V_{max} and R_{max} are known.

However, because of frictional effects, relative angular momentum m is likely not conserved outside the core region, especially close to the ocean surface. Thus, in observed wind profiles, the radial wind decay is closer to a relationship

$$r^x v = \text{cst} \tag{1.9}$$

with $x < 1$. This modified version of the Rankine vortex is often used to capture the variability of observed wind profiles. On average, x is close to $\frac{1}{2}$, as suggested by both observational (see for instance Riehl, 1963 or K. A. Emanuel, 1986) and theoretical (Klimenko, 2014) studies. Figure 1.12 shows a comparison between a Rankine profile (solid red curve) and a modified Rankine profile with $x = \frac{1}{2}$ (solid blue curve). Accordingly, the modified Rankine wind decays more slowly with radius than the Rankine wind profile.

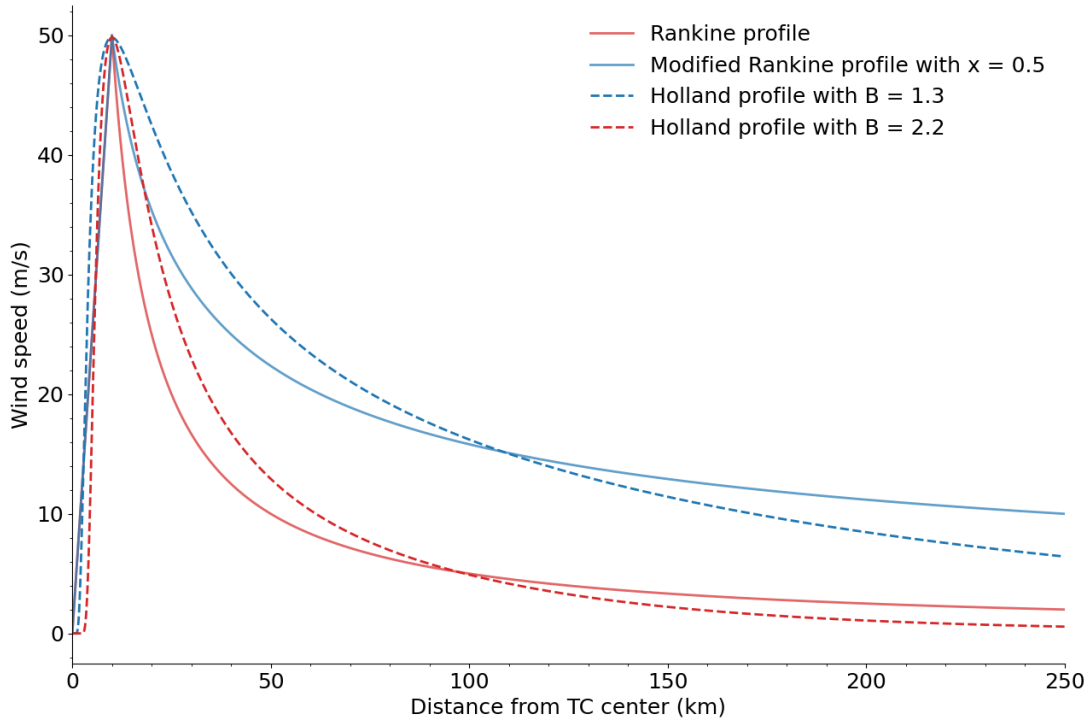

Figure 1.12 – Comparison between Rankine and Holland wind profiles applied to $v(r)$. Fixed parameters are V_{max} (50 m/s), R_{max} (10 km), and latitude (15°).

An other approach which captures the variability of observed wind profiles was proposed by Holland, 1980 and assumes gradient wind balance (Eq. 1.2). At tropical latitudes, f is of the order 10^{-5} s^{-1}. Close to the TC core, with r of the order 10 km, v often exceeds

50 m/s, so that in this region the Coriolis effect fv is small compared to the centrifugal force $\frac{v^2}{r}$. Neglecting this term in Eq. 1.2 leads to

$$\frac{v^2}{r} \approx \frac{1}{\rho}\frac{\partial P'}{\partial r} \tag{1.10}$$

which is called the *cyclostrophic approximation*. Then, assuming an empirical expression (logarithmic rectangular hyperbola) for the pressure profiles, based on observations (Schloemer, 1954), and substituting this expression into Eq. 1.2 while using the condition $\frac{dV}{dr}\Big|_{R_{max}} = 0$ for the cyclostrophic wind leads to

$$v(r) = \sqrt{V_{max}^2 (\frac{R_{max}}{r})^B e^{1-(\frac{R_{max}}{r})^B} + (\frac{rf}{2})^2} - \frac{rf}{2} \tag{1.11}$$

where B is a parameter characterizing the shape of the wind profile. Figure 1.12 displays two Holland wind profiles (dashed curves) for $B = 1.3$ and $B = 2.2$. The profile with the lower B (dashed blue curve) decays more slowly with radius than the one with the higher B (dashed red curve). The Holland parametric formulation was shown to match wind profiles estimated from flight-level aircraft measurements (Holland, 1980).

After the Holland wind profile, other parametric profiles were developed that also rely on the gradient/cyclostrophic balance (H. E. Willoughby et al., 2006), or on a more empirical basis to better fit observational data (Wood et al., 2013). Furthermore, a few studies developed asymmetric parametric winds (Loridan et al., 2015; Olfateh et al., 2017).

More physics-based solutions were also developed. K. Emanuel, 2004 derived a differential equation for the relative angular momentum m in the outer-core region by assuming a balance between subsidence due to radiative cooling and vertical velocity at the top of the BL due to Ekman pumping. An analytical solution of this equation has been recently proposed by Cronin, 2023. In the inner- and near-core regions, K. Emanuel and Rotunno, 2011 made the assumption, based on numerical simulations, that in steady-state the outflow has a Richardson number slightly below one and remains self-stratified by small-scale turbulence. Under their assumptions, an analytical solution may be obtained for $v(r)$ in the limit of cyclostrophic balance. Later, Chavas et al., 2015 geometrically merged these inner- and outer-core solutions to provide a formulation for the complete wind profile. This solution has been validated using Ku-band scatterometer data (QuikScat) but still needs to be confronted to better resolved measurements, especially in the inner- and near-core regions.

Parametric representations of the axial circulation allow to interpolate observations

in space and time when the latter are missing or noisy. The development of a parametric wind profile such as the Holland profile was thus a valuable aid in operations. However, the Holland profile was initially developed in conjunction with flight-level wind speed measurements and surface pressure estimated from the airborne instruments. Additionally, at the time, the central pressure estimates were often of higher quality and possessed greater utility than flight-level wind observations. Several natural risk applications, particularly for storm surge, used central pressure and an estimate of the radius of maximum wind to create parametric surface winds estimates (Vickery et al., 2009). Indeed, before the 1980s and the development of airborne SFMR, surface wind estimates at a high radial resolution were not available. Thus, the question naturally arose how close were these flight-level winds to the surface winds. In the 1980s, it was shown that the measured aircraft flight-level winds allowed to estimate the surface winds observed by buoys within an accuracy of ±10 % (Powell, 1980, 1982). These results were later confirmed by GPS-dropsondes data (Franklin et al., 2003).

1.3.3 The inflow angle

Air parcels trajectories are not completely circular because of radial motions u. As a result, an air parcel follows a spiralling trajectory from the outer-region to the TC center (see Fig. 1.9 for an example of wind vectors at the ocean surface). This spiralling circulation is characterized by the inflow angle

$$\alpha := \arctan(\frac{u}{v}) \tag{1.12}$$

In actual TCs, α is of the order ∼15-30°. In addition, several research studies consider that α is radially constant, at least sufficiently far from the TC center. In an attempt to justify this, Figure 1.13 represents the average inflow angle from more than ∼300 scatterometer acquisitions of mature TCs ($V_{max} > 25$ m/s). Although the standard deviation is large (shaded area), the average inflow angle varies slowly with radius for $r > 2R_{max}$. Close to the TC center, between 0 and $2R_{max}$, a linear increase of α with r is suggested, but note that in this area [14] the validity of scatterometer data is questioned (see above).

Assuming that the inflow angle is constant is equivalent to say that the trajectory of the air parcels can be described by logarithmic spirals. A few studies attempted to go one step further. Yurchak, 2007 added a hyperbolic component to the logarithmic spiral

14. On average $2R_{max}$ corresponds to R_{64}, the radius where the wind speed equals ∼33 m/s.

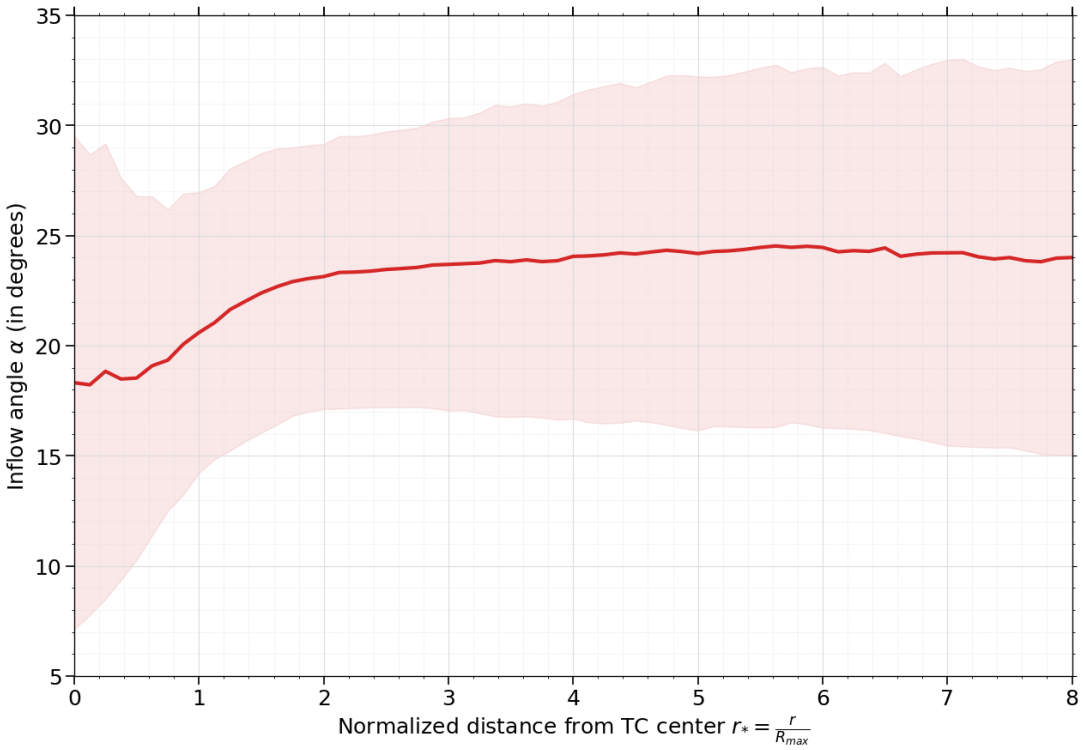

Figure 1.13 – Inflow angle composite from a database of 359 inter-calibrated scatterometer acquisitions, for mature TCs ($V_{max} > 25$ m/s) and at tropical latitudes (absolute latitude $\leq 30°$).

equation, while J. A. Zhang and Uhlhorn, 2012 derived a parametric formulation for α based on GPS-dropsondes observations. In the latter study, an average inflow angle of $\sim 23°$ is found.

1.3.4 The boundary layer

Because of friction at the ocean surface, a layer - the BL - develops in which the flow may no longer be described by frictionless equations. This layer was studied by Eliassen, 1971 and Eliassen and Lystad, 1977, who derived an analytical solution for M in the BL based on several assumptions. In their studies, the tangential and radial equations governing the BL are

$$\frac{\partial M}{\partial t} + u\frac{\partial M}{\partial r} + w\frac{\partial M}{\partial z} = \frac{\partial}{\partial z}\left(K\frac{\partial M}{\partial z}\right) \tag{1.13}$$

and

$$\frac{M^2}{r^3} = \frac{1}{\rho}\frac{\partial P'}{\partial r} - \frac{\partial}{\partial z}\left(K\frac{\partial u}{\partial z}\right) \tag{1.14}$$

where K is the turbulent eddy viscosity. In other words, a viscosity term is added to the angular momentum conservation equation and gradient wind balance. In addition, it is assumed that the BL is well mixed on the vertical, so that vertical gradients of P are small and further neglected. The absolute angular momentum M_g required to maintain gradient wind balance at the top of the BL satisfies

$$\frac{M_g^2}{r^3} = \frac{1}{\rho}\frac{\partial P'}{\partial r} \tag{1.15}$$

In the BL, M is assumed to remain of the same order as M_g, and we may write

$$M = M_g + M' \tag{1.16}$$

with $M' \ll M_g$. Substituting this relation into Eq. 1.14 and neglecting second order terms in M', we obtain

$$\frac{2M_g M'}{r^3} = -\frac{\partial}{\partial z}\left(K\frac{\partial u}{\partial z}\right) \tag{1.17}$$

Then, it is assumed that the time adjustment of the BL is small compared to the characteristic time of the system evolution, so that the time derivative term in Eq. 1.13 is neglected. In addition, because the BL is vertically well mixed, vertical advection of M may be neglected *versus* the radial advection of M. As a result, Eq. 1.13 becomes

$$u\frac{\partial M}{\partial r} = \frac{\partial}{\partial z}\left(K\frac{\partial M}{\partial z}\right) \tag{1.18}$$

where we further approximate M by M_g in the radial advection term, while M may be equivalently replaced by M' in the diffusion term. From here, K will be considered constant. This simplifies the system and will allow us to derive an analytical solution for M'. We derive twice Eq. 1.18 with respect to z, assuming that M_g is constant along the vertical, and combine it with Eq. 1.17 to obtain

$$\frac{\partial^4 M'}{\partial z^4} + \frac{N^2}{K^2}M' = 0 \tag{1.19}$$

where $N^2 := \frac{1}{r^3}\frac{\partial(M_g^2)}{\partial r}$ is the inertial stability of the gradient wind at the top of the

BL. Equation 1.19 can be solved analytically. Examples of solutions may for instance be found in (Vogl & Smith, 2009; Smith & Montgomery, 2020, 2021).

In addition, a characteristic scale for the BL height h emerges

$$h = \sqrt{\frac{2K}{N}} \tag{1.20}$$

In other words, the BL height increases with diffusivity and decreases with inertial stability. The characteristic adjustment time τ for the BL is then

$$\tau = \frac{2}{N} \tag{1.21}$$

and does not depend on K. Figure 1.14 presents the BL height h as a function of radius for the Holland wind profile from Fig. 1.12 with $B = 1.3$. For a large portion of the profile, h increases with radius. In agreement with Eq. 1.20 the diffusivity K increases the BL height h (shades of blue in Fig. 1.14).

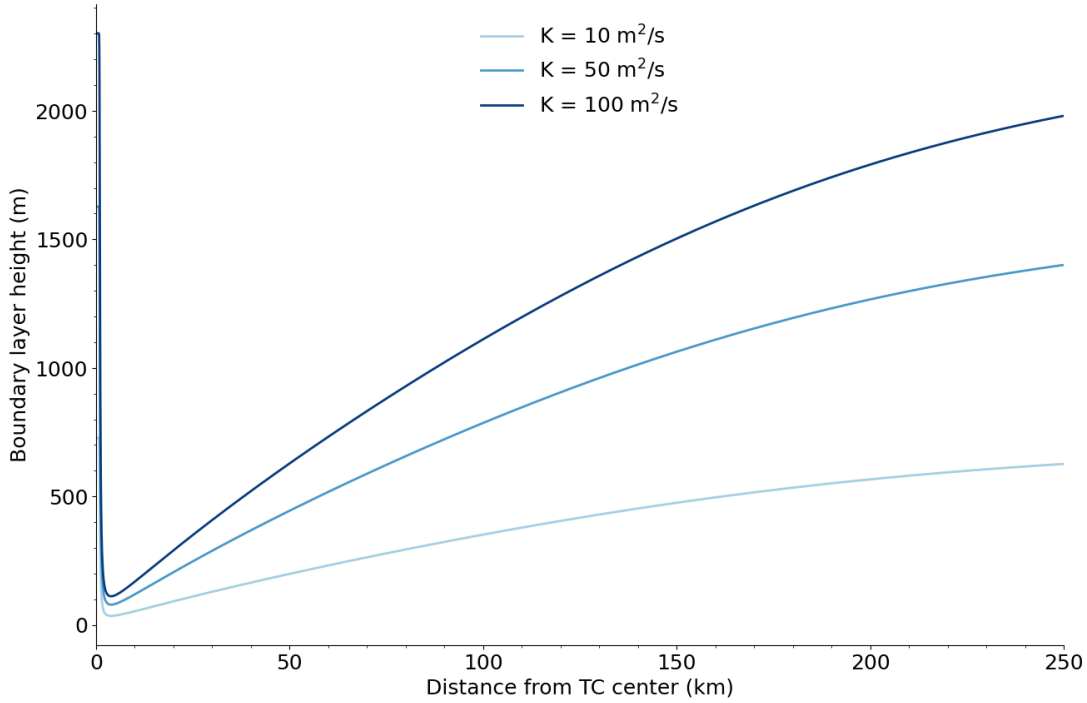

Figure 1.14 – Theoretical TCs BL height obtained by applying Eq. 1.20 to a Holland wind profile with $B = 1.3$ (see Fig. 1.12) for different values of K.

Note that h is of the order 1 km, as suggested by observational data (Powell et al.,

2003; Ren et al., 2019). Because the height of the whole TC system H, of the order 10 km, is much bigger than h, the BL adjusts almost instantaneously compared to the whole TC system evolution, supporting the assumption of steady-state in the BL.

The approach of Eliassen, 1971 and Eliassen and Lystad, 1977 to describe the BL served as a basis for other studies that provided analytical solutions for the asymmetric BL wind field in the steady-state case (Shapiro, 1983; Kepert, 2001). Indeed, because of their translation speed, TCs usually have larger wind speed values on their right side (with respect to their motion). Then, because the friction exerted by the ocean surface on overlying air parcels depends on the wind speed, asymmetries in the friction torque develop in the BL, which in turn produce asymmetries in the whole wind field.

The radial motions of the air parcels in the BL imply vertical motions because of the equation of continuity (Eq. 1.4). An expression for the vertical velocity at the top of the BL $w(z = h)$ may be obtained from Eq. 1.18 by imposing a surface boundary condition. In the general case, K is not considered constant, but a non-slip boundary condition is applied at the ocean surface, such that at $z = 0$,

$$K\rho\frac{\partial u}{\partial z} = C_d\rho\sqrt{(u_{10}^2 + v_{10}^2)}u_{10} =: \tau_{rs} \tag{1.22}$$

with u_{10} and v_{10} the radial and tangential components of the wind speed at an altitude of 10 m (*i.e* the altitude where TCs air-sea exchanges are assumed to take place). In the present manuscript we will further approximate this surface stress

$$\tau_{rs} \approx C_d\rho v_{10}u_{10} \tag{1.23}$$

Equivalently, we have

$$K\rho\frac{\partial M}{\partial z} \approx C_d\rho r v_{10}^2 =: r\tau_{\theta s} \tag{1.24}$$

at $z = 0$. Further considering that $K\frac{\partial M}{\partial z} = 0$ at $z = h$, Eq. 1.18 may be integrated from the surface to the top of the BL to yield

$$\int_0^h u\frac{\partial M}{\partial r}\,dz = -\frac{r\tau_{\theta s}}{\rho} \tag{1.25}$$

Then, integrating the continuity equation (Eq. 1.4) over the BL yields

$$w(z = h) = -\frac{1}{r}\int_0^h \frac{\partial}{\partial r}(ru)\,dz \tag{1.26}$$

where we considered $w(z = 0) = 0$. Assuming that $\frac{\partial M}{\partial r}$ may be replaced by its vertically averaged BL value in Eq. 1.25, and substituting for the resulting expression of $\int_0^h u\, dz$ in Eq. 1.26, we obtain

$$w(z = h) \approx \frac{1}{r}\frac{\partial}{\partial r}\left(\frac{C_d r v(z = 0)^2}{\frac{1}{r}\frac{\partial M}{\partial r}}\right) \tag{1.27}$$

Equation 1.27 expresses that vertical motions at the top of the BL are due to radial gradients of a competing effect between the friction torque (numerator) and the vertical component of absolute vorticity (denominator).

1.3.5 The heating mechanism

The radial motions of air parcels at the ocean surface allow the TC to further develop and be maintained through an air-sea interaction. Two theories emerged to model how TCs draw their energy from the ocean. The first suggests that the main mechanism for their development is the release of latent heat by cumuli, which is enhanced by the friction in the BL and the subsequent low-level moisture convergence. This view, where the cumuli are organized at large scale by the system, is referred to as the conditional instability of the second kind (CISK) and was first advanced by Charney and Eliassen, 1964 and Ooyama, 1964. The radial distribution of heating then depends on the amplitude of the vertical motions caused by friction in the BL which are characterized by C_d (see Eq. 1.27).

The second and more recent theory suggests that the TC energy predominantly comes from enthalpy fluxes at the air-sea interface rather than from condensation latent heat release. This second view, which is not incompatible with the first, is called the wind–induced surface heat exchange (WISHE) theory (K. A. Emanuel, 1986). At the air-sea interface, the moist entropy processes are controlled by the enthalpy exchange coefficient C_k, while the momentum fluxes are controlled by C_d. The WISHE theory thus highlighted the dependence of V_{max} on the ratio of exchange coefficients $\frac{C_k}{C_d}$ (see below). Both CISK and WISHE theories allow for analytical treatments on the TC wind structure.

Controlling the heating mechanism in one or the other theory, C_d and C_k both depend on the ocean surface roughness, and thus on wind speed. At low wind speeds (below ∼30 m/s), C_d increases with wind speed, while C_k remains nearly constant. The behaviour of C_d and C_k at high wind speeds (above ∼30 m/s) is an active field of research. Several observational and laboratory studies suggest that C_d saturates or even decreases with wind speed (Powell et al., 2003; M. Donelan et al., 2004; Black et al., 2007; Jarosz et

al., 2007; Bell et al., 2012; Soloviev et al., 2014; M. A. Donelan, 2018; Curcic & Haus, 2020), while little is known about the behaviour of C_k. For a review summarizing the state-of-the-art knowledge on C_d and C_k, see Sroka and Emanuel, 2021.

1.3.6 The meridional circulation

Whether TCs draw their energy from large-scale organized latent heat release or from surface heat exchanges, the resulting heating will impact the system flow. For a given radial distribution of heating, a meridional (secondary) circulation will develop so that the axial (primary) circulation remains balanced. In fact, an equation for this meridional circulation may be derived from the governing equations (Eliassen, 1951), assuming that the evolution of the flow is quasi-static (*i.e* the heat source evolves slowly with time compared to the whole system). The meridional circulation is better expressed by defining a stream function ψ such that

$$ru = -\frac{\partial \psi}{\partial z} \quad \text{and} \quad rw = \frac{\partial \psi}{\partial r} \tag{1.28}$$

which ensures that the continuity equation (Eq. 1.4) is satisfied.

Combining gradient wind and hydrostatic balance (Eqs. 1.2, 1.3), the thermal wind equation may be obtained and further written in terms of absolute angular momentum

$$\frac{1}{r^3}\frac{\partial M^2}{\partial z} = g\frac{\partial \tilde{\theta}}{\partial r} \tag{1.29}$$

This equation states that vertical gradients of momentum imply radial gradients of temperature, and conversely. For a given heat source, the resulting meridional circulation will ensure that the flow satisfies this thermal wind balance. To derive the equation for this meridional circulation, we first add a heat source term to Eq. 1.5, which now reads

$$\frac{\partial \tilde{\theta}}{\partial t} + u\frac{\partial \tilde{\theta}}{\partial r} + w\frac{\partial \tilde{\theta}}{\partial z} + \Gamma w = \frac{Q}{C_p \bar{T}} \tag{1.30}$$

with Q the heat source and C_p the heat capacity at constant pressure. Then, eliminating the time derivatives from Eq. 1.30 and Eq. 1.7 using Eq. 1.29 and further using the definition of the stream function Eq. 1.28, we obtain the so-called Sawyer-Eliassen equation:

$$\frac{\partial}{\partial r}\left(\frac{A}{r}\frac{\partial \psi}{\partial r}+\frac{B}{r}\frac{\partial \psi}{\partial z}\right)+\frac{\partial}{\partial z}\left(\frac{B}{r}\frac{\partial \psi}{\partial r}+\frac{C}{r}\frac{\partial \psi}{\partial z}\right)=\frac{g}{C_p\bar{T}}\frac{\partial Q}{\partial r} \tag{1.31}$$

with A, B and C the static stability, the baroclinic, and the inertial stability terms, respectively:

$$A := g\left(\frac{\partial \tilde{\theta}}{\partial z}+\Gamma\right), \quad B := -\frac{1}{r^3}\frac{\partial M^2}{\partial z}=-g\frac{\partial \tilde{\theta}}{\partial r}, \quad C := \frac{1}{r^3}\frac{\partial M^2}{\partial r}=N^2 \tag{1.32}$$

For a given radial distribution of heat source Q, if the distributions of M and $\tilde{\theta}$ are known, the meridional circulation ψ that must develop for the flow to remain balanced may be estimated using Eq. 1.31. By constraining ψ to vanish at the boundaries, *i.e* on a closed contour S, a unique solution for ψ inside S may be determined using Green functions. Note that a situation where $\frac{\partial Q}{\partial r}=0$ implies that $\psi \equiv 0$, *i.e* no meridional circulation develops. Eliassen, 1951 argued that this equation is valid for stable vortices only, in which case it can be shown by computing the discriminant of the equation that it is elliptical. The author then examined the meridional circulation created by a point-source of heat and applied this theory to describe Hadley and Ferrel cells (in which the prevailing westerlies and easterlies play the role of the primary circulation).

Although the balanced model and the corresponding Sawyer-Eliassen equation have some limitations because of the axisymmetric and balance assumptions (Bui et al., 2009), it provides a theoretical framework to assess the meridional circulation response to changes in the primary circulation and radial distribution of heating. For instance, using Bessel functions, Schubert and Hack, 1982 obtained analytical solutions for ψ for arbitrary piece-wise definitions of tangental wind (v), inertial stability (C) and heat source (Q), assuming constant static stability ($A = \text{cst}$) and barotropic vortex ($B = 0$). Their study highlighted the role of inertial stability for the TC development, although it didn't account for its role on the motions in the BL. Several other research studies have used the balanced model to examine the role of the meridional circulation in the TC evolution (Smith, 1981; Shapiro & Willoughby, 1982; H. Willoughby et al., 1982; Schubert & Hack, 1983; Hack & Schubert, 1986; Nolan et al., 2007; Vigh & Schubert, 2009). Numerical methods have also been developed to solve Eq. 1.31 for real or simulated TCs for which the discriminant is not everywhere elliptical (see for instance Möller and Shapiro, 2002).

Surprisingly, the balanced model was mostly used in combination with prescribed

distributions of heating Q, perhaps with the aim of estimating Q from real data and inferring the corresponding changes in the wind structure using Eq. 1.31. Yet, as noted by A. Kalashnik and Kalashnik, 2011, Q may also be treated as the unknown in Eq. 1.31. In particular, the meridional circulation ψ may be prescribed instead of Q. In this case, M and $\tilde{\theta}$ can be successively retrieved using Eq. 1.7 and Eq. 1.29, while Q is determined using Eq. 1.31. This view may be helpful when the wind structure is more accurately estimated than heating distributions.

1.3.7 The steady-state theory

In TCs theory (*e.g* Eliassen, 1951), it is common to assume that air parcels conserve their absolute angular momentum along their trajectory above the BL. The validity of this assumption may have been tested as early as when aircraft observations were available. Figure 1.15 presents estimates of the stream function ψ and surfaces of constant absolute angular momentum M for TC Daisy in 1958 (Riehl & Malkus, 1961). Notably, the M- (solid lines) and ψ-surfaces (dashed lines) are roughly congruent above a certain altitude.

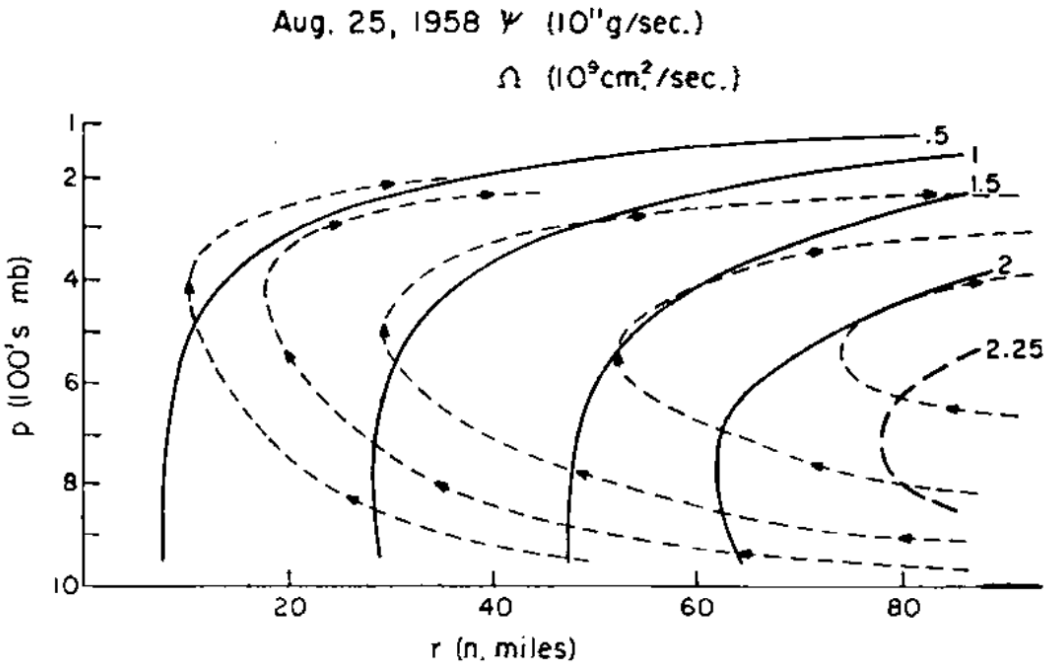

Figure 1.15 – Aircraft-based estimates of the structure of TC Daisy on 25^{th} August 1958. Solid lines denote constant absolute angular momentum surfaces, while dashed lines denote the Stokes stream function. Extracted from Riehl and Malkus, 1961.

Note that if M is approximately conserved along the outflow trajectory, a characteristic radius is naturally introduced. The radius where the outflow azimuthal velocity vanishes R_0 is directly related to the Rossby number evaluated at R_{max} via

$$\sqrt{2Ro_{max}} = \frac{R_0}{R_{max}} \tag{1.33}$$

where $Ro_{max} := \frac{V_{max}}{fR_{max}}$. Equation 1.33 gives an expression for V_{max} provided that f as well as the two characteristic radii R_0 and R_{max} are known. This explains why research studies have focused on trying to estimate these two radii using infrared data before the Dvorak method was developed (Hubert, 1969).

Because M is roughly conserved in the outflow, all the momentum losses occur in the BL. A simple way to characterize these losses, based on the PV conservation equation (Riehl, 1963), is to assume that

$$C_d r v^2 = \text{cst} \tag{1.34}$$

In Eq. 1.34, Riehl, 1963 assumed $C_d = \text{cst}$, which implies that $v \propto \frac{1}{r^{\frac{1}{2}}}$. In this steady-state study, the momentum losses were equated to the heat gained by air parcels at the ocean surface along their trajectory from outer radii toward inner radii, expressed in terms of equivalent potential temperature. Using an empirical relationship between the surface pressure deficit and the equivalent potential temperature increase in the BL from the ambient environment to the TC eyewall, Riehl, 1963 further obtained an equation for V_{max}^2 that depends on the ratio $\frac{R_0}{R_{max}}$.

In 1981, Shutts, 1981 assumed that the dry PV vanishes everywhere in the TC, arguing that this assumption is an extension of the Rankine profile for vortices that have radial temperature gradients. In cylindrical coordinates, the dry PV is

$$q = \frac{1}{\rho r}\left(\frac{\partial M}{\partial r}\frac{\partial \theta}{\partial z} - \frac{\partial M}{\partial z}\frac{\partial \theta}{\partial r}\right) \tag{1.35}$$

Then, the assumption of zero dry PV is equivalent to the assumption that θ is a function of M alone. Shutts, 1981 used this assumption to derive an equation for the slope of M-surfaces for a balanced TC. An analytical solution for the height of M-surfaces was then obtained. Figure 1.16 presents an example of the resulting TC structure when the surface outer-wind profile is a modified Rankine vortex with an exponent $x = \frac{1}{2}$ (Shutts, 1981).

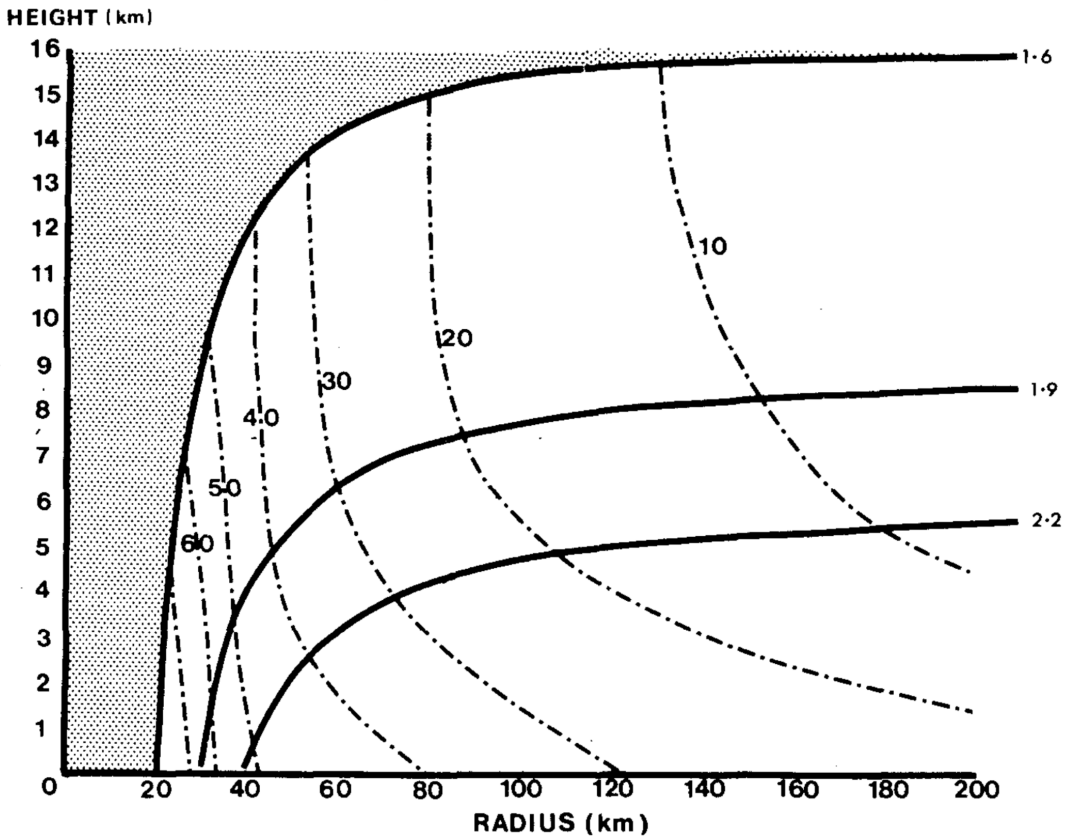

Figure 1.16 – Structure of a TC with zero dry PV, for an arbitrary radial wind profile ($v(r) = \frac{11000}{r^{\frac{1}{2}}}$ m/s). Solid curves represent M- and θ-surfaces labeled with values of M (10^6 m^2/s), while dotted dashed curves represent isotachs of v. Extracted from Shutts, 1981.

Shutts, 1981 did not account for turbulent fluxes inside the BL. A few years later, K. A. Emanuel, 1986 (hereafter E86) also derived an equation for the slope of M-surfaces for a balanced TC, but this time considered that saturated moist PV vanishes everywhere, rather than dry PV. Equivalently, the saturated moist entropy s^* is a function of M alone. In addition, E86 did not use an arbitrary surface wind profile, but instead linked the TC structure above the BL with that at the top of the BL. The equations of conservation of momentum and energy were thus integrated over the BL depth, introducing the surface fluxes of enthalpy and momentum. Here we present the main steps of the E86 theory.

In E86, the conceptual view of the TC above the BL starts with the thermal wind equation (Eq. 1.29), stated in (r, P) rather than in (r, z) coordinates. Further assuming the ideal gas law, the thermal wind equation may be expressed using only two state variables, pressure and moist entropy, leading to

$$\frac{1}{r^3}\left(\frac{\partial M^2}{\partial P}\right)_r = -\left(\frac{\partial T}{\partial P}\right)_{s^*}\left(\frac{\partial s^*}{\partial r}\right)_P \tag{1.36}$$

Then, because s^* depends on M alone, Eq. 1.36 may be rewritten

$$\frac{1}{r^3}\left(\frac{\partial M^2}{\partial P}\right)_r = -\left(\frac{\partial T}{\partial P}\right)_{s^*}\frac{ds^*}{dM}\left(\frac{\partial M}{\partial r}\right)_P \tag{1.37}$$

Dividing each side by $\frac{\partial M}{\partial r}$ yields

$$\frac{2M}{r^3}\left(\frac{\partial r}{\partial P}\right)_M = \left(\frac{\partial T}{\partial P}\right)_{s^*}\frac{ds^*}{dM} \tag{1.38}$$

Equation 1.38 may be integrated in pressure along an M-surface from the top of the BL (r_b, T_b) to an arbitrary altitude (r, T), leading to

$$\frac{1}{r_b^2} = \frac{1}{r^2} - (T_b - T)\frac{1}{M}\frac{ds^*}{dM} \tag{1.39}$$

Defining the outflow temperature T_o as the temperature an air parcel has when $r \to \infty$, and noting the value of the M-surface M_b for clarity, the previous equation becomes

$$\frac{1}{r_b^2} = -(T_b - T_o)\frac{1}{M_b}\frac{ds^*}{dM} \tag{1.40}$$

Further multiplying each side by $\frac{\partial M}{\partial r}$, we obtain

$$\frac{\partial M}{\partial r}\frac{1}{r_b^2} = -(T_b - T_o)\frac{1}{M_b}\frac{\partial s^*}{\partial r} \tag{1.41}$$

By integrating the steady-state equations of conservation of momentum and energy over the BL depth and further assuming that the BL is well-mixed and M-surfaces approximately vertical, it can be shown that

$$\left(\frac{\partial s}{\partial M}\right)_{z=h} = \frac{1}{T_s}\left(\frac{\tau_{ks}}{r_b \tau_{\theta s}}\right)_{z=0} \tag{1.42}$$

where T_s is the sea surface temperature and $\tau_{ks} := C_k\rho\sqrt{u_{10}^2 + v_{10}^2}(k_s^* - k_{10}) \approx C_k\rho v_{10}(k_s^* - k_{10})$ is the surface enthalpy flux, with C_k the enthalpy exchange coefficient, k_s^* the saturation enthalpy of the sea surface and k_{10} the enthalpy of air at the air-sea interface. Note that, because of the zero saturated moist PV assumption, we have $s^* = s$ at $z = h$. In addition, because the BL is well-mixed and M-surfaces approximately vertical, we have

$\frac{\partial s}{\partial M} = \frac{ds}{dM}$. See K. Emanuel and Rotunno, 2011 for discussions about these assumptions. With these relations, Eq. 1.42 may be rearranged

$$\frac{ds^*}{dM} = -\frac{C_k}{C_d}\frac{(k_s^* - k_{10})}{T_s r_b v_{10}} \tag{1.43}$$

and further substituted into Eq. 1.39 to yield

$$\frac{M_b v_{10}}{r_b} = \frac{C_k}{C_d}\frac{(T_b - T_o)}{T_s}(k_s^* - k_{10}) \tag{1.44}$$

It is often further assumed that $v_{10} \approx v_b$, where v_b is the wind speed value at the top of the BL, and that $T_b \approx T_s$, so that, in the limit of the cyclostrophic approximation, Eq. 1.44 provides an expression for the intensity of the TC

$$v_b^2 = \frac{C_k}{C_d}\frac{(T_s - T_o)}{T_s}(k_s^* - k_{10}) \tag{1.45}$$

This equation expresses the maximum intensity a TC can achieve and is referred to as the *maximum potential intensity* (MPI). Bister and Emanuel, 1998 further showed that if frictional dissipation at the ocean surface is accounted for in the heat source term (*i.e* by replacing τ_{ks} by $\tau_{ks} + \rho C_d v_{10}^3$ in Eq. 1.42), the expression for the potential intensity of TCs becomes

$$v_b^2 = \frac{C_k}{C_d}\frac{(T_s - T_o)}{T_o}(k_s^* - k_{10}) \tag{1.46}$$

Because T_s has been replaced by T_o in the denominator, the potential intensity a TC can achieve is in fact higher when dissipative heating is accounted for. More precisely, $\frac{T_s}{T_o} \approx \frac{3}{2}$.

A solution for the potential intensity such as Eq. 1.45 or Eq. 1.46 allows to estimate the maximum TC intensities based on typical oceanic and atmospheric conditions. For instance, Fig. 1.17 represents the minimum central surface pressure a TC can reach in September in the Atlantic and Indian Oceans or in the Pacific based on typical SST and atmospheric values (K. A. Emanuel, 1986). Remarkably, the dependence of V_{max} on these environmental parameters in E86 theory well explains, to a first order, why TCs may be more intense in the Pacific ocean than in the North Atlantic, as confirmed by observations (see Fig. 1.1).

Note that Shutts, 1981 obtained an equation similar to that of E86 for the slope of M-surfaces

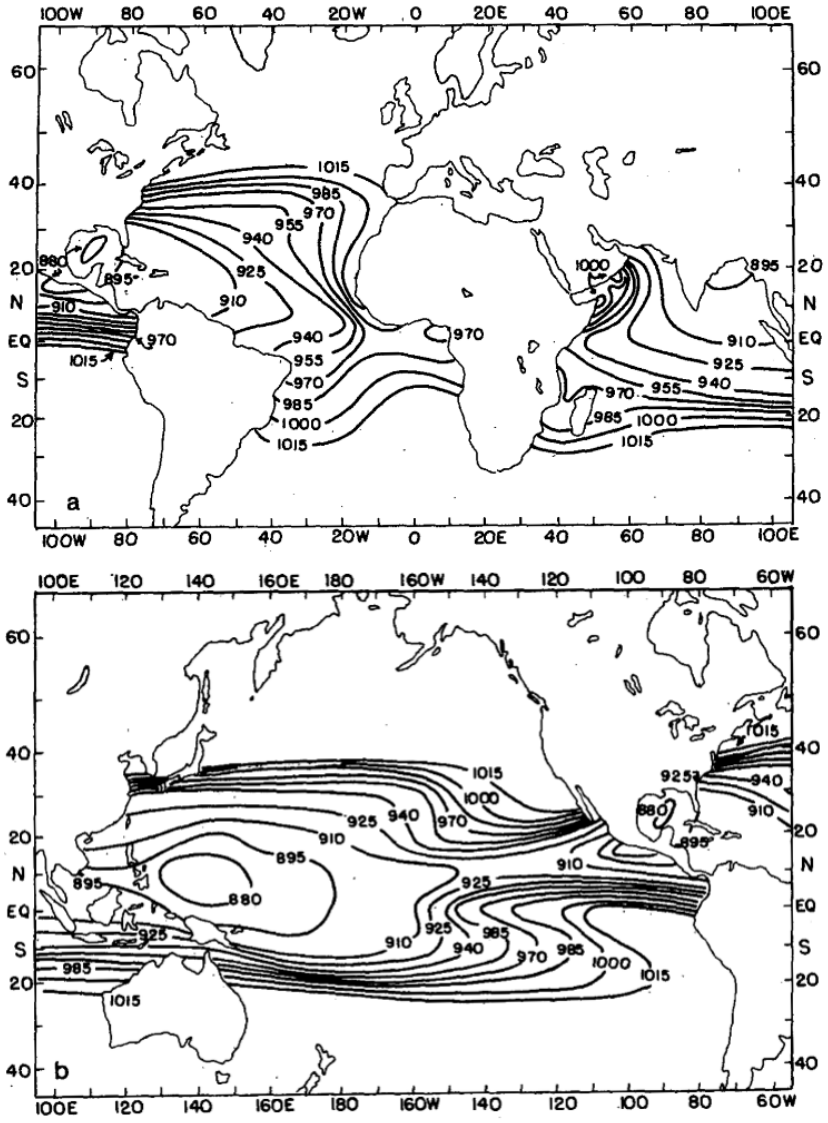

Figure 1.17 – TCs minimum attainable surface central pressure from E86 theory. Pressure values are expressed in mb and are based on typical oceanic and atmospheric parameters for September for the Atlantic and Indian Oceans (top) and for the Pacific Ocean (bottom). Extracted from K. A. Emanuel, 1986.

$$\frac{2M}{r^3}\left(\frac{\partial r}{\partial P}\right)_M = R_* \frac{P^{\kappa-1}}{P_O^{\kappa}} \frac{d\theta}{dM} \tag{1.47}$$

with the definition $\theta = T\left(\frac{P_0}{P}\right)^{\kappa}$ where P_0 is a reference pressure and $\kappa := \frac{R_*}{C_p}$ with R_* the gas constant, and the perfect gas law $P = \rho R_* T$. Had he integrated in pressure along

an M-surface, the author would have found

$$\frac{M_b}{r_b^2} = \frac{R_*}{\kappa}\frac{d\theta}{dM}\left(\frac{T_o}{\theta_o} - \frac{T_b}{\theta_b}\right) \tag{1.48}$$

with θ_o and θ_b the potential temperature of the outflow and at the top of the BL, respectively. Equation 1.48 is similar to Eq. 1.40. Because $s = C_p \ln(\theta) + \text{cst}$ (Bauer, 1908), $\frac{d\theta}{dM}$ scales as $\theta\frac{ds}{dM}$, which, in combination with Eq. 1.42, would allow for retrieving a potential intensity expression under the assumption that dry entropy is conserved along M-surfaces.

Although E86 is perhaps the most famous steady-state theory for the mature stage of TCs, it is not the only analytical work on this issue (see for instance Carrier et al., 1971; Anthes, 1974; Evans and Davies, 1979; Pearce, 2004; Leonov et al., 2014). However, the work of E86 highlighted that TCs may be considered as Carnot heat engines: isothermal expansion when the air parcel converges from outer radii to inner radii at the surface, isentropic expansion when the air parcel ascends along an M-surface, isothermal compression due to subsidence followed by isentropic compression when the air parcel returns to its initial position at the ocean surface.

The rate of mechanical energy generated during this Carnot cycle is expressed as

$$P := \left(\frac{T_o - T_s}{T_s}\right)\int_{\mathcal{A}} \tau_{ks}\, d\mathcal{A} = \left(\frac{T_o - T_s}{T_s}\right)\int_{\mathcal{A}} C_k \rho v_{10}(k_s^* - k_{10})\, d\mathcal{A} \tag{1.49}$$

while the dissipation rate is

$$D := \int_{\mathcal{A}} v_{10}\tau_{\theta s}\, d\mathcal{A} = \int_{\mathcal{A}} C_d \rho v_{10}^3\, d\mathcal{A} \tag{1.50}$$

where we assumed that all heating and dissipation were concentrated at the ocean surface on an area $\mathcal{A}$. Equating the energy gained by heating P to that lost by friction D in steady-state leads to Eq. 1.45, assuming that $v_{10} \sim V_{max}$ is constant on the effective area $\mathcal{A}$. Furthermore, accounting for dissipation in the heat source term (*i.e* replacing τ_{ks} by $\tau_{ks} + \rho C_d v_{10}^3$ in Eq.1.49) leads to Eq. 1.46. The Carnot cycle theory may thus be used to assess TCs steady-state (Denur, 2011; Ozawa & Shimokawa, 2015).

To summarize, the energy lost by the TC system increases with the cube of the surface velocity, while that generated by the TC system increases linearly with the surface velocity. Figure 1.18 schematically represents this situation. In steady-state, equating the energy production and dissipation rates leads to a unique nonzero solution for the surface velocity. V_{max} may then naturally be determined from these energetical considerations. In fact, this

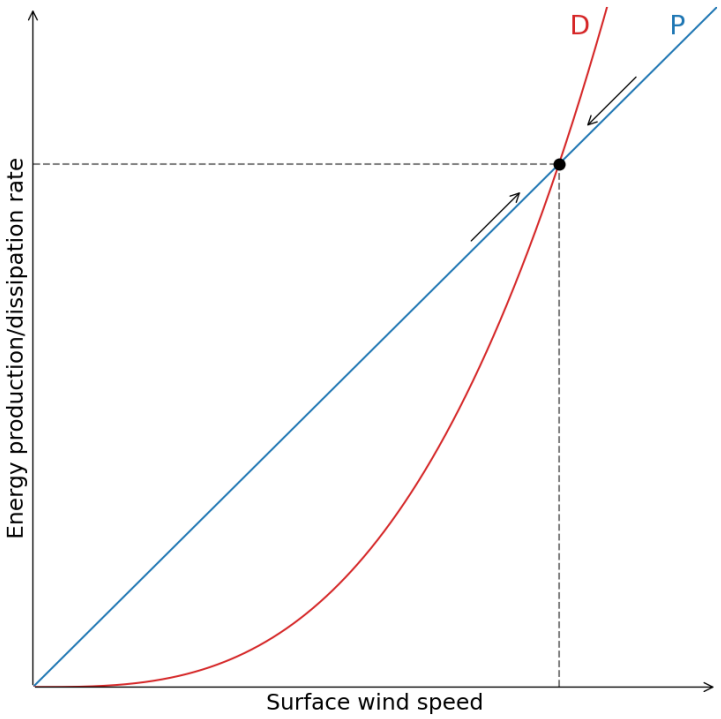

Figure 1.18 – Schematic illustration of the steady-state balance of energy production and dissipation for TCs. A stable equilibrium is reached when the energy production rate of energy (P, blue curve) equates the energy dissipation rate (D, red curve). Another (unstable) equilibrium is $P = D = 0$, not represented here. Adapted from Ozawa and Shimokawa, 2015.

reasoning also applies to polar lows (Golitsyn, 2008).

1.3.8 Analytical solutions for the evolution of tropical cyclones

Few studies have attempted to develop analytical solutions for the TC evolution. When developing the CISK theory, Charney and Eliassen, 1964 conducted a perturbation analysis for a balanced flow (*i.e* geostrophic and hydrostatic balance). Using Bessel functions, the authors obtained an analytical solution for the growth rate of TCs as a function of the radius separating the ascending motions from the descending motions. This radius characterizes the area where latent heat release is enhanced by low-level moisture convergence.

Perhaps the first analytical solution for the evolution of the complete wind profile was proposed by Eliassen, 1971 and Eliassen and Lystad, 1977. We recall that, in their framework, both M and u are assumed not to vary with altitude above the BL, so that,

for $z > h$, we note $M_g(r,t) = M(r,z,t)$ and $U(r,t) = u(r,z,t)$. Considering $w(z=H) = 0$ and integrating the continuity equation (Eq. 1.4) from the ocean surface $z = 0$ to the top of the TC system $z = H$, we obtain

$$\int_h^H u\,dz = (H-h)U = -\int_0^h u\,dz \tag{1.51}$$

Equation 1.25 implies that

$$\int_0^h u\,dz = -\frac{C_d r v_{10}^2}{\frac{\partial M_g}{\partial r}} \tag{1.52}$$

We thus have a solution for the radial velocity above the BL

$$U = \frac{1}{(H-h)}\frac{C_d r v_{10}^2}{\frac{\partial M_g}{\partial r}} \tag{1.53}$$

and finally, injecting this solution into the equation for conservation of M_g above the BL (see Eq. 1.7), we obtain

$$\frac{\partial M_g}{\partial t} = -U\frac{\partial M_g}{\partial r} = -\frac{C_d r v_{10}^2}{(H-h)} \tag{1.54}$$

We now assume that $M \approx rv$. In this case, because $\frac{\partial M}{\partial z}$ is assumed to be small both in and above the BL, we have $C_d r v_{10}^2 \approx C_d \frac{M_g^2}{r}$ and Eq. 1.54 becomes

$$\frac{\partial M_g}{\partial t} = -\frac{C_d}{H-h}\frac{M_g^2}{r} \tag{1.55}$$

Such an equation for the evolution of M at the gradient wind level was first proposed by Eliassen, 1971 and Eliassen and Lystad, 1977. The solution for Eq. 1.55 is

$$M_g(t) = \frac{M_0}{1 + \frac{C_d M_0}{(H-h)r}t} \tag{1.56}$$

where $M_g(t=0) =: M_0$ is an arbitrary initial condition. As noted by Eliassen and Lystad, 1977, this provides a characteristic time for the adjustment of the BL. We have

$$\tau_{BL} = \frac{(H-h)r}{C_d M_0} \tag{1.57}$$

where τ_{BL} is defined as the time required to reduce M_0 by a factor two. Note that Eq. 1.56 only models a decrease of angular momentum, since we considered that the ocean surface acts as a brake for the gradient wind above through Eq. 1.25. In Eliassen, 1971

and Eliassen and Lystad, 1977, the case of angular momentum increase is modelled by a spin-up action from the ocean surface on the flow in the BL. This case can be retrieved by inverting the sign in Eq. 1.52. Equation 1.56 then reduces to

$$M_g(t) = \frac{M_0}{1 - \frac{C_d M_0}{(H-h)r} t} \tag{1.58}$$

In this simple analytical solution, M_g increases more when the product of C_d and M_0 is large compared to the product of $(H - h)$ and r. Note that, for a fixed radius r, the solution diverges when $t \to \frac{(H-h)r}{C_d M_0}$, but the assumptions made above break down much before that time. In addition, for real cases both C_d and $H - h$ are not constant in time, so that the solution Eq. 1.58 is certainly only valid for a short time period. Yet, this simple framework demonstrates that the balanced equations are relevant to capture the evolution of TCs.

After these two pioneering studies, research works kept taking advantage of the balanced model to further examine TCs evolution. Using the Sawyer-Eliassen equation presented above, it is possible to analytically diagnose the secondary circulation associated with an arbitrary heating distribution and primary circulation. These equations are still valid if the prescribed heating source varies slowly with time, such that the TC always remains in balance with this forcing. The secondary circulation may then be analytically solved for at different time steps. For instance, Schubert and Hack, 1982 considered five different time steps of a typical TC intensification phase. Based on the Sawyer-Eliassen equation in a transformed coordinate system (*i.e* the one of Schubert and Hack, 1983), Frisius, 2005 further assumed zero dry PV (exactly like in Shutts, 1981) to obtain an analytical solution of the TC evolution for a prescribed heat source. Schubert et al., 2016 used a shallow-water framework and expressed the balanced vortex equations of Eliassen, 1951 in terms of PV. Using a wave-vortex approximation and filtering inertia-gravity waves, they obtained an analytical solution for the evolution of an initial PV field when an arbitrary piecewise mass sink is used as forcing. Hendricks et al., 2021 extended this approach by estimating the radial distribution of heating from observational data (*i.e* SFMR rain rates). The authors demonstrated that this balanced theory may be useful for short-term forecasting (*i.e* less than 24 hours).

As noted above, simple analytical solutions for the complete wind profile may also be found by prescribing the stream function rather than the radial distribution of heating. For instance, Kieu and Zhang, 2009 imposed an exponential growth rate for the vertical

motions inside R_{max} and zero vertical motion outside. The authors obtained an analytical solution for $u(r, z, t)$ using the continuity equation (Eq. 1.4) and then for $v(r, z, t)$ using the equation of conservation of tangential momentum (Eq. 1.1). They did not account for the thermodynamic equation (Eq. 1.5) and used a linear law for surface friction rather than a quadratic one, as emphasized by Montgomery and Smith, 2010. In addition, their solution was discontinuous at $r = R_{max}$. This discontinuity was further corrected by A. Kalashnik and Kalashnik, 2011, who also considered a linear friction term in the equation of conservation of tangential momentum

$$\frac{\partial m}{\partial t} + u\frac{\partial m}{\partial r} + w\frac{\partial m}{\partial z} + \lambda m + fru = 0 \tag{1.59}$$

where λ is their friction coefficient and we recall that m is the relative angular momentum. A. Kalashnik and Kalashnik, 2011 did not constrain the growth rate of vertical motions but imposed the shape of the complete stream function

$$u(r, z) = U_0 \begin{cases} \frac{rz}{LH} & \text{if } 0 < r < L \\ \frac{zL}{rH} & \text{if } r > L \end{cases} \tag{1.60}$$

and

$$w(r, z) = \frac{HU_0}{L} \begin{cases} (1 - \left(\frac{z}{H}\right)^2) & \text{if } 0 < r < L \\ 0 & \text{if } r > L \end{cases} \tag{1.61}$$

where U_0 and L are a characteristic velocity and a characteristic scale, both associated with radial motions. Using the method of characteristics, the authors obtained an analytical solution for Eq. 1.59 using (r, ψ) variables rather than (r, z). For instance, at the lowest level (the top of the BL, which corresponds to $z = 0$ in their paper), the tangential wind speed is given by

$$v(r, t) = fL \begin{cases} \frac{(\frac{r}{L})(1-e^{(2-\lambda)\frac{tU_0}{L}})}{\lambda-2} & \text{if } 0 < r < Le^{-\frac{tU_0}{L}} \\ \frac{\lambda(\frac{r}{L})^2-2(\frac{r}{L})^\lambda}{\lambda(\lambda-2)(\frac{r}{L})} - \frac{e^{-\lambda\frac{tU_0}{L}}}{\lambda r} & \text{if } Le^{-\frac{tU_0}{L}} < r < L \\ \frac{1-e^{-\lambda\frac{tU_0}{L}}}{\lambda(\frac{r}{L})} & \text{if } r > L \end{cases} \tag{1.62}$$

Note that neither Kieu and Zhang, 2009 nor A. Kalashnik and Kalashnik, 2011 tried to apply their analytical solution to an initial observed wind field. However, both studies obtained that the wind speed in the near-core region increases at a faster rate (*e.g* nearly exponentially with time) than that in the outer region (*e.g* nearly linearly with time).

Furthermore, both analytical solutions are strongly dependent on the radius of significant upward motions. In Kieu and Zhang, 2009, this radius coincides with R_{max}, while it is represented by L in A. Kalashnik and Kalashnik, 2011, and thus assumed constant from one TC to another. A last limitation of these two studies is that they focused on the intensification phase only.

While the studies mentioned above all provide an analytical solution for the evolution of the complete wind profile, future changes of V_{max} may be easily predicted using the the logistic growth equation (LGE) (DeMaria, 2009; Zhou et al., 2021; S. Wang & Toumi, 2022). The LGE was first introduced by Pierre Francois Verhulst in 1845 for population dynamics studies. It models the number of individuals (*i.e* population $\mathcal{P}$) as a function of time, by assuming that its rate of change ($\frac{d\mathcal{P}}{dt}$) is proportional to the initial number of individuals ($\mathcal{P}$) until it has reached a steady-state. The steady-state population is called the *carrying capacity* (κ) and is due to various factors (*e.g* food supply, predators) limiting the population growth rate (π). The LGE formulation is then

$$\frac{d\mathcal{P}}{dt} = \pi\mathcal{P}\left(1 - \frac{\mathcal{P}}{\kappa}\right) \tag{1.63}$$

Here we recognize an equation close to Eq. 1.55, provided that we add a radial advection term in Eq. 1.55, which becomes

$$\frac{\partial M_g}{\partial t} = -U_g\frac{\partial M_g}{\partial r} - \frac{C_d}{H-h}\frac{M_g^2}{r} \tag{1.64}$$

where U_g is the effective radial inflow of M_g. To derive a LGE for V_{max}, we further evaluate Eq. 1.64 at $r = R_{max}$ and assume that $M_g \approx rv$ close to R_{max}. We also assume $\frac{\partial M_g}{\partial r}\Big|_{r=R_{max}} \approx V_{max}$ and neglect the time derivative of R_{max} to obtain

$$\frac{dV_{max}}{dt} = \pi V_{max}\left(1 - \frac{V_{max}}{\kappa}\right) \tag{1.65}$$

with $\pi = \frac{-U_g}{R_{max}}$ and $\kappa = \frac{-U_g(H-h)}{C_d R_{max}}$ and U_g is now $U_g(r = R_{max})$. From Eq. 1.65, in the LGE framework, the higher the radial advection of angular momentum in the inflow layer ($-U_g$) and the smaller the radius of maximum wind (R_{max}), the greater the intensification rate (π). In addition, the achievable intensity (κ) is limited by the drag coefficient (C_d) and the radius of maximum wind (R_{max}), while being stimulated by additional advection of angular momentum in the inflow layer ($-U_g$) and increases in the height of the TC system that is above the BL ($H - h$). The LGE has a simple analytical solution

$$V_{max}(t) = \frac{V_{max,0}\kappa e^{\pi t}}{(\kappa - V_{max,0}) + V_{max,0}e^{\pi t}} \tag{1.66}$$

where $V_{max,0}$ is the initial maximum intensity. Thanks to its simplicity, the LGE framework can be used as a reference to assess the performance of other dynamical/statistical intensity prediction schemes.

Figure 1.19 presents a comparison of V_{max} evolution for 48 hours in three of the above-mentioned analytical models. Due to the variety of approaches used in the studies, the characteristic parameters of each of these models were arbitrarily chosen and the V_{max} values normalized so that they never exceed one (see figure caption for more details). The models all correspond to the intensification phase of TCs, except the one of A. Kalashnik and Kalashnik, 2011 which allows for capturing both the intensification and weakening phase of a TC if we chosse $\lambda > 1$. The analytical solution corresponding to this latter model may be investigated with respect to observational wind profile estimates to assess its capacity to capture the life cycle of TCs wind structure.

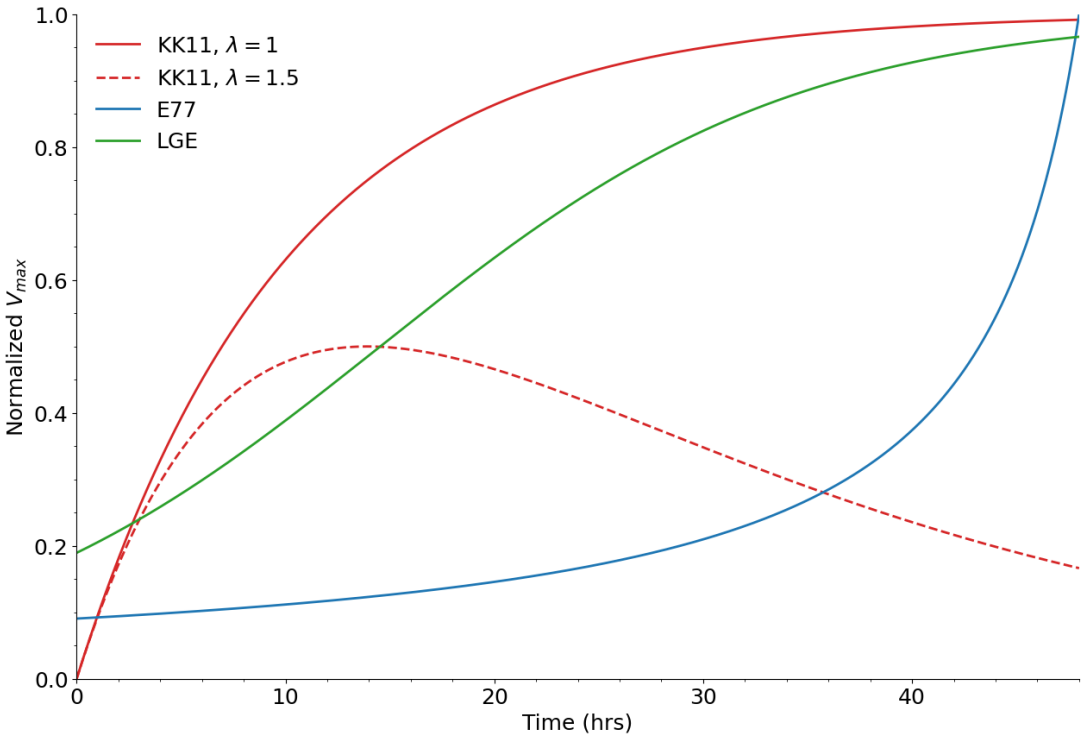

Figure 1.19 – Comparison of analytical solution for V_{max} evolution for 48 hours. The KK11 model is based on Eq. 1.62 evaluated at $r = Le^{-\frac{tU_0}{L}}$ using a latitude of 20°, $L = 300$ km, $U_0 = 8.3$ m/s (red curves). This corresponds to a characteristic velocity fL of 15 m/s, used to normalize the V_{max} values, and a characteristic time $\frac{L}{U_0}$ of 10 hrs. λ was either set to 1 (solid) or to 1.5 (dashed). The E77 model is based on Eq. 1.58 using $M_0 = 5 \times 18000$ m^2/s, $C_d = 10^{-2}$, $H = 10$ km and $h = 0.5$ km (blue curve). This corresponds to a final velocity of 55 m/s, used to normalize the V_{max} values, and a normalization time $\frac{(H-h)R_{max}}{C_d M_0}$ of 53 hrs. The LGE model is based on Eq. 1.66 using $V_{max,0} = 5$ m/s, $U_g = -0.5$ m/s, $R_{max} = 18$ km, $C_d = 10^{-2}$, $H = 10$ km and $h = 0.5$ km (green curve). This corresponds to a carrying capacity κ of 26 m/s, used to normalize the V_{max} values, and a characteristic time $\frac{1}{\pi}$ of 10 hrs.

Chapter 2

Relationship between tropical cyclone radius of maximum wind and outer-size

2.1 Introduction

From all the structural parameters currently included in best-track data, R_{max} is perhaps the most challenging to determine. In the absence of a SAR or SFMR observation, operational centers strongly rely on the use of imaging radiometers and scatterometers to reanalyze this parameter, but these instruments have known limitations regarding the estimation of wind speeds near the TC core (see Fig. 1.11).

Because an accurate estimate of R_{max} is needed for various TC applications, including surface wave studies, storm surge studies, and works on upper ocean responses to TC passages, several research investigations developed statistical methods in order to estimate R_{max} from better resolved parameters (Mueller et al., 2006; Kossin et al., 2007; Vickery & Wadhera, 2008; Chavas & Knaff, 2022; Tsukada & Horinouchi, 2023). Allowing for accurate estimates of R_{max} (Combot, Mouche, et al., 2020), SAR data is especially suited to revisit these statistical relationships.

In particular, Chavas and Knaff, 2022 recently offered to estimate R_{max} from V_{max}, f, and R_{34}, using a log-linear regression that is based on angular momentum conservation. In their framework, accurately estimating R_{max} amounts to determining how much angular momentum is lost by an air parcel in the inflow between R_{34} and R_{max}. Angular momentum losses may be characterized by an assumption suggested by PV conservation in the inflow, *i.e* $C_d r v^2 = \text{cst}$ (see Eq. 1.34). The consistency of their approach with this relationship needs to be investigated.

In this chapter, the challenge of R_{max} estimation from a measure of TC outer-size such as R_{34} is addressed through a twofold approach. First, the model coefficients from

Chavas and Knaff, 2022 are revised by using SAR R_{max} reference estimates and medium-resolution radiometers and scatterometers wind radii measurements. Second, the physical basis of the model is investigated, and the assumption $C_d r v^2 = \text{cst}$ is discussed with respect to the high-resolution SAR observations.

2.2 Article: "Reexamining the Estimation of Tropical Cyclones Radius of Maximum Wind from Outer Size with an Extensive Synthetic Aperture Radar Dataset"

Manuscript submitted to *Monthly Weather Review* on 14/06/2023, and accepted on 12/10/2023 (Avenas et al., 2023).

Generated using the official AMS LaTeX template v6.1 two-column layout.

Reexamining the Estimation of Tropical Cyclones Radius of Maximum Wind from Outer Size with an Extensive Synthetic Aperture Radar Dataset

Arthur Avenas,[a, b] Alexis Mouche,[a] Pierre Tandeo,[b] Jean-Francois Piolle,[a] Dan Chavas,[c] Ronan Fablet,[b] John Knaff,[d] Bertrand Chapron,[a]

[a] *Ifremer, Univ. Brest, CNRS, IRD, Laboratoire d'Océanographie Physique et Spatiale (LOPS), IUEM, F-29280, Plouzané, France*
[b] *IMT Atlantique, Lab-STICC, Université Bretagne Loire, Brest, France*
[c] *Purdue University, Department of Earth, Atmospheric, and Planetary Sciences, West Lafayette, Indiana*
[d] *NOAA/NESDIS Regional and Mesoscale Meteorological Branch, Fort Collins, Colorado*

ABSTRACT: The radius of maximum wind (R_{max}), an important parameter in tropical cyclones (TCs) ocean surface wind structure, is currently resolved by only a few sensors, so that, in most cases, it is estimated subjectively or via crude statistical models. Recently, a semi-empirical model relying on an outer wind radius, intensity and latitude was fit to best-track data. In this study we revise this semi-empirical model and discuss its physical basis. While intensity and latitude are taken from best-track data, R_{max} observations from high-resolution (3 km) spaceborne synthetic aperture radar (SAR) and wind radii from an inter-calibrated dataset of medium-resolution radiometers and scatterometers are considered to revise the model coefficients. The new version of the model is then applied to the period 2010-2020 and yields R_{max} reanalyses and trends more accurate than best-track data. SAR measurements corroborate that fundamental conservation principles constrain the radial wind structure on average, endorsing the physical basis of the model. Observations highlight that departures from the average conservation situation are mainly explained by wind profile shape variations, confirming the model's physical basis, which further shows that radial inflow, boundary layer depth and drag coefficient also play roles. Physical understanding will benefit from improved observations of the near-core region from accumulated SAR observations and future missions. In the meantime, the revised model offers an efficient tool to provide guidance on R_{max} when a radiometer or scatterometer observation is available, for either operations or reanalysis purposes.

1. Introduction

Estimating tropical cyclone (TC) ocean surface wind structure is challenging but crucial for several applications. In particular, TC surface wind spatio-temporal distributions are used as input to surface wave studies (Wright et al. 2001; Young 2017; Kudryavtsev et al. 2021), storm surge studies (Irish et al. 2008; Takagi and Wu 2016), or the upper ocean responses to TC passages (Price 1981; Ginis 2002; Kudryavtsev et al. 2019; Combot et al. 2020b). In such studies, the radius of maximum winds (hereafter R_{max}) is a critical parameter that significantly affects wave developments, surge estimates, sea surface height, temperature and salinity variations within the TC wakes. Most parametric surface wind fields, often used for those applications, assume that R_{max} is known (Holland 1980; Willoughby et al. 2006). Thus, R_{max} errors cascade into errors for the entire spatial distribution of wind speeds. For instance, a Rankine profile may be defined as

$$V_{Rankine}(r) = \begin{cases} V_{min} + (V_{max} - V_{min})(\frac{r}{R_{max}}) & \text{if } r \leq R_{max} \\ V_{min} + (V_{max} - V_{min})(\frac{R_{max}}{r}) & \text{if } r > R_{max} \end{cases} \quad (1)$$

Figure 1a shows a comparison between two Rankine profiles for two different R_{max} values representative of TC Lane, a North Eastern Pacific hurricane that reached category 5 on the Saffir-Simpson scale in 2018. TC Lane's wind speeds were estimated by a swath of satellite-based SAR observation on 23 August at 0438 UTC (Fig. 1b). From the SAR wind speeds, the azimuthally-averaged wind profile can be derived (dashed green curve in Fig. 1a). The inferred R_{max} is 15 km, about 2 to 3 times smaller than the 37 km value interpolated to the SAR aquisition time in the best-track data (Knapp et al. (2010); hereafter IBTrACS). Such a mismatch between best-track and SAR R_{max} estimates is representative of what has been reported in the literature (Combot et al. 2020a). In the present case (Fig. 1a), this discrepancy results into a Mean Absolute Error (MAE) as high as 28 ms^{-1} near the eyewall region when using subsequent Rankine profile estimates.

To date, airborne Stepped Frequency Microwave Radiometer (SFMR) surface winds (Uhlhorn et al. 2007) provide means to estimate R_{max}. Yet, airborne measurements have limited azimuthal coverage, and are operated over only few ocean regions and events. From a satellite perspective, high spatial resolution estimates of TC ocean surface wind field are now more systematically carried out, especially from SAR dedicated acquisitions (Mouche et al. 2017; Combot et al. 2020a). More reliable R_{max} estimates are then obtained for all ocean basins, though with limited spatio-temporal sampling. Presently, the most often available spaceborne observing systems, capable of probing the ocean surface during TC conditions, are the com-

Corresponding author: Arthur Avenas, arthur.avenas@ifremer.fr

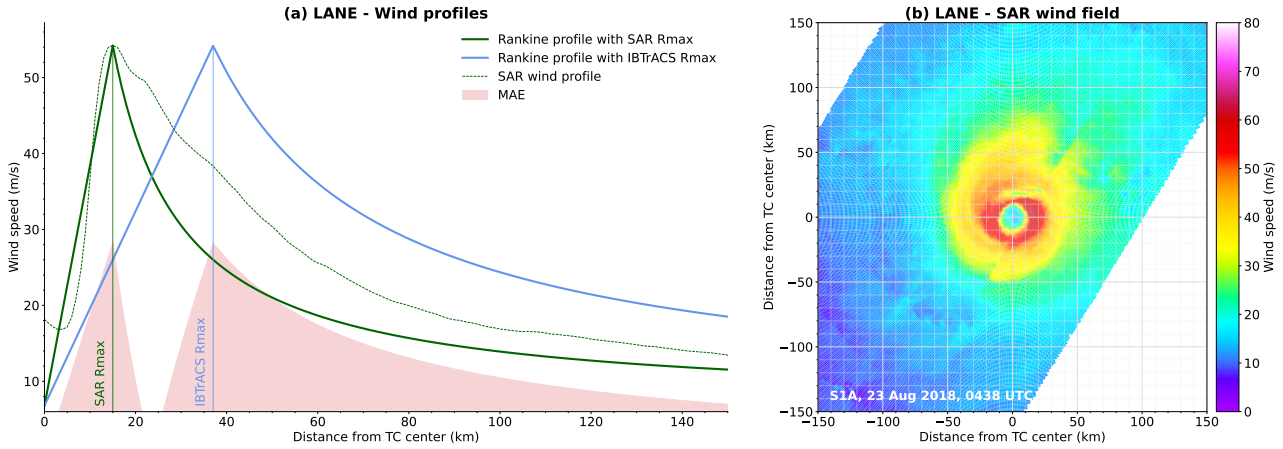

FIG. 1. Comparison between two Rankine profiles (left) inspired by the SAR acquisition over TC Lane on 23 August 2018 at 0438 UTC (right). Rankine profiles are defined with SAR R_{max} (15 km, solid green) or IBTrACS R_{max} (37 km, solid blue) and the same V_{max} (54 ms^{-1}) and V_{min} (7 ms^{-1}), consistently with the SAR azimuthally-averaged profile (dashed green). MAE between the two Rankine profiles is shaded in red.

bined capabilities from active scatterometers and passive radiometers (Quilfen et al. 2007). Compared to radiometers, scatterometers generally have an improved medium spatial resolution. Yet, the strong gradients of the surface wind existing at scales of a few kilometers may still be too smoothed to precisely locate the wind maxima, and the position of the center (Quilfen et al. 1998). In addition, scatterometers, especially those operating at Ku-band and higher microwave frequencies, can suffer from rain contamination. Signal sensitivity at high winds (above hurricane force wind: 33 ms^{-1}) has also been questioned (Donnelly et al. 1999; Mouche et al. 2019). Radiometer measurements may be less impacted by rain, especially those operating at L-band (Reul et al. 2012, 2017), and demonstrated to be still highly sensitive above hurricane force winds. However, actual spaceborne radiometers operating at L- or C-band have a lower spatial resolution. High wind speed gradients near the R_{max} region for most intense TCs are then generally indistinct. Direct estimates of R_{max} using scatterometers or radiometers are thus difficult to perform, possibly limited to particular large storm cases.

More indirect means to infer R_{max} were also considered. Both Mueller et al. (2006) and Kossin et al. (2007) used geostationary infrared satellite data. For the cases where a clear eye is well-defined on the infrared image, using linear regression to estimate R_{max} results in a MAE of only ~5 km when compared to aircraft-based estimates. Under less favourable conditions, R_{max} can still be estimated via multiple linear regression in combination with a principal components analysis, but leads to a degraded MAE of ~20 km. Notably, for the clear-eye case, Tsukada and Horinouchi (2023) trained the linear regression with available SAR R_{max} estimates and improved the method, decreasing the MAE to ~2 km.

In the absence of infrared data, a rough R_{max} estimate can also be obtained, considering the storm intensity and latitude known, as evidenced by Willoughby et al. (2006) and Vickery and Wadhera (2008). Indeed, following the angular momentum conservation, R_{max} must decrease when the intensity increases. On average, such a physical constrain agrees well with observations (see for instance Fig. 9 in Combot et al. (2020a)). In addition, it is also known that R_{max} increases with latitude (e.g. Willoughby and Rahn (2004)), another consequence of angular momentum conservation along with the decrease of intensity with latitude. Solely using intensity and latitude to predict R_{max} yields a root-mean square error of the order ~20 km. Results from Vickery and Wadhera (2008) show that in several cases, the observed R_{max} is inconsistent with the general principle of angular momentum conservation. This suggests that R_{max} natural variability can hardly be captured by such simple statistical models.

More recently, Chavas and Knaff (2022) - hereafter CK22 - suggested to use information on the TC outer-size in combination with latitude and intensity. In the CK22 framework, R_{max} is estimated from the TC intensity V_{max}, the radius of gale R_{34} (*i.e* the maximum radial extent of the 34-knots winds) and the Coriolis parameter, defined as $f = 2\Omega sin(\phi)$, where $\Omega = 7.292x10^{-5}$ s^{-1} is the Earth angular velocity and ϕ is the latitude of the TC center. Such an approach is practical, especially because R_{34} is well estimated by satellite scatterometers and radiometers (Brennan et al. 2009; Chou et al. 2013; Reul et al. 2017). In fact, R_{34} estimates are routinely produced for every TC and included in IBTrACS.

The CK22 framework is based on physical understanding of the radial wind structure (Emanuel 2004; Emanuel and Rotunno 2011) and phrased in terms of absolute angular momentum $M(r) = rV + \frac{1}{2}fr^2$, where f, r and V

are the Coriolis parameter, the radius and the tangential wind speed of an air parcel, respectively. If the ratio $\frac{M_{max}}{M_{34}} := \frac{M(r=R_{max})}{M(r=R_{34})}$ is prescribed, one can then estimate R_{max} provided estimates for the 3 above-mentioned parameters using:

$$R_{max} = \frac{V_{max}}{f}\left(\sqrt{1+\frac{2fM_{max}}{V_{max}^2}}-1\right). \quad (2)$$

CK22 fitted a log-linear regression model to estimate the ratio $\frac{M_{max}}{M_{34}}$ with the two predictors $X_{34}^{(1)} := (V_{max} - 17.5ms^{-1})$ and $X_{34}^{(2)} := (V_{max} - 17.5ms^{-1})(\frac{1}{2}fR_{34})$.

It is tempting to use this framework in combination with best-track data. CK22 used best-track estimates (in a region west of 50°W) of R_{max}, V_{max}, R_{34} and latitude to fit the log-linear regression model. As a result, their model inherited best-track biases. In particular, the reported R_{max} overestimation in best-tracks compared to SAR (Combot et al. 2020a) translated into an overestimation of the ratio $\frac{M_{max}}{M_{34}}$ during the regression training, further leading to overestimated R_{max} values.

The quality of R_{34} best-track estimates has also already been questioned (Sampson et al. 2017). This parameter is reanalyzed and compiled in IBTrACS since 2004 for North Atlantic and North Eastern Pacific and since 2016 for North Western Pacific (Knaff et al. 2021). Yet, surveying specialists who produce best-tracks in the Atlantic ocean (Landsea and Franklin 2013) are on average much less confident in their wind radii estimates (~25-50% of relative uncertainty) than in their intensity estimates (~10-20%).

In addition, best-tracks may also suffer from temporal and spatial heterogeneities (Schreck III et al. 2014; Wang and Toumi 2021). Indeed, the reanalysis methodology depends on the available data at each reanalysis time: best-track estimates of TC events covered by aircraft data are for instance more trustworthy (Landsea and Franklin 2013). Reanalysis is also subjective, each agency or Regional Specialized Meteorological Center (RSMC) specialist conducting their own weighting of the available observations. Furthermore, best-tracks are finalized annually and are not updated with evolving reanalysis methodology, creating a temporal discontinuity in the final IBTrACS database.

Finally, a possible limitation of the CK22 approach is the arbitrary choice of the outer wind radius R_{34}. Indeed, their model could well be trained using R_{50} or R_{64}. In CK22, the choice of R_{34} was motivated by the fact that best-track estimates of R_{50} and R_{64} are generally more uncertain than R_{34} estimates. With more reliable R_{50} and R_{64} estimates, possibly obtained from radiometers or scatterometers, one could assess whether using these wind radii would improve the CK22 model.

The physical basis for wind structure relationships such as CK22 is a long-running issue. The assumption that an outer wind radius partly constrains the wind structure dates back to Riehl (1963). Riehl (1963) used a two-layer conceptual model constrained by an angular momentum conservation in the outflow and a potential vorticity (PV) conservation in the inflow layer. Riehl (1963) could then derive a relationship between R_{max}, V_{max}, f, and an outer radius R_{out}, corresponding to a distance where the outflow velocity vanishes. Later, Kalashnik (1994) considered the Holland parametric profile (Holland 1980) within a theoretical framework, to analyze the dependence of the near-core wind structure on the wind profile. Emanuel and Rotunno (2011) also derived an analytical solution for the near-core wind profile based on an assumption on the outflow temperature.

While these studies offer theoretical guidance, these theoretical inferences of R_{max} are difficult to apply in practice. Indeed, most actual sensors fail to capture the wind profile shape used in Kalashnik (1994), while the model of Emanuel and Rotunno (2011) relies on parameters that are difficult to evaluate. Following Riehl (1963), the theoretical outer radius R_{out} is unknown and cannot be specified to correspond to a given surface wind speed.

Building on the above considerations, the aim of this study is twofold. First, the CK22 model is revised using SAR R_{max} estimates, different wind radii (referring hereafter to R_{34}, R_{50}, and R_{64}) estimated on inter-calibrated radiometers and scatterometers, and intensity and latitude best-track estimates. Second, the physical basis of the CK22 model is further assessed through an examination of conservation equations and a thorough analysis of the SAR database.

The data used in the present work are introduced in section 2 and further analysed in section 3. Then, the CK22 model is revised and its performance assessed in section 4. Finally, the physical basis of the model is discussed with respect to SAR observations in section 5. Concluding remarks and possible routes for future investigations are provided in the last section.

2. Data

In the present work, different radiometer and scatterometer data (table 1) over the period 2010-2020 were used to estimate wind radii (R_{34}, R_{50}, and R_{64}), while SAR data (table 2) were used to estimate the R_{max} values required to fit the CK22 log-linear model. Furthermore, IBTrACS provided intensity and latitude estimates (V_{max} and f).

We used different radiometer and scatterometer missions to constitute the most extensive dataset of R_{max} reanalyses. These sensors rely on different physical principles (passive or active sensors), and have different frequencies (L-band, C-band or Ku-band) and spatial resolutions. In order to ensure homogeneity of the wind radii estimates, we used radiometer and scatterometer winds inter-calibrated by Portabella et al. (2022). Note that surface wind speed estimates from the Cyclone Global Navigation Satellite

System (CYGNSS) do not belong to this inter-calibrated dataset. Indeed, even though a level 3 storm-centric gridded wind speed product has recently been developed to improve former CYGNSS wind speed retrievals, its capacity to correctly inform the TC surface wind structure, especially R_{50} and R_{64}, remains to be assessed and validated (Morris and Ruf 2017; Krien et al. 2018; Mayers et al. 2023).

Furthermore, a thorough analysis of this database revealed that the wind profiles issued from Ku-band scatterometer data barely exceed 64 knots, even for most intense TCs, as shown in appendix A. Thus, we chose to remove Ku-band scatterometers from the present analysis.

a. Radiometer missions

Because both the foam coverage and bubble surface layer thickness increase with surface wind speed (Reul and Chapron 2003), passive microwave measurements have long been known to display very high sensitivity under extreme wind conditions. With large ~1000 km swaths, satellite-borne radiometers are well suited to monitor TCs. However, they have nominally low spatial resolutions (~40 km) that generally prevent accurate retrieval of the extreme surface wind speeds associated with the inner-core of most intense TCs. The radiometer wind products used in this work are at 50 km spatial resolution with a 25 km grid spacing (Portabella et al. 2022).

In the present study, four different sources of radiometer data were used. Among them, the L-band (1.4 GHz, 21 cm wavelength) radiometers from the European Space Agency (ESA) Soil Moisture and Ocean Salinity (hereafter SMOS) mission and the National Aeronautics and Space Administration (NASA) Soil Moisture Active Passive (hereafter SMAP). The ability of L-band radiometers to retrieve ocean surface wind speeds under TCs has been discussed both in the case of SMOS (Reul et al. 2012, 2016) and SMAP (Yueh et al. 2016; Meissner et al. 2017). Reul et al. (2017) demonstrated that SMOS, SMAP, as well as AMSR-2 can be used to estimate wind radii.

The Japan Aerospace Exploration Agency launched the Advanced Microwave Scanning Radiometer 2 (hereafter AMSR-2) onboard the Global Change Observation Mission Water 1 satellite in 2012. This instrument is still operating today and uses 7 different frequencies (6.93, 7.3, 10.65, 18.7, 23.8, 36.5 and 89.0 GHz. For TCs, the first 3 channels (6.93, 7.3, and 10.65 GHz) are used. With two C-band channels, initially intended for radio-frequency interference identification, surface wind estimates are improved. Signals at these two C-band frequencies have similar sensitivity to the sea wind speed but differ in sensitivity to rain by about 12%. Accuracy of the AMSR-2-retrieved wind speed in storms is comparable to results obtained from SMOS and SMAP L-band sensors (Zabolotskikh et al. 2015; Reul et al. 2017).

Windsat is a polarimetric radiometer onboard Coriolis, a mission designed by the Naval Research Laboratory and the Air Force Research Laboratory, and launched in 2003. The sensor provided data until May 2021. This instrument operates at 5 different channels (6.8, 10.7, 18.7, 23.8 and 37.0 GHz). To minimize heavy precipitation impacts, the C-band 6.8 and the X-band 10.7 GHz channels are used for TC wind retrieval algorithms. Again, changes in the respective contribution of wind and rain to the signal measured by each channel can be used to better infer and discriminate both quantities (Klotz and Uhlhorn 2014). Heavy precipitation is still found to complicate surface wind speed retrieval with this sensor (Quilfen et al. 2007), and more recent studies addressed this issue (Meissner et al. 2021; Manaster et al. 2021).

b. Scatterometer missions

Scatterometers are active sensors that emit a pulse and measure the signal backscattered by the rough ocean surface with different viewing angles. Because backscatter signals are dependent upon both wind speed and wind direction, ocean surface wind vectors can be retrieved. The achieved nominal spatial resolution (up to ~25 km) is higher than satellite-borne radiometers. Actual scatterometers operate at different frequencies (C-band or Ku-band).

The Meteorological Operational satellite programme is a series of 3 satellites (Metop-A, -B and -C) launched by ESA (in 2006, 2012 and 2018, respectively) which include scatterometers (ASCAT, for "Advanced Scatterometer") operating at 5.3 GHz (C-band). With 3 antennas oriented at 45°, 90° and 135° with respect to the satellite track, the wind direction can be retrieved. ASCAT instruments have 2 sub-swaths, each having a width of ~550 km. At C-band, the signal may be influenced by very heavy rain. Backscatter signals also tend to saturate at high winds (Donnelly et al. 1999), and ASCAT measurements progressively lose sensitivity under high wind speeds (Soisuvarn et al. 2012; Polverari et al. 2021). The ASCAT wind product used in the present study is at 25 km spatial resolution with a 12.5 km grid spacing (Stoffelen et al. 2017; Portabella et al. 2022).

Scatterometers operating at Ku-band (~ 13.5 GHz) usually have larger swaths (~1000 km) than C-band scatterometers, but suffer more contamination in heavy rainfall conditions (see Quilfen et al. (2007) for more details). The Ku-band scatterometer wind products used in Portabella et al. (2022) were finally removed (see appendix A). They include the China National Space Administration (CNSA) Haiyang missions (hereafter HSCAT), the Indian Space Research Organisation (ISRO) OceanSat-2 and SCATSat-1 satellites (hereafter OSCAT), and the NASA RapidScat (hereafter RSCAT) onboard the International Space Station (Table 1).

RADIOMETER	SMOS	SMAP	AMSR-2	Windsat
Period	2010-2020	2015-2020	2012-2020	2010-2019
Spatial resolution	50 km	50 km	50 km	50 km
Pixel spacing	25 km	25 km	25 km	25 km
Frequency	L-band	L-band	C-band, X-band	C-band, X-band
SCATTEROMETER	ASCAT	HSCAT	OSCAT	RSCAT
Period	2010-2020 (Metop-A)	2012-2015 (HY-2A)	2010-2014 (Oceansat-2)	2014-2016
	2012-2020 (Metop-B)	2019-2020 (HY-2B)	2017-2020 (Scatsat-1)	
	2019-2020 (Metop-C)			
Spatial resolution	25 km	50 km	50 km	50 km
Pixel spacing	12.5 km	25 km	25 km	25 km
Frequency	C-band	Ku-band	Ku-band	Ku-band

TABLE 1. The radiometer and scatterometer data used in Portabella et al. (2022). The period, spatial resolution, and pixel spacing rows refer to the wind product. The same data were used for the present work, except the Ku-band scatterometers, which were removed from the analysis.

c. SAR missions

The SAR data used here come from three different missions: ESA Sentinel-1A and Sentinel-1B (hereafter S1A and S1B, respectively), and the Canadian Space Agency (CSA) Radarsat-2 (hereafter RS2). The SAR instrument onboard these three missions is an active sensor operating at 5.4 GHz (C-band). By analysing the received signal in both co- and cross-polarization, wind speeds can be inferred under TC conditions including at very high wind speeds (Mouche et al. 2017, 2019). Convincing comparisons with passive radiometers have been performed (Zhao et al. 2018). The ability of SAR-derived wind speeds to accurately capture the TC ocean surface wind structure, including R_{max}, has further been demonstrated and discussed by Combot et al. (2020a).

Today, SAR wide-swath acquisitions cannot be continuously performed over oceans. Based on track forecasts, it is still possible to best anticipate when the sensor will overpass a TC, and to trigger a SAR acquisition. ESA started the Satellite Hurricane Observation Campaign (SHOC) in 2016, resulting in more than ~500 acquisitions over TCs. The derived wind products (Mouche et al. 2017) are further interpolated on a regular polar grid based on the TC center (see appendix in Vinour et al. (2021)). The product has a 3 km spatial resolution, with a 1 km grid spacing. This spatial resolution approximates a 1-minute wind speed as a 50 ms^{-1} wind moves 3 km in a minute. In this study, a certain number of SAR cases have been discarded on a qualitative basis, e.g. when the detected TC center was judged to be wrong, or when the SAR file contained corrupted pixel values.

d. Best-tracks

Here, IBTrACS data were used for several purposes: the storm centers (latitude and longitude) allowed to azimuthally average the radiometer and scatterometer wind fields, while the wind radii (R_{34}, R_{50}, and R_{64}) were compared to satellite-based wind radii. Both IBTrACS latitude (to compute f) and maximum sustained wind speed (V_{max}) were used in the CK22 framework, and the distance to closest land (from the TC center) enabled filtering of the dataset. These parameters were extracted for the period 2010-2020.

In IBTrACS, some storm tracks are given on a six-hourly basis, while others are interpolated and thus given on a three-hourly basis. To account for this varying sampling time, all tracks and their associated parameters were interpolated to an hourly basis with a monotonic cubic interpolation. Lastly, because of varying definitions of the maximum sustained wind speed across the different agencies, we selected only USA agencies (*i.e* National Hurricane Center, Joint Typhoon Warning Center, and Central Pacific Hurricane Center) which all provide the 1-minute maximum sustained wind speed.

e. Data filtering

To further restrain the analysis to well-formed systems, i.e. for which R_{max} can be well determined from the axisymmetric mean profile, and to best ensure consistency with CK22 for further comparison, the following filters have been applied to our dataset:

1. $V_{max} > 20\ ms^{-1}$;
2. $R_{max} < 150\ km$;
3. Any wind radius must be $> 5\ km$;

SAR	S1A	S1B	RS2
Period	2016-2021	2016-2021	2012-2021
Spatial resolution	3 km	3 km	3 km
Pixel spacing	1 km	1 km	1 km
Frequency	C-band	C-band	C-band

TABLE 2. The SAR data used in the present study. The period, spatial resolution, and pixel spacing rows refer to the wind product.

4. Absolute latitude < 30°;

5. Distance to closest land > R_{34}.

Here and below, V_{max}, R_{max}, and "wind radii" refer to their values when estimated on azimuthally-averaged wind profiles (see below). Unlike CK22, we didn't apply any filter on longitude. Therefore, the method presented here applies in every basin and does not depend on the availability of aircraft analysis.

3. Methods and data analysis

a. Estimation of the CK22 predictors

In order to apply the CK22 framework to the inter-calibrated dataset of radiometer and scatterometer data, estimates of the predictors (V_{max}, R_{34}, f) were needed for every satellite file.

Regarding the wind radii, an azimuthally-averaged wind profile was first computed for every satellite file using the corresponding IBTrACS center linearly-interpolated to the acquisition time. For each of the three speed values of interest (*i.e* 34, 50 and 64 knots), we then selected the radius where the outer-profile matches this value to the closest kilometer. Should there be more than one radius value, the wind radius was defined as the smallest of the radii. During the process, wind radii estimates are affected by IBTrACS linearly-interpolated center uncertainties. By comparing SAR-based center estimates (see (Vinour et al. 2021)) with IBTrACS-based center estimates over the whole SAR database, the average uncertainty is ∼13 km, largely below the radiometer and scatterometer effective spatial resolutions.

Unlike the wind radii, V_{max} and f cannot be accurately estimated from radiometer and scatterometer data, especially for intense small TCs, but both parameters are systematically reanalyzed in the best-tracks. However, IBTrACS V_{max} definition does not strictly coincide with the axi-symmetric view adopted here. In particular, the analysis (appendix A) highlighted that V_{max} estimated using SAR azimuthally-averaged profiles were, on average, lower than IBTrACS V_{max}. This can be modeled by applying a linear regression (dashed grey line in Fig. A1) to IBTrACS V_{max} estimates. The resulting intensity estimates are denoted by V_{max}^{REG} and were used (instead of the raw IBTrACS V_{max}) to ensure the consistency with the wind radii defined on azimuthally-averaged wind profiles. The pair of parameters (V_{max}^{REG}, f) was then linearly-interpolated to the satellite acquisition time for every file.

b. Quality assessment of radiometer and scatterometer wind radii estimates

To assess the quality of the satellite-based wind radii, comparisons were performed with IBTrACS wind radii. A strict comparison cannot be achieved because of varying definitions. In IBTrACS, wind radii are relative to the geographical quadrants and correspond to the maximum radial extent of the associated wind speed in each of the four quadrants. To make IBTrACS values as close as possible to the satellite-based wind radii, the nonzero IBTrACS values were averaged over all the quadrants. Furthermore, both the methodologies and the available observational data can vary across the IBTrACS dataset. Here, the adopted strategy was to compare the whole IBTrACS wind radii dataset (including non-USA agencies for this section) to the satellite-based wind radii. Accounting for the differences between the specialists and agencies is beyond the scope of this study. Finally, after removing the Ku-band sensors (see appendix A), we separated radiometer wind radii from the C-band scatterometer wind radii to further investigate possible discrepancies between the remaining sensors.

Figure 2 shows a comparison between radiometer wind radii and IBTrACS values (top) and their corresponding distributions (bottom). While radiometer wind radii look well correlated with IBTrACS values, with R^2-scores ranging from 0.4 to 0.5, large discrepancies arise, with a Residual Standard Deviation (RSD) as high as 56.7 km for R_{34}. The RSD decreases to 37.3 km for R_{50}, and further to 24.1 km for R_{64}, reflecting the decrease of the mean wind radius, i.e. 181 km for R_{34} to 51 km for R_{64} in IBTrACS. In terms of relative uncertainties, this leads to ∼31%, ∼36%, and ∼41% for R_{34}, R_{50}, and R_{64}, respectively. Interestingly, the Mean Error (ME) is negative for both R_{34} and R_{50}, showing that, on average, these wind radii are lower when extracted from azimuthally-averaged radiometer profiles than from IBTrACS. This is likely the result of the differing definition of the wind radii in the satellite data and in IBTrACS. Indeed, on average, a wind radius extracted from an azimuthally-averaged profile is expected to be smaller than the maximum radial extent of the same wind speed.

Biases due to the differing definition are lower for R_{50} and R_{64} than for R_{34}, because these radii are smaller on average. This definition effect is illustrated on the distribution for R_{34}, where the radiometer R_{34} distribution is biased toward lower values compared to IBTrACS.

Figure 3 shows comparisons between C-band scatterometer wind radii and IBTrACS values. Again, an overall consistency emerges between both data sources for all wind radii. RSD values and R^2 scores are comparable to the previous comparisons between radiometer and IBTrACS. Data and methodology are thus consistent with IBTrACS (which is expected since radiometer and scatterometer data are often used during the reanalysis process), but it also shows that there is a good consistency between the various sensors in terms of wind radii.

Regarding R_{64}, the ME is slightly positive for both radiometer and scatterometer data (Figs. 2c and 3c), with a distribution of R_{64} skewed toward higher values for the satellite data compared to IBTrACS. First, this could be attributed to the satellite data limitations, such as low spatial resolution, signal saturation or rain contamination. Yet, Fig. 4 offers a different explanation. It again shows comparisons between scatterometer wind radii and IBTrACS values, but only over the 3-year period from 2018 to 2020. For such a period, the computed ME for R_{64} is only 1.5 km (Fig. 4c), and the RSD drops to 19.4 km (compared to 24.1 km for the period 2010 to 2020). Consistency between scatterometer and IBTrACS also improves for both R_{34} and R_{50} over the same period (Figs. 4a and 4b). The positive ME for R_{64} in Fig. 3 likely corresponds to the improving quality of IBTrACS over the years. Mentioned in the introduction, wind radii best-track values were not necessarily reanalyzed depending on the year and the basin. Similar conclusions were obtained with radiometer data (not shown).

To summarize, the comparison between IBTrACS and the inter-calibrated dataset shows that radiometers and scatterometers provide reliable wind radii estimates. Thus, for every radiometer or scatterometer acquisition, we can extract a corresponding set of predictors constituted by a satellite-based wind radius along with IBTrACS V_{max}^{REG} and f estimates.

c. *Collocations of radiometers and scatterometers with SAR*

In order to fit the CK22 model, we also needed an estimate of the predictand (R_{max}) for each set of predictors. The latter cannot be directly evaluated from radiometer and scatterometer data, but is well observed on SAR data by taking the location of the wind profile maximum. Thus, we looked for collocations between SAR and radiometer or scatterometer TC overpasses. Two images were considered to be collocated if their absolute acquisition time difference is less than 90 minutes.

Regarding radiometer data (table 3, first four columns), this procedure resulted in a total of 269 collocations, which further reduced to 145 collocations after applying filters presented in section 3e. Notably, no collocation was found between any of the 3 SAR missions (S1A, S1B, RS2) and AMSR-2. The average absolute time difference of the found collocations is ~19 minutes, during which we assume the TC wind structure to remain stationary.

Regarding scatterometer data, no collocation was found between SAR and ASCAT (Table 3, penultimate column). In what follows, we thus refer to the dataset obtained by this collocation procedure as the "SAR-radiometer collocation dataset". It consists in predictors estimated on radiometer data (wind radii) or corresponding IBTrACS values (V_{max}^{REG} and f), and predictands estimated on SAR (R_{max}). Note that we could equally have used SAR wind radii estimates to fit the CK22 model, but this would have reduced the number of available wind radii estimates because SAR instruments have smaller swaths than radiometer.

4. Results

a. *Fitting CK22 model*

As explained in the introduction, the CK22 model relies on the estimation of the ratio $\frac{M_{max}}{M_{34}}$ via a log-linear regression model, using $(X_{34}^{(1)}, X_{34}^{(2)})$ as input. While CK22 used R_{34} in their study, this method is in fact agnostic from the choice of wind radius. Therefore, the ratio $\frac{M_{max}}{M_{50}}$ can also be estimated using $X_{50}^{(1)} := V_{max} - 25.7ms^{-1}$ and $X_{50}^{(2)} := (V_{max} - 25.7ms^{-1})(\frac{1}{2}fR_{50})$ as input (or $\frac{M_{max}}{M_{64}}$ using $X_{64}^{(1)} := V_{max} - 32.9ms^{-1}$ and $X_{64}^{(2)} := (V_{max} - 32.9ms^{-1})(\frac{1}{2}fR_{64})$ as input).

CK22 estimated the coefficients of the log-linear regression model based solely on IBTrACS rather than direct observational estimates, and only for the ratio $\frac{M_{max}}{M_{34}}$. In the present work, we use observational data not only to obtain improved estimates of the predictors in the CK22 model framework, but also to obtain improved estimates of the model coefficients that relate the parameters to one another. We also extend the CK22 model for the ratios $\frac{M_{max}}{M_{50}}$ and $\frac{M_{max}}{M_{64}}$. A log-linear regression model was fitted for each of the three ratios using the SAR-radiometer collocation dataset previously presented. The following relationships were obtained:

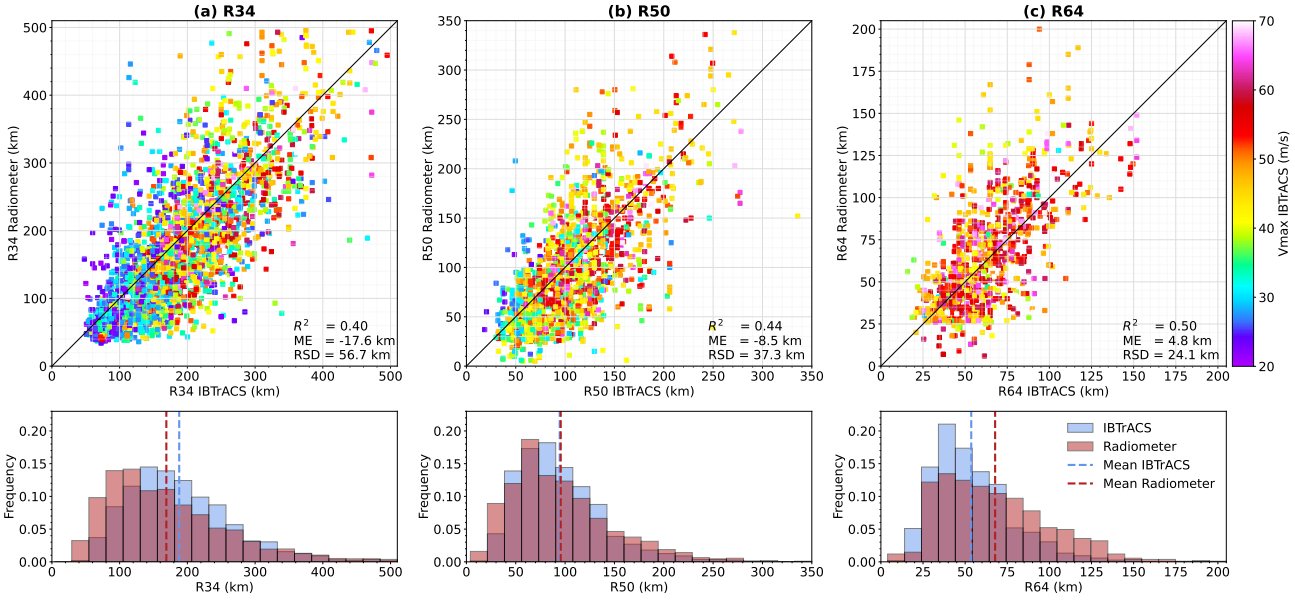

FIG. 2. (Top) Comparison between radiometer (y-axis) and corresponding IBTrACS (x-axis) wind radii. Coefficient of determination (R^2), Mean Error (ME) and Residual Standard Deviation (RSD) are displayed. (Bottom) Corresponding distributions and averages.

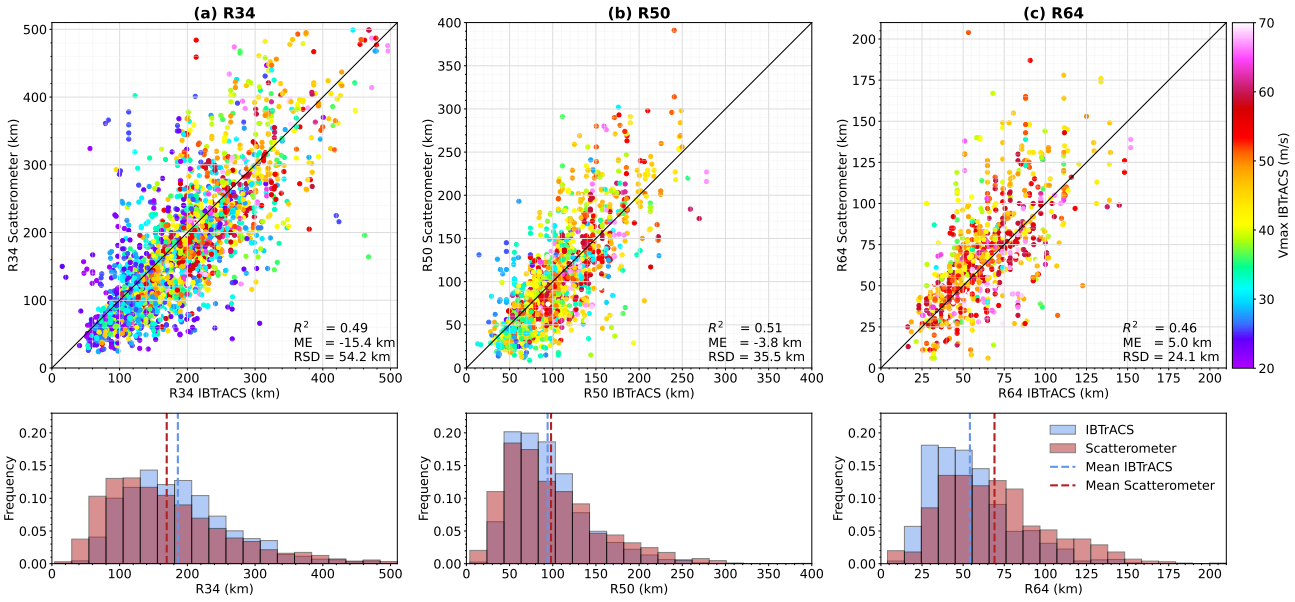

FIG. 3. Same as Fig. 2, but for the C-band scatterometer wind radii.

$$\frac{M_{max}}{M_{34}} = 0.531\exp\{-0.00214(V_{max}^{REG} - 17.5ms^{-1}) - 0.00314(V_{max}^{REG} - 17.5ms^{-1})(\frac{1}{2}fR_{34})\}, \quad (3)$$

$$\frac{M_{max}}{M_{50}} = 0.626\exp\{0.00282(V_{max}^{REG} - 25.7ms^{-1}) - 0.00724(V_{max}^{REG} - 25.7ms^{-1})(\frac{1}{2}fR_{50})\}, \quad (4)$$

$$\frac{M_{max}}{M_{64}} = 0.612\exp\{0.00946(V_{max}^{REG} - 32.9ms^{-1}) - 0.01183(V_{max}^{REG} - 32.9ms^{-1})(\frac{1}{2}fR_{64})\}. \quad (5)$$

With these formulas, R_{max} can then be estimated using the steps presented in the introduction (eq. 2). Subsequent estimates will be referred to as $R_{max}^{CK22-R_{34}}$, $R_{max}^{CK22-R_{50}}$, or $R_{max}^{CK22-R_{64}}$ depending on which wind radius is used.

b. Assessment of the resulting R_{max} estimates

To check the fitting procedure, we compared $R_{max}^{CK22-R_{34}}$ estimates and SAR R_{max} references (Fig. 5a). The consistency between both is reasonably good, with a R^2-score

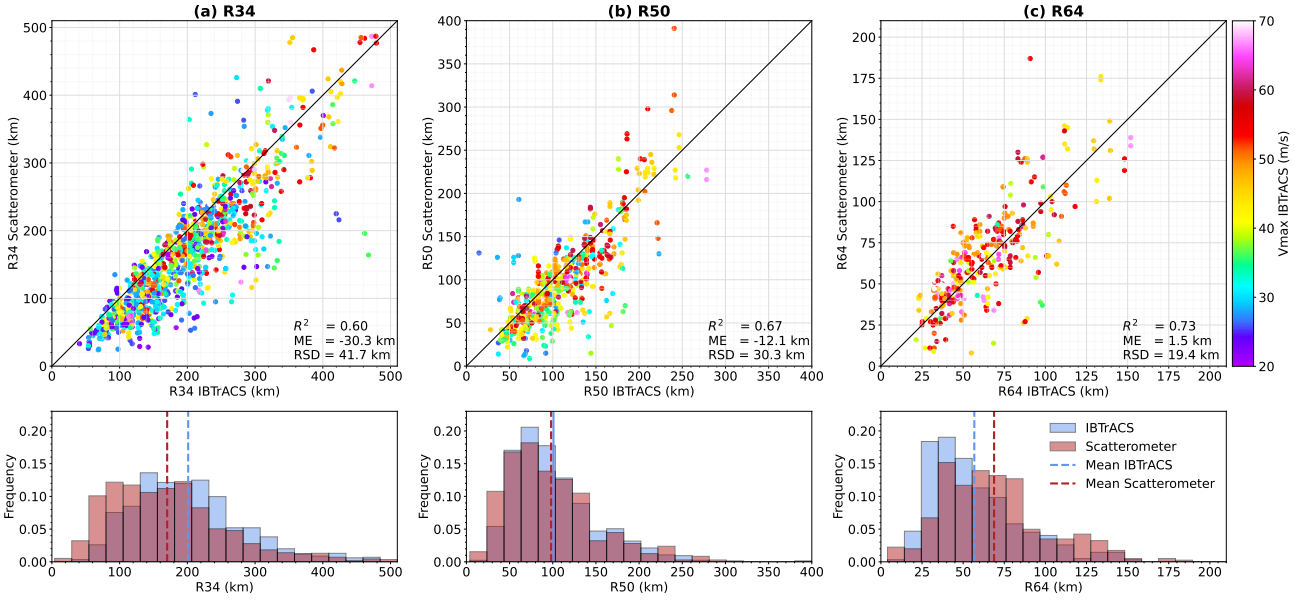

FIG. 4. Same as Fig. 3, but only for the 3-year period 2018-2020.

	SMOS	SMAP	AMSR-2	Windsat	ASCAT	TOTAL
Before filtering	106	63	0	100	0	269
After filtering	67	33	0	45	0	145
Average Δt (mins)	12	21		31		19

TABLE 3. Number of collocations between SAR and the inter-calibrated dataset (radiometer and ASCAT), and corresponding average absolute time difference.

of 0.41 and a RSD of 10.6 km. A low ME of 3.7 km is observed, which can be related to the distribution of $R_{max}^{CK22-R_{34}}$ being slightly skewed toward higher R_{max} values compared to SAR.

Because R_{50} and R_{64} are closer to R_{max} than R_{34}, using one or the other wind radii thresholds should improve the quality of the ratio estimate compared to R_{34}. Ideally, an estimate of R_{max} should be performed with R_{64} if available. If R_{64} is not defined (*i.e* if V_{max} is less than 33 ms^{-1}), R_{50} should be used. R_{34} should only be used if both R_{64} and R_{50} were not defined. Following this procedure, we further estimated R_{max} using the "best" available wind radius.

Figure 5b shows a comparison between these estimates (hereafter $R_{max}^{CK22-BR}$) and SAR R_{max} references. The R^2-score increased to 0.63 and the ME decreased to 0.9 km compared to the $R_{max}^{CK22-R_{34}}$ methodology, while RSD decreased from 10.6 km to 8.8 km. Therefore, using wind radii closer to R_{max} does improve the estimate quality. In addition, such a low RSD demonstrates the efficiency of the fitted CK22 relationships (eqs. 3-5) to provide reliable R_{max} estimates.

In their paper, the R_{max} predicted by CK22 had a systematic bias that could be bias-adjusted in post-processing to improve the model. Here we find that our model does not require a bias adjustment, which may be an indication of the benefit of using direct observational data for R_{max} (SAR).

While the method is successful on average, it is remarkable that errors can be large (more than ~10 km), even for cases where R_{64} predictors are used (see for instance Kong-Rey and Mangkhut in Fig. 5b). Before discussing how to explain these large uncertainties, a single TC life cycle was chosen to illustrate the potential of the present methodology.

c. Application to TC Kilo life cycle

Producing $R_{max}^{CK22-BR}$ estimates every time a radiometer or a scatterometer TC overpass is available can be an efficient tool for characterizing the time evolution of R_{max} for any given TC. Figure 6 shows TC Kilo R_{max} and V_{max}^{REG} time series between 27 August and 10 September 2015, a period over which V_{max}^{REG} was larger than 20 ms^{-1}. TC Kilo evolved in the Pacific ocean, reaching category 4 on the Saffir-Simpson scale. It intensified from 20 to 49 ms^{-1} between 27 August and 30 August before entering a weakening phase. In the meantime, R_{max} first varied between

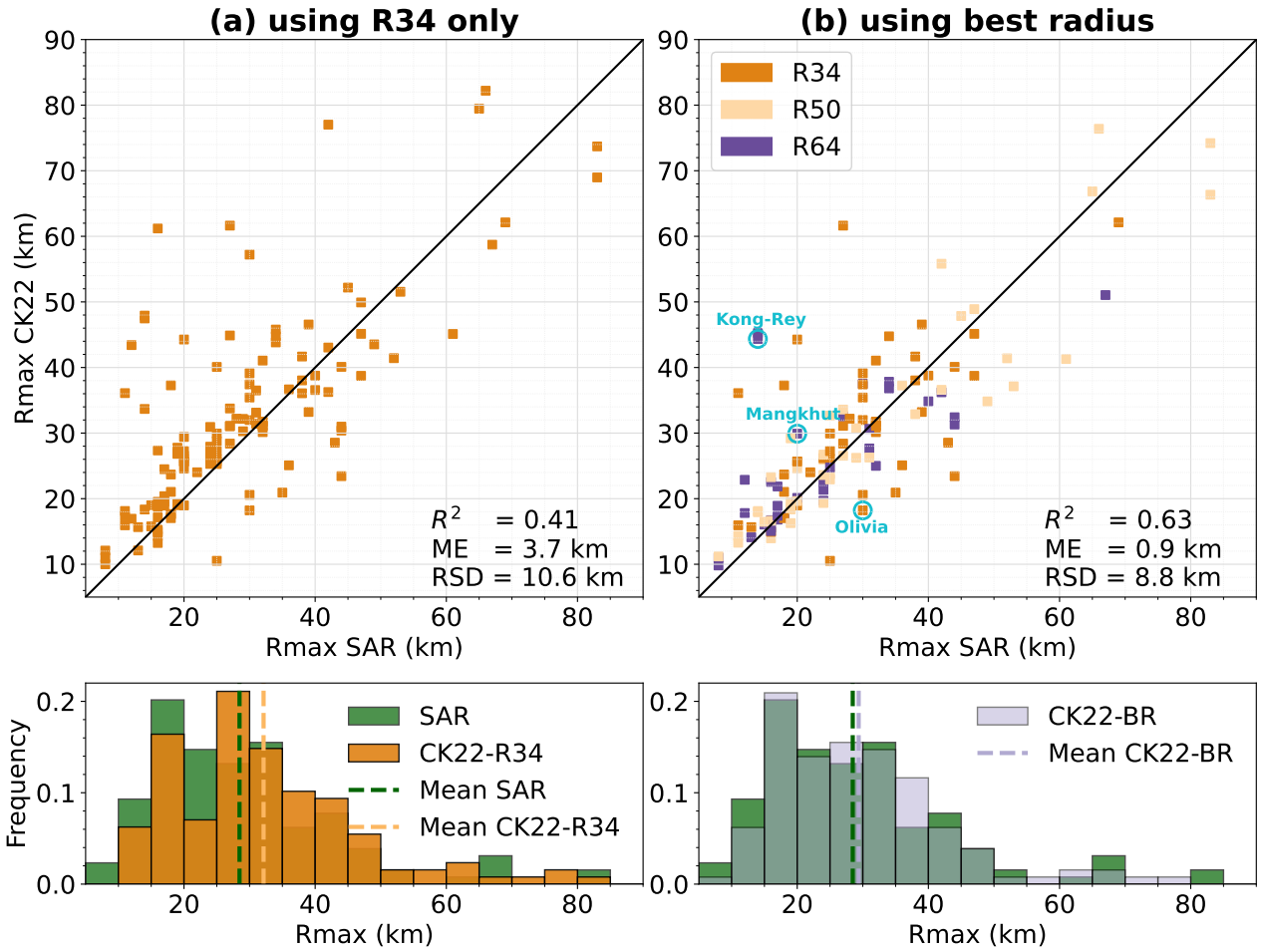

FIG. 5. Comparison between R_{max} estimates using the CK22 model and SAR R_{max} (top) and corresponding distributions (bottom) for $R_{max}^{CK22-R_{34}}$ (a) and $R_{max}^{CK22-BR}$ (b). For analysis purposes, color reveals which radius was used to define $R_{max}^{CK22-BR}$ for each case.

55 and 15 km according to IBTrACS, then stagnated at 37 km between 30 August and 2 September, before varying again after these date. Stagnation phases of R_{max} from IBTrACS are likely not physical according to the V_{max}^{REG} variations during that time interval (see section 5) and the two eyewall replacement cycles (ERCs) suggested by passive microwave observations (not shown). $R_{max}^{CK22-BR}$ estimates show much more pronounced variations during those phases, with an increasing trend between 30 August and 8 September. This particular phase corresponds to an overall decrease of V_{max}^{REG} and an overall increase of R_{64} in our data (not shown), both of which would be expected to be associated with an increase in R_{max}.

For reference, 3 SAR R_{max} estimates were available during TC Kilo's life cycle (green stars). The first SAR R_{max} (10 km) on 27 August, doesn't match with our first estimate of R_{max} (35 km). This illustrates the limitations of our proposed methodology and is discussed hereafter. The second and third SAR R_{max} estimates are in better agreement with the $R_{max}^{CK22-BR}$ estimates, especially if we account for the overall R_{max} trend given by our estimates. A large eye is also depicted in passive microwave data during this period (not shown), supporting the robustness of the $R_{max}^{CK22-BR}$ estimates.

Notably, there is more spread in the CK22 estimates on the last two days of the study period. Despite this increasing uncertainty, the increase of R_{max} is well depicted, suggesting R_{max} would significantly increase before 8 September in contradiction with the IBTrACS trend.

In summary, every time a radiometer or scatterometer wind profile is available, a subsequent $R_{max}^{CK22-BR}$ estimate can be obtained, using the proposed objective method. In such a way, one can estimate R_{max} trends that are more realistic than IBTrACS, less impacted from spatial or temporal heterogeneities. Such a framework could also be used operationally.

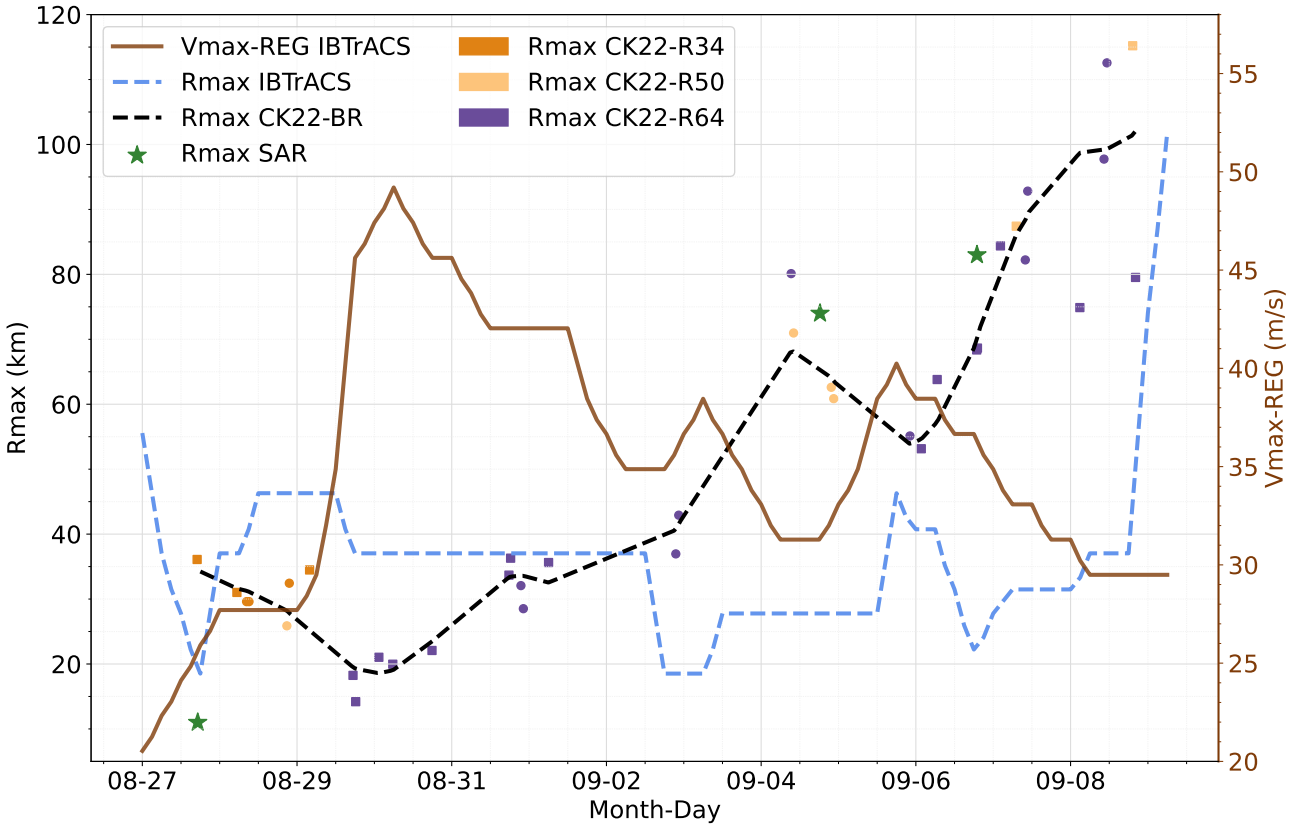

FIG. 6. Kilo (2015) time series of IBTrACS R_{max} (left axis, dashed blue), radiometer- and scatterometer-based $R_{max}^{CK22-BR}$ (left axis, dashed black), and IBTrACS-based V_{max}^{REG} (right axis, solid brown). Also displayed are radiometers (squares), scatterometers (circles) $R_{max}^{CK22-BR}$ estimates (color reveals which radius was used to define $R_{max}^{CK22-BR}$ for each observation), and SAR R_{max} estimates (green stars). The dashed black line was obtained by applying a support vector regression to the radiometer- and scatterometer-based $R_{max}^{CK22-BR}$ estimates.

5. Discussion

The previous section demonstrated the potential of the CK22 model fitted with SAR, when used in combination with inter-calibrated medium-resolution radiometer and scatterometer data. Still, $R_{max}^{CK22-BR}$ estimates can display rather large uncertainties, despite the expected improved use of R_{64} as predictor. To better understand the sources of such uncertainties, three other case studies (cyan circles on Fig. 5a) were considered before examining theoretical aspects and drawing a picture of the average situation.

a. Case studies from the SAR-radiometer dataset

The first case (Fig. 7, left column) is TC Olivia in 2018, an Eastern Pacific ocean hurricane that reached category 4 on the Saffir-Simpson scale. It reached a first intensity peak (~56 ms^{-1}) on 5 September, then weakened before restrengthening (~59 ms^{-1}) during the night between 6 and 7 September. On 8 September, both RS2 at 1510 UTC and Windsat at 1533 UTC overflew Olivia (Figs. 7a and 7d). Its eyewall, depicted by the high-resolution SAR observation, was clearly defined though asymmetric. With its rather low spatial resolution, the radiometer failed to map the inner core areas with high wind speed gradients, and eyewall asymmetries. These differences between SAR and radiometer two-dimensional observations translate into differences in the azimuthally-averaged wind profiles. From the SAR wind profile, Olivia's R_{max} was 30 km at that time, with a V_{max} of 32 ms^{-1} (Fig. 7g). Notably, Windsat failed to estimate V_{max} correctly, with a negative bias of almost 10 ms^{-1} when compared to SAR V_{max} and V_{max}^{REG} which are in good agreement at that time. This bias is largely attributable to sensor spatial averaging effects. In fact, the entire azimuthally-averaged wind profile is negatively biased, leading to an underestimation of R_{34}, further reflected in $R_{max}^{CK22-BR}$. This case illustrates how wind radii uncertainties translate into $R_{max}^{CK22-BR}$ uncertainties. Note that in other cases uncertainties on V_{max}^{REG} could also affect $R_{max}^{CK22-BR}$ uncertainties.

The second case (Fig. 7, middle column), Mangkhut, was a super typhoon (category 5 on Saffir-Simpson scale), causing considerable damage in the Western Pacific region

in 2018. It reached its peak intensity (~80 ms^{-1}) on 12 September. On 11 September, both S1B at 2048 UTC and Windsat at 2126 UTC overflew Mangkhut (Figs. 7b and 7e). According to the SAR observation, Mangkhut had a clearly-defined symmetric eyewall at that time. Note that the eyebrow shape in the high winds to the left of the eyewall (Fig. 7b) is probably due to rain contamination (for discussion about such a feature see Mouche et al. (2019)). The extent of high winds was seemingly well captured by the radiometer sensor, but the eye was not resolved. Nevertheless, a very good agreement between S1B and Windsat wind outer-profiles is obtained for this case (Fig. 7h), with only ~3 km difference between R_{64} estimates from the two sensors. Still, the estimate given by $R_{max}^{CK22-BR}$ (~30 km) largely overestimates the actual SAR R_{max} (~20 km). Note that in this case the clear eye depicted by infrared data and the ring captured by passive microwave sensors are both rather small (not shown), supporting the small SAR R_{max} estimate. With its large R_{64} and small R_{max} at that time, Mangkhut illustrates the high variability that occurs in nature. Such a case is likely to depart from any statistical relationship (like CK22) that links a wind radius to R_{max}.

The last case study (Fig. 7, right column), Kong-Rey, in 2018, was a super typhoon reaching category 5 on the Saffir-Simpson scale, also evolving over the Western North Pacific ocean. Following a ~72 ms^{-1} peak intensity on 2 October Kong-Rey experienced an ERC and entered its weakening phase. Kong-Rey was captured on 2 October by both S1A at 2111 UTC and SMAP at 2133 UTC (Figs. 7c and 7f). The SAR observation depicts a well-defined symmetric eyewall, with a secondary ring of maximum winds further out from the TC center. In fact, Kong-Rey exhibited two eyewalls in 89 GHz imagery at this time (not shown). These two high wind regions were not well captured by the radiometer. The radiometer wind profile saturates in the 80 km inner-part of the TC, while the SAR wind profile exhibits two wind speed local maxima (Fig. 7i). Despite the inability of the radiometer sensor to capture the duel wind maxima observed at this time, the outer-part of the azimuthally-averaged wind profiles match well, both yielding a R_{64} estimate of ~128 km. Though, $R_{max}^{CK22-BR}$ is 42 km, far from the 14 km of SAR R_{max}. However, it is noteworthy that $R_{max}^{CK22-BR}$ lies between the two SAR wind maxima. The complex shape of Kong-Rey during its ERC is the main cause to explain such a huge discrepancy. Indeed, the R_{64} estimate is pushed to an outer radius due to the existence of secondary wind maxima.

b. Structural aspects

From these examples, we see that neither the use of high quality data (SAR) to train the algorithm nor the use of a radius that is very close to R_{max} (*i.e* R_{64}) precludes large uncertainties of R_{max} estimates using the CK22 framework. Underlying CK22, the use of an outer wind radius (*e.g* R_{34}[1]) to estimate R_{max} is justified by the angular momentum conservation principle: an air parcel, advected from the outer radii to the innermost radii, must lose angular momentum due to surface friction. The ratio $\frac{M_{max}}{M_{34}}$ thus represents the ability for an air parcel to keep its angular momentum while being advected from R_{34} to R_{max}. In the log-linear framework, this ratio solely depends on V_{max}, R_{34}, and f.

The use of these three parameters to estimate $\frac{M_{max}}{M_{34}}$ was discussed in Chavas et al. (2015) and Chavas and Lin (2016). In these studies, the ability of a radial parametric wind profile to represent the variability of observational data was tested. In brief, the radial parametric profile geometrically merges an inner-part profile with an outer-part profile, previously anticipated from theoretical studies (Emanuel and Rotunno 2011; Emanuel 2004). Chavas and Lin (2016) concluded that the ratio $\frac{M_{max}}{M_0}$ between the angular momentum at R_{max} and at an outer-radius R_0 solely depends on four parameters: V_{max}, fR_0, $\frac{C_k}{C_d}$, and $\frac{W_{cool}}{C_d}$, where C_k and C_d are the heat and momentum exchange coefficients, while W_{cool} models the radiative-subsidence rate in the free troposphere of the outer-part model. Considering $R_0 = R_{34}$, a log-linear dependence of $\frac{M_{max}}{M_{34}}$ on (V_{max}, R_{34}, f) thus neglects the variations of both $\frac{C_k}{C_d}$ and $\frac{W_{cool}}{C_d}$.

Besides, the axisymmetric and steady-state theory of Emanuel and Rotunno (2011) invokes a direct relationship between $\frac{M_{max}}{M_{34}}$ and $\frac{C_k}{C_d}$, that can be stated as

$$\frac{M_{max}}{M_{34}} = \pi(\frac{C_k}{C_d}), \tag{6}$$

with $\pi(x) := (\frac{1}{2}x)^{\frac{1}{2-x}}$ a monotonically increasing function (see their eq. 38). This relationship assumes the TC is in steady-state and the Richardson number in the outflow is slightly below one. The latter implies the outflow is self-stratified by small-scale turbulence. Using numerical simulations that resolved convection, Emanuel and Rotunno (2011) showed that such an assumption was satisfied in an outflow region near R_{max}. This assumption might then not hold true further out. Chavas et al. (2015) suggested that the optimal merging radius between the inner- and outer-part of the model was $\sim 2-3R_{max}$ when fitting the complete parametric profile to observational data. While not strictly corresponding to the region where the theoretical developments of Emanuel and Rotunno (2011) could remain valid, it identifies the region where the inner-part of the model is most likely to apply to the observations.

When writing eq. 6, one assumes that the model of Emanuel and Rotunno (2011) is still valid at R_{34}, which largely exceeds $3R_{max}$ in nature. This might be a strong

[1]In this section we chose R_{34} as outer wind radius for clarity, but the reasoning well applies to any other wind radius (*e.g* R_{50} and R_{64}).

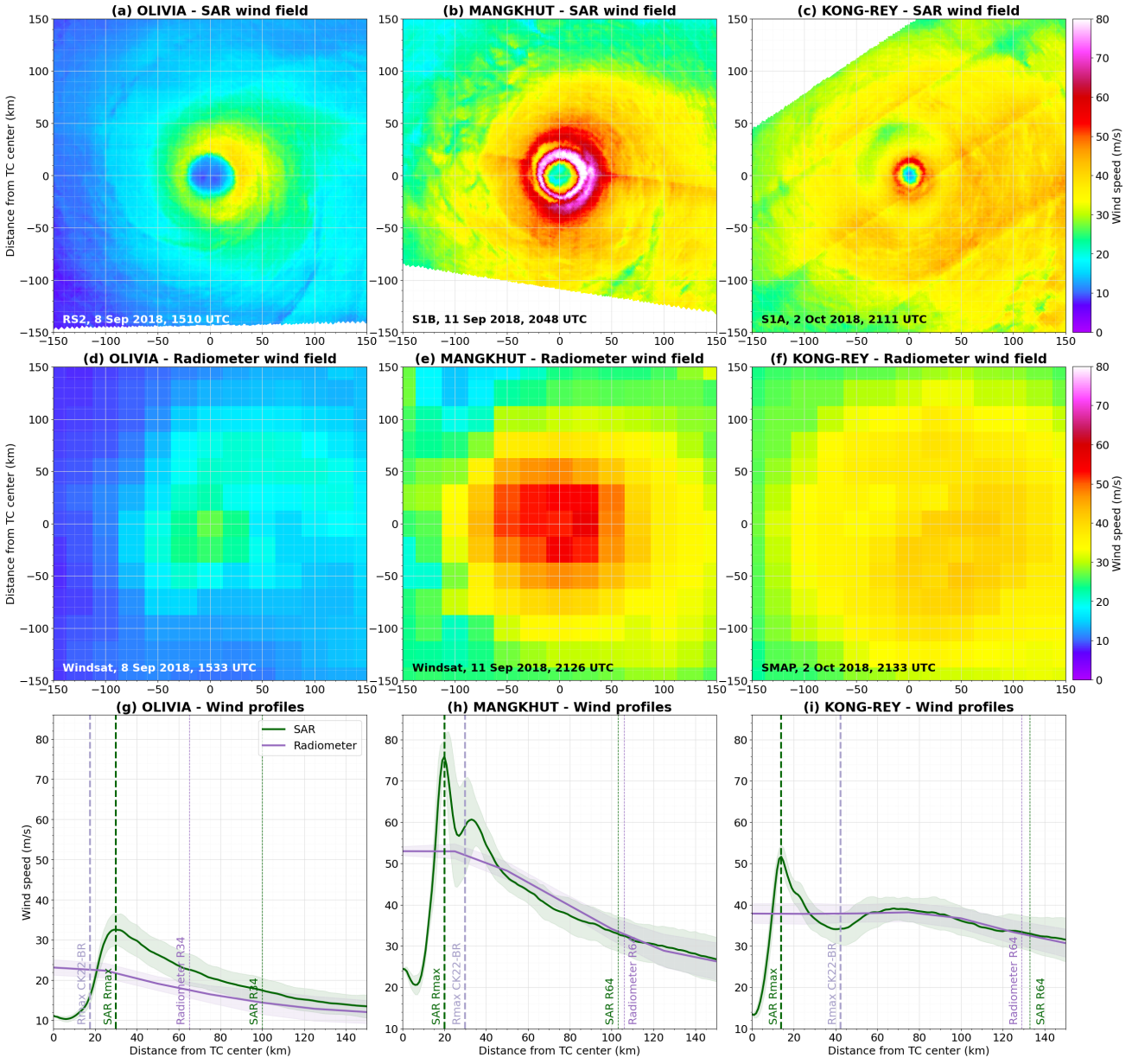

FIG. 7. Comparison of SAR and radiometer wind fields (top and middle rows, TCs are translating toward the top of each panel) and corresponding wind profiles (bottom row) for Olivia (left column), Mangkhut (middle column) and Kong-Rey (right column).

approximation, but it offers an instructive relationship between the rate of conservation of angular momentum (left-hand side) to a function of $\frac{C_k}{C_d}$, characterizing the balance between energy generation and friction loss (right-hand side). Most importantly, $\frac{C_k}{C_d}$ controls the shape of the parametric radial wind profile, with higher values corresponding to more peaked profiles. In practice, unlike $\frac{C_k}{C_d}$ values, this shape of the near-peak radial wind profile is more easily quantifiable using SAR data.

To highlight these considerations, we present TC cases that have the same CK22 predictors (V_{max}, R_{64}, f) but different wind profile shapes near their peak intensities. Figure 8 is representative of such a situation. SAR acquisitions over TC Rammasun (West Pacific, red curve) and TC Marie (East Pacific, blue curve), occurred on 17 July 2014 at 1027 UTC and on 3 October 2020 at 1419 UTC, respectively. Both storms display similar outer-core profiles, with almost the same R_{64} (~52 and ~49 km), V_{max} (~42 and ~43 $m.s^{-1}$) and f (~4.3 and ~4.6 s^{-1}). Applying CK22 to these cases (vertical dashed lines) thus leads to almost the same $R_{max}^{CK22-BR}$ value (~25 and ~22 km). However, SAR derived wind profiles provide different estimates, R_{max} (~34 and ~24 km, respectively).

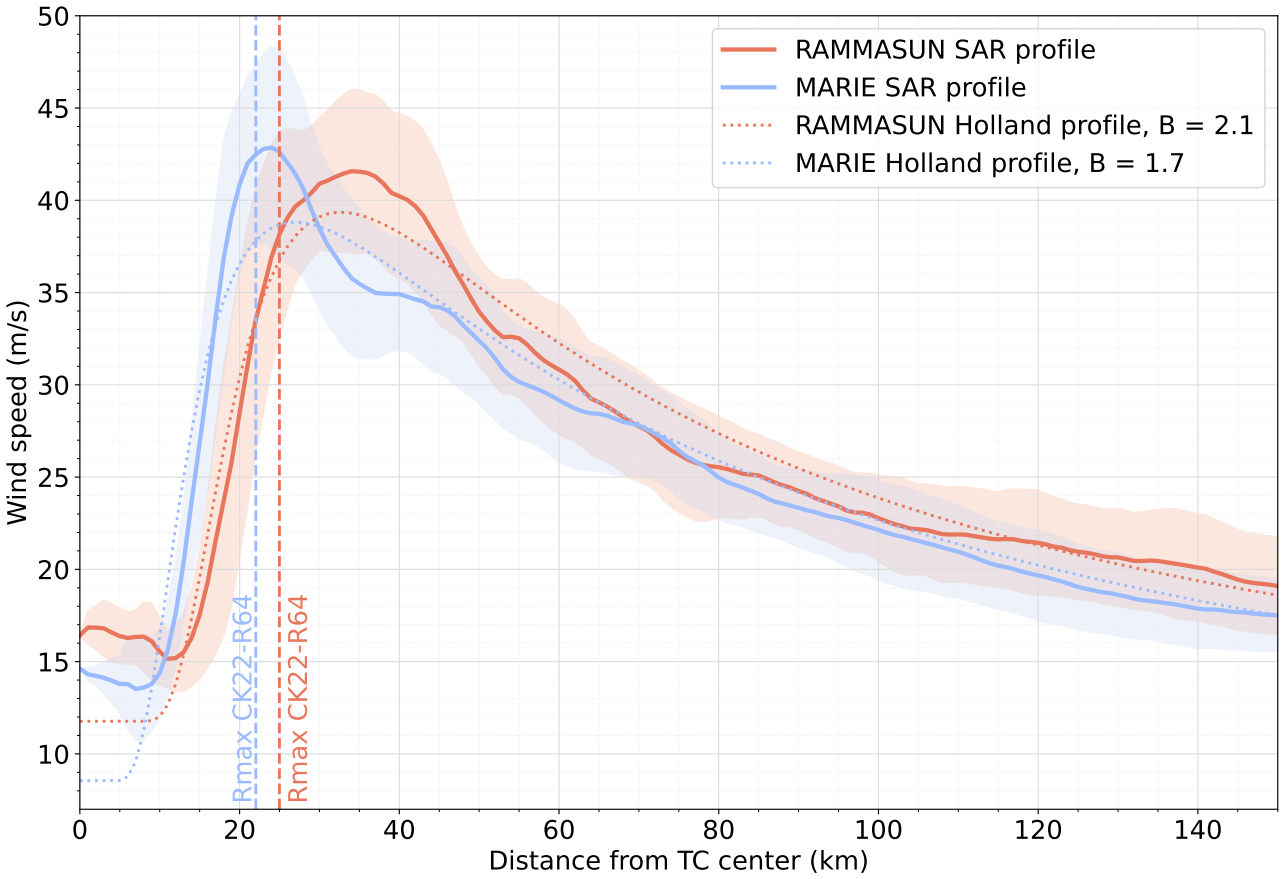

FIG. 8. SAR wind profiles for Rammasun (solid red) and Marie (solid blue) and associated Holland best-fit profiles (dotted curves) fitted on $0 \leq r \leq 500km$.

Comprehensively, the CK22 model cannot fully adjust to peculiar local wind profiles. To quantify the wind profile shapes, a Holland parametric profile (Holland 1980) was adjusted to each SAR azimuthally-averaged wind profile:

$$V_{Holland}(r) = V_{min} + \sqrt{(V_{max} - V_{min})^2 (\frac{R_{max}}{r})^B e^{1-(\frac{R_{max}}{r})^B} + (\frac{rf}{2})^2} - \frac{rf}{2}.$$

This parametric formulation is useful to quantify variations in the shape of observed wind profiles. In particular, the empirical B parameter controls the rate of radial decay of the tangential winds, with higher (smaller) values corresponding to narrower (broader) vortices. In addition, this parameter was found to be sensitive to TC intensity and size while independent of R_{max} (Knaff et al. 2011).

Note, Holland's profiles were designed for gradient-level wind and are not necessarily suited for surface wind profiles with nonzero wind speeds at the TC center, well captured using SAR observations. A complementary degree of freedom (V_{min}) was thus included in eq. b to cope with the existence of nonzero minimum wind speeds.

Using the full extent of the wind profile, a solution for V_{min}, V_{max}, R_{max} and B can be estimated via least squares. Applied to TC Rammasun and Maria, the fitting procedure results in two different B values, ~2.1 and ~1.7, respectively (Fig. 8). Such a difference quantifies the remaining variability of the near-core wind profile for comparable outer-core wind profiles.

c. *Analysis framework*

The shape of the near-core wind profile is generally associated with the radial gradient of absolute angular momentum and thus the loss of angular momentum when an air parcel is advected from R_{34} to R_{max}. To guide the analysis, we recall the equation of angular momentum conservation for an axi-symmetric vortex:

$$\frac{\partial M}{\partial t} + u\frac{\partial M}{\partial r} + w\frac{\partial M}{\partial z} = \frac{r}{\rho}\frac{\partial \tau_{\theta z}}{\partial z}, \quad (7)$$

with u and w, the radial and vertical velocities, $\tau_{\theta z}$ a tangential stress component, and ρ the density. The continuity equation links u and w as

$$\frac{1}{r}\frac{\partial (ru)}{\partial r} + \frac{\partial w}{\partial z} = 0. \quad (8)$$

Under steady state condition, eq. 7 can be integrated from the surface to a boundary layer height, h, where the stress vanishes:

$$\int_0^h u\frac{\partial M}{\partial r}\,dz + \int_0^h w\frac{\partial M}{\partial z}\,dz = -\frac{r\tau_{\theta s}}{\rho} = -C_d r V^2, \quad (9)$$

with $\tau_{\theta s} \approx C_d \rho V^2$ the surface stress, C_d a drag coefficient and V the tangential surface wind component. Assuming $w(z=0) = 0$ and the use of the continuity equation (eq. 8), the second term of the left hand-side in eq. 9 is integrated by parts, following developments presented by Kalashnik (1994), to obtain

$$\int_0^h u\frac{\partial M}{\partial r}\,dz + [wM]|_{z=h} + \int_0^h \frac{M}{r}\frac{\partial (ru)}{\partial r}\,dz = -C_d r V^2. \quad (10)$$

Grouping the two integrals yields

$$\frac{1}{r}\frac{d}{dr}\left(r\int_0^h uM\,dz\right) + [wM]|_{z=h} = -C_d r V^2. \quad (11)$$

Defining $\overline{u} := \frac{1}{h}\int_0^h u\,dz$ we can approximate the integral $\int_0^h uM\,dz \approx h\overline{u}M|_{z=h}$ and rewrite the continuity equation $w|_{z=h} = -\frac{h}{r}\frac{d}{dr}(r\overline{u})$. Rearrangement finally yields:

$$rV^2 \approx -\frac{h\overline{u}}{C_d}\frac{dM}{dr}, \quad (12)$$

where $\frac{dM}{dr}$ is the radial gradient of absolute angular momentum at the top of the boundary layer. Assuming the latter is closely related to its value at the surface, eq.12 then explicitly links the shape of the wind profile $\frac{dM}{dr}$ to rV^2.

Using SAR measurements, both quantities can be accurately estimated, and the validity of eq. 12 assessed. Figure 9a represents $R_{max}V_{max}^2$ (y-axis) as a function of $R_{34}V_{34}^2$ (x-axis) and colored by the fitted B values[2]. On average, *i.e* $B \simeq 1.8$, a relationship emerges when comparing $R_{max}V_{max}^2$ and $R_{34}V_{34}^2$. Departures from a one-to-one relationship, related to conservation of the rV^2 parameter, are seemingly well explained by B values. Large B, corresponding to very peaked wind profiles near V_{max}, leads to larger $R_{max}V_{max}^2$ for a given $R_{34}V_{34}^2$. For broader wind profiles, corresponding to smaller B, smaller $R_{max}V_{max}^2$ are generally found.

Moreover, the space spanned in the ($R_{34}V_{34}^2$, $R_{max}V_{max}^2$)-plane is still apparently large, even at constant B. From eq. 12, this increased variability is possibly associated with the factor $\frac{h\overline{u}}{C_d}$. Overall, these results suggest that the variability encountered in nature does not solely depend on the three predictors (V_{max}, R_{34}, f).

To further illustrate this diagnosis, Fig. 9b displays the same ($R_{34}V_{34}^2$, $R_{max}V_{max}^2$)-plane, but using the radiometer and scatterometer database, and corresponding V_{max}^{REG}, R_{34} and $R_{max}^{CK22-BR}$ estimates. As expected, the variability captured by using R_{34} or R_{50} to estimate R_{max} via CK22 is poor. While using R_{64} increases this variability, the overall spread is reduced compared to Fig. 9a, suggesting that the variability of the wind profile shapes associated with the $R_{max}^{CK22-BR}$ estimates is low.

Note, the average situation $rV^2 \approx$ constant which is depicted in our study thanks to the SAR database has already been discussed by Riehl (1963) when he argued that PV is conserved within the inflow layer. PV conservation implies the vertical component of the curl of the frictional force to be zero, or

$$\frac{r}{\rho}\frac{\partial \tau_{\theta z}}{\partial z} = \text{constant}. \quad (13)$$

Integrating this equation over the boundary layer height yields (assuming constant density):

$$\frac{r\tau_{\theta s}}{\rho} = C_d r V^2 = \text{constant}. \quad (14)$$

Thus, for a constant or slowly varying drag coefficient C_d, PV conservation leads to $rV^2 \approx$ constant (Riehl 1963). Mentioned above, such a relationship is, on average, consistent with the SAR estimates. However, for this relationship, the only source of variability comes from C_d. From arguments raised above (eq. 12), h and $\overline{u}$ should also be further considered.

Lastly, one limitation of our observational analysis is that SAR V_{max} is an estimate of the maximum total wind speed rather than the maximum tangential wind speed. Knowing how the total wind speed is distributed between its tangential and radial component near the eyewall region would allow to better estimate the impact of $\overline{u}$ on PV conservation and its variability.

d. Comparison of $R_{max}^{CK22-BR}$ with existing R_{max} estimates

With these results in mind, we assessed how much $R_{max}^{CK22-BR}$ estimates improved existing R_{max} estimates. Figure 10 displays density contours of (V_{max}, R_{max}) joint distributions using IBTrACS R_{max} (dashed blue)

[2] B, as a scalar value, was used instead of a criterion based on $\frac{dM}{dr}$ to describe the shape of the wind profile

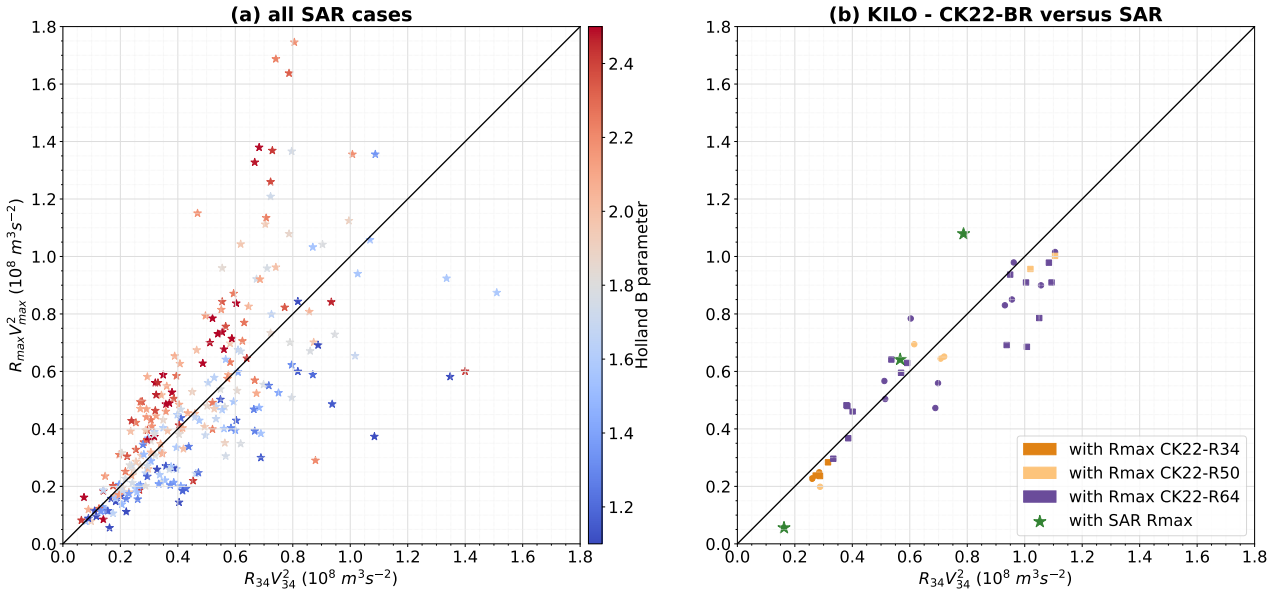

FIG. 9. Evaluation of the PV conservation assumption in the SAR dataset (a) and for Kilo's life cycle (b) using R_{34} estimated on radiometer and scatterometer data along with corresponding $R_{max}^{CK22-BR}$ estimates and V_{max}^{REG}. The three SAR cases (green stars) are also displayed for reference.

or $R_{max}^{CK22-BR}$ estimates (solid black). For comparison, the same density contours are shaded for the SAR dataset (green).

We remind readers that SAR wide-swath acquisitions cannot be continuously performed over the ocean. As a consequence, not only does the SAR dataset contain much fewer cases, it is also biased towards higher intensities. Indeed, acquisition orders are most often requested to observe higher intensity systems. Thus, for the lowest V_{max} (less than $\sim$ 30 ms^{-1}), possible inconsistencies in R_{max} densities arise when comparing SAR to radiometer and scatterometer or IBTrACS. The density contours suggest that both IBTrACS R_{max} and $R_{max}^{CK22-BR}$ estimates are larger than SAR R_{max}, while, in fact, this is just a consequence of the lack of SAR data at these intensities.

Nevertheless, and more importantly for high surface winds, discrepancies in R_{max} densities are observed. Indeed, on average IBTrACS density contours are centered on a higher R_{max} ($\sim$30 km) than SAR (progressively decreasing to $\sim$20 km). Confirming the efficacy of the revised model, radiometer- and scatterometer-based density contours display an average $R_{max}^{CK22-BR}$ ($\sim$20 km) that is consistent with SAR R_{max}. Depicted by the R_{max} density curves (right panel), for low R_{max}, IBTrACS density is lower than both SAR and $R_{max}^{CK22-BR}$ values.

For further comparison, we computed R_{max} estimates from R_{34} on the radiometer and scatterometer data using eq. 7 of Chavas and Knaff (2022). The corresponding density curve (dotted red) shows only a minor improvement compared to IBTrACS at low R_{max}.

Finally, the density contours of the radiometer and scatterometer dataset with $R_{max}^{CK22-BR}$ span a larger space than IBTrACS in the (V_{max}, R_{max})-plane (compare for instance the 20%-contours in Fig. 10, *i.e* the black and blue outermost contours). This shows that the former captures more variability than best-track data. This is likely due to the use of R_{64} in the regression, a result already suggested by Fig. 9b. Even though the datasets don't have the same V_{max} distributions, Fig. 10 also suggests that the radiometer and scatterometer density contours span less space than SAR observations in the (V_{max}, R_{max})-plane. While this is consistent with the above analysis, more SAR cases are needed to properly interpret Fig. 10.

6. Conclusions and perspectives

Understanding TC intensity changes certainly remains an observationally challenging problem. As expressed during the Tenth International Workshop on Tropical Cyclones (IWTC-10, recommendation 4), both the operational and research communities recognize the need for more homogeneous and standardized datasets for TC wind structure parameters, such as R_{max} and the wind radii. The fact that R_{34} was not systematically reanalyzed in all basins, and that R_{max} is still not reanalyzed today (best-track R_{max} value typically stems from its operational estimate) hampers the consolidation of such a dataset. Systematic and standardized wind radii are needed when using, and further improving, a semi-empirical model such as CK22. Although satellite sensors have their limitations, especially regarding the inter-calibration of different missions and

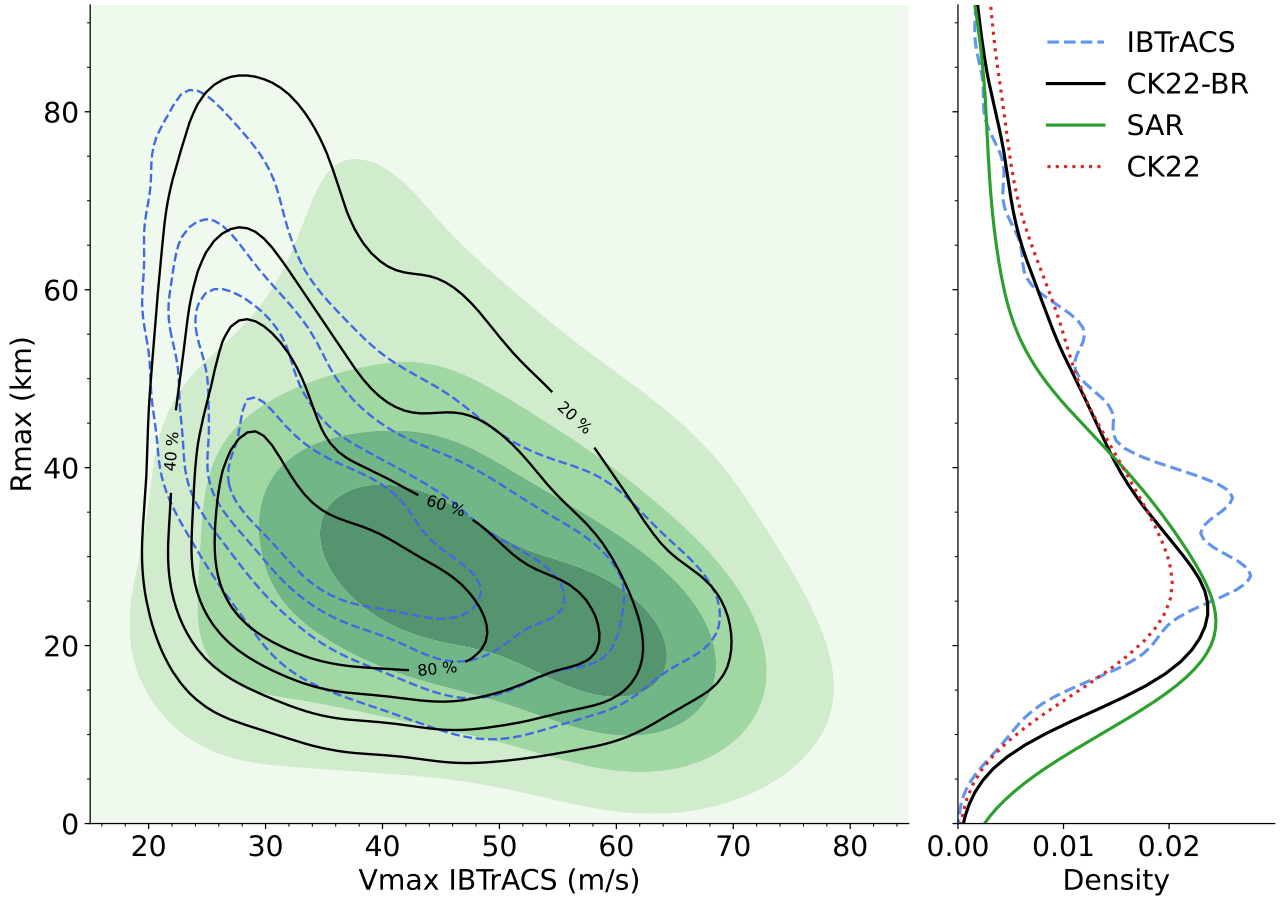

FIG. 10. Density contours of (V_{max}, R_{max}) joint distribution for the SAR dataset (shaded green, V_{max} based on IBTrACS), for the dataset based upon radiometers and scatterometers with $R_{max}^{CK22-BR}$ (solid black) and based on corresponding IBTrACS R_{max} values (dashed blue). All contours correspond to iso-proportions (with 20% increments, see the black contours labels) in density obtained by two-dimensional gaussian kernel density estimation. For instance the area outside the 80%-contour contains 80% of the probability mass. The corresponding R_{max} density curves are displayed on the right panel, along with R_{max} estimates obtained by applying eq. 7 of Chavas and Knaff (2022) to the radiometer- and scatterometer-based dataset (dotted red).

sensors, resulting multi-modal observations shall serve for such a systematic and global approach, at least for wind radii estimation.

More specifically and thanks to high-resolution (SAR) data, it is now possible to more systematically estimate R_{max}. Fitted with SAR estimates and used in conjunction with the closest wind radius to R_{max}, our study proposed a revised CK22 model. It is shown to be an efficient tool to provide improved reliable estimates, with an average uncertainty of $\sim 9\ km$. Because outer-core wind radii can be estimated from radiometer or C-band scatterometer data, the developed framework thus allows to produce a more extensive dataset of reanalyzed R_{max} estimates. The resulting time series are generally more realistic than those obtained from best-track R_{max} estimates. The method can also be used to provide operational guidance on the location of the maximum intensity every time a radiometer or C-band scatterometer overflies the TC, as long as its intensity and location are also estimated, noting that such estimates are routinely available from operational centers. In fact, the developed framework is relevant to any situation where V_{max} and an outer size are known and R_{max} is biased or unknown. This includes low-resolution weather and climate modelling applications where the outer-core (*i.e*, near R_{34}) is better resolved than the inner-core (*i.e*, near R_{max}), and risk modelling with synthetic TCs (Gori et al. 2022) where V_{max} and an outer size are commonly used as input, while R_{max} must be predicted in conjunction with a wind profile model. The proposed method could also be used to guide the best-tracking process when no reliable R_{max} observation is available.

The efficacy of the semi-empirical CK22 model stems from fundamental conservation principles. Indeed, the high-resolution SAR database highlights that TCs, on average, conserve their PV, with a resulting approximation $rV^2 \approx$ constant. Accordingly, the use of CK22 to retrieve R_{max}, based on an outer-radius wind observation coupled with an intensity estimate is, on average, justified. Single

cases can still depart considerably from the PV conservation assumption, especially those at very high intensity (V_{max}) or with large inner- (R_{max}) or outer-size (R_{34}). And, to first order, those deviations are well explained by variations of the observed wind profile shapes.

While the use of R_{64} can account for some of the deviations due to the radial gradient of absolute angular momentum, the CK22 model seems to fail to capture the remaining variability observed in the SAR database. Large variability is apparently still occurring near the TC core. To further advance our understanding, there continues to be a need for spaceborne SAR and airborne SFMR sensors as these are the only tools that resolve surface winds in this area. Both sensors however suffer from a lack of spatio-temporal sampling, and airborne measurements suffer from a lack of azimuthal coverage. The future is bright with the recently launched RADARSAT Constellation Mission (RCM) operated by CSA, which should improve the satellite SAR spatio-temporal sampling. RCM has already proved useful by providing significantly more R_{max} estimates than anticipated for the 2022-2023 season. And, increasing the number of available SAR cases will certainly allow to better understand how absolute angular momentum gradients are constrained in the near-core region. Objective estimates of TC eye sizes or core sizes at intermediate levels are also routinely performed with spaceborne infrared or passive microwave data (Knapp et al. 2018; Cossuth 2014). While such information may complement SAR or SFMR surface observations in a multi-modal approach, there still is a need to better understand how they relate to the TC wind structure.

Furthermore, the integrated equations show that both the boundary layer depth (h), the average radial inflow ($\overline{u}$), and the drag (C_d) also impact the relationship between PV conservation and the near-core wind profile shape. While the C_d behaviour under very high winds is still actively debated (Powell et al. 2003; Bell et al. 2012; Donelan 2018; Curcic and Haus 2020), measurements of both h and $\overline{u}$ may be facilitated by the Doppler-based motions derived from the Imaging Wind and Rain Airborne Profiler (IWRAP) instrument (Sapp et al. 2022). For the radial inflow, improved estimates at the surface, in the near-core region, shall be made possible with the future Harmony mission (ESA 2022), the ESA Earth Explorer 10. This mission will augment Sentinel 1D observations with two satellite companions, providing azimuth diversity from these bistatic observations. In addition, the Second Generation Meteorological Operational satellite programme (Metop-SG) will operate in both co- and cross-polarization. Unlike the current spaceborne instruments, ASCAT, which have only co-polarization measurements, the higher sensitivity of cross-polarized signals to ocean breaking waves may thus improve the ocean surface wind vectors measured by scatterometers, approaching the TC core regions. Also, the coming Copernicus Imaging Microwave Radiometer (CIMR) promises to offer large swath with improved resolution, low uncertainty observation capabilities, combining L-, C- and X-band frequencies. The presence of 1.4 GHz L-band channel on board CIMR will open up the possibility to further interpret the high-resolution C- and X-band measurements, to provide improved surface wind vector estimates under extreme conditions (Kilic et al. 2018).

Finally, in the absence of high-resolution observations, the shape of the near-core wind profile may also be indirectly estimated. Given the relation $rV^2 \approx$ constant under a steady-state assumption, a departure from this relation can help understand the temporal variations of absolute angular momentum. Estimates of these temporal variations may then be used to evaluate how much the near-core wind profile shape departs from the average relationship. The wind profile shape is also linked to the drag coefficient (see for instance the steady-state view of Emanuel and Rotunno (2011)), which modulates asymmetries in the boundary layer response (Shapiro 1983; Kepert 2001). Asymmetries possibly captured by medium- or low-resolution observations (scatterometers or radiometers), may thus help to infer boundary layer frictional drag terms, and to quantify the resulting shape of the wind profile.

Acknowledgments. This work was financially supported by the ERC Synergy project 856408-STUOD, the ANR projects OceaniX and ISblue, and the ESA Marine Atmosphere eXtreme Satellite Synergy project (MAXSS). The radiometer and scatterometer dataset used in this report is part of the MAXSS project. The SAR database was obtained from IFREMER/CyclObs and produced with the SAR wind processor co-developed by IFREMER and CLS. J. Knaff thanks NOAA/Center for Satellite Applications and Research for providing the time work on this subject. The views, opinions, and findings contained in this report are those of the authors and should not be construed as an official National Oceanic and Atmospheric Administration or U.S. government position, policy, or decision. We also acknowledge three anonymous reviewers for their comments, especially regarding the enriching suggestions about infrared and passive microwave data.

Data availability statement. The data used in this study are freely available online for both the dataset of radiometer and scatterometer winds (`https://www.odatis-ocean.fr/donnees-et-services/acces-aux-donnees/catalogue-complet/#/metadata/6c56bcde-050f-42eb-92b8-8e882e1f4db9`) and the SAR database (`https://cyclobs.ifremer.fr/`).

APPENDIX A

Scatterometer wind speed estimates

As explained in section 2, the wind speed estimates from different radiometer and scatterometer sensors have been inter-calibrated prior to our study. During this process, the C-band ASCAT missions were calibrated using a 25 km resolution, while the Ku-band scatterometer sensors were calibrated using a 50 km resolution. Spatial resolution was already demonstrated to impact how well TCs intensities are resolved in numerical models (Davis 2018) and observations (Quilfen et al. 1998). Here, we expect discrepancies between the C- and Ku-band observational wind products.

To quantify this resolution effect, SAR wind fields were degraded to both 25 and 50 km spatial resolution and then azimuthally-averaged. The V_{max} values estimated from these degraded wind profiles were then compared to IBTrACS V_{max}, as represented by the green (25 km) and red (50 km) stars of Fig. A1. Here, SAR V_{max} refers to the maximum found in an azimuthally-averaged wind profile. We thus expect slight discrepancies with IBTrACS V_{max}, whose definition does not strictly coincide with a wind profile maximum. The comparison between SAR azimuthal means and IBTrACS is indicated by the grey stars and modelled by a linear fit (grey dashed line in Fig. A1) which defines V_{max}^{REG}:

$$V_{max}^{REG} = 0.6967 V_{max}^{IBTrACS} + 6.1992. \qquad \text{(A1)}$$

The green and red scatters in Fig. A1 should be compared to this regression line (grey dashed) rather than the 1:1 line. The 25- and 50-km simulated V_{max} values show that as spatial resolution decreases V_{max} also decreases, and the decreasing tendency is more pronounced as intensity increases. On average, a V_{max} of ~38 ms^{-1} observed at the full-resolution azimuthally-averaged wind profile (*i.e* the raw SAR wind profile) would yield ~32 ms^{-1} when observed at a 25 km spatial resolution and ~28 ms^{-1} at a 50 km spatial resolution. Second-order polynomial fits were constructed to model this spatial resolution effect.

Using these linear and polynomial fits as reference, we then compared C-band and Ku-band scatterometer V_{max} values with IBTrACS in Fig. A2. It shows that C-band scatterometer V_{max} values are consistent with the 25 km spatial resolution polynomial model (green dashed curve). In contrast, Ku-band scatterometer V_{max} are still underestimated when compared to IBTrACS values following the correction for their 50 km resolution (red dashed curve). In particular, Ku-band scatterometer V_{max} estimates rarely exceed 64 knots (33 ms^{-1}), precluding their use to estimate wind radii in our analysis.

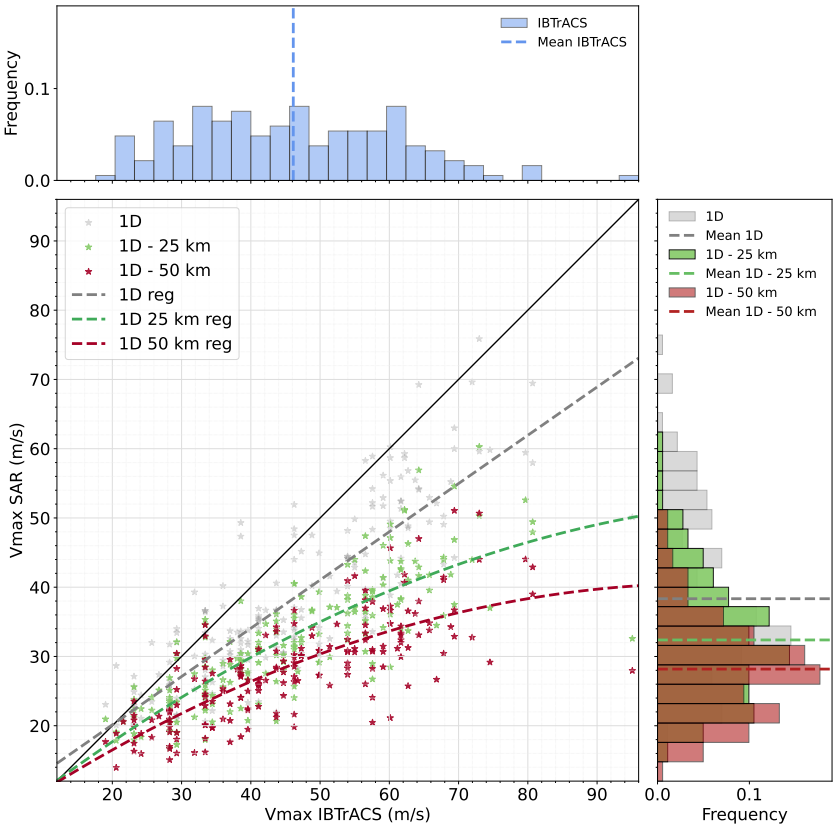

FIG. A1. Comparison between SAR (y-axis) and IBTrACS (x-axis) V_{max} for the raw dataset (grey) and when degraded at 25 km (green) or 50 km (red) resolution. Dashed lines represent best linear fit for the raw dataset (grey) and best second order polynomial fits for the 25 km (green) and 50 km (red) datasets. A solid black line represents identity. V_{max} distributions and averages are displayed for the different SAR samples (right) and for corresponding IBTrACS values (top).

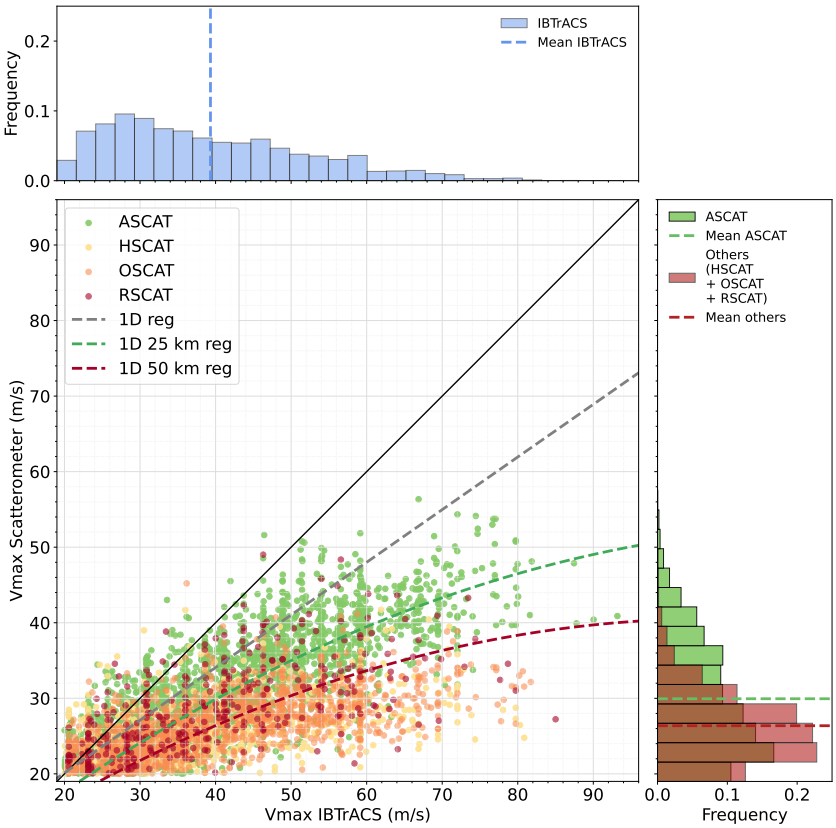

FIG. A2. Comparison between scatterometer (y-axis) and IBTrACS (x-axis) V_{max} for ASCAT (green), HSCAT (yellow), OSCAT (orange), and RSCAT (red). Solid and dashed lines are identical to Fig. A1. V_{max} distributions and averages are displayed for the different scatterometer datasets (right) and for corresponding IBTrACS values (top).

References

Bell, M. M., M. T. Montgomery, and K. A. Emanuel, 2012: Air–sea enthalpy and momentum exchange at major hurricane wind speeds observed during cblast. *Journal of the Atmospheric Sciences*, **69 (11)**, 3197–3222.

Brennan, M. J., C. C. Hennon, and R. D. Knabb, 2009: The operational use of quikscat ocean surface vector winds at the national hurricane center. *Weather and Forecasting*, **24 (3)**, 621–645.

Chavas, D. R., and J. A. Knaff, 2022: A simple model for predicting the tropical cyclone radius of maximum wind from outer size. *Weather and Forecasting*, **37 (5)**, 563–579.

Chavas, D. R., and N. Lin, 2016: A model for the complete radial structure of the tropical cyclone wind field. part ii: Wind field variability. *Journal of the Atmospheric Sciences*, **73 (8)**, 3093–3113.

Chavas, D. R., N. Lin, and K. Emanuel, 2015: A model for the complete radial structure of the tropical cyclone wind field. part i: Comparison with observed structure. *Journal of the Atmospheric Sciences*, **72 (9)**, 3647–3662.

Chou, K.-H., C.-C. Wu, and S.-Z. Lin, 2013: Assessment of the ascat wind error characteristics by global dropwindsonde observations. *Journal of Geophysical Research: Atmospheres*, **118 (16)**, 9011–9021.

Combot, C., A. Mouche, J. Knaff, Y. Zhao, Y. Zhao, L. Vinour, Y. Quilfen, and B. Chapron, 2020a: Extensive high-resolution synthetic aperture radar (sar) data analysis of tropical cyclones: Comparisons with sfmr flights and best track. *Monthly Weather Review*, **148 (11)**, 4545–4563.

Combot, C., Y. Quilfen, A. Mouche, J. Gourrion, C. de Boyer Montégut, B. Chapron, and J. Tournadre, 2020b: Space-based observations of surface signatures in the wakes of the 2018 eastern pacific tropical cyclones. *Journal of Operational Oceanography*, **13 (Suppl. 1)**.

Cossuth, J. H., 2014: Exploring a comparative climatology of tropical cyclone core structures. Ph.D. thesis, The Florida State University.

Curcic, M., and B. K. Haus, 2020: Revised estimates of ocean surface drag in strong winds. *Geophysical research letters*, **47 (10)**, e2020GL087 647.

Davis, C., 2018: Resolving tropical cyclone intensity in models. *Geophysical Research Letters*, **45 (4)**, 2082–2087.

Donelan, M. A., 2018: On the decrease of the oceanic drag coefficient in high winds. *Journal of Geophysical Research: Oceans*, **123 (2)**, 1485–1501.

Donnelly, W. J., J. R. Carswell, R. E. McIntosh, P. S. Chang, J. Wilkerson, F. Marks, and P. G. Black, 1999: Revised ocean backscatter models at c and ku band under high-wind conditions. *Journal of Geophysical Research: Oceans*, **104 (C5)**, 11 485–11 497.

Emanuel, K., 2004: Tropical cyclone energetics and structure. *Atmospheric turbulence and mesoscale meteorology*, **165**, 192.

Emanuel, K., and R. Rotunno, 2011: Self-stratification of tropical cyclone outflow. part i: Implications for storm structure. *Journal of the Atmospheric Sciences*, **68 (10)**, 2236–2249.

ESA, 2022: Report for mission selection: Earth explorer 10 candidate mission harmony. Tech. rep., ESA, Noordwijk, The Netherlands, 369 pp.

Ginis, I., 2002: Tropical cyclone-ocean interactions. *Advances in Fluid Mechanics Series*, **33**.

Gori, A., N. Lin, D. Xi, and K. Emanuel, 2022: Tropical cyclone climatology change greatly exacerbates us extreme rainfall–surge hazard. *Nature Climate Change*, **12 (2)**, 171–178.

Holland, G. J., 1980: An analytic model of the wind and pressure profiles in hurricanes.

Irish, J. L., D. T. Resio, and J. J. Ratcliff, 2008: The influence of storm size on hurricane surge. *Journal of Physical Oceanography*, **38 (9)**, 2003–2013.

Kalashnik, M., 1994: On the maximum wind velocity in the tropical cyclone. *Izvestiâ Akademii nauk SSSR. Fizika atmosfery i okeana*, **30 (1)**, 26–30.

Kepert, J., 2001: The dynamics of boundary layer jets within the tropical cyclone core. part i: Linear theory. *Journal of the Atmospheric Sciences*, **58 (17)**, 2469–2484.

Kilic, L., and Coauthors, 2018: Expected performances of the copernicus imaging microwave radiometer (cimr) for an all-weather and high spatial resolution estimation of ocean and sea ice parameters. *Journal of Geophysical Research: Oceans*, **123 (10)**, 7564–7580.

Klotz, B. W., and E. W. Uhlhorn, 2014: Improved stepped frequency microwave radiometer tropical cyclone surface winds in heavy precipitation. *Journal of Atmospheric and Oceanic Technology*, **31 (11)**, 2392–2408.

Knaff, J. A., C. R. Sampson, P. J. Fitzpatrick, Y. Jin, and C. M. Hill, 2011: Simple diagnosis of tropical cyclone structure via pressure gradients. **26**, 1020 – 1031, https://doi.org/https://doi.org/10.1175/WAF-D-11-00013.1.

Knaff, J. A., and Coauthors, 2021: Estimating tropical cyclone surface winds: Current status, emerging technologies, historical evolution, and a look to the future. *Tropical Cyclone Research and Review*, **10 (3)**, 125–150.

Knapp, K. R., M. C. Kruk, D. H. Levinson, H. J. Diamond, and C. J. Neumann, 2010: The international best track archive for climate stewardship (ibtracs) unifying tropical cyclone data. *Bulletin of the American Meteorological Society*, **91 (3)**, 363–376.

Knapp, K. R., C. S. Velden, and A. J. Wimmers, 2018: A global climatology of tropical cyclone eyes. *Monthly Weather Review*, **146 (7)**, 2089–2101.

Kossin, J. P., J. A. Knaff, H. I. Berger, D. C. Herndon, T. A. Cram, C. S. Velden, R. J. Murnane, and J. D. Hawkins, 2007: Estimating hurricane wind structure in the absence of aircraft reconnaissance. *Weather and Forecasting*, **22 (1)**, 89–101.

Krien, Y., and Coauthors, 2018: Can we improve parametric cyclonic wind fields using recent satellite remote sensing data? *Remote Sensing*, **10 (12)**, 1963.

Kudryavtsev, V., A. Monzikova, C. Combot, B. Chapron, and N. Reul, 2019: A simplified model for the baroclinic and barotropic ocean response to moving tropical cyclones: 2. model and simulations. *Journal of Geophysical Research: Oceans*, **124 (5)**, 3462–3485.

Kudryavtsev, V., M. Yurovskaya, and B. Chapron, 2021: Self-similarity of surface wave developments under tropical cyclones. *Journal of Geophysical Research: Oceans*, **126 (4)**, e2020JC016 916.

Landsea, C. W., and J. L. Franklin, 2013: Atlantic hurricane database uncertainty and presentation of a new database format. *Monthly Weather Review*, **141 (10)**, 3576–3592.

Manaster, A., L. Ricciardulli, and T. Meissner, 2021: Tropical cyclone winds from windsat, amsr2, and smap: Comparison with the hwrf model. *Remote Sensing*, **13 (12)**, 2347.

Mayers, D. R., C. S. Ruf, and A. M. Warnock, 2023: Cygnss storm-centric tropical cyclone gridded wind speed product. *Journal of Applied Meteorology and Climatology*, **62 (3)**, 329–339.

Meissner, T., L. Ricciardulli, and A. Manaster, 2021: Tropical cyclone wind speeds from windsat, amsr and smap: Algorithm development and testing. *Remote Sensing*, **13 (9)**, 1641.

Meissner, T., L. Ricciardulli, and F. J. Wentz, 2017: Capability of the smap mission to measure ocean surface winds in storms. *Bulletin of the American Meteorological Society*, **98 (8)**, 1660–1677.

Morris, M., and C. S. Ruf, 2017: Determining tropical cyclone surface wind speed structure and intensity with the cygnss satellite constellation. *Journal of Applied Meteorology and Climatology*, **56 (7)**, 1847–1865.

Mouche, A., B. Chapron, J. Knaff, Y. Zhao, B. Zhang, and C. Combot, 2019: Copolarized and cross-polarized sar measurements for high-resolution description of major hurricane wind structures: Application to irma category 5 hurricane. *Journal of Geophysical Research: Oceans*, **124 (6)**, 3905–3922.

Mouche, A. A., B. Chapron, B. Zhang, and R. Husson, 2017: Combined co-and cross-polarized sar measurements under extreme wind conditions. *IEEE Transactions on Geoscience and Remote Sensing*, **55 (12)**, 6746–6755.

Mueller, K. J., M. DeMaria, J. Knaff, J. P. Kossin, and T. H. Vonder Haar, 2006: Objective estimation of tropical cyclone wind structure from infrared satellite data. *Weather and forecasting*, **21 (6)**, 990–1005.

Polverari, F., M. Portabella, W. Lin, J. W. Sapp, A. Stoffelen, Z. Jelenak, and P. S. Chang, 2021: On high and extreme wind calibration using ascat. *IEEE Transactions on Geoscience and Remote Sensing*, **60**, 1–10.

Portabella, M., A. S. Rabaneda, and G. Grieco, 2022: Maxss: Algorithm theoretical baseline document for sfmr-based satellite-derived extreme wind recalibration (v2. 0).

Powell, M. D., P. J. Vickery, and T. A. Reinhold, 2003: Reduced drag coefficient for high wind speeds in tropical cyclones. *Nature*, **422 (6929)**, 279–283.

Price, J. F., 1981: Upper ocean response to a hurricane. *Journal of Physical Oceanography*, **11 (2)**, 153–175.

Quilfen, Y., B. Chapron, T. Elfouhaily, K. Katsaros, and J. Tournadre, 1998: Observation of tropical cyclones by high-resolution scatterometry. *Journal of Geophysical Research: Oceans*, **103 (C4)**, 7767–7786.

Quilfen, Y., C. Prigent, B. Chapron, A. Mouche, and N. Houti, 2007: The potential of quikscat and windsat observations for the estimation of sea surface wind vector under severe weather conditions. *Journal of Geophysical Research: Oceans*, **112 (C9)**.

Reul, N., and B. Chapron, 2003: A model of sea-foam thickness distribution for passive microwave remote sensing applications. *Journal of Geophysical Research: Oceans*, **108 (C10)**.

Reul, N., B. Chapron, E. Zabolotskikh, C. Donlon, Y. Quilfen, S. Guimbard, and J.-F. Piolle, 2016: A revised l-band radio-brightness sensitivity to extreme winds under tropical cyclones: The five year smos-storm database. *Remote Sensing of Environment*, **180**, 274–291.

Reul, N., J. Tenerelli, B. Chapron, D. Vandemark, Y. Quilfen, and Y. Kerr, 2012: Smos satellite l-band radiometer: A new capability for ocean surface remote sensing in hurricanes. *Journal of Geophysical Research: Oceans*, **117 (C2)**.

Reul, N., and Coauthors, 2017: A new generation of tropical cyclone size measurements from space. *Bulletin of the American Meteorological Society*, **98 (11)**, 2367–2385.

Riehl, H., 1963: Some relations between wind and thermal structure of steady state hurricanes. *Journal of Atmospheric Sciences*, **20 (4)**, 276–287.

Sampson, C. R., E. M. Fukada, J. A. Knaff, B. R. Strahl, M. J. Brennan, and T. Marchok, 2017: Tropical cyclone gale wind radii estimates for the western north pacific. *Weather and Forecasting*, **32 (3)**, 1029–1040.

Sapp, J., Z. Jelenak, P. Chang, C. Shoup, and J. Carswell, 2022: Processing of high-resolution hurricane ida boundary layer winds from the iwrap instrument on the noaa wp-3d aircraft. *IGARSS 2022-2022 IEEE International Geoscience and Remote Sensing Symposium*, IEEE, 7286–7289.

Schreck III, C. J., K. R. Knapp, and J. P. Kossin, 2014: The impact of best track discrepancies on global tropical cyclone climatologies using ibtracs. *Monthly Weather Review*, **142 (10)**, 3881–3899.

Shapiro, L. J., 1983: The asymmetric boundary layer flow under a translating hurricane. *Journal of Atmospheric Sciences*, **40 (8)**, 1984–1998.

Soisuvarn, S., Z. Jelenak, P. S. Chang, S. O. Alsweiss, and Q. Zhu, 2012: Cmod5. h—a high wind geophysical model function for c-band vertically polarized satellite scatterometer measurements. *IEEE Transactions on Geoscience and Remote Sensing*, **51 (6)**, 3744–3760.

Stoffelen, A., J. A. Verspeek, J. Vogelzang, and A. Verhoef, 2017: The cmod7 geophysical model function for ascat and ers wind retrievals. *IEEE Journal of Selected Topics in Applied Earth Observations and Remote Sensing*, **10 (5)**, 2123–2134.

Takagi, H., and W. Wu, 2016: Maximum wind radius estimated by the 50 kt radius: improvement of storm surge forecasting over the western north pacific. *Natural Hazards and Earth System Sciences*, **16 (3)**, 705–717.

Tsukada, T., and T. Horinouchi, 2023: Strong relationship between eye radius and radius of maximum wind of tropical cyclones. *Monthly Weather Review*, **151 (2)**, 569–588.

Uhlhorn, E. W., P. G. Black, J. L. Franklin, M. Goodberlet, J. Carswell, and A. S. Goldstein, 2007: Hurricane surface wind measurements from an operational stepped frequency microwave radiometer. *Monthly Weather Review*, **135 (9)**, 3070–3085.

Vickery, P. J., and D. Wadhera, 2008: Statistical models of holland pressure profile parameter and radius to maximum winds of hurricanes from flight-level pressure and h* wind data. *Journal of Applied Meteorology and climatology*, **47 (10)**, 2497–2517.

Vinour, L., S. Jullien, A. Mouche, C. Combot, and M. Mangeas, 2021: Observations of tropical cyclone inner-core fine-scale structure, and

its link to intensity variations. *Journal of the Atmospheric Sciences*, **78 (11)**, 3651–3671.

Wang, S., and R. Toumi, 2021: Recent tropical cyclone changes inferred from ocean surface temperature cold wakes. *Scientific Reports*, **11 (1)**, 22 269.

Willoughby, H., and M. Rahn, 2004: Parametric representation of the primary hurricane vortex. part i: Observations and evaluation of the holland (1980) model. *Monthly Weather Review*, **132 (12)**, 3033–3048.

Willoughby, H. E., R. Darling, and M. Rahn, 2006: Parametric representation of the primary hurricane vortex. part ii: A new family of sectionally continuous profiles. *Monthly weather review*, **134 (4)**, 1102–1120.

Wright, C. W., and Coauthors, 2001: Hurricane directional wave spectrum spatial variation in the open ocean. *Journal of Physical Oceanography*, **31 (8)**, 2472–2488.

Young, I. R., 2017: A review of parametric descriptions of tropical cyclone wind-wave generation. *Atmosphere*, **8 (10)**, 194.

Yueh, S. H., A. G. Fore, W. Tang, A. Hayashi, B. Stiles, N. Reul, Y. Weng, and F. Zhang, 2016: Smap l-band passive microwave observations of ocean surface wind during severe storms. *IEEE Transactions on Geoscience and Remote Sensing*, **54 (12)**, 7339–7350.

Zabolotskikh, E. V., L. M. Mitnik, N. Reul, and B. Chapron, 2015: New possibilities for geophysical parameter retrievals opened by gcom-w1 amsr2. *IEEE journal of selected topics in applied earth observations and remote sensing*, **8 (9)**, 4248–4261.

Zhao, Y., A. A. Mouche, B. Chapron, and N. Reul, 2018: Direct comparison between active c-band radar and passive l-band radiometer measurements: Extreme event cases. *IEEE Geoscience and Remote Sensing Letters*, **15 (6)**, 897–901.

2.3 Conclusion

In this chapter we have revisited a statistical relationship between R_{max} and a measure of the TC outer-size using high-resolution SAR observations and low-resolution radiometers and scatterometers acquisitions (Avenas et al., 2023). This methodology offers a potential solution for creating a dataset of reanalyzed R_{max} estimates that are more realistic than those obtained from best-track data, a necessary step in the development of homogeneous and standardized TC wind structure datasets.

The efficacy of the statistical model is attributed to its grounding in fundamental conservation principles, specifically the average PV conservation in the TC inflow. While deviations in individual cases are identified and related to the decay of the wind speed near the core of the TC, the equation $C_d r v^2 = \text{cst}$ and the statistical model are justified on average. However, the study suggests that future understanding of the large variability near the TC core is essential, and pointing to the need for further accumulating high-resolution measurements such as those from spaceborne SAR instruments.

Chapter 3

The tropical cyclone kinetic energy balance

3.1 Introduction

In **Chapter 2** we have demonstrated that the knowledge of a TC outer-size constrains the near-core wind structure within a certain degree of precision limited by the natural variability of the wind profile shape. An important result is that the assumption suggested by PV conservation in the TC inflow $C_d r v^2 = \text{cst}$ is rather consistent, on average, with high-resolution SAR wind profiles estimates.

Such a relationship strongly constrains the TC system. Indeed, the amplitude of vertical velocities at the top of the BL are linked to the radial gradient of the quantity $C_d r v^2$ through Eq. 1.27. In simple theoretical frameworks, the local heat source of the TC system may be assumed proportional to the strength of upward motions (Charney & Eliassen, 1964; M. Kalashnik, 1994). Furthermore, the quantity $C_d r v^2$ also characterizes the momentum losses due to surface friction. Thus, assuming that this quantity does not vary with radius certainly has strong implications for the TC kinetic energy balance between heat and momentum sources.

The accurate TC wind profiles estimates from SAR instruments provide an opportunity to examine how Eq. 1.34 impacts this balance. Furthermore, by supplying accurate estimates of the radial decay of the wind speed near the TC core, which is likely encoded in the global constant C_d, SAR observations may help identifying cases that deviate from the average conservation law Eq. 1.34 and how the kinetic energy balance is changed for these events. Such an approach, that combines both theoretical and observational perspectives, is presented in this chapter.

3.2 Article: "On the steadiness of the tropical cyclone integrated kinetic energy"

Manuscript submitted on 18/01/2024.

On the steadiness of the tropical cyclone integrated kinetic energy

A. Avenas[1] A. Mouche[1], J. Knaff[2], X. Carton[1], B. Chapron[1]

[1]Ifremer, Univ. Brest, CNRS, IRD, Laboratoire d'Océanographie Physique et Spatiale (LOPS), IUEM, F-29280, Plouzané, France
[2]NOAA/NESDIS Regional and Mesoscale Meteorological Branch, Fort Collins, Colorado

Key Points:

- High-resolution spaceborne synthetic aperture radar measurements inform on tropical cyclones kinetic energy stability
- Balance of tropical cyclones integrated kinetic energy is controlled by the surface wind decay and thermodynamical characteristics
- Accumulating high-resolution surface winds measurements shall allow to better assess short- and long-term trends in TC destructive potential

Corresponding author: Author One, arthur.avenas@ifremer.fr, ,

Corresponding author: Arthur Avenas, `arthur.avenas@ifremer.fr`

Abstract

Current global historical reanalyses prevent to adequately examine the role of the near-core surface wind structural properties on tropical cyclones climate trends. Here we provide theoretical and observational evidences that they are crucial for the monitoring of integrated kinetic energy. Two characteristic scales are defined and uniquely estimated using high-resolution ocean surface winds from all-weather spaceborne synthetic aperture radar: the radius of significant upward motions in the inflow layer and the radius of vanishing azimuthal velocity in the outflow layer. The instantaneous knowledge of these two characteristic scales is shown to inform on the steadiness of integrated kinetic energy. The resulting criterion of steadiness depends on a multiplicative constant characterizing the system thermodynamics. Consequently, accumulated high-resolution acquisitions of the ocean surface shall allow to better monitor integrated kinetic energy transitions and provide new means to tackle climatological studies of tropical cyclones destructiveness.

Plain Language Summary

Studying the long-term climate trends of tropical cyclones is challenging because the historical data is not always reliable. One particular issue concerns the accurate reporting of surface wind properties near the core of these storms in past and present records. This study uses both theory and high-resolution surface wind observations from satellite radar to highlight the importance of investigating these properties, specifically for monitoring the integrated kinetic energy, which is a measure of a storm destructive potential. Two spatial scales associated respectively with upward motions and maximum winds in tropical cyclones are identified and may be efficiently measured thanks to the high-resolution sensor. By comparing precise measurements of these two scales from several storm events with ancillary estimates of how integrated kinetic energy varied over time, we established a way to determine how stable a storm energy is. The criterion of stability is in theory influenced by the temperature characteristics of a storm, which are themselves modulated by environmental and climatological conditions. Consequently, future high-resolution observations from the satellite radar should help better understanding the dependence of integrated kinetic energy with space and time.

1 Introduction

Expressing the combined effect of intensity and size, Integrated Kinetic Energy (IKE) measures the destructive potential of TCs (Powell & Reinhold, 2007). Precisely monitoring this integrated quantity and understanding how it evolves in a global warming context is thus of major importance. Until this day, research studies focused on the climate-dependence of intensity (K. Emanuel, 2005; Webster et al., 2005; Sobel et al., 2016; Kossin, 2017; Patricola & Wehner, 2018; Kossin et al., 2020; Wang & Toumi, 2021; K. Emanuel, 2021) and more recently, of size (Chavas & Emanuel, 2010; Knaff et al., 2014; Wang & Toumi, 2021). Modulated by climate change, the sea surface temperature and the atmospheric temperature and humidity vertical profiles control both TCs intensity (K. Emanuel, 2007; Wing et al., 2015; Strazzo et al., 2015; Gilford et al., 2017; Done et al., 2022) and size (Lin et al., 2015; Chavas et al., 2016). While a few methods have been tested to assess past and future IKE trends (Misra et al., 2013; Morris & Ruf, 2017; Wang & Toumi, 2021; Kreussler et al., 2021), less is known about how oceanic and atmospheric parameters affect IKE and its variations. This lack of knowledge may be problematic for both operations and research, especially if the TC vitals were to fail capturing parameters that are critical to IKE balance.

In steady-state theories describing axisymmetric TCs, kinetic energy gained through the heat source is hypothesized to balance that lost through the dissipation source (Riehl, 1963; Anthes, 1974; Ooyama, 1982; K. A. Emanuel, 1986; Kalashnik, 1994; K. A. Emanuel,

1995; Pearce, 2004; Golitsyn, 2008). Analytical criteria expressing this steady-state balance may then be derived provided further assumptions on the outflow and inflow layer of TCs. For instance, Riehl (1963) assumes conservation of absolute angular momentum in the upper outflow of TCs. Momentum losses then solely occur in the surface inflow. Without reliable surface wind speed estimates, one way to express momentum losses is to assume potential vorticity (PV) conservation in the inflow, which leads to (Riehl, 1963):

$$C_d r v^2 = \text{cst} \tag{1}$$

with C_d, r and v drag coefficient, radius (*i.e* distance from TC center) and tangential velocity, respectively. Under hydrostatic and cyclostrophic balances, the heat source, expressed as the vertical gradient of atmospheric temperature, may be related to the gradient-level wind structure. While the accuracy of Eq. 1 in TCs remains to be substantiated, steady-state balance can still be temptingly assessed using surface wind estimates only.

The justification of an overall PV conservation was first facilitated by aircraft data (Riehl & Malkus, 1961; Riehl, 1963) and later by numerical modelling capacities (Ooyama, 1982; K. A. Emanuel, 1986). Observational and experimental research efforts then concentrated on a better characterization of the C_d parameter under high wind speed conditions (Powell et al., 2003; M. Donelan et al., 2004; Black et al., 2007; Jarosz et al., 2007; Bell et al., 2012; Soloviev et al., 2014; M. A. Donelan, 2018; Curcic & Haus, 2020) following Emanuel's steady-state theory (K. A. Emanuel, 1986, 1995). In such a context, Synthetic Aperture Radar (SAR) has emerged as a promising satellite technology capable of producing fine-scale, wide-swath TC boundary-layer process data in nearly all-weather conditions (A. A. Mouche et al., 2017; A. Mouche et al., 2019). SAR surface wind estimates provide an unprecedented opportunity to examine TCs radial wind structure (Combot et al., 2020; Avenas et al., 2023) and complete existing theories for steady IKE balance.

Following theoretical developments (Riehl, 1963; Charney & Eliassen, 1964; Kalashnik, 1994) and the use of an extended SAR database (178 cases), we demonstrate that an instantaneous surface wind structure observation provides information on the propensity of a TC to have a steady/unsteady IKE. A criterion of IKE steadiness is expressed in terms of wind structure parameters all measurable on high-resolution SAR data, and confronted to IKE variations estimates from best-track data. The relationship between the SAR-derived surface wind structure parameters and thermodynamic quantities that are most relevant to IKE balance is emphasized. Consequences of Eq. 1 on the drag coefficient are also examined through the lens of the SAR measurements. Our investigation suggests that systematic knowledge of the wind structure parameters, especially if they were included in TC vitals, would not only help the monitoring of TCs undergoing unsteady IKE transitions, but also improve future climatological IKE studies.

2 Preliminary SAR diagnostic

Spaceborne SAR allows for high spatial resolution estimates of TCs surface wind speeds (see Text S1 in Supporting Information). From the 178 SAR surface wind field estimates, Fig 1a displays that of TC Lane on August 23th, 2018, while Fig. 1b displays that of TC Meranti on September 12th, 2016. Both the outer-, near- and inner-core regions of TCs are well captured by SAR observations. The resulting axisymmetric profiles (green curves in Figs. 1c, d) show that both the axisymmetric maximum intensity (V_{max}) and radius of maximum wind (R_{max}) may be accurately retrieved (Combot et al., 2020). The system center can also be precisely located (Vinour et al., 2021), whose latitude provides the Coriolis parameter (f).

In this study the surface wind decay is shown to be critical for TCs IKE balance. It may be quantified in terms of an effective Holland B_s parameter (Holland, 1980), once

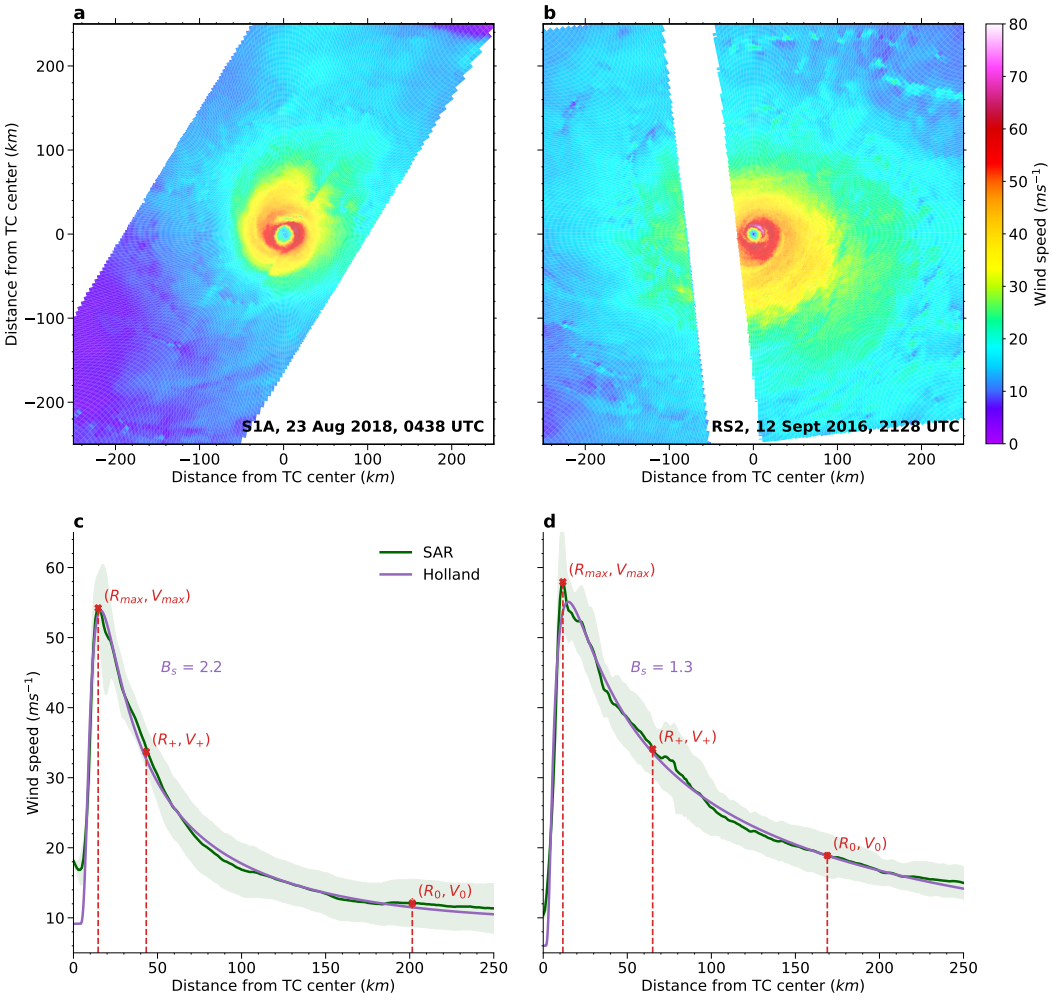

Figure 1. SAR wind speed estimates for (a) Lane and (b) Meranti. Corresponding axisymmetric wind profile (green) and adjusted Holland parametric wind profile (purple) for (c) Lane and (d) Meranti.

a Holland parametric wind profile is adjusted (purple curves in Figs. 1c, d) to the SAR axisymmetric wind profiles estimates (see Text S2 in Supporting Information).

According to best-track IKE time derivative estimates (see below and Text S3 in Supporting Information), at the time of their respective SAR acquisitions, Lane's IKE remained stable, while Meranti was experiencing an unsteady IKE transition. From the SAR axisymmetric wind profiles, these two TCs had similar TC vitals (*i.e* V_{max} and R_{max} values), but substantially different wind decay. Controlling both the momentum losses and the amplitude of vertical velocities at the top of the boundary layer, the surface wind decay is critical to TCs IKE balance, as will be shown below.

3 Deriving the criterion of IKE steadiness

3.1 Characteristic radii: definition and analysis

Assuming a constant air density, the steady-state balance between momentum sink and heat source writes (see Text S4 in Supporting Information):

$$\int_0^{R_0} \left[C_d r v^3 \right]_{z=0} dr = U_c^2 \left[\frac{C_d r v^2}{\omega_z + f} \right]_{z=0,\ r=R_+} \tag{2}$$

with $\omega_z = \frac{1}{r}\frac{\partial}{\partial r}(rv)$ the vertical component of relative vorticity and U_c a constant which depends on the thermodynamics of the system. Note, $z = 0$ refers to the top of the boundary layer. R_+ and R_0 are two radii characteristic of the IKE balance. The former defines the region of significant upward motions, while the latter defines the integration volume. The amplitude of vertical motions at the top of the boundary layer due to Ekman pumping are expressed by

$$w_E(r) = \frac{1}{r}\frac{d}{dr}\left(\frac{C_d r v^2}{\omega_z + f} \right) \tag{3}$$

Considering a slow numerator variation $C_d r v^2 \approx \text{cst}$, ω_z decreases with r, and w_E becomes close to zero for radii where ω_z is of the same order of the Coriolis parameter f. Conversely, significant upward motions occur in a region where ω_z is at least a few times higher than f. Thus, R_+ may be defined as

$$\omega_z(R_+) = 5f \tag{4}$$

With this definition, the characteristic radius (R_+) and the corresponding surface wind speed (V_+) can be directly estimated using a SAR axisymmetric wind profile (Figs. 1c, d).

Specifying the integration volume, R_0 is introduced as a natural characteristic radius because of the assumption of absolute angular momentum conservation in the outflow layer (Riehl & Malkus, 1961). Accordingly, if R_0 is defined as the radius where the outflow velocity vanishes, it is directly related to $Ro_{max} := \frac{V_{max}}{f R_{max}}$, the Rossby number evaluated at R_{max} via

$$\sqrt{2Ro_{max}} = \frac{R_0}{R_{max}} \tag{5}$$

This radius (R_0) and the corresponding surface wind speed (V_0) can thus be directly estimated from the SAR surface wind speeds (Figs. 1c, d).

The two characteristic radii R_0 and R_+ are controlled by the wind structure parameters Ro_{max} and B_s (see Text S5 in Supporting Information). Hence, in what follows we propose to reduce the steady-state balance (*e.g* Eq. 2) to a relationship involving these structural (B_s and Ro_{max}), in addition to a thermodynamical (U_c) parameter.

3.2 Criterion of IKE steadiness

Equation 2 involves quantities from the inflow layer, so that recalling the argument of PV conservation (Eq. 1), it is tempting to divide each side of Eq. 2 by $C_d r v^2$. Equivalently, this corresponds to consider a constant drag coefficient C_d and a relation of the kind $rv^2 \approx$ cst, consistent with the view of K. A. Emanuel (1986) for typical air-sea temperature differences.

Figure 2 shows how the normalized ratio $\pi := \frac{rv^2}{R_+ V_+^2}$ varies as a function of the normalized radius $r_* := \frac{r}{R_+}$ for all the wind profiles of the SAR database. On average (solid black curve), the normalized ratio varies slowly with radius, confirming the approximation $rv^2 =$ cst. Note that these slow radial variations reach a maximum at $r = R_+$. While Eq. 4 has been quite arbitrarily, yet reasonably, defined, R_+ appears to correspond to the radius that maximizes, on average, the integrand of the IKE over the SAR database. This local maximum provides information on the radius and area where a TC is the most efficient, *i.e* where heating is maximum and momentum sink is minimum. This *a posteriori* justifies our definition for R_+.

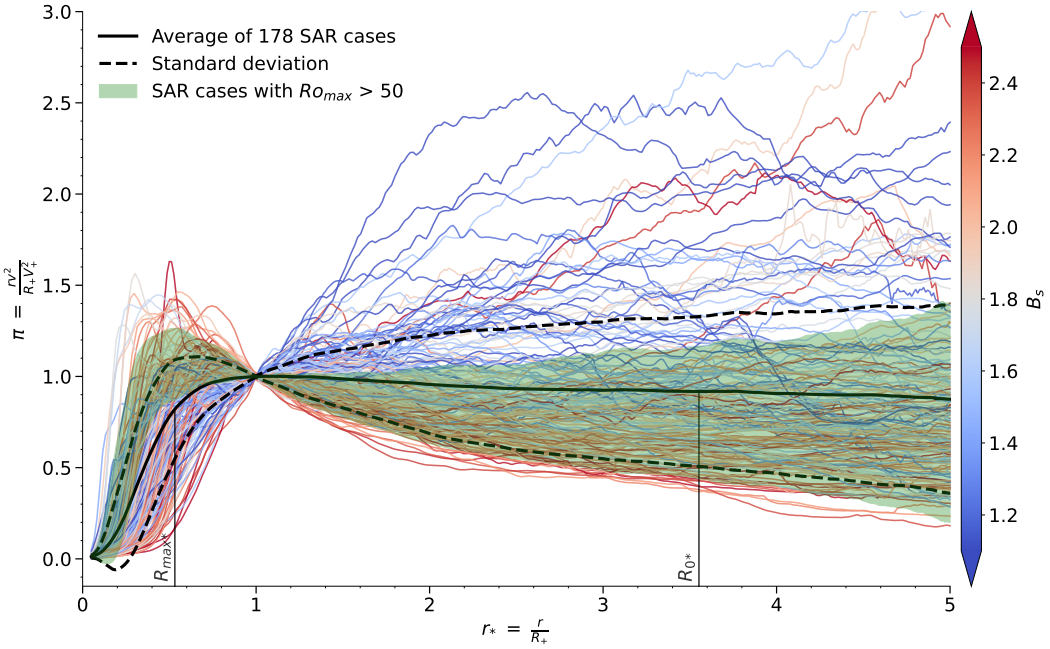

Figure 2. SAR-derived π profiles colored by adjusted Holland B_s parameter (blue to red) and average π profile (black) estimated from the SAR database. Shaded green area denotes the standard deviation interval inside which SAR cases satisfy $Ro_{max} > 50$.

For single cases, variations of this normalized ratio π with radius mostly stress the variations in B_s and Ro_{max}. Deviations from the average $\pi \approx 1$ have opposite signs at R_{max} and R_0. For instance, high B_s and Ro_{max} values (red profiles covered by the shaded green area) result in $\pi(R_{max}) > 1$ and $\pi(R_0) < 1$, suggesting that errors in-

side R_+ compensate those outside R_+ when considering $rv^2 \approx$ cst and simplifying the integral in Eq. 2.

Following these results, Eq. 2 can be rewritten as

$$\int_0^{R_0} v(z=0)\, dr = \frac{U_c^2}{6f} \tag{6}$$

Now, the aim is to further express Eq. 6 in terms of parameters that can be estimated from SAR data, *i.e* V_{max}, B_s and Ro_{max}. Here and after it is assumed that the SAR surface wind speed estimates and the corresponding parameters are close to their boundary layer top counterparts. We also recall that, lacking reliable high resolution ocean surface wind vectors data, these parameters were computed using the total wind speed (as provided by SAR) rather than its tangential component. The integral in Eq. 6 is approximated as

$$\int_0^{R_0} v(z=0)\, dr \approx \frac{V_{max} R_0}{2\sqrt{B_s}} \tag{7}$$

leading to

$$\frac{V_{max} R_0}{\sqrt{B_s}} \approx \frac{U_c^2}{3f} \tag{8}$$

With use of Eq. 5, a TC with steady-state conditions should then obey the following rule:

$$V_{max}^2 = \frac{U_c^2}{3\sqrt{2}} \sqrt{B_s Ro_{max}} \tag{9}$$

which expresses the TC IKE balance. The criterion of IKE steadiness now reduces to structural parameters (B_s and Ro_{max}) that we can estimate from SAR data. Before testing this criterion over the entire SAR database, the degree of IKE steadiness must be estimated.

4 Assessment of the criterion of IKE steadiness

4.1 Best-track estimates of IKE variations

Equation 9 assumes that the TC is in steady-state, *i.e* that the partial time derivative of azimuthal wind speed and potential temperature can be neglected at each radii. The current spatio-temporal sampling of TC surface observations, including SAR measurements, prevents a direct estimation of the time evolution of these quantities. Yet, neglecting time variations in the potential energy equation, a TC departs from the steady-state assumptions when the absolute temporal variation of IKE is large. Temporal evolution of IKE is given by:

$$\frac{\partial \mathrm{IKE}}{\partial t} = \frac{\partial}{\partial t} \left(\int_0^H \int_0^{R_0} \bar{\rho_0} r v^2 \, dr \, dz \right) \tag{10}$$

Building on our observational knowledge on the π ratio, (Fig. 2), the double integral in Eq. 10 can be simplified by considering the constant rv^2 at a fixed relevant radius. To evaluate $\frac{\partial IKE}{\partial t}$, we would then need partial time derivative estimates of v and

r at this fixed radius. Because of the limited temporal sampling of SAR data, temporal evolutions of these parameters must be evaluated using best-track (Knapp et al., 2010) reanalyses. However, while V_{max} best-track uncertainty is rather low (Torn & Snyder, 2012; Landsea & Franklin, 2013), R_{max} best-track estimates have been shown to be often inconsistent with SAR R_{max} estimates (Combot et al., 2020). Indeed, R_{max} is not systematically reanalyzed (unlike V_{max}). From best-track data, the most reliable size parameter is the radius of gale R_{34}, *i.e* the maximum radial extent of the 34-knots winds (Knaff et al., 2021). Thus, we use the following approximation:

$$\frac{\partial \mathrm{IKE}}{\partial t} \approx \frac{\partial}{\partial t}\left(\int_0^H \bar{\rho_0} R_{34}^2 V_{34}^2 \, dz\right) \tag{11}$$

where V_{34} is the azimuthal surface wind speed at $r = R_{34}$. Limited by observational capabilities, the dependence of R_{34} in z is unknown. The integral on the vertical component is thus simplified by a multiplication by H. Because PV is small in TCs, it can be assumed that surfaces of constant potential temperature and absolute angular momentum coincide, so that in steady-state H scales as (Shutts, 1981)

$$H = \frac{V_{max}^2}{g\frac{\Delta\theta}{\theta_0}} \tag{12}$$

where g is standard gravity and $\Delta\theta$ the difference between the potential temperature at the vortex center and its environmental value noted θ_0. Finally, Eq. 11 writes

$$\frac{\partial \mathrm{IKE}}{\partial t} = \frac{\bar{\rho_0} V_{34}^2}{g\frac{\Delta\theta}{\theta_0}} \frac{\partial}{\partial t}\left(V_{max}^2(t) R_{34}^2(t)\right) \tag{13}$$

where $\bar{\rho_0} \approx 1.15 kg.m^{-3}$ and $\frac{\Delta\theta}{\theta_0} \approx 10^{-2}$ are assumed constant in time. Now we may assess how consistent is the criterion of IKE steadiness (Eq. 9) with observational data.

4.2 Assessment of the criterion of IKE steadiness in the SAR database

In Eq. 9, we can assume that U_c does not vary too much across different TCs, especially for the present analysis which was restrained to tropical and sub-tropical latitudes (see methods). Figure 3 then shows the SAR observations in a (V_{max}^2, $\sqrt{B_s Ro_{max}}$) log-linear plane. The corresponding values of absolute partial time derivative of IKE (Eq. 13) evaluated using best-track data are also represented (colors). Cases with the lowest third absolute IKE time derivative estimates (black stars) roughly satisfy the relation of proportionality suggested by Eq. 9, with a variance probably due to both observational errors and variations in the characteristic velocity U_c. This expected relation of proportionality may be modelled by a linear function and fitted to the cases with the lowest absolute IKE time derivatives using a least-squares regression (dashed black curve). Remarkably, cases with higher absolute IKE time derivative estimates (red stars) are distributed apart from this linear model. Furthermore, the distance between a single case and the regression curve seems to increase with the absolute IKE time derivative value. Providing this distance, an instantaneous SAR observation thus provides information on the propensity for a given TC to have a steady/unsteady IKE.

For TC Lane, well captured by a SAR observation (Figs. 1a, c), the relation of proportionality Eq. 9 (Fig. 3) is seemingly closely achieved. Accordingly, Lane's temporal variation of IKE is small (∼-0.7 $PJhr^{-1}$), corresponding to small temporal variations of V_{max} and R_{34} in best-track data. TC Meranti (Figs. 1b, d) however departs from the

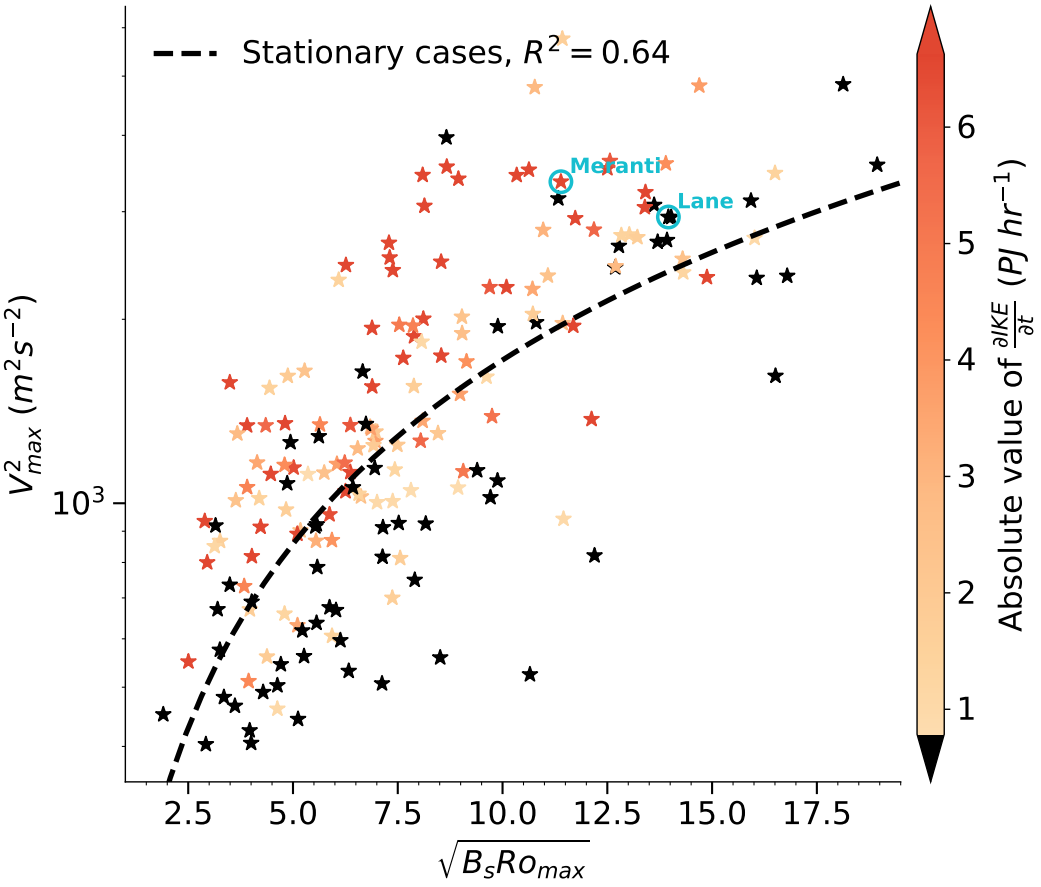

Figure 3. Wind structure parameters estimated from SAR observations (stars) in the plane suggested by Eq. 9 (y-axis is in logarithmic scale), and colored by absolute value of $\frac{\partial \text{IKE}}{\partial t}$. Dashed line denotes best-fit linear regression to cases with the lowest third absolute IKE time derivative estimates (black stars) using a fixed zero intercept.

relation of proportionality Eq. 9 (Fig. 3). For this case, the high (positive) temporal variation of IKE ($\sim$24.3 $PJhr^{-1}$) is mostly explained by a high temporal variation of R_{34} ($\sim$4.4 $kmhr^{-1}$) due to an eyewall replacement cycle, while V_{max} stayed relatively stable ($\sim$0.3 $ms^{-1}hr^{-1}$).

The velocity U_c characterizes the steady IKE balance in Eq. 9. Using known values of thermodynamic constants and assuming that heating occurs in the lowest layers of the TC, we find that $U_c \sim 32$ m/s from its definition (see Text S4 in Supporting Information). Based on the steady IKE linear regression slope (black dashed curve in Fig. 3), the SAR observations lead to $U_c \sim 27$ m/s, which is close to the theoretical value. We remind readers that this characteristic velocity is that of an average situation. In nature, U_c certainly varies from one TC to another.

5 Concluding remarks

Based on existing steady-state theories describing axisymmetric TCs and a PV conservation argument in the inflow, an analytical criterion to characterize TCs IKE steadiness was reduced to parameters measurable on high-resolution surface data. Two characteristic scales, suggested by the theory, appear of the greatest importance: the radius where surface vertical motions become significant, R_+, and the radius where the outflow velocity vanishes, R_0. Highlighted by high-resolution SAR data, a coincident knowledge of these two characteristic scales provides information on whether a TC is undergoing high IKE variations or not. Thus, SAR acquisitions may assist in monitoring steady/unsteady IKE transitions, especially with the increasing number of spaceborne SAR sensors (*e.g* the recently launched Radarsat Constellation Mission).

In Riehl (1963) conceptual framework, the momentum losses are characterized by an assumption of PV conservation close to the surface. Equation 1 was thus considered in the inflow layer and C_d further assumed constant. The SAR database analysis reveals that the distribution of the regions where this assumption is valid depends on the Rossby number Ro_{max}. Indeed, in Fig. 2, SAR cases with $Ro_{max} < 50$ (curves outside the green shaded area) have a π ratio that increases with r, so that if Eq. 1 was valid, C_d would decrease with r and thus increase with v, in agreement with the reported literature (Powell et al., 2003; M. Donelan et al., 2004) for wind speeds below hurricane force winds ($\sim$33 m/s). At higher Rossby numbers $Ro_{max} > 50$ (curves inside the green shaded area), the decrease of π with r between R_+ and R_{max} suggests that C_d decreases/saturates. For such TCs, hurricane force winds are largely exceeded in this area and the suggested decrease/saturation of C_d agrees with reported estimates under hurricane conditions (Powell et al., 2003; M. Donelan et al., 2004; Black et al., 2007; Jarosz et al., 2007; Bell et al., 2012; Soloviev et al., 2014; M. A. Donelan, 2018; Curcic & Haus, 2020). At radii greater than R_+, the assumption expressed by Eq. 1 certainly breaks down because the π ratio decreases with r. A relation of relative angular momentum conservation $rv \approx$ cst is approached, so that friction is presumably small in this region. As a result, vertical velocities at the top of the boundary layer are close to zero, because both $C_d r v^2$ and ω_z are small in Eq. 3. Further understanding how R_+, or more generally the wind decay, is related to C_d increase/decrease with wind speed is beyond the scope of this study, but SAR observations may be instrumental to help better determining the spatial distribution of C_d.

Our analysis demonstrates that a SAR observation provides an indirect estimate of the characteristic velocity U_c associated with the system's thermodynamics. Strongly influencing the steady IKE balance (Eq. 9), this characteristic velocity depends on both oceanic and atmospheric parameters. As a consequence, our understanding of both the basin- and the climate-dependence of U_c should benefit from the accumulation of SAR measurements and the corresponding U_c estimates. In turn, it may be assessed whether more unsteady IKE transitions are expected in a given ocean basin or climate scenario. Lastly, in the absence of SAR, the developed theory suggests that the knowledge of V_{max},

R_0 and R_+ should be sufficient to estimate the TC characteristic velocity U_c or assess the IKE balance. Presently, while V_{max} may be one of the most reliable parameters in the TC vitals, accurate estimates of R_+ or R_0 are not systematically available. Consistently including reliable estimates of such parameters in operational and historical records would allow, in combination with theory, to better anticipate short- and long-term changes in TCs destructive potential.

Open Research

Datasets for this research are freely available online at `https://cyclobs.ifremer.fr/app/tropical` using the steps described at `https://cyclobs.ifremer.fr/app/docs/`.

Acknowledgments

This work was financially supported by the ERC Synergy project 856408-STUOD. The SAR database was obtained from IFREMER/CyclObs and produced with the SAR wind processor co-developed by IFREMER and CLS. J. Knaff thanks NOAA/Center for Satellite Applications and Research for providing the time work on this subject. The views, opinions, and findings contained in this report are those of the authors and should not be construed as an official National Oceanic and Atmospheric Administration or U.S. government position, policy, or decision.

References

Anthes, R. A. (1974). The dynamics and energetics of mature tropical cyclones. *Reviews of Geophysics*, *12*(3), 495–522.

Avenas, A., Mouche, A., Tandeo, P., Piolle, J.-F., Chavas, D., Fablet, R., ... Chapron, B. (2023). Reexamining the estimation of tropical cyclones radius of maximum wind from outer size with an extensive synthetic aperture radar dataset. *Monthly Weather Review*.

Bell, M. M., Montgomery, M. T., & Emanuel, K. A. (2012). Air–sea enthalpy and momentum exchange at major hurricane wind speeds observed during cblast. *Journal of the Atmospheric Sciences*, *69*(11), 3197–3222.

Black, P. G., D'Asaro, E. A., Drennan, W. M., French, J. R., Niiler, P. P., Sanford, T. B., ... Zhang, J. A. (2007). Air–sea exchange in hurricanes: Synthesis of observations from the coupled boundary layer air–sea transfer experiment. *Bulletin of the American Meteorological Society*, *88*(3), 357–374.

Charney, J. G., & Eliassen, A. (1964). On the growth of the hurricane depression. *Journal of Atmospheric Sciences*, *21*(1), 68–75.

Chavas, D. R., & Emanuel, K. A. (2010). A quikscat climatology of tropical cyclone size. *Geophysical Research Letters*, *37*(18).

Chavas, D. R., Lin, N., Dong, W., & Lin, Y. (2016). Observed tropical cyclone size revisited. *Journal of Climate*, *29*(8), 2923–2939.

Combot, C., Mouche, A., Knaff, J., Zhao, Y., Zhao, Y., Vinour, L., ... Chapron, B. (2020). Extensive high-resolution synthetic aperture radar (sar) data analysis of tropical cyclones: Comparisons with sfmr flights and best track. *Monthly Weather Review*, *148*(11), 4545–4563.

Curcic, M., & Haus, B. K. (2020). Revised estimates of ocean surface drag in strong winds. *Geophysical research letters*, *47*(10), e2020GL087647.

Done, J. M., Lackmann, G. M., & Prein, A. F. (2022). The response of tropical cyclone intensity to changes in environmental temperature. *Weather and Climate Dynamics*, *3*(2), 693–711.

Donelan, M., Haus, B. K., Reul, N., Plant, W., Stiassnie, M., Graber, H., ... Saltzman, E. (2004). On the limiting aerodynamic roughness of the ocean in very

strong winds. *Geophysical Research Letters*, *31*(18).

Donelan, M. A. (2018). On the decrease of the oceanic drag coefficient in high winds. *Journal of Geophysical Research: Oceans*, *123*(2), 1485–1501.

Emanuel, K. (2005). Increasing destructiveness of tropical cyclones over the past 30 years. *Nature*, *436*(7051), 686–688.

Emanuel, K. (2007). Environmental factors affecting tropical cyclone power dissipation. *Journal of Climate*, *20*(22), 5497–5509.

Emanuel, K. (2021). Atlantic tropical cyclones downscaled from climate reanalyses show increasing activity over past 150 years. *Nature communications*, *12*(1), 7027.

Emanuel, K. A. (1986). An air-sea interaction theory for tropical cyclones. part i: Steady-state maintenance. *Journal of Atmospheric Sciences*, *43*(6), 585–605.

Emanuel, K. A. (1995). Sensitivity of tropical cyclones to surface exchange coefficients and a revised steady-state model incorporating eye dynamics. *Journal of Atmospheric Sciences*, *52*(22), 3969–3976.

Gilford, D. M., Solomon, S., & Emanuel, K. A. (2017). On the seasonal cycles of tropical cyclone potential intensity. *Journal of Climate*, *30*(16), 6085–6096.

Golitsyn, G. (2008). Polar lows and tropical hurricanes: Their energy and sizes and a quantitative criterion for their generation. *Izvestiya, Atmospheric and Oceanic Physics*, *44*, 537–547.

Holland, G. J. (1980). An analytic model of the wind and pressure profiles in hurricanes. *Monthly Weather Review*, *108*, 1212–1218.

Jarosz, E., Mitchell, D. A., Wang, D. W., & Teague, W. J. (2007). Bottom-up determination of air-sea momentum exchange under a major tropical cyclone. *Science*, *315*(5819), 1707–1709.

Kalashnik, M. (1994). On the maximum wind velocity in the tropical cyclone. *Izvestiâ Akademii nauk SSSR. Fizika atmosfery i okeana*, *30*(1), 26–30.

Knaff, J. A., Longmore, S. P., & Molenar, D. A. (2014). An objective satellite-based tropical cyclone size climatology. *Journal of Climate*, *27*(1), 455–476.

Knaff, J. A., Sampson, C. R., Kucas, M. E., Slocum, C. J., Brennan, M. J., Meissner, T., ... others (2021). Estimating tropical cyclone surface winds: Current status, emerging technologies, historical evolution, and a look to the future. *Tropical Cyclone Research and Review*, *10*(3), 125–150.

Knapp, K. R., Kruk, M. C., Levinson, D. H., Diamond, H. J., & Neumann, C. J. (2010). The international best track archive for climate stewardship (ibtracs) unifying tropical cyclone data. *Bulletin of the American Meteorological Society*, *91*(3), 363–376.

Kossin, J. P. (2017). Hurricane intensification along united states coast suppressed during active hurricane periods. *Nature*, *541*(7637), 390–393.

Kossin, J. P., Knapp, K. R., Olander, T. L., & Velden, C. S. (2020). Global increase in major tropical cyclone exceedance probability over the past four decades. *Proceedings of the National Academy of Sciences*, *117*(22), 11975–11980.

Kreussler, P., Caron, L.-P., Wild, S., Loosveldt Tomas, S., Chauvin, F., Moine, M.-P., ... others (2021). Tropical cyclone integrated kinetic energy in an ensemble of highresmip simulations. *Geophysical research letters*, *48*(5), e2020GL090963.

Landsea, C. W., & Franklin, J. L. (2013). Atlantic hurricane database uncertainty and presentation of a new database format. *Monthly Weather Review*, *141*(10), 3576–3592.

Lin, Y., Zhao, M., & Zhang, M. (2015). Tropical cyclone rainfall area controlled by relative sea surface temperature. *Nature Communications*, *6*(1), 6591.

Misra, V., DiNapoli, S., & Powell, M. (2013). The track integrated kinetic energy of atlantic tropical cyclones. *Monthly Weather Review*, *141*(7), 2383–2389.

Morris, M., & Ruf, C. S. (2017). Estimating tropical cyclone integrated kinetic energy with the cygnss satellite constellation. *Journal of Applied Meteorology and*

Climatology, *56*(1), 235–245.

Mouche, A., Chapron, B., Knaff, J., Zhao, Y., Zhang, B., & Combot, C. (2019). Copolarized and cross-polarized sar measurements for high-resolution description of major hurricane wind structures: Application to irma category 5 hurricane. *Journal of Geophysical Research: Oceans*, *124*(6), 3905–3922.

Mouche, A. A., Chapron, B., Zhang, B., & Husson, R. (2017). Combined co-and cross-polarized sar measurements under extreme wind conditions. *IEEE Transactions on Geoscience and Remote Sensing*, *55*(12), 6746–6755.

Ooyama, K. V. (1982). Conceptual evolution of the theory and modeling of the tropical cyclone. *Journal of the Meteorological Society of Japan. Ser. II*, *60*(1), 369–380.

Patricola, C. M., & Wehner, M. F. (2018). Anthropogenic influences on major tropical cyclone events. *Nature*, *563*(7731), 339–346.

Pearce, R. P. (2004). An axisymmetric model of a mature tropical cyclone incorporating azimuthal vorticity. *Quarterly Journal of the Royal Meteorological Society*, *130*(596), 259–293.

Powell, M. D., & Reinhold, T. A. (2007). Tropical cyclone destructive potential by integrated kinetic energy. *Bulletin of the American Meteorological Society*, *88*(4), 513–526.

Powell, M. D., Vickery, P. J., & Reinhold, T. A. (2003). Reduced drag coefficient for high wind speeds in tropical cyclones. *Nature*, *422*(6929), 279–283.

Riehl, H. (1963). Some relations between wind and thermal structure of steady state hurricanes. *Journal of Atmospheric Sciences*, *20*(4), 276–287.

Riehl, H., & Malkus, J. (1961). Some aspects of hurricane daisy, 1958. *Tellus*, *13*(2), 181–213.

Shutts, G. (1981). Hurricane structure and the zero potential vorticity approximation. *Monthly Weather Review*, *109*(2), 324–329.

Sobel, A. H., Camargo, S. J., Hall, T. M., Lee, C.-Y., Tippett, M. K., & Wing, A. A. (2016). Human influence on tropical cyclone intensity. *Science*, *353*(6296), 242–246.

Soloviev, A. V., Lukas, R., Donelan, M. A., Haus, B. K., & Ginis, I. (2014). The air-sea interface and surface stress under tropical cyclones. *Scientific reports*, *4*(1), 5306.

Strazzo, S., Elsner, J. B., & LaRow, T. (2015). Quantifying the sensitivity of maximum, limiting, and potential tropical cyclone intensity to sst: Observations versus the fsu/coaps global climate model. *Journal of Advances in Modeling Earth Systems*, *7*(2), 586–599.

Torn, R. D., & Snyder, C. (2012). Uncertainty of tropical cyclone best-track information. *Weather and Forecasting*, *27*(3), 715–729.

Vinour, L., Jullien, S., Mouche, A., Combot, C., & Mangeas, M. (2021). Observations of tropical cyclone inner-core fine-scale structure, and its link to intensity variations. *Journal of the Atmospheric Sciences*, *78*(11), 3651–3671.

Wang, S., & Toumi, R. (2021). Recent tropical cyclone changes inferred from ocean surface temperature cold wakes. *Scientific Reports*, *11*(1), 22269.

Webster, P. J., Holland, G. J., Curry, J. A., & Chang, H.-R. (2005). Changes in tropical cyclone number, duration, and intensity in a warming environment. *Science*, *309*(5742), 1844–1846.

Wing, A. A., Emanuel, K., & Solomon, S. (2015). On the factors affecting trends and variability in tropical cyclone potential intensity. *Geophysical Research Letters*, *42*(20), 8669–8677.

Supporting Information for "On the steadiness of the tropical cyclone integrated kinetic energy"

A. Avenas[1], A. Mouche[1], J. Knaff[2], X. Carton[1], B. Chapron[1]

[1]Ifremer, Univ. Brest, CNRS, IRD, Laboratoire d'Océanographie Physique et Spatiale (LOPS), IUEM, F-29280, Plouzané, France

[2]NOAA/NESDIS Regional and Mesoscale Meteorological Branch, Fort Collins, Colorado

Contents of this file

1. Texts S1 to S5
2. Figures S1 to S2

Text S1: SAR observations

High spatial resolution observations of the ocean surface are obtained with spaceborne SAR. The SAR instrument operates at 5.4 GHz (C-band) and receives the signal back-scattered by the ocean surface in both co- and cross-polarization. This allows to estimate ocean surface wind speeds under TC conditions, including at very high wind speeds and in the near-core region (A. A. Mouche et al., 2017; A. Mouche et al., 2019; Combot et al., 2020).

Because SAR wide-swath acquisitions cannot be continuously performed over oceans, they have to be triggered based on track forecasts to anticipate when the sensor will

overpass a TC. Since 2016, more than ∼500 acquisitions over TCs from ESA Sentinel-1A and Sentinel-1B and Canadian Space Agency Radarsat-2 missions were gathered as part of the Satellite Hurricane Observation Campaign (SHOC).

The wind product derived by A. A. Mouche et al. (2017) has a 3 km spatial resolution with a 1 km grid spacing and is interpolated on a regular polar grid based on the TC center (see appendix in Vinour, Jullien, Mouche, Combot, and Mangeas (2021)). For each SAR case, a wind profile is then obtained by averaging the wind estimates on all azimuths. Typical standard deviations of wind speed along the azimuthal direction are displayed in Figs. 1c, d from the main text (green shaded areas). In addition, a certain number of SAR cases have been discarded on a qualitative basis, *e.g* when the detected TC center was judged to be wrong, or when the SAR file contained corrupted pixel values.

To restrain the analysis to well-formed systems, after estimating the SAR parameters (see below), we select only SAR cases for which $V_{max} > 20$ m/s, $R_{max} < 150$ km, and absolute latitude $< 30°$. Based on best-track data, we also ensure that, for each SAR case, the distance to closest land from TC center is greater than SAR-derived R_{34} estimate.

Text S2: Parameters estimation

In order to reduce the problem dimension, scalar parameters characterizing the TC axisymmetric wind profiles are computed based on the high spatial resolution SAR total wind estimates. These include the maximum intensity amplitude (V_{max}) and location (R_{max}), the Coriolis parameter (f) based on the TC center latitude, the radius of significant upward motions (R_+) defined by Eq. 4 from the main text and the corresponding wind speed (V_+). The radius of zero outflow velocity (R_0) is then derived based on (V_{max},

R_{max}, f) and the corresponding wind speed (V_0) is further computed on the SAR axisymmetric wind profile.

To quantify the surface wind decay, a Holland wind parametric profile and the corresponding B parameter are used (Holland, 1980). Based on gradient wind balance, Holland parametric wind profile is not necessarily suited for surface wind profiles with nonzero wind speeds at the TC center, well captured using SAR observations. A complementary degree of freedom is thus added to minimize the impact of these nonzero wind speeds on the resulting B values. For each SAR wind profile, a modified Holland parametric profile

$$V_{Holland}(r) = V_{min} + \sqrt{(V_{max} - V_{min})^2 (\frac{R_{max}}{r})^{B_s} e^{1-(\frac{R_{max}}{r})^{B_s}} + (\frac{rf}{2})^2} - \frac{rf}{2} \qquad (1)$$

is adjusted to each SAR azimuthally-averaged wind profile using the full extent of the wind profile and estimating solutions for V_{min}, V_{max}, R_{max} and B_s via least squares, while f was fixed by the TC center estimated on the SAR acquisition. The modified Holland parameter B_s is used to quantify the surface wind decay for each SAR azimuthally-averaged wind profile.

Lastly, note that to estimate R_+, an estimate of ω_z is first needed, which requires to compute a radial derivative. Radial derivatives are difficult to estimate directly on SAR observations because of local jumps in the wind speed estimates implied by high spatial resolution, even though a substantial part of this noise has been smoothed by azimuthally-averaging. Thus, the adjusted parametric profiles are used to estimate ω_z, and then R_+ using Eq. 4 from the main text.

Text S3: Best-track data

Time derivatives of TCs intensity ($\frac{\partial V_{max}}{\partial t}$) and outer-size ($\frac{\partial R_{34}}{\partial t}$) are obtained from best-track data. Indeed, direct estimates of these quantities on SAR data only is currently prevented by the limited spatio-temporal sampling of the SAR instruments.

Both $\frac{\partial V_{max}}{\partial t}$ and $\frac{\partial R_{34}}{\partial t}$ are computed from best-track by first averaging V_{max} and R_{34} time series using a four-hour moving window to smooth out noisy values and then computing second order accurate central differences. Then, these two parameters, along with the distance to closest land, are linearly interpolated to each SAR acquisition time.

Lastly, because of varying definitions of the maximum sustained wind speed across the different agencies, we selected only USA agencies (*i.e* National Hurricane Center, Joint Typhoon Warning Center, and Central Pacific Hurricane Center) which all provide the 1-minute maximum sustained wind speed.

Text S4: Kinetic energy balance

Here, we derive Eq. 2 from the main text, starting with the primitive equations and following the developments of (Kalashnik, 1994). While air density may be assumed constant, we first treat the more general case of anelastic approximation, where air density is decomposed as $\rho =: \bar{\rho}(z) + \rho'$ with $\rho' \ll \bar{\rho}(z)$. Pressure then reduces to $P =: \bar{P}(z) + P'$ with $P' \ll \bar{P}(z)$ and potential temperature to $\theta =: \bar{\theta}(z) + \theta'$ with $\theta' \ll \bar{\theta}(z)$. Then, the equations of conservation of tangential momentum, gradient wind and hydrostatic balance, continuity, and conservation of energy reduce to

$$\frac{\partial v}{\partial t} + u\frac{\partial v}{\partial r} + w\frac{\partial v}{\partial z} + \frac{uv}{r} + fu = 0 \tag{2}$$

$$\frac{v^2}{r} + fv = \frac{\partial \Phi}{\partial r} \tag{3}$$

$$\frac{\partial \Phi}{\partial z} = g\tilde{\theta} \tag{4}$$

$$\frac{1}{r}\frac{\partial}{\partial r}(ru) + \frac{1}{\bar{\rho}}\frac{\partial}{\partial z}(\bar{\rho}w) = 0 \tag{5}$$

$$\frac{\partial \tilde{\theta}}{\partial t} + u\frac{\partial \tilde{\theta}}{\partial r} + w\frac{\partial \tilde{\theta}}{\partial z} + \Gamma w = \frac{Q}{C_p \bar{T}} \tag{6}$$

with u, v, and w the radial, azimuthal and vertical components of velocity, r, z the radial and vertical coordinates, t the time, Q the heat source and C_p the heat capacity. The notations are $\Phi := \frac{P'}{\bar{\rho}}$, $\tilde{\theta} := \frac{\theta'}{\bar{\theta}}$, $\Gamma := \frac{1}{\bar{\theta}}\frac{d\bar{\theta}}{dz}$.

The volume on which these equations are considered is defined by $0 \leq r \leq R_0$ and $0 \leq z \leq H$, where $z = 0$ corresponds to the top of the boundary layer. It is also assumed that $w(z = H) = 0$ at all radii and that $v(r = R_0) = 0$ at all levels. A schematic illustration of the TC system considered here along with the assumptions used in the present paper is given in Fig. S1.

Momentum sink

First, noting $K := \frac{V^2}{2}$, we multiply Eq. 2 by v and using Eq. 3:

$$\frac{\partial K}{\partial t} + u\frac{\partial K}{\partial r} + w\frac{\partial K}{\partial z} + u\frac{\partial \Phi}{\partial r} = 0 \tag{7}$$

After multiplication by $\bar{\rho}$, Eq. 7 is integrated on the volume $\langle(.)\rangle := \int_0^H \int_0^{R_0} (.) r\, dr\, dz$. The first term of the integrated equation is rewritten as $\frac{\partial}{\partial t}\langle \bar{\rho} K \rangle$.

Before integrating the other terms, we notice that for any variable χ integration by parts and continuity equation yields:

$$\int_0^{R_0} \bar{\rho} r u \frac{\partial \chi}{\partial r}\, dr = \Big[\bar{\rho} r u \chi\Big]_0^{R_0} - \int_0^{R_0} \chi \frac{\partial (\bar{\rho} r u)}{\partial r}\, dr = \int_0^{R_0} \chi \frac{\partial}{\partial z}(\bar{\rho} r w)\, dr \tag{8}$$

With this result, the second and third terms of Eq. 7 become, after integration

$$\begin{aligned} \int_0^H \int_0^{R_0} \left(\bar{\rho} r u \frac{\partial K}{\partial r} + \bar{\rho} r w \frac{\partial K}{\partial z}\right) dr\, dz &= \int_0^H \int_0^{R_0} \left(K \frac{\partial}{\partial z}(\bar{\rho} r w) + \bar{\rho} r w \frac{\partial K}{\partial z}\right) dr\, dz \\ &= \int_0^{R_0} \Big[\bar{\rho} r w K\Big]_{z=0} dr \end{aligned} \tag{9}$$

where we used Eq. 8 and $w(z = H) = 0$. Finally, the last integrated term of Eq. 7 is

$$\int_0^H \int_0^{R_0} \bar{\rho} r u \frac{\partial \Phi}{\partial r}\, dr\, dz = \int_0^H \int_0^{R_0} \Phi \frac{\partial}{\partial z}(\bar{\rho} r w)\, dr\, dz \tag{10}$$

By permuting the integrals, integrating by parts, and using $w(z = H) = 0$, we further rearrange:

$$\int_0^H \int_0^{R_0} \Phi \frac{\partial}{\partial z}(\bar{\rho} r w)\, dr\, dz = \int_0^{R_0} \Big[\bar{\rho} r w \Phi\Big]_{z=0} dr - \int_0^H \int_0^{R_0} \bar{\rho} r w \frac{\partial \Phi}{\partial z}\, dr\, dz \tag{11}$$

where, because of Eq. 4, the last term is simply $g\langle \bar{\rho} w \tilde{\theta} \rangle$.

Using eqs. 9, 11, the integration of Eq. 7 finally yields:

$$\frac{\partial}{\partial t}\langle \bar{\rho} K \rangle - \int_0^{R_0} \Big[\bar{\rho} r w (K + \Phi)\Big]_{z=0} dr = g\langle \bar{\rho} w \tilde{\theta} \rangle \tag{12}$$

Using the expression for the Ekman vertical velocity (Eq. 3 from the main text) the second term of Eq. 12 can be written

$$\int_0^{R_0} \left[\bar{\rho} r w (K+\Phi)\right]_{z=0} dr = \int_0^{R_0} \left[\bar{\rho} \frac{d}{dr}\left(\frac{C_d r v^2}{\omega_z + f}\right)(K+\Phi)\right]_{z=0} dr \tag{13}$$

Before rearranging this term further, we first notice that gradient wind balance (Eq. 3) implies that

$$\frac{\partial}{\partial r}(K+\Phi) = v(\omega_z + f) \tag{14}$$

Integrating Eq. 13 by parts to use Eq. 14, then substituting for this expression in Eq. 12 yields

$$\frac{\partial}{\partial t}\langle \bar{\rho} K \rangle + \int_0^{R_0} \left[\bar{\rho} C_d r v^3\right]_{z=0} dr = g \langle \bar{\rho} w \tilde{\theta} \rangle \tag{15}$$

Heat source

Now, Eq. 6 is integrated on the volume $\langle\langle(.)\rangle\rangle := \int_0^H \int_0^z \int_0^{R_0} (.) r \, dr \, dz \, dz$, after multiplication by $\bar{\rho}$. The first term of the equation becomes $\frac{\partial}{\partial t}\langle\langle \bar{\rho}\tilde{\theta}\rangle\rangle$.

When summing the second and third terms of the integrated equation, we obtain:

$$\begin{aligned}
\int_0^H \int_0^z \int_0^{R_0} \left(\bar{\rho} r u \frac{\partial \tilde{\theta}}{\partial r} + \bar{\rho} r w \frac{\partial \tilde{\theta}}{\partial z}\right) dr \, dz \, dz &= \int_0^H \int_0^z \int_0^{R_0} \left(\tilde{\theta}\frac{\partial}{\partial z}(\bar{\rho} r w) + \bar{\rho} r w \frac{\partial \tilde{\theta}}{\partial z}\right) dr \, dz \, dz \\
&= \int_0^H \int_0^{R_0} \left[\bar{\rho} r w \tilde{\theta}\right]_0^z dr \, dz \\
&= \langle \bar{\rho} w \tilde{\theta} \rangle - H \int_0^{R_0} \left[\bar{\rho} r w \tilde{\theta}\right]_{z=0} dr
\end{aligned} \tag{16}$$

where we used Eq. 8. Next, the stratification term is integrated as

$$\int_0^H \int_0^z \int_0^{R_0} \bar{\rho} r w \Gamma \, dr \, dz \, dz = \int_0^z \int_0^{R_0} \left(\left[\bar{\rho} r w ln(\bar{\theta}) \right]_0^H - \int_0^H \frac{\partial}{\partial z} \left(\bar{\rho} r w \right) ln(\bar{\theta}) \, dz \right) dr \, dz$$
$$= 0 \tag{17}$$

where, in the first raw, the first term is zero at $z = H$ because $w(z = H) = 0$ and zero at $z = 0$ because $\int_0^{R_0} r w_E \, dr = 0$, while the second term is zero by applying the continuity equation and recalling that $ln(\bar{\theta})$ is independent from r.

In order to integrate the heat source term, Q must be prescribed. Here it is taken as proportional to the Ekman pumping w_E (Eq. 3 from the main text) in the region of significant vertical motions and zero elsewhere

$$Q(r, z) = \begin{cases} \beta(z) q_b L w_E(r), & r \leq R_+ \\ 0 & r > R_+ \end{cases} \tag{18}$$

with $\beta(z)$ a vertical heat profile which is normalized on the interval $[0, H]$ and has the dimension of inverse length, q_b the specific humidity in the boundary layer and L the latent heat of condensation.

Finally, integrating the heat source term yields

$$\int_0^H \int_0^z \int_0^{R_0} \frac{\bar{\rho} r Q}{C_p \bar{T}} \, dr \, dz \, dz = \int_0^H \int_0^z \frac{\bar{\rho} \beta q_b L}{C_p \bar{T}} \int_0^{R_0} r w_E \, dr \, dz \, dz$$
$$= \alpha \left[\frac{C_d r v^2}{\omega_z + f} \right]_{z=0,\ r=R_+} \tag{19}$$

where we defined

$$\alpha := \frac{q_b L}{C_p} \int_0^H \int_0^z \frac{\bar{\rho}(z) \beta(z)}{\bar{T}(z)} \, dz \, dz \tag{20}$$

In the end, integration of Eq. 6 yields, after multiplication by g:

$$g\frac{\partial}{\partial t}\langle\langle\bar{\rho}\theta\rangle\rangle + g\langle\bar{\rho}w\theta\rangle = g\alpha\left[\frac{C_d r v^2}{\omega_z + f}\right]_{z=0,\ r=R_+} \tag{21}$$

where we further neglected the heat fluxes $H\int_0^{R_0}\left[\bar{\rho}rw\tilde{\theta}\right]_{z=0} dr$ in Eq. 16.

Steady-state balance

Equations 15 and 21 are valid under the anelastic approximation, *i.e* when ρ is everywhere not far from the average vertical profile $\bar{\rho}(z)$. To further simplify, we now consider the case of constant air density $\bar{\rho}(z) \equiv \bar{\rho}_0$. Then, in steady-state, Eqs. 15, 21 can be combined to obtain:

$$\int_0^{R_0}\left[C_d r v^3\right]_{z=0} dr = U_c^2\left[\frac{C_d r v^2}{\omega_z + f}\right]_{z=0,\ r=R_+} \tag{22}$$

with $U_c := \sqrt{\frac{g\alpha}{\bar{\rho}_0}}$ is homogeneous to a velocity.

Characteristic velocity

In order to estimate the characteristic velocity U_c, we may assume that the heating is concentrated in the lowest layers of the TC, *e.g* in the boundary layer. Further assuming that the temperature in the boundary layer is a constant $\bar{T}_0$, the characteristic velocity becomes

$$U_c^2 = \frac{g q_b L \beta_0}{C_p \bar{T}_0} \tag{23}$$

where $\beta_0 := \int_0^H \int_0^z \beta(z)\, dz\, dz$. We may use an analytical form for $\beta(z)$, for instance $\beta(z) := \frac{e^{-\frac{z}{\delta}}}{\delta(1-e^{-\frac{H}{\delta}})}$, which leads to $\beta_0 = \frac{H}{1-e^{-\frac{H}{\delta}}} - \delta$. To further estimate U_c, we need an estimate of δ, which should correspond to the boundary layer height. By prescribing $\delta \sim \frac{H}{20}$ (corresponding for instance to a TC that is $\sim$ 10 km high and whose boundary

layer is ~ 0.5 km high), we find $\beta_0 \sim \frac{H}{19}$, which we can use along with Eq. 12 from the main text to rearrange Eq. 23. We obtain

$$U_c^2 = \frac{V_{max}^2 q_b L}{19 C_p \bar{T_0} \frac{\Delta\theta}{\theta_0}} \tag{24}$$

Typical values for the remaining parameters are $q_b \sim 20$ g/kg, $L \sim 2.5 \times 10^6$ J/kg, $C_p \sim 1 \times 10^3$ J/kg/K, and $\bar{T_0} \sim 300$ K. For $V_{max} \sim 34$ m/s, the average V_{max} for the most steady IKE cases of the SAR database (black stars in Fig. 3 from the main text), we find $U_c \sim 32$ m/s.

Text S5: Wind structure parameters

The characteristic radii R_0 and R_+ may be extracted from the 178 wind profiles of the SAR database. Figure S2 represents the ratio $\frac{R_+}{R_{max}}$ as a function of Ro_{max} for all these cases. A relation of proportionality between this ratio and Ro_{max} is apparent. In addition, for a given Ro_{max}, higher B_s values (*i.e* increased surface wind decay) decrease the ratio $\frac{R_+}{R_{max}}$ (see for instance Lane and Meranti in Fig. S2).

The controlling effect of Ro_{max} and B_s on the wind structure may then be interpreted in terms of distances of R_0 and R_+ from the TC center in units of R_{max} because Ro_{max} increases with both $\frac{R_+}{R_{max}}$ (Fig. S2) and $\frac{R_0}{R_{max}}$ (Eq. 5 from the main text) while B_s decreases with $\frac{R_+}{R_{max}}$ (Fig. S2).

References

Combot, C., Mouche, A., Knaff, J., Zhao, Y., Zhao, Y., Vinour, L., ... Chapron, B. (2020). Extensive high-resolution synthetic aperture radar (sar) data analysis of tropical cyclones: Comparisons with sfmr flights and best track. *Monthly Weather*

Review, *148*(11), 4545–4563.

Holland, G. J. (1980). An analytic model of the wind and pressure profiles in hurricanes. *Monthly Weather Review*, *108*, 1212–1218.

Kalashnik, M. (1994). On the maximum wind velocity in the tropical cyclone. *Izvestiâ Akademii nauk SSSR. Fizika atmosfery i okeana*, *30*(1), 26–30.

Mouche, A., Chapron, B., Knaff, J., Zhao, Y., Zhang, B., & Combot, C. (2019). Copolarized and cross-polarized sar measurements for high-resolution description of major hurricane wind structures: Application to irma category 5 hurricane. *Journal of Geophysical Research: Oceans*, *124*(6), 3905–3922.

Mouche, A. A., Chapron, B., Zhang, B., & Husson, R. (2017). Combined co-and cross-polarized sar measurements under extreme wind conditions. *IEEE Transactions on Geoscience and Remote Sensing*, *55*(12), 6746–6755.

Vinour, L., Jullien, S., Mouche, A., Combot, C., & Mangeas, M. (2021). Observations of tropical cyclone inner-core fine-scale structure, and its link to intensity variations. *Journal of the Atmospheric Sciences*, *78*(11), 3651–3671.

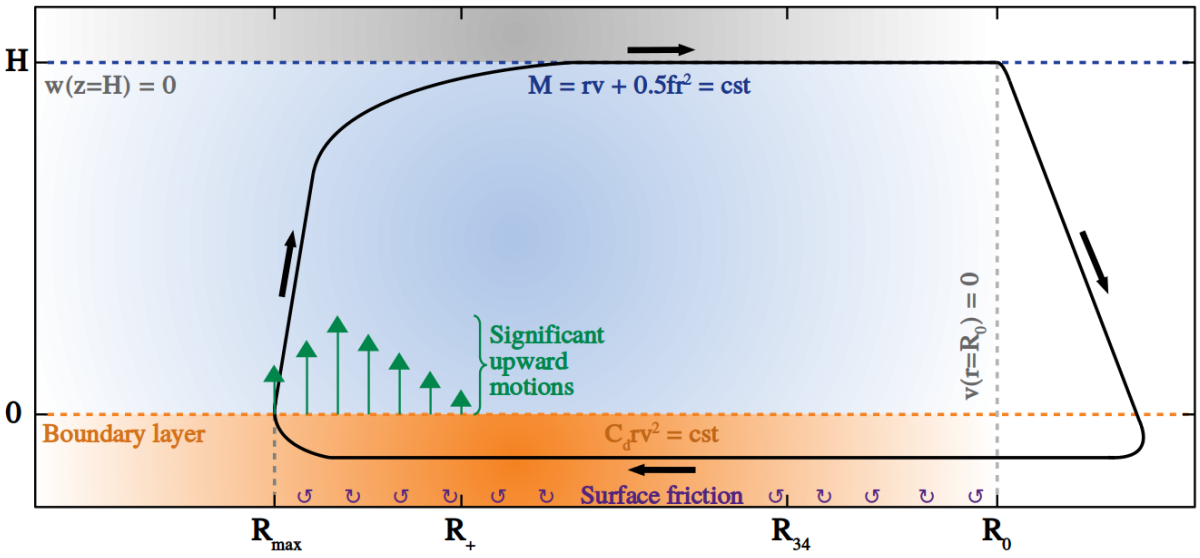

Figure S1. Schematic illustration of the TC system. The meridional circulation (black lines) is represented in a (r, z)-plane, with black arrows indicating the sense of the circulation. In the region of significant upward motions, green arrows represent the vertical velocity at the top of the boundary layer due to Ekman pumping. The radii used in this study are placed in the order given by their average value in the SAR database: $R_{max} \sim 32$ km, $R_{+} \sim 57$ km, $R_{34} \sim 139$ km, and $R_0 \sim 216$ km.

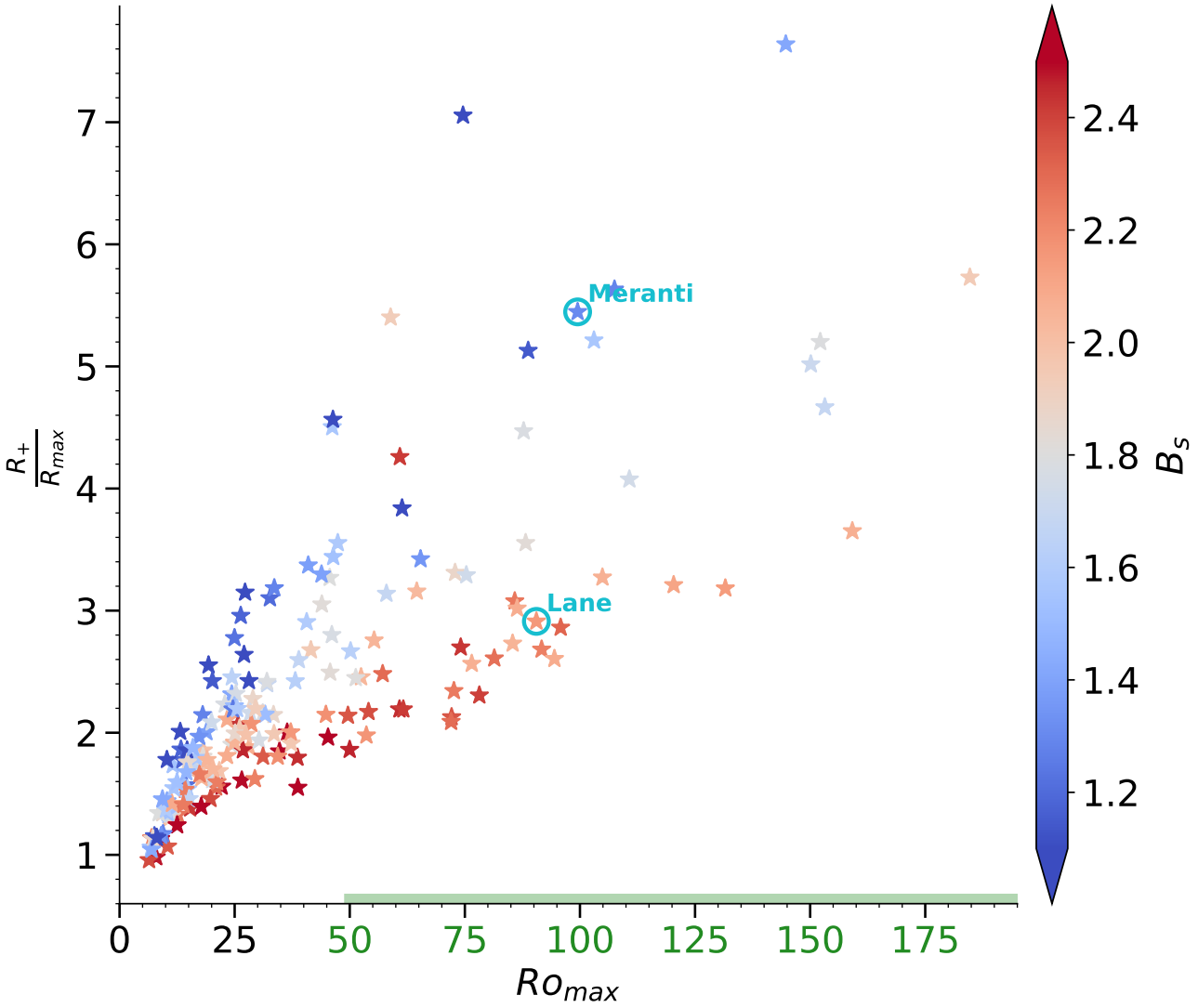

Figure S2. Observed dependency of $\frac{R_+}{R_{max}}$ on Ro_{max} and B_s. Each star represents a SAR observation. The x-axis is shaded in green for $Ro_{max} > 50$.

3.3 Conclusion

In this chapter, an analytical criterion was proposed to characterize the steadiness of TCs integrated kinetic energy. Two characteristic scales, namely the radius where surface vertical motions become significant (R_+) and the radius where outflow velocity vanishes (R_0), are shown to be crucial for the TC kinetic energy balance. Measurable with high-resolution SAR wind surface data, the knowledge of these two characteristic scales can provide information on whether a TC is undergoing kinetic energy variations.

The assumption $C_d r v^2 = \text{cst}$ was also discussed with respect to the complete SAR wind profiles estimates. For the least intense events (*i.e* events for which the maximum winds do not reach 30-35 m/s), this assumption is consistent with an increase of C_d with wind speed. For the most intense events (*i.e* events for which the maximum winds are larger than 30-35 m/s), a saturation/decrease of C_d with wind speed is suggested in the region between R_{max} and R_+, while the assumption $C_d r v^2 = \text{cst}$ certainly breaks down for radii larger than R_+. At such radii, the wind speed is nearly proportional to $\frac{1}{r}$, suggesting that angular momentum is roughly conserved for these cases and in this region.

Lastly, the analysis demonstrated that a SAR observation provides an indirect estimate of a characteristic velocity (U_c) associated with the TC thermodynamics and influencing its kinetic energy balance. This characteristic velocity depends on both oceanic and atmospheric parameters, and the accumulation of SAR measurements in the future is expected to enhance the understanding of the basin- and climate-dependence of U_c. Hence, including structural parameters such as R_0, and R_+ in TC wind structure reference datasets should help improving the anticipation of short- and long-term TC kinetic energy changes.

Chapter 4

The short-term evolution of the tropical cyclone wind structure

4.1 Introduction

The role of the radius of significant upward motions (R_+) on the TC dynamics was highlighted in **Chapter 3**. This radius characterizes the area of the TC system where the kinetic energy is most efficiently gained. In addition, it is known that prescribing the TC secondary circulation in the primitive governing equations is equivalent to prescribing the radial distribution of heating (see for instance the discussion in A. Kalashnik and Kalashnik, 2011). Based on these remarks, a system of equations may be developed to describe the TC system, in which the advection of momentum is maximal at R_+.

The present chapter investigates such a system of equations. The system is described by the equation of absolute angular momentum conservation, in which a linear frictional term is added in order to represent the frictional effects of the BL on the flow above. The radial advection of angular momentum is imposed such that it is maximal at R_+. Further assumptions are made on the linear momentum term, based on classical BL dynamics. The resulting system of equation admits an analytical solution, which is compared with SAR wind profiles estimates.

4.2 Article: "Revealing short-term dynamics of tropical cyclone wind speeds from satellite synthetic aperture radar"

Manuscript submitted on 31/01/2024.

Revealing short-term dynamics of tropical cyclone wind speeds from satellite synthetic aperture radar

Arthur Avenas[1,*], Bertrand Chapron[1], Alexis Mouche[1], Paul Platzer[1], and Léo Vinour[1]

[1]Ifremer, Univ. Brest, CNRS, IRD, Laboratoire d'Océanographie Physique et Spatiale (LOPS), IUEM, F-29280, Plouzané, France
[*]arthur.avenas@ifremer.fr

ABSTRACT

Both unresolved physics in numerical models and limited theoretical understanding of the small-scale diffusion processes occurring near the ocean surface hamper predictability of tropical cyclone (TC) wind changes. An analytical model is here developed to diagnose the short-term evolution of the TC wind profile. An effective frictional parameter is introduced to control the unknown diffusion effects. When this frictional parameter is adjusted to match the TC intensity change, solutions are consistent with observed high-resolution ocean surface wind speeds from satellite synthetic aperture radar (SAR). The initial high-resolution estimate of the near-core wind structure is then found to strongly modulate the wind profile evolution. The frictional parameter can, unfortunately, not efficiently be calibrated using outer-core wind speed changes. Low-resolution observations or standard numerical weather predictions may thus not be directly used to reinterpret and anticipate short-term TC wind changes. The expected accumulation of orbiting SAR sensors as well as improved measurements of the ocean-atmosphere boundary layer characteristics shall then become essential to more precisely monitor TC dynamics.

Introduction

Diagnosing short-term tropical cyclone (TC) wind profile changes is still very challenging. Numerical weather prediction currently faces limited capacity to address this difficult task[1–3]. Small-scale processes governing the TC dynamics may not be sufficiently well known and represented, especially when parameterized at coarse spatial resolution. Correcting biases in TC characteristics (intensity, radius of maximum wind) is thus an active field of research[4–7].

However, TC dynamics may theoretically be described in a simple but comprehensive way, for both the steady[8–10] and unsteady[11–14] phase. Using high-resolution simulations[15,16], and supported with observational data[17], small-scale diffusion near the ocean surface is evidenced to alter the absolute angular momentum conservation and the TC wind structure. Analytical solutions for the steady TC phases can be adjusted to observed surface wind speeds to quantify small-scale turbulent exchanges[18]. The size of the TC core, controlled by small-scale diffusion, has been linked to unsteady phases[19,20] and may support the diagnosis of the central pressure tendency[21]. Practical estimates of wind profile changes are then strongly constrained by the quality of observational data, especially near the TC core. Spaceborne scatterometers can be used, but surface wind speed estimates in the core region may often be limited by instrument resolution[22], rain contamination and signal sensitivity issues[23,24]. TC core size estimates in best-track data is also debated, especially for the most intense TC systems[25].

In that context, satellite observation capabilities were extended by new acquisition modes and surface wind speed algorithms designed for spaceborne synthetic aperture radar (SAR) data. SAR observations of TCs now provide more accurate two-dimensional ocean surface wind speed estimates at very high-resolution ($\sim$1 km), including the inner-core region[24,26]. Figures 1a, b, c present three SAR acquisitions of TC Goni, a West Pacific system that reached category 5 on the Saffir-Simpson scale in 2020[27]. Successive acquisitions were taken at short time intervals ($\sim$ 12 hours), to examine the evolution of the TC axisymmetric wind profile (Fig. 1d) including the location (R_{max}) and amplitude (V_{max}) of its maximum.

Given these new observational opportunities, our motivation is to propose an analytical framework to help understanding and interpreting the short-term ($\sim$ 12 hours) evolution of the TC axisymmetric structure. Following a previous framework[14], analytical solutions are extended for observed non-zero initial wind profiles to diagnose the TC evolution with a scalar parameter that characterizes the effects of frictional dissipation. After assessing the performance of the derived analytical solution compared to SAR data, its potential to enhance lower resolution tools is discussed. The benefit of future satellite capabilities to help estimating this frictional parameter is also emphasized, paving the way for future work on the monitoring and prediction of TC wind structural short-term changes.

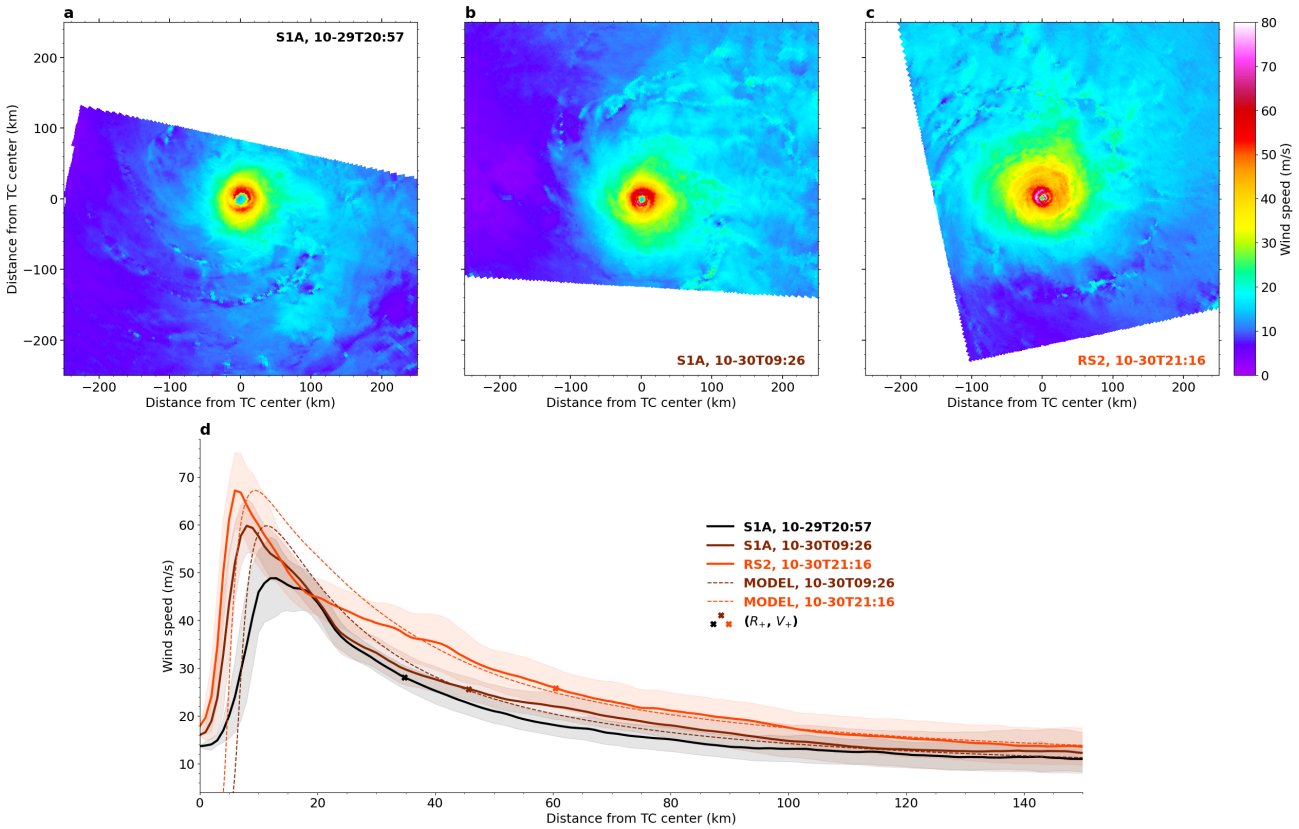

Figure 1. (a), (b), (c) SAR wind speed estimates for TC Goni in 2020 at three different times and (d) corresponding axisymmetric wind profiles (solid curves), standard deviation along each radius (shaded area), and analytical model predictions (dashed curves). For each wind profile, the cross mark indicates the radius R_+ of significant upward motions (see Eq. 2) and the corresponding wind speed V_+. Note, $h_+ = 2.5$ km (see Eq. 9) for the first model prediction (brown dashed curve) and $h_+ = 3.6$ km for the second model prediction (orange dashed curve).

Theoretical framework

Evolution of the wind profile

In the present work, the evolution of the TC wind profile is based on angular momentum conservation. When the radial circulation is prescribed (see for instance Eq. 9 from this study[14]), and considering a Rayleigh linear friction term, air parcels are governed by

$$\frac{\partial m}{\partial t} + u\left(\frac{\partial m}{\partial r} + fr\right) + \lambda m = 0, \tag{1}$$

where $m = rv$ is the relative angular momentum, r the distance from TC center, t the time, f the Coriolis parameter, and u, v the radial and tangential components of the wind speed, respectively. The effective frictional parameter λ has inverse time dimension and may be a function of r.

A natural characteristic time that normalizes Eq. 1 is $\frac{1}{f}$. Already using SAR observations and a theoretical framework, a previous study[28] showed that a relevant characteristic length for TC dynamics is the radius R_+ of significant upward motions in the ocean-atmosphere boundary layer (BL), defined as

$$\omega_z(R_+) = 5f, \tag{2}$$

where $\omega_z(r) = \frac{1}{r}\frac{\partial m}{\partial r}$ is the relative vorticity. R_+ can be interpreted as the location where angular momentum is most efficiently gained by the TC system. Further normalizing the problem variables with the two characteristic scales f and R_+ (*i.e* u and v are both normalized by fR_+ and λ by f), Eq. 1 is non-dimensionally reduced.

The radial wind is then imposed to take the following non-dimensional form

$$u = \begin{cases} -ar & \text{if } 0 < r < 1 \\ -\frac{a}{r} & \text{if } r > 1 \end{cases}, \tag{3}$$

where a characterizes the inflow amplitude. With this definition, the absolute radial wind is maximal at $r = 1$, corresponding to R_+ in dimensional form.

Using Eq. 3 and a given initial arbitrary wind profile $v_0(r) := v(r, t = 0)$, Eq. 1 can be solved using the method of characteristics (see Text S1 in Supporting Information), yielding in non-dimensional form :

$$v(r,t) = \begin{cases} v_0(re^{at})e^{(a-\lambda)t} + \frac{ar(1-e^{(2a-\lambda)t})}{\lambda-2a} & \text{if } 0 \le r \le e^{-at} \\ \sqrt{1+2(\ln(r)+at)}\, v_0\left(\sqrt{1+2(\ln(r)+at)}\right)\frac{e^{-\lambda t}}{r} + \frac{a(\lambda r^2 - 2ar^{\frac{\lambda}{a}})}{\lambda(\lambda-2a)r} - \frac{ae^{-\lambda t}}{\lambda r} & \text{if } e^{-at} \le r \le 1 \\ \sqrt{1+\frac{2at}{r^2}}\, v_0\left(\sqrt{r^2+2at}\right)e^{-\lambda t} + \frac{a(1-e^{-\lambda t})}{\lambda r} & \text{if } r \ge 1 \end{cases}. \tag{4}$$

Note, the linear effective friction term enables practical analytical solutions, Eq. 4, considered valid on a short enough duration, *i.e* for $t \sim \frac{1}{f}$.

The effective frictional parameter

According to Eq. 4, the wind profile evolution solely depends on the initial distribution of winds v_0, the inflow amplitude a, and the effective frictional parameter λ. The latter shall describe the frictional influence of the BL on the flow. To further interpret this parameter, we recall the equation of angular momentum conservation in cylindrical coordinates for an axisymmetric vortex:

$$\frac{\partial m}{\partial t} + u\left(\frac{\partial m}{\partial r} + fr\right) + w\frac{\partial m}{\partial z} = \frac{r}{\rho}\frac{\partial \tau_{\theta z}}{\partial z}, \tag{5}$$

where z is a vertical coordinate, w the vertical component of the wind speed, ρ the density, and $\tau_{\theta z}$ a tangential stress component whose value at the ocean surface is assumed to be $C_d\rho v^2$, with C_d a drag coefficient. In this cylindrical formulation, the frictional term $\frac{r}{\rho}\frac{\partial \tau_{\theta z}}{\partial z}$ varies with both r and z. In the present study's framework, the frictional term λm affects an air parcel along its characteristic curve (see Text S1 in Supporting Information) and is thus expressed as a function of r only.

With the aim of reducing the frictional parameter $\lambda(r)$ to a scalar quantity, we propose to link its prescription in a framework based on the characteristic curves, used in the present work, with the cylindrical formulation (Eq. 5). We define the BL height h as the altitude where $\tau_{\theta z}$ vanishes. Averaging Eq. 5 over the BL depth and assuming a steady flow, we have[7]:

$$\overline{u}\left(\overline{\frac{\partial m}{\partial r}}+fr\right)=-\frac{C_d r v^2}{h}, \tag{6}$$

where an overbar denotes a quantity averaged over the BL depth, *e.g* $\overline{u}=\frac{1}{h}\int_0^h u\,dz$. By analogy with this BL balance, the dimensional form of λ may be assumed to satisfy:

$$\lambda m \propto \frac{\widetilde{C_d} r v^2}{h}, \tag{7}$$

where the planetary part of angular momentum has been neglected for simplicity and $\widetilde{C_d}$ is an effective drag coefficient encoding the integrated effect of surface friction over the characteristic trajectory of air parcels. Note that the value of this effective drag coefficient $\widetilde{C_d}$ is expected to differ from the value of its cylindrical counterpart C_d (Eq. 5).

Suggested by the potential vorticity conservation equation and aircraft wind speed measurements, it may be stated that the TC axisymmetric wind structure in the inflow is constrained by[7,29]

$$\widetilde{C_d} r v^2 = \text{cst}. \tag{8}$$

Using Eq. 8 and further defining $h = h_+ g(r)$, where h_+ is the value of h at R_+ and $g(r)$ is a non-dimensional function of r, we may rewrite Eq. 7

$$\lambda \propto \frac{\widetilde{C_{d+}} R_+ V_+^2}{h_+ g(r) m}, \tag{9}$$

where $\widetilde{C_{d+}}$ and V_+ are the effective drag coefficient and the wind speed both evaluated at R_+. In Eq. 9, the quantities $R_+ V_+^2$ and m can be determined from the initial wind profile $v_0(r)$ so that, for a fixed function $g(r)$ and corresponding value of $\widetilde{C_{d+}}$, determining λ in Eq. 9 amounts to estimating a multiplicative constant which characterizes h_+.

Data and Methods

Satellite data

The dataset of SAR high-resolution ocean surface wind speed estimates has already been described extensively[7,28], and contains acquisitions from Sentinel-1A (S1A), Sentinel-1B (S1B) and Radarsat-2 (RS2) missions. Numerous studies demonstrated capabilities of spaceborne SAR C-band instruments to estimate ocean surface wind speeds under TC conditions, including at very high wind speeds and in the near-core region[24–26].

Low-resolution ocean surface wind speed estimates from one passive L-band radiometer acquisition of the Soil Moisture Active Passive (SMAP) mission are also examined in the present work. The capacity of SMAP L-band brightness temperature measurements to retrieve ocean surface wind speeds in TCs has also been assessed in several studies[30,31], and the consistency of such measurements with those from the SAR instrument evidenced[32].

Pairing the SAR observations

A pair of SAR acquisitions of the same TC system is retained only if the time difference between the two observations is within 10 and 14 hours. To restrain the analysis to well-formed systems, we only select cases for which the SAR V_{max} estimate (*i.e* the axisymmetric maximum wind speed) is higher than 25 m/s, the SAR R_{max} estimate (*i.e* the axisymmetric radius of maximum wind) smaller than 150 km, and the absolute latitude of the TC center smaller than 30°. We also ensure that, for each SAR case, the distance to closest land from the TC center is greater than the SAR R_{34} estimate (*i.e* the radius where the axisymmetric outer-wind profile equals 34 knots). Under these constraints, a dataset of 18 SAR pairs is created, with an average time difference between two successive acquisitions of 12.9 hours.

Adjustment of the analytical model

For this study, a, $g(r)$ and $\widetilde{C_{d+}}$ are chosen constant across all TCs in the proposed theoretical framework (Eqs. 3, 4, 9). When adjusting the analytical model, a is set to 0.5. Such a value was found to yield overall good performances of the analytical solution (see Fig. 2).

The definition of $g(r)$ modulates the effective frictional parameter λ in Eq. 9. Here, we impose a linear form $g(r) = r$. While determining a more appropriate definition for $g(r)$ would improve the analytical solution, such an investigation should require a more extensive dataset of SAR acquisitions than what is available at the time of this study, and is thus left for future investigations. In addition, the simple linear definition still provides wind profile changes in the near-core region that are consistent with those observed in the SAR dataset of pairs (Fig. 2).

The value of $\widetilde{C_{d+}}$ must be consistent with realistic values of h_+ in Eq. 9. The height h_+ at which $\tau_{\theta z}(R_+)$ vanishes can be estimated with the SAR dataset and ranges between $\sim$0.6 and $\sim$2.7 km, with a mean value of $\sim$1.4 km (see Text S2 in Supporting Information). When λ is adjusted to the different SAR pairs to match the intensity change (see below), $\widetilde{C_{d+}}$ must be set to 1.2×10^{-4} in order for the adjusted values of h_+ in Eq. 9 to be consistent with an average of $\sim$1.4 km.

The analytical model requires the estimation of R_+, which involves the computation of a radial derivative (see Eq. 2). Radial derivatives may be difficult to directly compute from SAR observations, *e.g* high wind speed estimates at high resolution may exhibit strong local variations (see for instance Fig. 1d). Hence, like in previous studies[7,28], a parametric wind profile based on the Holland analytical model[33] is adjusted to each SAR wind profile estimate. The adjusted parametric wind profiles are used to compute the quantities of interest (see below) as well as to perform comparisons (see Fig. 2).

For each pair of observations, the frictional parameter λ is adjusted using the following procedure. The normalization constants f and R_+, as well as the quantities V_+ and m in Eq. 9 are all computed from the first (initial) acquisition of the SAR pair. The first SAR wind profile (parametric) estimate provides the initial condition v_0 in Eq. 4. Thereafter, the multiplicative constant h_+ that determines λ is chosen so that, at the time of the second (final) acquisition of the SAR pair, the observed V_{max} is matched by the analytical solution Eq. 4.

Results

We assess the performance of the analytical solution (Eqs. 3, 4) when λ, prescribed by Eq. 9 and fully determined by the scalar quantity h_+, is adjusted to match the observed intensity changes. Considering the TC Goni observations, the two pairs cover $\sim$ 24 hours from its intensification phase. Figure 1d shows that TC Goni intensified from $V_{max} = 49$ m/s to $V_{max} = 60$ m/s and then to $V_{max} = 67$ m/s, while R_{max} decreased from 13 to 8 km and then further to 6 km (solid curves). With the adjusted effective frictional parameter, the analytical model (dashed curves) is in qualitatively good agreement with the SAR wind profile estimates. The model predicts a R_{max} value of 11 km (dashed brown curve) when taking the first (solid black curve) SAR wind profile estimate as initial condition, and 9 km (dashed orange curve) when the second (solid brown curve) SAR wind profile estimate is used as initial condition (Fig. 1d). While in good agreement with the SAR R_{max} estimates, the small discrepancies in R_{max} result in slight differences of wind speed estimates in that region. Note, the model wind speeds converge quickly toward zero with decreasing radius. This is a consequence of Eq. 9 and the linear assumption on $g(r)$. To complement the analysis of TC Goni, four other case studies are presented in Text S3 in Supporting Information.

The analytical model is further assessed with respect to the complete dataset of SAR pairs, and compared to persistent expectations. Figure 2 presents the relative error for the persistence (*i.e* the prediction is just the initial SAR wind profile, Fig. 2a) and for the analytical model (Fig. 2b) as a function of normalized radius $r_* := \frac{r}{R_{max}}$. To complement the analysis, the same comparison in terms of absolute error is presented in Text S4 in Supporting Information.

The relative error considering persistent conditions (Fig. 2a) is low on average (black thick solid curve), especially for $1 \leq r_* \leq 5$, because the dataset consists in both weakening, stagnating and intensifying phases of TCs. When weakening phases (blue) are solely considered, the relative error is positive, as expected, and may be as large as 35% in the region near R_{max}. Conversely, for intensifying phases (red), the relative error is negative, of the order 30% near R_{max}. Lastly, the relative error is rather low for cases that have small V_{max} variations (grey).

Regarding the analytical model (Fig. 2b), the average relative error is also low (black thick solid curve), but positive for $1 \leq r_* \leq 5$, suggesting that wind speeds are slightly overestimated by the model in this region. This is associated with a positive bias of the model in the prediction of R_{max}. In contrast to persistent predictions, there is no systematic bias specific to the phase of the TC life cycle (*i.e* weakening, stagnating or intensifying). Furthermore, the distribution of relative error values is narrower than that of persistent predictions (black thick solid curves). Near R_{max} (*i.e* for $r_* \sim 1$), both the average relative error and the spread are small, suggesting that the analytical model performs better than persistence in this region.

Inside the core region (*i.e* for $r_* < 1$), the relative error takes large values for both predictions. Considering persistence, the large errors in this region are introduced by variations in R_{max} between the initial and the final SAR wind profile estimates. For the analytical model, the relative error is largely negative, associated with the quick convergence of the analytical solution

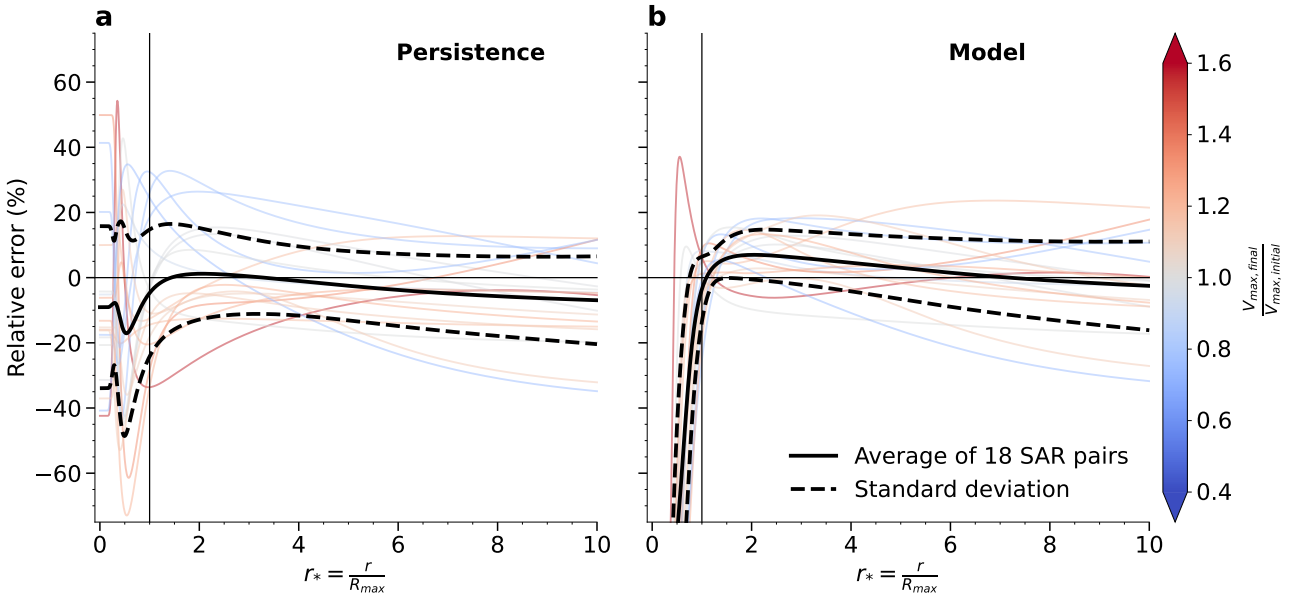

Figure 2. Relative error between (a) initial and final SAR wind profile estimates and (b) analytical model predictions and final SAR wind profile estimates of each SAR pair as a function of normalized radius ($r_* = \frac{r}{R_{max}}$ where R_{max} is that of the final SAR wind profile). The different cases (thin curves) are colored by ratio of the final over the initial SAR V_{max} estimates, while the average relative error (solid thick black curve) is displayed with plus or minus the standard deviation (dashed thick black curves).

toward zero with decreasing radius. One case drastically deviates from this rule and has a relative error maximum of 37% at $r_* \sim 0.5$. This case corresponds to TC Sam (see Text S3 in Supporting Information), for which the model overall captures the wind profile but fails to accurately reproduce the sharpness of the high winds region.

Discussion

The systematic assessment of the model and the comparison with persistent conditions suggest that the adjusted analytical model captures the short-term evolution of the TC axisymmetric wind structure in a wide range of situations, especially near the TC core. In the present study, the effective frictional parameter is adjusted using both a high-resolution wind profile measured at the initial time step and an estimate of V_{max} at the final time step. The question arises whether the frictional parameter could also be adjusted using an information on the final outer-core wind profile, generally well captured by low-resolution measurements.

Figure 3 presents a wind profile estimate from a passive radiometer instrument (SMAP, purple solid thick curve) collocated with the SAR wind profile estimate from TC Goni (brown solid thick curve in Fig. 1d and in Fig. 3). For radii larger than 30 km, both wind profile estimates are consistent. As expected near the TC core, the peak wind speeds are largely underestimated by the passive radiometer, mainly because of the coarse nominal spatial resolution ($\sim$ 50 km) of the radiometer instrument[7]. Initialized on the previous SAR wind profile estimate (black solid curve in Fig. 1d, not shown in Fig. 3), the analytical solution is also displayed, once λ was adjusted (*i.e* $h_+ = 2.5$ km, brown dashed curve in Fig. 1d and in Fig. 3), and when this value was doubled (*i.e* $h_+ = 1.2$ km, brown dotted thin curve in Fig. 3) or halved (*i.e* $h_+ = 4.9$ km, brown dash-dotted thin curve in Fig. 3). For these three values, the SAR and radiometer outer-core wind profiles are matched by the analytical model, but the corresponding V_{max} estimates span a large range of values (between $\sim$47 and $\sim$72 m/s). For this case, the capabilities of current spaceborne passive radiometers or active scatterometers, which are limited when approaching the TC core, would not allow to adjust the frictional parameter. This suggests that an information on the near-core surface winds is critical to diagnose the TC evolution.

Despite this wide range of predicted intensities, the range of model R_{max} estimates (between $\sim$10 and $\sim$14 km, thin solid brown curve in Fig. 3) obtained when varying the effective frictional parameter is reasonably narrow and close to the actual SAR R_{max} estimate ($\sim$8 km). Furthermore, the R_{max} predictions from this ensemble of analytical solutions are consistent with those obtained by applying existing statistical rules[7] (thin solid green curve in Fig. 3), also based on angular momentum conservation, to the ensemble V_{max} and outer-core analytical estimates. Thus, for a given initial high-resolution wind profile, in the absence of any accurate V_{max} estimate to calibrate λ, the analytical solution may still be used to create an ensemble of possible wind profile changes that shall be realistic in the outer-core region (see Fig. 2) and that are all physically consistent in

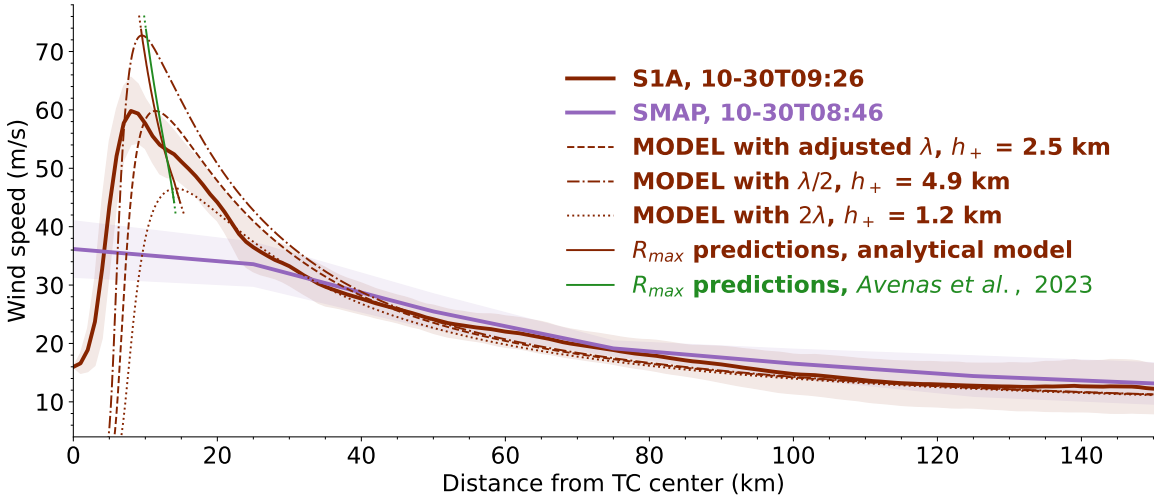

Figure 3. SAR wind profile estimate (solid thick brown curve, *i.e* the second of the three SAR wind profile estimates in Fig. 1) and radiometer wind profile estimate (solid thick purple curve) collocated in time (*i.e* with a 40-min time difference) for TC Goni. For each observed wind profile, the shaded area denotes the standard deviation along each radius. Analytical model predictions (thin dashed, dotted and dash-dotted brown curves) for three different values of λ (see text for details) and corresponding R_{max} estimates (thin solid brown curve, obtained using an ensemble of λ values). For comparison, the R_{max} estimates obtained by considering steady angular momentum conservation[7] to the ensemble of analytical solutions (*i.e* the model V_{max} and outer size predictions obtained when varying λ) are shown in green.

the near-core region. More precisely, not only R_{max} but also R_+ is well represented by the analytical solution (see Text S5 in Supporting Information). These two radii control the radial gradient of the near-core wind speed and thus modulate the TC steady-state balance[28]. Producing physically consistent estimates of R_{max} and R_+ is thus essential to monitor the TC wind structure.

While the analysis suggests that the performances of the analytical model are reasonable, its limitations, such as the linear assumption on $g(r)$ and the simple prescription of u (Eq. 3), should be kept in mind. These assumptions should certainly be revisited when more SAR data will be available. Furthermore, deeper knowledge of the BL characteristics such as its actual height or the radial wind distribution would allow to further constrain the effective frictional parameter (Eq. 9) and the inflow amplitude a.

Conclusion

An analytical solution for the short-term evolution of the TC axisymmetric wind structure, that relies on an effective frictional parameter, is developed and found consistent with observed high-resolution wind profiles. The frictional parameter is reduced to a scalar multiplicative constant and calibrated using an intensity change estimate. Seemingly, such a model adjustment could not efficiently be performed solely from the outer-core wind profile changes. The presented framework may then be used in at least two situations. First, to predict the complete wind profile at the current time, given a previous (*e.g* $\sim$12 hours before) high-resolution wind profile estimate and a current intensity estimate (*e.g* from Dvorak analysis[34]). Second, to provide an ensemble of physically possible future wind profiles given a current high-resolution wind profile estimate and an ensemble of possible intensity change estimates[35].

The proposed framework could also guide the analysis or reanalysis of the surface winds over a longer time period of the TC life cycle given a time series of V_{max} estimates, by iterating the analytical model over several successive short time steps, starting from an initial observed high-resolution wind profile. Such intensity estimates could come from best-track reanalyses[36] or objective analyses from spaceborne data[37]. Although the consistency between these intensity estimates and the SAR dataset may be high on average[25], large discrepancies can occur for single cases. A consistent methodology to systematically calibrate the effective frictional parameter based on an ancillary intensity time series may thus still require further work.

The proposed simple analytical framework also informs on how future measurements of the surface winds and BL characteristics shall benefit the understanding of the TC wind structure evolution. In the coming years, satellite missions such as the Second Generation Meteorological Operational satellite program (Metop-SG), or the Harmony mission[38] will provide improved TC ocean surface wind vectors estimates. Algorithms to estimate wind directions from the SAR sensors are also being

developed, *e.g* based on local gradients analysis[39]. Airborne acquisitions from the Imaging Wind and Rain Airborne Profiler (IWRAP) instrument[40] shall also yield useful information on both the BL depth and wind vectors. These BL measurements will then certainly help understanding how the small-scale processes modulate the frictional parameter (see Eq. 9).

Despite its simplicity, the proposed framework clearly emphasizes that reliable near-core surface wind speed estimates are crucial to anticipate changes in the TC wind structure. The expected accumulation of high-resolution observations due to the increasing number of spaceborne SAR sensors (*e.g* the recently launched Radarsat Constellation Mission) shall thus serve more in depth analysis of the TC dynamics[41].

Lastly, the TC destructive potential is controlled by the complete wind structure[42], while operational and research communities mainly focused on predicting intensity changes[43]. The proposed analytical framework may be practical in describing changes of the complete wind structure with only one scalar parameter, which efficiently characterizes the combination of an initial high-resolution wind profile and an intensity change. This shall in turn benefit the real-time evaluation of potential impacts (storm surges, waves, upwelling, currents) associated with an evolving TC.

References

1. Camargo, S. J. & Wing, A. A. Tropical cyclones in climate models. *Wiley Interdiscip. Rev. Clim. Chang.* **7**, 211–237 (2016).
2. Davis, C. Resolving tropical cyclone intensity in models. *Geophys. Res. Lett.* **45**, 2082–2087 (2018).
3. Bian, G.-F., Nie, G.-Z. & Qiu, X. How well is outer tropical cyclone size represented in the era5 reanalysis dataset? *Atmospheric Res.* **249**, 105339 (2021).
4. Chavas, D. R. & Knaff, J. A. A simple model for predicting the tropical cyclone radius of maximum wind from outer size. *Weather. Forecast.* **37**, 563–579 (2022).
5. Faranda, D. *et al.* Correcting biases in tropical cyclone intensities in low-resolution datasets using dynamical systems metrics. *Clim. Dyn.* 1–17 (2023).
6. Chen, R. *et al.* An adaptive learning approach for tropical cyclone intensity correction. *Remote. Sens.* **15**, 5341 (2023).
7. Avenas, A. *et al.* Reexamining the estimation of tropical cyclones radius of maximum wind from outer size with an extensive synthetic aperture radar dataset. *Mon. Weather. Rev.* **151**, 3169–3189 (2023).
8. Emanuel, K. Tropical cyclone energetics and structure. *Atmospheric turbulence mesoscale meteorology* **165**, 192 (2004).
9. Emanuel, K. & Rotunno, R. Self-stratification of tropical cyclone outflow. part i: Implications for storm structure. *J. Atmospheric Sci.* **68**, 2236–2249 (2011).
10. Cronin, T. W. An analytic model for tropical cyclone outer winds. *Geophys. Res. Lett.* **50**, e2023GL103942 (2023).
11. Eliassen, A. On the ekman layer in a circular vortex. *J. Meteorol. Soc. Jpn. Ser. II* **49**, 784–789 (1971).
12. Eliassen, A. & Lystad, M. The ekman layer of a circular vortex-a numerical and theoretical study. *Geophys. Norvegica* **31**, 1–16 (1977).
13. Kieu, C. Q. & Zhang, D.-L. An analytical model for the rapid intensification of tropical cyclones. *Q. J. Royal Meteorol. Soc. A journal atmospheric sciences, applied meteorology physical oceanography* **135**, 1336–1349 (2009).
14. Kalashnik, A. & Kalashnik, M. Analytical model of the intensification of a tropical cyclone. *Izvestiya, Atmospheric Ocean. Phys.* **47**, 766–779 (2011).
15. Rotunno, R. *et al.* Large-eddy simulation of an idealized tropical cyclone. *Bull. Am. Meteorol. Soc.* **90**, 1783–1788 (2009).
16. Rotunno, R. & Bryan, G. H. Effects of parameterized diffusion on simulated hurricanes. *J. Atmospheric Sci.* **69**, 2284–2299 (2012).
17. Gopalakrishnan, S. G. *et al.* A study of the impacts of vertical diffusion on the structure and intensity of the tropical cyclones using the high-resolution hwrf system. *J. Atmospheric Sci.* **70**, 524–541 (2013).
18. Chavas, D. R., Lin, N. & Emanuel, K. A model for the complete radial structure of the tropical cyclone wind field. part i: Comparison with observed structure. *J. Atmospheric Sci.* **72**, 3647–3662 (2015).
19. Carrasco, C. A., Landsea, C. W. & Lin, Y.-L. The influence of tropical cyclone size on its intensification. *Weather. Forecast.* **29**, 582–590 (2014).
20. Stern, D. P., Vigh, J. L., Nolan, D. S. & Zhang, F. Revisiting the relationship between eyewall contraction and intensification. *J. Atmospheric Sci.* **72**, 1283–1306 (2015).

21. Sparks, N. & Toumi, R. The dependence of tropical cyclone pressure tendency on size. *Geophys. Res. Lett.* **49**, e2022GL098926 (2022).

22. Quilfen, Y., Chapron, B., Elfouhaily, T., Katsaros, K. & Tournadre, J. Observation of tropical cyclones by high-resolution scatterometry. *J. Geophys. Res. Ocean.* **103**, 7767–7786 (1998).

23. Donnelly, W. J. *et al.* Revised ocean backscatter models at c and ku band under high-wind conditions. *J. Geophys. Res. Ocean.* **104**, 11485–11497 (1999).

24. Mouche, A. *et al.* Copolarized and cross-polarized sar measurements for high-resolution description of major hurricane wind structures: Application to irma category 5 hurricane. *J. Geophys. Res. Ocean.* **124**, 3905–3922 (2019).

25. Combot, C. *et al.* Extensive high-resolution synthetic aperture radar (sar) data analysis of tropical cyclones: Comparisons with sfmr flights and best track. *Mon. Weather. Rev.* **148**, 4545–4563 (2020).

26. Mouche, A. A., Chapron, B., Zhang, B. & Husson, R. Combined co-and cross-polarized sar measurements under extreme wind conditions. *IEEE Transactions on Geosci. Remote. Sens.* **55**, 6746–6755 (2017).

27. Yurovskaya, M. *et al.* Surface wave developments under tropical cyclone goni (2020): multi-satellite observations and parametric model comparisons. *Remote. Sens.* **14**, 2032 (2022).

28. Avenas, A., Mouche, A., Knaff, J., Carton, X. & Chapron, B. On the steadiness of the tropical cyclone integrated kinetic energy. *Submitted* (2024).

29. Riehl, H. Some relations between wind and thermal structure of steady state hurricanes. *J. Atmospheric Sci.* **20**, 276–287 (1963).

30. Yueh, S. H. *et al.* Smap l-band passive microwave observations of ocean surface wind during severe storms. *IEEE Transactions on Geosci. Remote. Sens.* **54**, 7339–7350 (2016).

31. Meissner, T., Ricciardulli, L. & Wentz, F. J. Capability of the smap mission to measure ocean surface winds in storms. *Bull. Am. Meteorol. Soc.* **98**, 1660–1677 (2017).

32. Zhao, Y., Mouche, A. A., Chapron, B. & Reul, N. Direct comparison between active c-band radar and passive l-band radiometer measurements: Extreme event cases. *IEEE Geosci. Remote. Sens. Lett.* **15**, 897–901 (2018).

33. Holland, G. J. An analytic model of the wind and pressure profiles in hurricanes. *Mon. Weather. Rev.* **108**, 1212–1218 (1980).

34. Dvorak, V. F. *Tropical cyclone intensity analysis using satellite data*, vol. 11 (US Department of Commerce, National Oceanic and Atmospheric Administration . . . , 1984).

35. Cangialosi, J. P. *et al.* Recent progress in tropical cyclone intensity forecasting at the national hurricane center. *Weather. Forecast.* **35**, 1913–1922 (2020).

36. Knapp, K. R., Kruk, M. C., Levinson, D. H., Diamond, H. J. & Neumann, C. J. The international best track archive for climate stewardship (ibtracs) unifying tropical cyclone data. *Bull. Am. Meteorol. Soc.* **91**, 363–376 (2010).

37. Velden, C. S. & Herndon, D. A consensus approach for estimating tropical cyclone intensity from meteorological satellites: Satcon. *Weather. Forecast.* **35**, 1645–1662 (2020).

38. ESA. Report for mission selection: Earth explorer 10 candidate mission harmony. Tech. Rep., ESA, Noordwijk, The Netherlands (2022).

39. Koch, W. Directional analysis of sar images aiming at wind direction. *IEEE Transactions on Geosci. Remote. Sens.* **42**, 702–710 (2004).

40. Sapp, J., Jelenak, Z., Chang, P., Shoup, C. & Carswell, J. Processing of high-resolution hurricane ida boundary layer winds from the iwrap instrument on the noaa wp-3d aircraft. In *IGARSS 2022-2022 IEEE International Geoscience and Remote Sensing Symposium*, 7286–7289 (IEEE, 2022).

41. Faranda, D. *et al.* Dynamical footprints of hurricanes in the tropical dynamics. *Chaos: An Interdiscip. J. Nonlinear Sci.* **33** (2023).

42. Powell, M. D., Vickery, P. J. & Reinhold, T. A. Reduced drag coefficient for high wind speeds in tropical cyclones. *Nature* **422**, 279–283 (2003).

43. Kaplan, J., DeMaria, M. & Knaff, J. A. A revised tropical cyclone rapid intensification index for the atlantic and eastern north pacific basins. *Weather. forecasting* **25**, 220–241 (2010).

44. Zhang, J. A. & Uhlhorn, E. W. Hurricane sea surface inflow angle and an observation-based parametric model. *Mon. Weather. Rev.* **140**, 3587–3605 (2012).

Acknowledgements

This work was financially supported by the ERC Synergy project 856408-STUOD. The SAR database was obtained from IFREMER/CyclObs and produced with the SAR wind processor co-developed by IFREMER and CLS. We also acknowledge two anonymous reviewers for helpful comments.

Author contributions statement

A.A designed the study, analysed the results and wrote the manuscript. B.C, A.M, P.P, and L.V wrote the manuscript.

Additional information

Supplementary information accompanies this paper.

Competing financial interests: The authors declare no competing financial interests.

Data availability statement: Datasets for this research are freely available online at https://cyclobs.ifremer.fr/app/tropical using the steps described at https://cyclobs.ifremer.fr/app/docs/.

Revealing short-term dynamics of tropical cyclone wind speeds from satellite synthetic aperture radar: Supporting information

Arthur Avenas[1,*], **Bertrand Chapron**[1], **Alexis Mouche**[1], **Paul Platzer**[1], **Léo Vinour**[1]

[1]Ifremer, Univ. Brest, CNRS, IRD, Laboratoire d'Océanographie Physique et Spatiale (LOPS), IUEM, F-29280, Plouzané, France
[*]arthur.avenas@ifremer.fr

Contents of this file

1. Texts S1 to S5
2. Figures S1 to S4

Text S1: Solution of the angular momentum equation

Here we solve the following angular momentum equation

$$\frac{\partial m}{\partial t} + u\left(\frac{\partial m}{\partial r} + fr\right) + \lambda m = 0 \tag{1}$$

for a given initial condition $m(r,t=0) := m_0(r) = rv_0(r)$ when the radial wind is prescribed by

$$u = \begin{cases} -ar & \text{if } 0 < r < 1 \\ -\frac{a}{r} & \text{if } r > 1 \end{cases} \tag{2}$$

Following the method of characteristics, we search a curve $(R(T),T)$ such that $R(t) = r$. Along such a curve, we have:

$$\begin{cases} \frac{dm(R(T),T)}{dT} = \frac{dR}{dT}\frac{\partial m(R(T),T)}{\partial r} + \frac{\partial m(R(T),T)}{\partial t} = -\lambda m - Ru \\ m(R(0),0) = m_0(R(0)) \end{cases} \tag{3}$$

where u takes the values given by Eq. 2 depending on the value of R. The piece-wise definition of u leads us to distinguish between three cases.

First case

We first consider a characteristic such that $0 \leq R(0) \leq 1$. With this condition, the characteristic satisfies the system

$$\begin{cases} \frac{dR}{dT} = -aR \\ R(t) = r \end{cases} \tag{4}$$

The characteristic is thus described by

$$R(T) = re^{a(t-T)} \tag{5}$$

The system satisfied by $m(R(T),T)$ becomes

$$\begin{cases} \frac{dm(R(T),T)}{dT} = -\lambda m(R(T),T) + ar^2 e^{2a(t-T)} \\ m(R(0),0) = m_0(re^{at}) \end{cases} \tag{6}$$

Solving this system leads to

$$m(R(T),T) = m_0(re^{at})e^{-\lambda T} + \frac{ar^2 e^{2a(t-T)}(1-e^{(2a-\lambda)T})}{\lambda - 2a} \tag{7}$$

Then, we evaluate this expression for $T = t$

$$m(r,t) = m_0(re^{at})e^{-\lambda t} + \frac{ar^2(1-e^{(2a-\lambda)t})}{\lambda - 2a} \tag{8}$$

Finally, we have

$$v(r,t) = v_0(re^{at})e^{(a-\lambda)t} + \frac{ar(1-e^{(2a-\lambda)t})}{\lambda - 2a} \tag{9}$$

This equation is valid when $0 \leq R(0) \leq 1$, or equivalently $0 \leq r \leq e^{-t}$.

Second case

We now consider a characteristic such that $R(0) \geq 1$ and $R(t) = r \geq 1$. With this condition, the characteristic satisfies the system

$$\begin{cases} \frac{dR}{dT} = -\frac{a}{R} \\ R(t) = r \end{cases} \tag{10}$$

The characteristic is described by

$$R(T)^2 = r^2 + 2a(t-T) \tag{11}$$

The system satisfied by $m(R(T),T)$ along such a characteristic then becomes

$$\begin{cases} \frac{dm(R(T),T)}{dT} = -\lambda m(R(T),T) + a \\ m(R(0),0) = m_0(\sqrt{r^2+2at}) \end{cases} \tag{12}$$

and is solved by

$$m(R(T),T) = m_0(\sqrt{r^2+2at})e^{-\lambda T} + \frac{a(1-e^{-\lambda T})}{\lambda} \tag{13}$$

Evaluating this expression at $T = t$ yields

$$m(r,t) = m_0(\sqrt{r^2+2at})e^{-\lambda t} + \frac{a(1-e^{-\lambda t})}{\lambda} \tag{14}$$

Finally, we write

$$v(r,t) = \sqrt{1+\frac{2at}{r^2}}v_0(\sqrt{r^2+2at})e^{-\lambda t} + \frac{a(1-e^{-\lambda t})}{\lambda r} \tag{15}$$

We recall that this equation is valid when $R(t) = r \geq 1$.

Third case

In the third case, a characteristic such that $R(0) \geq 1$ and $R(t) = r \leq 1$ is considered. Denoting T_1 the time when $R(T_1) = 1$, the characteristic satisfies the system

$$\begin{cases} \frac{dR}{dT} = -aR \\ R(t) = r \end{cases} \tag{16}$$

where $T \leq t$ is such that $R(T) \leq 1$. The characteristic is described by

$$R(T) = re^{a(t-T)} = e^{a(T_1-T)} \tag{17}$$

with

$$T_1 = \frac{ln(r)}{a} + t \tag{18}$$

The system satisfied by $m(R(T),T)$ is

$$\begin{cases} \frac{dm(R(T),T)}{dT} = -\lambda m(R(T),T) + ae^{2a(T_1-T)} \\ m(R(T_1),T_1) = m_0(\sqrt{1+2aT_1})e^{-\lambda T_1} + \frac{a(1-e^{-\lambda T_1})}{\lambda} \end{cases} \tag{19}$$

Solving this system yields

$$m(r,t) = m_0(\sqrt{1+2(ln(r)+at)})e^{-\lambda T} + \frac{a}{\lambda(\lambda-2a)}\left[\lambda r^2 e^{2a(t-T)} - 2ar^{\frac{\lambda}{a}}e^{\lambda(t-T)}\right] - \frac{ae^{-\lambda T}}{\lambda} \tag{20}$$

Taking $T = t$ in this expression, we obtain

$$m(r,t) = m_0(\sqrt{1+2(ln(r)+at)})e^{-\lambda t} + \frac{a(\lambda r^2 - 2ar^{\frac{\lambda}{a}})}{\lambda(\lambda-2a)} - \frac{ae^{-\lambda t}}{\lambda} \tag{21}$$

Finally, we have

$$v(r,t) = \sqrt{1+2(ln(r)+at)}v_0(\sqrt{1+2(ln(r)+at)})\frac{e^{-\lambda t}}{r} + \frac{a(\lambda r^2 - 2ar^{\frac{\lambda}{a}})}{\lambda(\lambda-2a)r} - \frac{ae^{-\lambda t}}{\lambda r} \tag{22}$$

This last equation is valid when $e^{-t} \leq R(t) = r \leq 1$.

Complete solution

Finally, the complete solution is

$$v(r,t) = \begin{cases} v_0(re^{at})e^{(a-\lambda)t} + \frac{ar(1-e^{(2a-\lambda)t})}{\lambda-2a} & \text{if} 0 \leq r \leq e^{-at} \\ \sqrt{1+2(\ln(r)+at)}v_0(\sqrt{1+2(\ln(r)+at)})\frac{e^{-\lambda t}}{r} + \frac{a(\lambda r^2 - 2ar^{\frac{\lambda}{a}})}{\lambda(\lambda-2a)r} - \frac{ae^{-\lambda t}}{\lambda r} & \text{if } e^{-at} \leq r \leq 1 \\ \sqrt{1+\frac{2at}{r^2}}v_0(\sqrt{r^2+2at})e^{-\lambda t} + \frac{a(1-e^{-\lambda t})}{\lambda r} & \text{if } r \geq 1 \end{cases} \tag{23}$$

Text S2: SAR h_+ estimates

Assuming $C_d r v^2 \approx$ cst, we can rewrite Eq. 6 from the main text

$$h_+ = -\frac{C_{d+} R_+ V_+^2}{\overline{u_+}\left(\overline{\frac{\partial m}{\partial r}}\Big|_{R_+} + f R_+\right)}, \tag{24}$$

where C_{d+} and $\overline{u_+}$ are the drag coefficient and the averaged radial wind speed both evaluated at R_+. In Eq. 24, C_{d+} is set to 2.5×10^{-3} based on the literature[1], while f, R_+ and V_+ can be estimated from a SAR wind profile estimate. The radial gradient of relative angular momentum averaged over the BL $\overline{\frac{\partial m}{\partial r}}\Big|_{R_+}$ is assumed to be close to that at the surface, so that it may also be computed on a SAR axisymmetric wind profile estimate. Because u_+ quickly decreases from the surface to the top of the BL, it can not be assumed independent from altitude in the BL. Instead, an exponential form may be assumed for the vertical distribution of the radial wind

$$u_+(z) = -\frac{V_+}{2} e^{-\frac{\alpha z}{h}}, \tag{25}$$

where α is constant and where we assumed that at the surface u_+ takes the value $\frac{V_+}{2}$. This value corresponds to a surface inflow angle of $\sim$26° at R_+, in agreement with *in-situ* measurements[2].
By taking

$$\alpha = \ln\left(\frac{V_+}{2 a f R_+}\right), \tag{26}$$

the expression also satisfies $u_+ = -a f R_+$ at the top of the BL, which is an assumption of our model. Averaging Eq. 25 over the BL depth, we obtain

$$\overline{u_+} = \frac{V_+}{2\alpha}\left(e^{-\alpha} - 1\right). \tag{27}$$

Equations 24, 26, 27 can then be used to estimate h_+ for a given SAR wind profile estimate. Figure 1 displays the distribution of the SAR estimates of h_+ for the complete SAR dataset (grey bars) and for the SAR pairs considered in this study (blue bars). For the complete SAR dataset, the h_+ estimates range between $\sim$0.6 and $\sim$2.7 km, with a mean value of $\sim$1.4 km. For the dataset of 18 SAR pairs considered in this study, the h_+ estimates are higher on average, ranging between $\sim$1 and $\sim$2.7 km, with a mean value of $\sim$1.8 km. For the three SAR acquisitions of TC Goni, the h_+ estimates are $\sim$1.8, $\sim$1.4 and $\sim$1.3 km, close to the mean values from the two datasets.

Text S3: Application to four case studies

Four pairs of SAR wind profiles estimates and their corresponding predictions from the analytical model are displayed in Fig. 2. These case studies are described below.
Figure 2a presents a first case, TC Cebile, which evolved over the South-West Indian ocean in 2018 and reached category 4 on the Saffir-Simpson scale. During the beginning of its life cycle, TC Cebile was overflown by S1B on 2 January at 0022 UTC (black solid curve) and by S1A at 1323 UTC (orange solid curve). During this period, TC Cebile intensified from $V_{max} = 36$ m/s to $V_{max} = 45$ m/s, while the radius of significant upward motions contracted from $R_+ = 84$ km to $R_+ = 78$ km. For this case with a large and stagnating R_{max} $\sim$40 km, the analytical model (dashed orange curve) seemingly captures the wind speed increase in the near-core region, even though R_{max} is slightly overestimated, by $\sim$ 8 km. Within the inner-core region, *i.e* for radii below 30 km, the model underestimates the wind speed and quickly converges toward zero with decreasing radius.
A second case is presented in Fig. 2b and is that of TC Sam, a North Atlantic major hurricane of the 2021 season, which reached category 4 on the Saffir-Simpson scale. Two SAR acquisitions of TC Sam were successively performed by S1B and RS2 on 29 September at 2203 UTC and on 30 September at 0959 UTC, respectively. This period corresponds to a phase of rapid intensification, where V_{max} increased from 44 to 69 m/s, while R_+ contracted from 56 to 47 km. The increase of wind speed in the near-core region seems to be well captured by the analytical model. The stagnation of R_{max} at $23-24$ km is also caught by the analytical model, which predicts a value of 22 km. However, the sharpness of the high winds region is slightly

overestimated by the analytical model, so that, in the inner-core region, wind speeds are overestimated for radii between 10 and 20 km.
Fig. 2c displays a third case, TC Hector, which traversed the Pacific ocean during the 2018 season and reached category 4 on the Saffir-Simpson scale. During its life cycle, TC Hector was overflown by several spaceborne SAR instruments, including RS2 on 7 August at 1545 UTC and S1A on 8 August at 0414 UTC. This corresponds to a period when both V_{max} and R_+ were stagnating, at 52 m/s and 37 km, respectively. Accordingly, the two wind profiles estimated by the SAR instruments are similar. The analytical model well captures this stagnation phase in the near-core region, including the R_{max} which is located at $16-18$ km from the TC center.
A last case is showed in Fig. 2d and is that of TC Haleh, which evolved over the South-West Indian ocean in 2019 and reached category 4 on the Saffir-Simpson scale. During a weakening phase, TC Haleh was overflown by S1B at two successive times, on 6 March at 1354 UTC and on 7 March at 0049 UTC. During this period, V_{max} decreased from 41 to 30 m/s, while R_+ slightly increased from 70 to 73 km. The wind speed predicted by the analytical model is in agreement with the SAR wind profile estimate for radii larger than 60 km. However, the analytical model fails to capture the stagnation of R_{max} and predicts a value of 66 km, much larger than the $41-42$ km suggested by the SAR wind profiles estimates. As a consequence, the analytical model largely underestimates wind speeds for radii below 60 km. This last case illustrates how an error of the analytical model in the prediction of the radius of maximum winds might affect other parts of the wind profile.

Text S4: Absolute error of the analytical model

Figure 3 presents the absolute error for the persistence (Fig. 3a) and for the analytical model (Fig. 3b) as a function of normalized radius $r_* := \frac{r}{R_{max}}$.
Like for the relative error (see Fig. 2 from the main text), the absolute error considering persistent conditions (Fig. 3a) is low on average (black thick solid curve). When weakening phases (blue) are solely considered, the absolute error is positive and may be as large as 13 m/s in the region near R_{max}. Conversely, for intensifying phases (red), the absolute error is negative, of the order -20 m/s near R_{max}. Lastly, the absolute error is rather low for cases that have small V_{max} variations (grey).
Regarding the analytical model (Fig. 3b), the average absolute error is low (black thick solid curve) and positive for $1 \leq r_* \leq 5$. In contrast to persistent predictions, there is no systematic bias specific to the phase of the TC life cycle (*i.e* weakening, stagnating or intensifying). Furthermore, the distribution of absolute error values is narrower than that of persistent predictions (black thick solid curves). Near R_{max} (*i.e* for $r_* \sim 1$), both the average absolute error (2 m/s) and the spread ($\pm$2 m/s) are small.

Text S5: Model R_{max} and R_+ estimates

The performances of the analytical model in terms of radii R_{max} and R_+ are analyzed in Fig. 4. For R_{max} (Fig. 4a), the model estimates are in agreement with the final SAR estimates ($R^2 = 0.76$), although a small positive bias is apparent ($\sim$4.5 km). This bias results from the small positive bias of the model near the core region (see Fig. 3, or Fig. 2 from the main text). Remarkably, the performances of the model for R_{max} are much higher for the smaller R_{max} values, *i.e* the most intense cases.
Regarding R_+ (Fig. 4b), the model estimates are also in agreement with the final SAR estimates ($R^2 = 0.79$) and are negatively biased ($\sim$-4.0 km). This negative bias is small compared to the average R_+ value ($\sim$60 km).

References

1. Powell, M. D., Vickery, P. J. & Reinhold, T. A. Reduced drag coefficient for high wind speeds in tropical cyclones. *Nature* **422**, 279–283 (2003).
2. Zhang, J. A. & Uhlhorn, E. W. Hurricane sea surface inflow angle and an observation-based parametric model. *Mon. Weather. Rev.* **140**, 3587–3605 (2012).

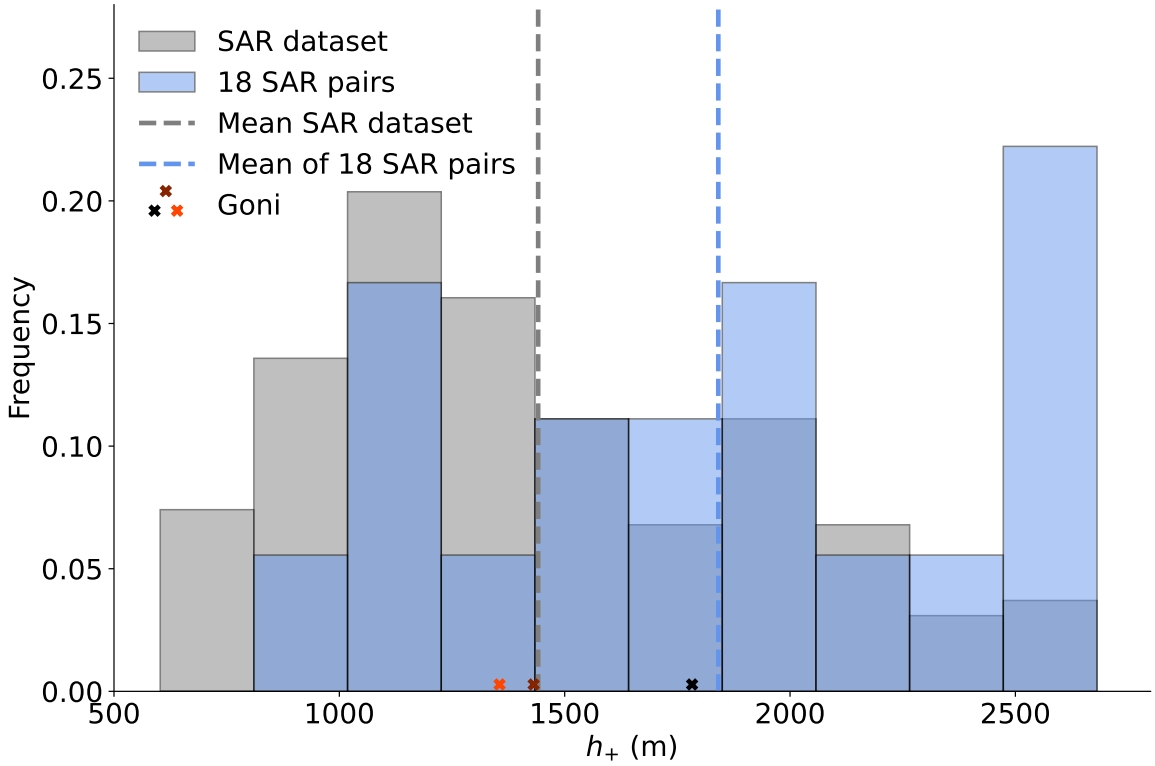

Figure 1. SAR estimates of h_+ after applying Eqs. 24, 26, 27 for the complete SAR dataset (grey bars) and for the dataset of 18 SAR pairs considered in the present study (blue bars). Dashed vertical lines correspond to the mean values from both datasets, while the three cross marks indicate the values corresponding to the three SAR acquisitions of TC Goni, following the color code used in Fig. 1 from the main text.

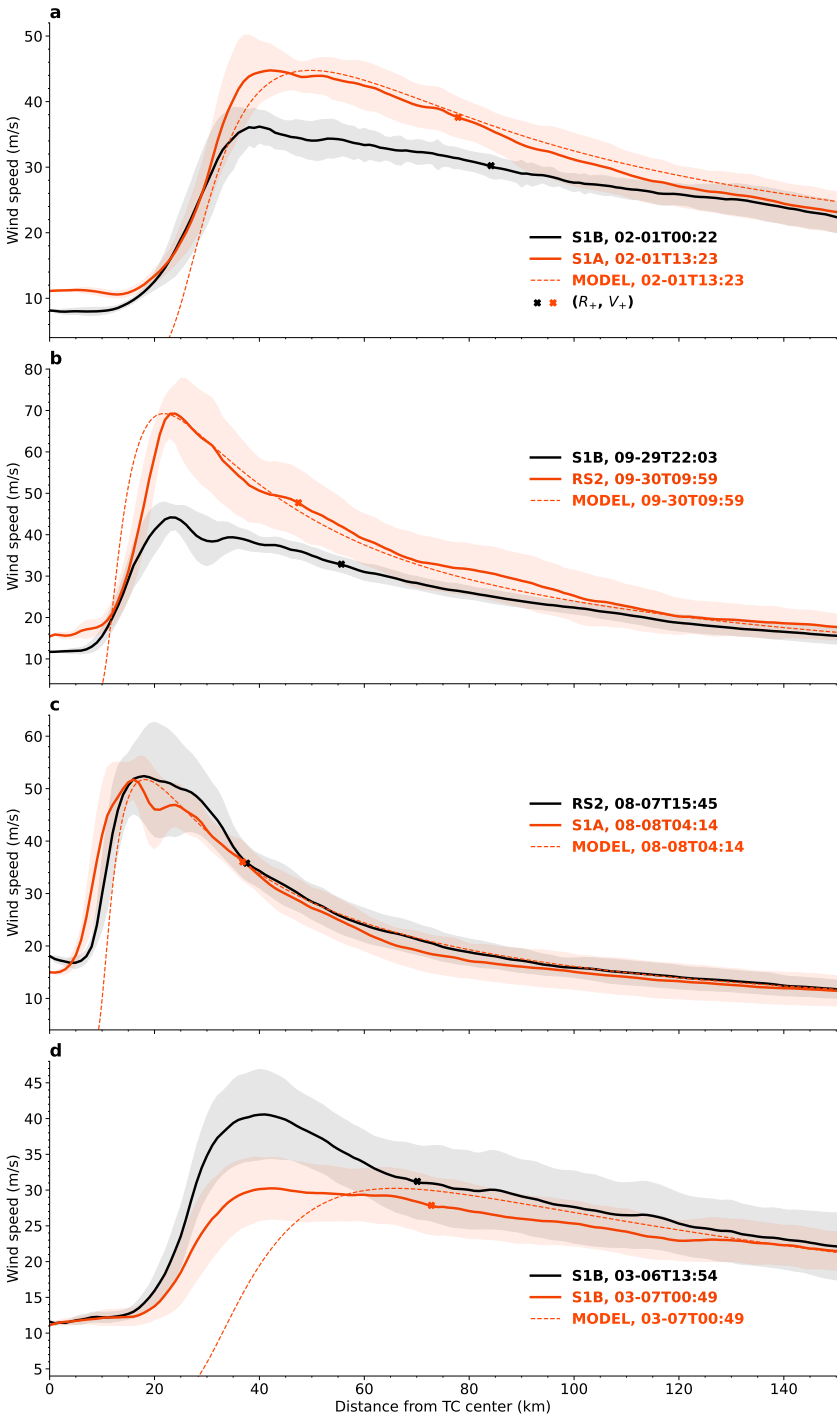

Figure 2. Initial (black solid curve) and final (orange solid curve) SAR wind profiles estimates, standard deviation along each azimuth (dashed area), as well as analytical model predictions (orange dashed curve) for (a) TC Cebile in 2018, (b) TC Sam in 2021, (c) TC Hector in 2018 and (d) TC Haleh in 2019.

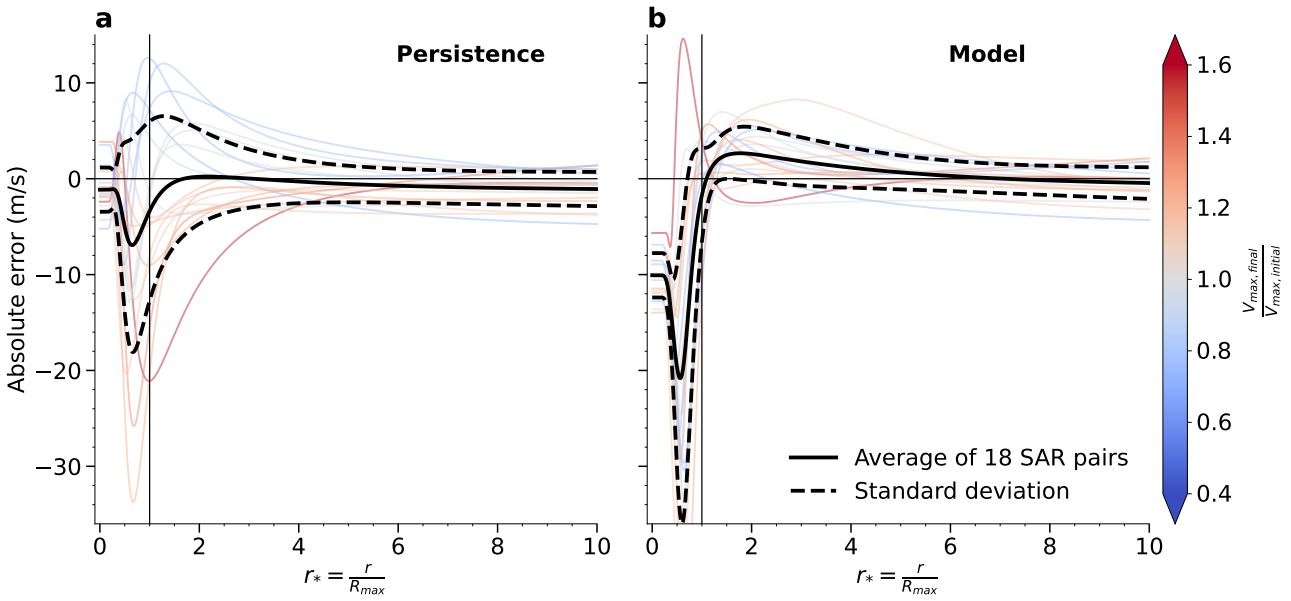

Figure 3. Same as Fig. 2 from the main text, but for absolute error (m/s).

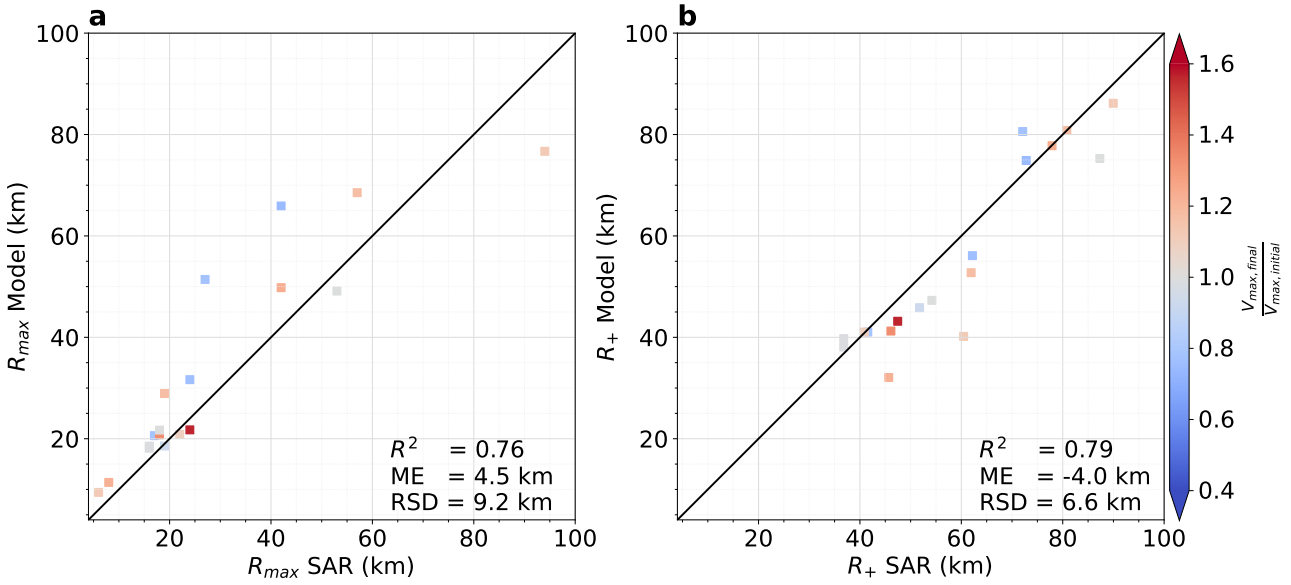

Figure 4. Comparison between model (y-axis) and SAR (x-axis) R_{max} estimates (a), and R_+ estimates (b). The different SAR pairs (squares) are colored by ratio of the final over the initial SAR V_{max} estimates. R^2 is the coefficient of determination, ME the mean error, RSD the residual standard deviation.

4.3 Conclusion

In this chapter we developed an analytical solution for the short-term evolution of the TC wind structure. The analytical model relies on an effective frictional parameter λ and was validated against SAR wind profile estimates. The analysis highlights how the initial high-resolution wind profile and the corresponding location of the radius of significant upward motions R_+ modulate the wind structure evolution.

The persistence of observed outer-core wind profiles poses challenges for efficient adjustment of the analytical model from low-resolution observations or numerical simulations. Currently, the calibration of λ requires a future intensity estimate, and the proposed framework suggests using best-track reanalyses or objective analyses from spaceborne data. Future satellite missions and airborne acquisitions that shall provide improved wind vectors estimates in the near-core region are expected to enhance our understanding of TC dynamics.

In the proposed framework, the dependence of the boundary layer depth h on radius is assumed linear when prescribing λ. However, in classic linear BL theories, h does not depend linearly on radius. Rather, h is controlled by both the wind profile v and the viscosity coefficient K (Eq. 1.20). Hence, analytical solutions such as that presented in this chapter may be used to directly assess the value of K when the radial circulation is prescribed (see for instance Pandey and Maurya, 2018), and further work is needed to combine such an approach with a time series of observed TC wind profiles.

CONCLUSION

In this thesis we evaluated how the near-core structural features, only resolved by high-resolution instruments, contribute to the TC life cycle, and established spatio-temporal constraints on the surface wind structure, based on fundamental conservation laws. Here we synthesize the main results of the present manuscript, and discuss the perspectives that it opens up.

As mentioned in **Chapter 1**, the spaceborne instruments that are historically the most often used to sense the ocean surface below TCs (*i.e* orbiting scatterometers and radiometers) fail to accurately capture the surface wind decay near the core of the most intense TCs. Even though these sensors are well suited to estimate the TC outer-core properties, theories suggest that both the amplitude of the strongest winds (V_{max}) and their radial extent (R_{max}) are critical for TCs dynamics. Until a better spatio-temporal sampling of the high-resolution instruments is achieved, the lack of systematic reliable near-core surface wind structure estimates needs to be addressed.

A natural way to tackle this issue is to assess whether near-core structural features may be estimated from the TC outer-core properties. In **Chapter 2**, a database of high-resolution TC ocean surface wind speed estimates from SAR measurements was used to statistically adjust R_{max} in the lower-resolution wind speed estimates provided a coincident knowledge of V_{max}. In such a situation, a statistical approach is rather efficient because of fundamental conservation laws (PV conservation close to the surface or angular momentum conservation in the above flow). Yet, the variability of the surface wind decay encountered in nature, which encodes and modulates these fundamental conservation laws, is too large to be captured by simple statistical relationships, so that for some events, the correction fails. The dynamical properties of such cases, which may only be identified with high-resolution measurements, should be investigated.

This matter is treated in **Chapter 3**, starting from the basic consideration that the surface wind decay controls the amplitude of vertical velocities in the TC system. Due to Ekman pumping in the BL, these upward motions are significant in a domain that goes from inside the core of the TC to approximately twice the radius of maximum wind. At such radii, where key turbulent air-sea exchanges occur, the vertical velocities can be

related to the total heat gained by the TC system, while the surface wind decay encodes the energy lost by friction. This near-core region, which may be efficiently identified with a SAR high-resolution observation, is thus crucial for the TC kinetic energy steady-state equilibrium. Analysis of TCs surface wind decay estimated using SAR measurements and kinetic energy time changes estimated from reference datasets (best-tracks) corroborate that an instantaneous knowledge of the near-core surface wind decay informs on future changes in TC kinetic energy.

A natural extension of these results is to develop a model for the evolution of the complete TC wind structure from an instantaneous high-resolution wind profile estimate. This is attempted in **Chapter 4**, where such a model is analytically derived. In the proposed theoretical framework, the evolution of the wind profile can be predicted on short periods ($\sim$12 hours) when the intensity change is known. The analytical model is shown to be in agreement with SAR measurements. The analysis also showed the limitations of using such a simplified model: with the axisymmetric and small inflow angle assumptions, the TC outer-core wind profile is roughly persistent in time, while the near-core wind speeds may experience drastic changes. Such an outcome prevents the potential correction of lower-resolution near-core measurements solely from the variations of the outer-core wind speed estimates.

These last remarks illustrate two of the main limitations of the present thesis. First, from a theoretical perspective, the assumption of axisymmetry hampers the appropriate treatments of three-dimensional turbulent processes that are important for the TC evolution (Persing et al., 2013). In particular, asymmetries in the BL are known to be controlled by the turbulent diffusivity coefficient once the translation speed is prescribed (Shapiro, 1983; Kepert, 2001). Because surface asymmetries may manifest themselves on large spatial scales, they could be investigated with lower-resolution measurements. In our axisymmetric framework, the benefit of using the vortex asymmetries measured from lower-resolution sensors to better constrain the system equations, in particular the drag coefficient, could not have been exploited. Second, an assumption of small inflow angle was made all along the manuscript, *i.e* the radial component of the wind speed was neglected *versus* the tangential component. Hence, scalar wind intensity estimates from SAR were used to address the thesis questions, whereas the developed theoretical framework would have ideally required the knowledge of tangential wind speeds. Though corroborated by dropsondes observations, the assumption mainly results from a measurement limitation. Indeed, the development of an algorithm able to routinely estimate two-dimensional wind

directions over the whole vortex, including near the TC core, from existing sensors (*e.g* from SAR), is still ongoing. Such a product would, in fact, set a milestone in the field of TCs surface wind measurements, in the same way SAR cross-polarization did when it was first used to extend surface wind speeds estimates at high winds. With such data, the results of this thesis should certainly be revisited.

Apart from these algorithmic considerations, the issue of directional estimates in TCs may also be tackled by instrumental developments. In the future, improved surface wind vectors estimates should be provided at medium-resolution by the second generation meteorological operational satellite programme (Metop-SG), starting 2025. Unlike the current Metop instrument, ASCAT, which only has co-polarization measurements, scatterometers onboard Metop-SG will operate with both co- and cross-polarization. Hence, near the core of the TC, the wind vectors estimates will benefit from the higher sensitivity of cross-polarized signals to ocean breaking waves. In addition, the coming Copernicus imaging microwave radiometer (CIMR), planned for 2025, promises to offer a global coverage thanks to its large swath, with improved resolution and low uncertainty observation capabilities. Combining L-, C- and X-band frequencies, this mission shall provide improved surface wind vectors estimates under TC conditions (Kilic et al., 2018).

Despite its lower spatio-temporal sampling, improved surface wind vectors estimates near the core of the TC may also be possible at high-resolution with the future Harmony mission, the ESA Earth Explorer 10, whose launch is expected by the end of the decade (ESA, 2022). Augmenting Sentinel-1D observations with two satellite companions, this mission shall provide azimuth diversity from these bi-static observations and help to better characterize turbulent processes near the ocean surface. Lastly, measurements of wind vectors profiles in the BL may be allowed by the Doppler-based motions derived from the imaging wind and rain airborne profiler (IWRAP) instrument. Limited to a few TC events, measurements from this sensor are already being analyzed and processed (Sapp et al., 2022). As suggested by this thesis and the equations of angular momentum conservation, acquisitions from both the Harmony mission and the IWRAP instrument shall allow to better appreciate the BL height and inflow characteristics, including near the TC core, to investigate air-sea turbulent exchanges.

In addition to these future missions, the spatio-temporal sampling of SAR instruments is expected to drastically increase in the next few years. For instance, the C-band SAR coverage was recently augmented by the Radarsat constellation mission (RCM), a series of three satellites launched in 2019. Furthermore, the Sentinel-1 next generation (S1-NG)

mission, planned for the next decade, shall ensure the continuity of the C-band SAR services from Sentinel-1A and -B. To complement these sensors, a myriad of L-band SAR instruments, which shall be less impacted by rain than their C-band counterparts, will also be launched. This includes the advanced land observing satellite 4 (ALOS-4) and the NASA-ISRO synthetic aperture radar (NISAR) missions, which should be launched in the current year, and the radar observation system for Europe in L-band (ROSE-L) mission, which is planned for 2028.

By providing a theoretical framework to investigate TCs evolution and dynamical properties, the present thesis anticipates and prepares the significant increase in the number of SAR acquisitions. An analytical guide to interpret the large amount of information contained in these high-resolution measurements, which shall soon be available at a high temporal sampling, is essential. Conversely, the accumulation of SAR observations may be useful to further investigate issues raised by this thesis. For instance, regarding turbulent air-sea exchanges, our results suggest a decrease or saturation of the drag coefficient with wind speed at high winds (above $\sim$30 m/s). While this preliminary outcome deserves further examination, SAR measurements may be instrumental to better characterize turbulent air-sea properties under extreme winds conditions, a prerequisite to assess the upper bound of the TC intensity. Analysis of the observations also shows that, along their life cycle, TCs are close to a steady-state in which their intensity is controlled by a characteristic velocity, which depends on oceanic and atmospheric environmental variables. Although this fact was well known from TCs theories, the thesis reveals that a given SAR observation provides an indirect estimate of this characteristic velocity. Hence, the accumulation of SAR measurements shall inform on how the steady-state intensity and equilibrium are affected by the environmental background from a given ocean region or climate scenario.

To complement surface observations and better assess how the oceanic and atmospheric background influence the TC dynamical properties, other instruments may be used, that sense the system at different levels. In the ocean, the SST controls the steady-state equilibrium of TCs (K. A. Emanuel, 1986). Furthermore, the upper ocean salinity stratification contains a predictive information on the TC intensification (Balaguru et al., 2020). Hence, both SST and SSS, which may be assessed with global coverage using passive microwave satellite data, could help better characterizing the TC dynamical properties. In addition, estimating the SSH in the wake of TCs, for instance using spaceborne microwave altimetry, may inform on the relationship between the TC near-core

wind structure and the upper ocean (Combot, Quilfen, et al., 2020). Observations of the oceanic near-surface conditions can be supplemented by in-situ measurements, which may also provide a precious knowledge of the water column properties. For instance, buoys, underwater gliders, and dropsondes, are all undergoing constant innovation and developments, and shall be soon complemented by saildrones (C. Zhang et al., 2023). In the atmosphere, vertical distributions estimates of atmospheric temperature in the TC system from spaceborne sounding microwave instruments should allow to better constrain the wind structure. Cloud characteristics at the top of the TC can also be used for this purpose. In particular, the contribution of the radius of vanishing winds (R_0) in the outflow to the TC life cycle is known from both theoretical (Riehl, 1963) and empirical (Dvorak, 1975, 1984) studies. In this thesis, this radius was estimated from surface measurements based on angular momentum conservation in the outflow. Yet, direct estimates of R_0 from geostationary satellite visible or infrared data would certainly help refining the theoretical framework presented here. More generally, better understanding the link between the TC surface wind structure and these cloud properties would allow to leverage the high spatial and temporal resolution of geostationary satellites measurements to reinterpret historical data and better monitor future events.

Although no mission exclusively dedicated to the measurement of TCs ocean surface wind speeds is expected in the next years, the future is bright, with a myriad of medium- and high-resolution instruments to come, that will help assessing the wind structure near the TC core. Yet, should such a specific mission be under consideration, like with the recent cyclone global navigation satellite (CYGNSS) mission (Ruf et al., 2012), a few scientific requirements can be drawn from this thesis. Emphasized in the present work, both V_{max} and R_{max} are crucial for the TC life cycle. From historical records, the strongest winds ever reported, those of TC Tip in 1979, exceeded ∼95 m/s. Hence, for a hypothetical dedicated mission, the instrument specifications should allow two-dimensional surface wind vectors measurements at least up to ∼100 m/s, to capture such intensities and anticipate the more violent events expected in the future. To characterize the smallest possible R_{max} values, the sensor should have have a spatial resolution of ∼5 km or lower, according to the SAR database. If V_{max} and R_{max} estimates can already be obtained by ancillary data (*e.g* orbiting SAR instruments and/or geostationary satellite indirect estimates), the thesis revealed that the knowledge of the surface wind decay, or equivalently, the radius of significant upward motions (R_+), is essential. From the SAR database, R_+ can correspond to wind speeds as high as ∼45 m/s, and be located as close as ∼30 km from

the TC center, providing more accessible orders of magnitude. Because the system size, *e.g* R_0, can be estimated from V_{max}, R_{max}, and the latitude of the TC center (or f), the instrument swath may be rather small. Yet, the highest R_+ estimates exceed ∼90 km, and asymmetries in the surface wind field may occur at even larger spatial scales. Thus, a swath of ∼500 km or higher, is recommended. In addition, the larger the swath width, the shorter the revisit time of the sensor. From the present work, a high-resolution wind profile measurement may allow for short-term (∼12 hours) predictions. Consequently, a temporal sampling of at least ∼24 hours for the hypothetical mission to fill the gaps is required. While this manuscript provides a rough first baseline for a mission that would be dedicated to TCs surface wind fields measurements, once again, the accumulation of SAR measurements in the future shall help refining these orders of magnitude.

Even though the assimilation of low-resolution satellite data has improved the representation of the synoptic scale steering flow and hence the forecasting of TCs trajectory over the past ∼20 years, it had little impact on intensity predictions. Physical processes associated with changes in the TC intensity, such as turbulent BL exchanges, are of much smaller scale than what can currently be resolved in the relatively coarse standard remote sensing products. Revealed by our analysis of a SAR database, the key contribution of the near-core surface wind structure on the TC dynamics could thus have been anticipated. More generally, the large amount of details that spaceborne high-resolution instruments provide on the TC system certainly requires a methodological guide to be interpreted without loss of relevant information. Using a theoretical framework, this thesis revealed the importance of the radius of significant upward motions (R_+) and corroborated that of the radius of vanishing winds (R_0) for the TC evolution. The identification of such critical parameters shall benefit the training of neural network models, especially with the coming increase in the spatio-temporal sampling of high-resolution sensors. Lastly, while the present work focused on TCs, the more general question of how an instantaneous and rich, though partial observation of a system state informs on its evolution, may be encountered in the study of various other dynamical phenomena.

BIBLIOGRAPHY

Allison, L. J., Rodgers, E. B., Wilheit, T. T., & Fett, R. W., (1974), Tropical cyclone rainfall as measured by the nimbus 5 electrically scanning microwave radiometer, *Bulletin of the American Meteorological Society*, *55 9*, 1074–1090.

Anthes, R. A., (1974), The dynamics and energetics of mature tropical cyclones, *Reviews of Geophysics*, *12 3*, 495–522.

Avenas, A., Mouche, A., Tandeo, P., Piolle, J.-F., Chavas, D., Fablet, R., Knaff, J., & Chapron, B., (2023), Reexamining the estimation of tropical cyclone radius of maximum wind from outer size with an extensive synthetic aperture radar dataset, *Monthly Weather Review*, *151 12*, 3169–3189.

Balaguru, K., Foltz, G. R., Leung, L. R., Kaplan, J., Xu, W., Reul, N., & Chapron, B., (2020), Pronounced impact of salinity on rapidly intensifying tropical cyclones, *Bulletin of the American Meteorological Society*, *101 9*, E1497–E1511.

Bandeen, W., Kunde, V., & Thompson, H., (1964), Tiros iii meteorological satellite radiation observations of a tropical hurricane, *Tellus*, *16 4*, 481–502.

Bauer, L., (1908), The relation between" potential temperature" and" entropy.", *Physical Review (Series I)*, *26 2*, 177.

Bell, M. M., Montgomery, M. T., & Emanuel, K. A., (2012), Air–sea enthalpy and momentum exchange at major hurricane wind speeds observed during cblast, *Journal of the Atmospheric Sciences*, *69 11*, 3197–3222.

Beucher, F., Belamari, S., & Beau, I., (2010), *Météorologie tropicale: des alizés au cyclone*, Météo-France.

Bian, G.-F., Nie, G.-Z., & Qiu, X., (2021), How well is outer tropical cyclone size represented in the era5 reanalysis dataset?, *Atmospheric Research*, *249*, 105339.

Bigler, S. G., (1981), Radar: a short history, *Weatherwise*, *34 4*, 158–163.

Bister, M., & Emanuel, K. A., (1998), Dissipative heating and hurricane intensity, *Meteorology and Atmospheric Physics*, *65*, 233–240.

Black, P. G., D'Asaro, E. A., Drennan, W. M., French, J. R., Niiler, P. P., Sanford, T. B., Terrill, E. J., Walsh, E. J., & Zhang, J. A., (2007), Air–sea exchange in hurri-

canes: synthesis of observations from the coupled boundary layer air–sea transfer experiment, *Bulletin of the American Meteorological Society*, *88 3*, 357–374.

Born, G., Dunne, J., & Lame, D., (1979), Seasat mission overview, *Science*, *204 4400*, 1405–1406.

Brennan, M. J., Hennon, C. C., & Knabb, R. D., (2009), The operational use of quikscat ocean surface vector winds at the national hurricane center, *Weather and Forecasting*, *24 3*, 621–645, https://doi.org/10.1175/2008WAF2222188.1

Bui, H. H., Smith, R. K., Montgomery, M. T., & Peng, J., (2009), Balanced and unbalanced aspects of tropical cyclone intensification, *Quarterly Journal of the Royal Meteorological Society: A journal of the atmospheric sciences, applied meteorology and physical oceanography*, *135 644*, 1715–1731.

Carrier, G., Hammond, A., & George, O., (1971), A model of the mature hurricane, *Journal of Fluid Mechanics*, *47 1*, 145–170.

Charney, J. G., & Eliassen, A., (1964), On the growth of the hurricane depression, *Journal of Atmospheric Sciences*, *21 1*, 68–75.

Chavas, D. R., & Knaff, J. A., (2022), A simple model for predicting the tropical cyclone radius of maximum wind from outer size, *Weather and Forecasting*, *37 5*, 563–579.

Chavas, D. R., Lin, N., & Emanuel, K., (2015), A model for the complete radial structure of the tropical cyclone wind field. part i: comparison with observed structure, *Journal of the Atmospheric Sciences*, *72 9*, 3647–3662.

Combot, C., (2023), *Mixing and sea surface anomalies in the inertial wake of tropical cyclones: processes and contribution of microwave satellite data* (Doctoral dissertation), Brest.

Combot, C., Mouche, A., Knaff, J., Zhao, Y., Zhao, Y., Vinour, L., Quilfen, Y., & Chapron, B., (2020), Extensive high-resolution synthetic aperture radar (sar) data analysis of tropical cyclones: comparisons with sfmr flights and best track, *Monthly Weather Review*, *148 11*, 4545–4563.

Combot, C., Quilfen, Y., Mouche, A., Gourrion, J., de Boyer Montégut, C., Chapron, B., & Tournadre, J., (2020), Space-based observations of surface signatures in the wakes of the 2018 eastern pacific tropical cyclones, *Journal of Operational Oceanography*, *13 Suppl. 1*.

Cronin, T. W., (2023), An analytic model for tropical cyclone outer winds, *Geophysical Research Letters*, *50 11*, e2023GL103942.

Curcic, M., & Haus, B. K., (2020), Revised estimates of ocean surface drag in strong winds, *Geophysical research letters*, *47 10*, e2020GL087647.

DeMaria, M., (2009), A simplified dynamical system for tropical cyclone intensity prediction, *Monthly Weather Review*, *137 1*, 68–82.

Demuth, J. L., DeMaria, M., & Knaff, J. A., (2006), Improvement of advanced microwave sounding unit tropical cyclone intensity and size estimation algorithms, *Journal of applied meteorology and climatology*, *45 11*, 1573–1581.

Demuth, J. L., DeMaria, M., Knaff, J. A., & Haar, T. H. V., (2004), Evaluation of advanced microwave sounding unit tropical-cyclone intensity and size estimation algorithms, *Journal of Applied Meteorology and Climatology*, *43 2*, 282–296.

Denney, W. J., (1969), The eastern pacific hurricane season of 1968, *Monthly Weather Review*, *97 3*, 207–224.

Denur, J., (2011), The apparent "super-carnot" efficiency of hurricanes: nature's steam engine versus the steam locomotive, *American Journal of Physics*, *79 6*, 631–643.

Deppermann, C. E., (1947), Notes on the origin and structure of philippine typhoons, *Bulletin of the American Meteorological Society*, 399–404.

Donelan, M., Haus, B. K., Reul, N., Plant, W., Stiassnie, M., Graber, H., Brown, O. B., & Saltzman, E., (2004), On the limiting aerodynamic roughness of the ocean in very strong winds, *Geophysical Research Letters*, *31 18*.

Donelan, M. A., (2018), On the decrease of the oceanic drag coefficient in high winds, *Journal of Geophysical Research: Oceans*, *123 2*, 1485–1501.

Donnelly, W. J., Carswell, J. R., McIntosh, R. E., Chang, P. S., Wilkerson, J., Marks, F., & Black, P. G., (1999), Revised ocean backscatter models at c and ku band under high-wind conditions, *Journal of Geophysical Research: Oceans*, *104 C5*, 11485–11497.

Dunion, J. P., Houston, S. H., Velden, C. S., & Powell, M. D., (2002), Application of surface-adjusted goes low-level cloud-drift winds in the environment of atlantic tropical cyclones. part ii: integration into surface wind analyses, *Monthly weather review*, *130 5*, 1347–1355.

Duong, Q.-P., Wimmers, A., Herndon, D., Tan, Z.-M., Zhuo, J.-Y., Knaff, J., Al Abdulsalam, I., Horinouchi, T., Miyata, R., & Avenas, A., (2023), Objective satellite methods including ai algorithms reviewed for the tenth international workshop on tropical cyclones (iwtc-10), *Tropical Cyclone Research and Review*.

Dvorak, V. F., (1972), A technique for the analysis and forecasting of tropical cyclone intensities from satellite pictures, NOAA Tech. Memo. NESS 36, 15 pp.

Dvorak, V. F., (1973), A technique for the analysis and forecasting of tropical cyclone intensities from satellite pictures, NOAA Tech. Memo. NESS 45, 19 pp.

Dvorak, V. F., (1975), Tropical cyclone intensity analysis and forecasting from satellite imagery, *Monthly Weather Review*, *103 5*, 420–430.

Dvorak, V. F., (1984), *Tropical cyclone intensity analysis using satellite data* (Vol. 11), US Department of Commerce, National Oceanic; Atmospheric Administration ...

Eliassen, A., (1971), On the ekman layer in a circular vortex, *Journal of the Meteorological Society of Japan. Ser. II*, *49*, 784–789.

Eliassen, A., (1951), Slow thermally or frictionally controlled meridional circulation in a circular vortex, *Astrophisica Norvegica, v. 5, p. 19*, *5*, 19.

Eliassen, A., & Lystad, M., (1977), The ekman layer of a circular vortex-a numerical and theoretical study, *Geophysica Norvegica*, *31 7*, 1–16.

Emanuel, K., (2004), Tropical cyclone energetics and structure, *Atmospheric turbulence and mesoscale meteorology*, *165*, 192.

Emanuel, K., & Rotunno, R., (2011), Self-stratification of tropical cyclone outflow. part i: implications for storm structure, *Journal of the Atmospheric Sciences*, *68 10*, 2236–2249.

Emanuel, K. A., (1986), An air-sea interaction theory for tropical cyclones. part i: steady-state maintenance, *Journal of Atmospheric Sciences*, *43 6*, 585–605.

ESA, (2022), *Report for mission selection: earth explorer 10 candidate mission harmony* (tech. rep.), ESA, Noordwijk, The Netherlands, European Space Agency.

Evans, H., & Davies, D., (1979), On the use of an analytic solution in estimating eddy viscosity distribution and water vapour flux in a mature hurricane, *Quarterly Journal of the Royal Meteorological Society*, *105 445*, 551–569.

Fett, R. W., (1964), Aspects of hurricane structure: new model considerations suggested by tiros and project mercury observations, *Monthly Weather Review*, *92 2*, 43–60.

Franklin, J. L., Black, M. L., & Valde, K., (2003), Gps dropwindsonde wind profiles in hurricanes and their operational implications, *Weather and forecasting*, *18 1*, 32–44.

Frisius, T., (2005), An atmospheric balanced model of an axisymmetric vortex with zero potential vorticity, *Tellus A: Dynamic Meteorology and Oceanography*, *57 1*, 55–64.

Fritz, S., Hubert, L. F., & Timchalk, A., (1966), Some inferences from satellite pictures of tropical disturbances, *Monthly Weather Review*, *94 4*, 231–236.

Fu, L.-L., (1982), *Seasat views oceans and sea ice with synthetic-aperture radar* (Vol. 81), California Institute of Technology, Jet Propulsion Laboratory.

Gaiser, P. W., St Germain, K. M., Twarog, E. M., Poe, G. A., Purdy, W., Richardson, D., Grossman, W., Jones, W. L., Spencer, D., Golba, G., et al., (2004), The windsat spaceborne polarimetric microwave radiometer: sensor description and early orbit performance, *IEEE Transactions on Geoscience and Remote Sensing*, *42 11*, 2347–2361.

Gentry, R. C., Fujita, T. T., & Sheets, R. C., (1970), Aircraft, spacecraft, satellite and radar observations of hurricane gladys, 1968, *Journal of Applied Meteorology and Climatology*, *9 6*, 837–850.

Goldberg, M. D., Crosby, D. S., & Zhou, L., (2001), The limb adjustment of amsu-a observations: methodology and validation, *Journal of Applied Meteorology and Climatology*, *40 1*, 70–83.

Golitsyn, G., (2008), Polar lows and tropical hurricanes: their energy and sizes and a quantitative criterion for their generation, *Izvestiya, Atmospheric and Oceanic Physics*, *44*, 537–547.

Gonzalez, F., Thompson, T., Brown Jr, W., & Weissman, D., (1982), Seasat wind and wave observations of northeast pacific hurricane iva, august 13, 1978, *Journal of Geophysical Research: Oceans*, *87 C5*, 3431–3438.

Goodberlet, M., Swift, C., & Wilkerson, J., (1989), Remote sensing of ocean surface winds with the special sensor microwave/imager, *Journal of Geophysical Research: Oceans*, *94 C10*, 14547–14555.

Gray, W. M., (1968), Global view of the origin of tropical disturbances and storms, *Monthly Weather Review*, *96 10*, 669–700.

Hack, J. J., & Schubert, W. H., (1986), Nonlinear response of atmospheric vortices to heating by organized cumulus convection, *Journal of Atmospheric Sciences*, *43 15*, 1559–1573.

Harrington, R. F., (1980), *The development of a stepped frequency microwave radiometer and its application to remote sensing of the earth*, Old Dominion University.

Hawkins, J. D., & Black, P. G., (1983), Seasat scatterometer detection of gale force winds near tropical cyclones, *Journal of Geophysical Research: Oceans*, *88 C3*, 1674–1682.

Hendricks, E. A., Vigh, J. L., & Rozoff, C. M., (2021), Forced, balanced, axisymmetric shallow water model for understanding short-term tropical cyclone intensity and wind structure changes, *Atmosphere*, *12 10*, 1308.

Herndon, D., Velden, C., Hawkins, J., Olander, T., & Wimmers, A., (2010), The cimss satellite consensus (satcon) tropical cyclone intensity algorithm, *29th Conference on Hurricanes and Tropical Meteorology D*, *4*.

Hilleary, D., & Christensen, F., (1957), *Instrumentation of national hurricane research project aircraft*, US Department of Commerce, Weather Bureau.

Hock, T. F., & Franklin, J. L., (1999), The ncar gps dropwindsonde, *Bulletin of the American Meteorological Society*, *80 3*, 407–420.

Hodges, K., Cobb, A., & Vidale, P. L., (2017), How well are tropical cyclones represented in reanalysis datasets?, *Journal of Climate*, *30 14*, 5243–5264.

Holland, G. J., (1980), An analytic model of the wind and pressure profiles in hurricanes, *Monthly Weather Review*, *108*, 1212–1218.

Holland, G. J., (1982), *Tropical cyclone motion: environmental interaction plus a beta effect*, Department of Atmospheric Science, Colorado State University.

Hollinger, J., et al., (1989), Dmsp special sensor microwave/imager calibration/validation, *Final report*, *1*, 51.

Horstmann, J., Thompson, D., Monaldo, F., Iris, S., & Graber, H., (2005), Can synthetic aperture radars be used to estimate hurricane force winds?, *Geophysical Research Letters*, *32 22*.

Hubert, L. F., (1969), *Estimating maximum wind speed of tropical storms from high resolution of infrared data* (Vol. 50), US Department of Commerce, Environmental Science Services Administration ...

Hwang, P. A., Stoffelen, A., van Zadelhoff, G.-J., Perrie, W., Zhang, B., Li, H., & Shen, H., (2015), Cross-polarization geophysical model function for c-band radar backscattering from the ocean surface and wind speed retrieval, *Journal of Geophysical Research: Oceans*, *120 2*, 893–909.

Hwang, P. A., Zhang, B., & Perrie, W., (2010), Depolarized radar return for breaking wave measurement and hurricane wind retrieval, *Geophysical Research Letters*, *37 1*.

Jaiswal, N., Kumar, P., & Kishtawal, C., (2019), Scatsat-1 wind products for tropical cyclone monitoring, prediction and surface wind structure analysis, *Current Science*, *117 6*, 983–992.

Jarosz, E., Mitchell, D. A., Wang, D. W., & Teague, W. J., (2007), Bottom-up determination of air-sea momentum exchange under a major tropical cyclone, *Science*, *315 5819*, 1707–1709.

Jones, W. L., Black, P. G., Delnore, V. E., & Swift, C. T., (1981), Airborne microwave remote-sensing measurements of hurricane allen, *Science*, *214 4518*, 274–280.

Jones, W. L., Schroeder, L. C., Boggs, D. H., Bracalente, E. M., Brown, R. A., Dome, G. J., Pierson, W. J., & Wentz, F. J., (1982), The seasat-a satellite scatterometer: the geophysical evaluation of remotely sensed wind vectors over the ocean, *Journal of Geophysical Research: Oceans*, *87 C5*, 3297–3317.

Jordan, A. K., Purves, C. G., & Diggs, J. F., (1976), An analysis of skylab ii s193 scatterometer data, *IEEE Transactions on Geoscience Electronics*, *14 2*, 97–100.

Jordan, C. L., (1952), On the low-level structure of the typhoon eye, *Journal of Atmospheric Sciences*, *9 4*, 285–290.

Kalashnik, A., & Kalashnik, M., (2011), Analytical model of the intensification of a tropical cyclone, *Izvestiya, Atmospheric and Oceanic Physics*, *47 6*, 766–779.

Kalashnik, M., (1994), On the maximum wind velocity in the tropical cyclone, *Izvestiâ Akademii nauk SSSR. Fizika atmosfery i okeana*, *30 1*, 26–30.

Katsaros, K. B., Vachon, P. W., Black, P. G., Dodge, P. P., & Uhlhorn, E. W., (2000), Wind fields from sar: could they improve our understanding of storm dynamics?, *Johns Hopkins APL Technical Digest*, *21 1*, 86–93.

Kepert, J., (2001), The dynamics of boundary layer jets within the tropical cyclone core. part i: linear theory, *Journal of the Atmospheric Sciences*, *58 17*, 2469–2484.

Kidder, S. Q., Gray, W. M., & Vonder Haar, T. H., (1978), Estimating tropical cyclone central pressure and outer winds from satellite microwave data, *Monthly Weather Review*, *106 10*, 1458–1464.

Kieu, C. Q., & Zhang, D.-L., (2009), An analytical model for the rapid intensification of tropical cyclones, *Quarterly Journal of the Royal Meteorological Society: A journal of the atmospheric sciences, applied meteorology and physical oceanography*, *135 642*, 1336–1349.

Kilic, L., Prigent, C., Aires, F., Boutin, J., Heygster, G., Tonboe, R. T., Roquet, H., Jimenez, C., & Donlon, C., (2018), Expected performances of the copernicus imaging microwave radiometer (cimr) for an all-weather and high spatial resolution estimation of ocean and sea ice parameters, *Journal of Geophysical Research: Oceans*, *123 10*, 7564–7580.

Klimenko, A., (2014), Strong swirl approximation and intensive vortices in the atmosphere, *Journal of fluid mechanics*, *738*, 268–298.

Knaff, J. A., & DeMaria, M., (2006), A multi-platform satellite tropical cyclone wind analysis system, *AMS 14th Conference on Satellite Meteorology and Oceanography*, *29*.

Knaff, J. A., DeMaria, M., Molenar, D. A., Sampson, C. R., & Seybold, M. G., (2011), An automated, objective, multiple-satellite-platform tropical cyclone surface wind analysis, *Journal of Applied Meteorology and Climatology*, *50 10*, 2149–2166, https://doi.org/10.1175/2011JAMC2673.1

Knaff, J. A., Sampson, C. R., Kucas, M. E., Slocum, C. J., Brennan, M. J., Meissner, T., Ricciardulli, L., Mouche, A., Reul, N., Morris, M., et al., (2021), Estimating tropical cyclone surface winds: current status, emerging technologies, historical evolution, and a look to the future, *Tropical Cyclone Research and Review*, *10 3*, 125–150.

Knapp, K. R., Kruk, M. C., Levinson, D. H., Diamond, H. J., & Neumann, C. J., (2010), The international best track archive for climate stewardship (ibtracs) unifying tropical cyclone data, *Bulletin of the American Meteorological Society*, *91 3*, 363–376.

Kossin, J. P., Knaff, J. A., Berger, H. I., Herndon, D. C., Cram, T. A., Velden, C. S., Murnane, R. J., & Hawkins, J. D., (2007), Estimating hurricane wind structure in the absence of aircraft reconnaissance, *Weather and Forecasting*, *22 1*, 89–101.

La Seur, N., & Hawkins, H. F., (1963), An analysis of hurricane cleo (1958) based on data from research reconnaissance aircraft, *Monthly Weather Review*, *91 10*, 694–709.

Landsea, C. W., & Franklin, J. L., (2013), Atlantic hurricane database uncertainty and presentation of a new database format, *Monthly Weather Review*, *141 10*, 3576–3592.

Leonov, A. I., et al., (2014), Analytical models for hurricanes, *Open Journal of Marine Science*, *4 03*, 194.

Li, M., Zhang, J. A., Matak, L., & Momen, M., (2023), The impacts of adjusting momentum roughness length on strong and weak hurricane forecasts: a comprehensive analysis of weather simulations and observations, *Monthly Weather Review*, *151 5*, 1287–1302.

Loridan, T., Khare, S., Scherer, E., Dixon, M., & Bellone, E., (2015), Parametric modeling of transitioning cyclone wind fields for risk assessment studies in the western north pacific, *Journal of Applied Meteorology and Climatology*, *54 3*, 624–642.

Marks Jr, F. D., & Houze Jr, R. A., (1984), Airborne doppler radar observations in hurricane debby, *Bulletin of the American Meteorological Society*, *65 6*, 569–582.

McTaggart-Cowan, R., Bosart, L. F., Davis, C. A., Atallah, E. H., Gyakum, J. R., & Emanuel, K. A., (2006), Analysis of hurricane catarina (2004), *Monthly Weather Review*, *134 11*, 3029–3053.

Meissner, T., Ricciardulli, L., & Wentz, F. J., (2017), Capability of the smap mission to measure ocean surface winds in storms, *Bulletin of the American Meteorological Society*, *98 8*, 1660–1677.

Meissner, T., & Wentz, F., (2005), Ocean retrievals for windsat: radiative transfer model, algorithm, validation, *Proceedings of OCEANS 2005 MTS/IEEE*, 130–133.

Meissner, T., & Wentz, F. J., (2009), Wind-vector retrievals under rain with passive satellite microwave radiometers, *IEEE Transactions on Geoscience and Remote Sensing*, *47 9*, 3065–3083.

Möller, J. D., & Shapiro, L. J., (2002), Balanced contributions to the intensification of hurricane opal as diagnosed from a gfdl model forecast, *Monthly weather review*, *130 7*, 1866–1881.

Momen, M., Parlange, M. B., & Giometto, M. G., (2021), Scrambling and reorientation of classical atmospheric boundary layer turbulence in hurricane winds, *Geophysical Research Letters*, *48 7*, e2020GL091695.

Montgomery, M. T., & Smith, R. K., (2010), On an analytical model for the rapid intensification of tropical cyclones, *Quarterly Journal of the Royal Meteorological Society: A journal of the atmospheric sciences, applied meteorology and physical oceanography*, *136 647*, 549–551.

Moore, R., Chaudhry, A., & Birrer, I., (1983), Errors in scatterometer-radiometer wind measurement due to rain, *IEEE Journal of Oceanic Engineering*, *8 1*, 37–49.

Mouche, A., Chapron, B., Knaff, J., Zhao, Y., Zhang, B., & Combot, C., (2019), Copolarized and cross-polarized sar measurements for high-resolution description of major hurricane wind structures: application to irma category 5 hurricane, *Journal of Geophysical Research: Oceans*, *124 6*, 3905–3922.

Mouche, A. A., Chapron, B., Zhang, B., & Husson, R., (2017), Combined co-and cross-polarized sar measurements under extreme wind conditions, *IEEE Transactions on Geoscience and Remote Sensing*, *55 12*, 6746–6755.

Mueller, K. J., DeMaria, M., Knaff, J., Kossin, J. P., & Haar, T. H. V., (2006), Objective estimation of tropical cyclone wind structure from infrared satellite data, *Weather and forecasting*, *21 6*, 990–1005.

Njoku, E., & Swanson, L., (1983), Global measurements of sea surface temperature, wind speed and atmospheric water content from satellite microwave radiometry, *Monthly weather review*, *111 10*, 1977–1987.

Nolan, D. S., Moon, Y., & Stern, D. P., (2007), Tropical cyclone intensification from asymmetric convection: energetics and efficiency, *Journal of the Atmospheric Sciences*, *64 10*, 3377–3405.

Olander, T. L., & Velden, C. S., (2007), The advanced dvorak technique: continued development of an objective scheme to estimate tropical cyclone intensity using geostationary infrared satellite imagery, *Weather and Forecasting*, *22 2*, 287–298.

Olfateh, M., Callaghan, D. P., Nielsen, P., & Baldock, T. E., (2017), Tropical cyclone wind field asymmetry—development and evaluation of a new parametric model, *Journal of Geophysical Research: Oceans*, *122 1*, 458–469.

Ooyama, K., (1964), A dynamical model for the study of tropical cyclone development., *Geofisica Internacional (Mexico)*, *4*, 187–198.

Ozawa, H., & Shimokawa, S., (2015), Thermodynamics of a tropical cyclone: generation and dissipation of mechanical energy in a self-driven convection system, *Tellus A: Dynamic Meteorology and Oceanography*, *67 1*, 24216.

Pandey, S. K., & Maurya, J. P., (2018), Exact solutions for unsteady axisymmetric vortex motions governing atmospheric vortices, *Dynamics of Atmospheres and Oceans*, *83*, 111–121.

Pearce, R. P., (2004), An axisymmetric model of a mature tropical cyclone incorporating azimuthal vorticity, *Quarterly Journal of the Royal Meteorological Society*, *130 596*, 259–293.

Persing, J., Montgomery, M. T., McWilliams, J. C., & Smith, R. K., (2013), Asymmetric and axisymmetric dynamics of tropical cyclones, *Atmospheric Chemistry and Physics*, *13 24*, 12299–12341.

Phillips, O., (1988), Radar returns from the sea surface—bragg scattering and breaking waves, *Journal of physical oceanography*, *18 8*, 1065–1074.

Piddington, H., (1848), *The sailor's horn-book for the law of storms*, 1st ed., Smith, Elder; Co., 292 pp.

Polverari, F., Portabella, M., Lin, W., Sapp, J. W., Stoffelen, A., Jelenak, Z., & Chang, P. S., (2021), On high and extreme wind calibration using ascat, *IEEE Transactions on Geoscience and Remote Sensing*, *60*, 1–10.

Powell, M. D., (1980), Evaluations of diagnostic marine boundary-layer models applied to hurricanes, *Monthly Weather Review*, *108 6*, 757–766.

Powell, M. D., (1982), The transition of the hurricane frederic boundary-layer wind field from the open gulf of mexico to landfall, *Monthly Weather Review*, *110 12*, 1912–1932.

Powell, M. D., Houston, S. H., Amat, L. R., & Morisseau-Leroy, N., (1998), The hrd real-time hurricane wind analysis system, *Journal of Wind Engineering and Industrial Aerodynamics*, *77*, 53–64.

Powell, M. D., Vickery, P. J., & Reinhold, T. A., (2003), Reduced drag coefficient for high wind speeds in tropical cyclones, *Nature*, *422 6929*, 279–283.

Quilfen, Y., Chapron, B., Elfouhaily, T., Katsaros, K., & Tournadre, J., (1998), Observation of tropical cyclones by high-resolution scatterometry, *Journal of Geophysical Research: Oceans*, *103 C4*, 7767–7786.

Quilfen, Y., Vandemark, D., Chapron, B., Feng, H., & Sienkiewicz, J., (2011), Estimating gale to hurricane force winds using the satellite altimeter, *Journal of Atmospheric and Oceanic Technology*, *28 4*, 453–458.

Ramsay, H., (2017), The global climatology of tropical cyclones. *In Oxford research encyclopedia of natural hazard science*.

Ren, Y., Zhang, J. A., Guimond, S. R., & Wang, X., (2019), Hurricane boundary layer height relative to storm motion from gps dropsonde composites, *Atmosphere*, *10 6*, 339.

Reul, N., Chapron, B., Zabolotskikh, E., Donlon, C., Mouche, A., Tenerelli, J., Collard, F., Piolle, J.-F., Fore, A., Yueh, S., et al., (2017), A new generation of tropical cyclone size measurements from space, *Bulletin of the American Meteorological Society*, *98 11*, 2367–2385.

Reul, N., Tenerelli, J., Chapron, B., Vandemark, D., Quilfen, Y., & Kerr, Y., (2012), Smos satellite l-band radiometer: a new capability for ocean surface remote sensing in hurricanes, *Journal of Geophysical Research: Oceans*, *117 C2*.

Ricciardulli, L., Howell, B., Jackson, C. R., Hawkins, J., Courtney, J., Stoffelen, A., Langlade, S., Fogarty, C., Mouche, A., Blackwell, W., et al., (2023), Remote sensing

and analysis of tropical cyclones: current and emerging satellite sensors, *Tropical Cyclone Research and Review*.

Riehl, H., (1963), Some relations between wind and thermal structure of steady state hurricanes, *Journal of Atmospheric Sciences*, *20 4*, 276–287.

Riehl, H., & Malkus, J., (1961), Some aspects of hurricane daisy, 1958, *Tellus*, *13 2*, 181–213.

Robinson, A. R., (2012), *Eddies in marine science*, Springer Science & Business Media.

Rodgers, E., & Adler, R., (1981), Tropical cyclone rainfall characteristics as determined from a satellite passive microwave radiometer, *Monthly Weather Review*, *109 3*, 506–521.

Rodgers, E., Gentry, R. C., Shenk, W., & Oliver, V., (1979), The benefits of using short-interval satellite images to derive winds for tropical cyclones, *Monthly Weather Review*, *107 5*, 575–584.

Rodgers, E. B., Chang, S. W., & Pierce, H. F., (1994), A satellite observational and numerical study of precipitation characteristics in western north atlantic tropical cyclones, *Journal of Applied Meteorology and Climatology*, *33 2*, 129–139.

Ross, D., (1975), A comparison of skylab s-193 and aircraft views of surface roughness and a look toward seasat, *NASA. Lyndon B. Johnson Space Center NASA Earth Resources Surv. Symp., Vol. 1-C, M-2*.

Ruf, C. S., Gleason, S., Jelenak, Z., Katzberg, S., Ridley, A., Rose, R., Scherrer, J., & Zavorotny, V., (2012), The cygnss nanosatellite constellation hurricane mission, *2012 IEEE International Geoscience and Remote Sensing Symposium*, 214–216.

Sampson, C. R., Fukada, E. M., Knaff, J. A., Strahl, B. R., Brennan, M. J., & Marchok, T., (2017), Tropical cyclone gale wind radii estimates for the western north pacific, *Weather and Forecasting*, *32 3*, 1029–1040, https://doi.org/10.1175/WAF-D-16-0196.1

Sampson, C. R., & Schrader, A. J., (2000), The automated tropical cyclone forecasting system (version 3.2), *Bulletin of the American Meteorological Society*, *81 6*, 1231–1240.

Sapp, J., Jelenak, Z., Chang, P., Shoup, C., & Carswell, J., (2022), Processing of high-resolution hurricane ida boundary layer winds from the iwrap instrument on the noaa wp-3d aircraft, *IGARSS 2022-2022 IEEE International Geoscience and Remote Sensing Symposium*, 7286–7289.

Schenkel, B. A., & Hart, R. E., (2012), An examination of tropical cyclone position, intensity, and intensity life cycle within atmospheric reanalysis datasets, *Journal of Climate*, *25 10*, 3453–3475.

Schloemer, R. W., (1954), *Analysis and synthesis of hurricane wind patterns over lake okeechobee, florida*, US Department of Commerce, Weather Bureau.

Schreck III, C. J., Knapp, K. R., & Kossin, J. P., (2014), The impact of best track discrepancies on global tropical cyclone climatologies using ibtracs, *Monthly Weather Review*, *142 10*, 3881–3899.

Schubert, W. H., & Hack, J. J., (1982), Inertial stability and tropical cyclone development, *Journal of the Atmospheric Sciences*, *39 8*, 1687–1697.

Schubert, W. H., & Hack, J. J., (1983), Transformed eliassen balanced vortex model, *Journal of Atmospheric Sciences*, *40 6*, 1571–1583.

Schubert, W. H., Slocum, C. J., & Taft, R. K., (2016), Forced, balanced model of tropical cyclone intensification, *Journal of the Meteorological Society of Japan. Ser. II*, *94 2*, 119–135.

Scowcroft, G., Ginis, I., Knowlton, C., Yablonsky, R., & Morin, H., (2011), *Hurricanes: science and society*, University of Rhode Island.

Shapiro, L. J., (1983), The asymmetric boundary layer flow under a translating hurricane, *Journal of Atmospheric Sciences*, *40 8*, 1984–1998.

Shapiro, L. J., & Willoughby, H. E., (1982), The response of balanced hurricanes to local sources of heat and momentum, *Journal of the Atmospheric Sciences*, *39 2*, 378–394.

Shibata, A., (2002), Amsr/amsr-e sea surface wind speed algorithm, *EORC Bull.*

Shibata, A., (2006), A wind speed retrieval algorithm by combining 6 and 10 ghz data from advanced microwave scanning radiometer: wind speed inside hurricanes, *Journal of oceanography*, *62*, 351–359.

Shutts, G., (1981), Hurricane structure and the zero potential vorticity approximation, *Monthly Weather Review*, *109 2*, 324–329.

Smith, R. K., (1981), The cyclostrophic adjustment of vortices with application to tropical cyclone modification, *Journal of Atmospheric Sciences*, *38 9*, 2021–2030.

Smith, R. K., & Montgomery, M. T., (2021), The generalized ekman model for the tropical cyclone boundary layer revisited: addendum, *Quarterly Journal of the Royal Meteorological Society*, *147 736*, 1471–1476.

Smith, R. K., & Montgomery, M. T., (2020), The generalized ekman model for the tropical cyclone boundary layer revisited: the myth of inertial stability as a restoring force, *Quarterly Journal of the Royal Meteorological Society*, *146 732*, 3435–3449.

Soloviev, A. V., Lukas, R., Donelan, M. A., Haus, B. K., & Ginis, I., (2014), The air-sea interface and surface stress under tropical cyclones, *Scientific reports*, *4 1*, 5306.

Soreide, N., Woody, C., & Holt, S., (2001), Overview of ocean based buoys and drifters: present applications and future needs, *MTS/IEEE Oceans 2001. An Ocean Odyssey. Conference Proceedings (IEEE Cat. No. 01CH37295)*, *4*, 2470–2472.

Sprigg, W. A., Bosart, L. F., Council, N. R., et al., (1998), *The meteorological buoy and coastal marine automated network for the united states*, National Academies Press.

Sroka, S., & Emanuel, K., (2021), A review of parameterizations for enthalpy and momentum fluxes from sea spray in tropical cyclones, *Journal of Physical Oceanography*, *51 10*, 3053–3069.

Sumner, H., (1944), North atlantic hurricanes and tropical disturbances of 1944, *Monthly Weather Review*, *72 12*, 237–240.

Torn, R. D., & Snyder, C., (2012), Uncertainty of tropical cyclone best-track information, *Weather and Forecasting*, *27 3*, 715–729.

Tsukada, T., & Horinouchi, T., (2023), Strong relationship between eye radius and radius of maximum wind of tropical cyclones, *Monthly Weather Review*, *151 2*, 569–588.

Uhlhorn, E. W., & Black, P. G., (2003), Verification of remotely sensed sea surface winds in hurricanes, *Journal of Atmospheric and Oceanic Technology*, *20 1*, 99–116.

Uhlhorn, E. W., Black, P. G., Franklin, J. L., Goodberlet, M., Carswell, J., & Goldstein, A. S., (2007), Hurricane surface wind measurements from an operational stepped frequency microwave radiometer, *Monthly Weather Review*, *135 9*, 3070–3085.

Vachon, P. W., Katsaros, K., Black, P., & Dodge, P., (1999), Radarsat synthetic aperture radar measurements of some 1998 hurricanes, *IEEE 1999 International Geoscience and Remote Sensing Symposium. IGARSS'99 (Cat. No. 99CH36293)*, *3*, 1631–1633.

Vachon, P. W., & Wolfe, J., (2010), C-band cross-polarization wind speed retrieval, *IEEE Geoscience and Remote Sensing Letters*, *8 3*, 456–459.

Velden, C., Harper, B., Wells, F., Beven, J. L., Zehr, R., Olander, T., Mayfield, M., Guard, C. “, Lander, M., Edson, R., et al., (2006), The dvorak tropical cyclone intensity estimation technique: a satellite-based method that has endured for over 30 years, *Bulletin of the American Meteorological Society*, *87 9*, 1195–1210.

Velden, C. S., & Herndon, D., (2020), A consensus approach for estimating tropical cyclone intensity from meteorological satellites: satcon, *Weather and Forecasting*, *35 4*, 1645–1662.

Velden, C. S., Olander, T. L., & Wanzong, S., (1998), The impact of multispectral goes-8 wind information on atlantic tropical cyclone track forecasts in 1995. part i: dataset methodology, description, and case analysis, *Monthly Weather Review*, *126 5*, 1202–1218.

Velden, C. S., Olander, T. L., & Zehr, R. M., (1998), Development of an objective scheme to estimate tropical cyclone intensity from digital geostationary satellite infrared imagery, *Weather and Forecasting*, *13 1*, 172–186.

Velden, C. S., & Smith, W. L., (1983), Monitoring tropical cyclone evolution with noaa satellite microwave observations, *Journal of Applied Meteorology and Climatology*, *22 5*, 714–724.

Vickery, P. J., Masters, F. J., Powell, M. D., & Wadhera, D., (2009), Hurricane hazard modeling: the past, present, and future, *Journal of Wind Engineering and Industrial Aerodynamics*, *97 7*, 392–405, https://doi.org/10.1016/j.jweia.2009.05.005

Vickery, P. J., & Wadhera, D., (2008), Statistical models of holland pressure profile parameter and radius to maximum winds of hurricanes from flight-level pressure and h* wind data, *Journal of Applied Meteorology and climatology*, *47 10*, 2497–2517.

Vigh, J. L., & Schubert, W. H., (2009), Rapid development of the tropical cyclone warm core, *Journal of the Atmospheric Sciences*, *66 11*, 3335–3350.

Vogl, S., & Smith, R. K., (2009), Limitations of a linear model for the hurricane boundary layer, *Quarterly Journal of the Royal Meteorological Society: A journal of the atmospheric sciences, applied meteorology and physical oceanography*, *135 641*, 839–850.

Wang, S., & Toumi, R., (2022), On the intensity decay of tropical cyclones before landfall, *Scientific reports*, *12 1*, 3288.

Wang, Y., & Pu, Z., (2021), Assimilation of radial velocity from coastal nexrad into hwrf for improved forecasts of landfalling hurricanes, *Weather and Forecasting*, *36 2*, 587–599.

Weinkle, J., Landsea, C., Collins, D., Musulin, R., Crompton, R. P., Klotzbach, P. J., & Pielke Jr, R., (2018), Normalized hurricane damage in the continental united states 1900–2017, *Nature Sustainability*, *1 12*, 808–813.

Weissman, D. E., King, D. B., & Thompson, T. W., (1979), Relationship between hurricane surface winds and l-band radar backscatter from the sea surface, *Journal of Applied Meteorology and Climatology*, *18 8*, 1023–1034.

Whiton, R. C., Smith, P. L., Bigler, S. G., Wilk, K. E., & Harbuck, A. C., (1998a), History of operational use of weather radar by us weather services. part i: the pre-nexrad era, *Weather and Forecasting*, *13 2*, 219–243.

Whiton, R. C., Smith, P. L., Bigler, S. G., Wilk, K. E., & Harbuck, A. C., (1998b), History of operational use of weather radar by us weather services. part ii: development of operational doppler weather radars, *Weather and forecasting*, *13 2*, 244–252.

Willoughby, H., Clos, J., & Shoreibah, M., (1982), Concentric eye walls, secondary wind maxima, and the evolution of the hurricane vortex, *Journal of Atmospheric Sciences*, *39 2*, 395–411.

Willoughby, H. E., Darling, R., & Rahn, M., (2006), Parametric representation of the primary hurricane vortex. part ii: a new family of sectionally continuous profiles, *Monthly weather review*, *134 4*, 1102–1120.

Withee, G. W., (1975), *Buoy observations during hurricane eloise, september 19 to october 11, 1975: data report*, National Oceanic; Atmospheric Administration, Environmental Sciences ...

Wood, V. T., White, L. W., Willoughby, H. E., & Jorgensen, D. P., (2013), A new parametric tropical cyclone tangential wind profile model, *Monthly weather review*, *141 6*, 1884–1909.

Young, I. R., (1993), An estimate of the geosat altimeter wind speed algorithm at high wind speeds, *Journal of Geophysical Research: Oceans*, *98 C11*, 20275–20285.

Yueh, S. H., Fore, A. G., Tang, W., Hayashi, A., Stiles, B., Reul, N., Weng, Y., & Zhang, F., (2016), Smap l-band passive microwave observations of ocean surface wind during severe storms, *IEEE Transactions on Geoscience and Remote Sensing*, *54 12*, 7339–7350.

Yueh, S. H., Stiles, B. W., Tsai, W.-Y., Hu, H., & Liu, W. T., (2001), Quikscat geophysical model function for tropical cyclones and application to hurricane floyd, *IEEE transactions on geoscience and remote sensing*, *39 12*, 2601–2612.

Yurchak, B. S., (2007), Description of cloud-rain bands in a tropical cyclone by a hyperbolic-logarithmic spiral, *Russian Meteorology and Hydrology*, *32 1*, 8–18.

Zabolotskikh, E. V., Reul, N., & Chapron, B., (2015), Geophysical model function for the amsr2 c-band wind excess emissivity at high winds, *IEEE Geoscience and Remote Sensing Letters*, *13 1*, 78–81.

Zagrodnik, J. P., & Jiang, H., (2013), Investigation of pr and tmi version 6 and version 7 rainfall algorithms in landfalling tropical cyclones relative to the nexrad stage-iv multisensor precipitation estimate dataset, *Journal of Applied Meteorology and Climatology*, *52 12*, 2809–2827.

Zhang, B., & Perrie, W., (2012), Cross-polarized synthetic aperture radar: a new potential measurement technique for hurricanes, *Bulletin of the American Meteorological Society*, *93 4*, 531–541.

Zhang, B., Perrie, W., Zhang, J. A., Uhlhorn, E. W., & He, Y., (2014), High-resolution hurricane vector winds from c-band dual-polarization sar observations, *Journal of Atmospheric and Oceanic Technology*, *31 2*, 272–286.

Zhang, C., Foltz, G. R., Chiodi, A. M., Mordy, C. W., Edwards, C. R., Meinig, C., Zhang, D., Mazza, E., Cokelet, E. D., Burger, E. F., et al., (2023), Hurricane observations by uncrewed systems, *Bulletin of the American Meteorological Society*, *104 10*, E1893–E1917.

Zhang, J. A., & Uhlhorn, E. W., (2012), Hurricane sea surface inflow angle and an observation-based parametric model, *Monthly Weather Review*, *140 11*, 3587–3605.

Zhou, Y., Zhao, J., Zhan, R., Chen, P., Wu, Z., & Wang, L., (2021), A logistic-growth-equation-based intensity prediction scheme for western north pacific tropical cyclones, *Advances in Atmospheric Sciences*, *38 10*, 1750–1762.

COLLEGES SCIENCES
BRETAGNE POUR L'INGENIEUR
LOIRE ET LE NUMERIQUE

IMT Atlantique
Bretagne-Pays de la Loire
École Mines-Télécom

Titre : Dynamique du cyclone tropical révélée par observations satellites de la vitesse des vents de surface : la contribution majeure de la structure du vent de surface près du cœur

Mot clés : Cyclones tropicaux ; Interactions air-mer ; Observations par satellite ; Télédétection

Résumé : Malgré les avancées dans la prédiction de la trajectoire des cyclones tropicaux et des vitesses de vent en périphérie du système, la représentation numérique des vents les plus forts associés aux événements les plus intenses demeure une question ouverte, principalement en raison de la faible taille du cœur du cyclone et de la difficulté à comprendre et résoudre les échanges turbulents entre l'océan et l'atmosphère. Des limites observationnelles ont longtemps entravé des mesures précises de la surface océanique près du cœur dans des conditions de vents forts, tandis que les satellites géostationnaires aident à caractériser les motifs nuageux mais ne donnent pas d'information directe sur l'interface air-mer. Récemment, le radar à ouverture synthétique (SAR) a émergé comme une technologie satellitaire prometteuse capable de produire des mesures à haute résolution et bidimensionnelles des vitesses du vent à la surface de l'océan, grâce à de nouveaux modes d'acquisition et à des développements algorithmiques. Compte tenu de ces nouvelles opportunités d'observation, nous explorons la contribution des caractéristiques structurelles près du cœur, exclusivement discernables à travers des instruments haute résolution, à la dynamique des cyclones. En utilisant un cadre théorique simple et examinant sa cohérence avec les mesures SAR, nous démontrons que les vents en surface près du cœur controllent l'évolution de la structure du vent du cyclone. Le cadre développé permet d'illustrer comment les futures mesures des caractéristiques de la couche limite océan-atmosphère pourraient bénéficier du suivi à court et à long terme des cyclones tropicaux.

Title: Tropical cyclone dynamics revealed by satellite ocean surface wind speeds observations: the key contribution of the near-core surface wind structure

Keywords: Tropical cyclones ; Air-sea interactions ; Satellite observations ; Remote sensing

Abstract: Despite advances in predicting the tropical cyclones (TCs) trajectory and outer-core wind speeds, the numerical representation of the strongest winds associated with the most intense events is still an open issue, essentially because of the small radial extent of the TC core and the difficulty in understanding and resolving turbulent air-sea exchanges. Observational limitations have for a long time hindered accurate measurements of the ocean surface near the core region in extreme wind conditions, while geostationary satellites help characterizing the cloud patterns but lack direct information on the air-sea interface. Recently, synthetic aperture radar (SAR) has emerged as a promising satellite technology capable of producing high-resolution two-dimensional measurements of the ocean surface wind speeds, thanks to new acquisition modes and algorithmic developments. Given these new observational opportunities, we investigate the contribution of near-core structural features, exclusively discernible through high-resolution instruments, to the TC dynamics. Using a simple theoretical framework and examining its consistency with SAR measurements, we demonstrate that the near-core surface winds modulate the evolution of the TC wind structure. The developed framework allows to illustrate how future measurements of ocean-atmosphere boundary layer characteristics could benefit the short- and long-term monitoring of TCs.